Journal of Biomechanics 206 (2026) 113531



Contents lists available at ScienceDirect

Journal of Biomechanics

journal homepage: www.elsevier.com/locate/jbiomech



Topological analysis of bladder filling

Arturo Tozzi

ASL Napoli 1 Centro, Distretto 27, Via Comunale del Principe 13/a, 80145 Naples, Italy

A R T I C L E I N F O

Keywords:
Urodynamics
Persistent homology
Biomechanical modeling
Geometric invariants
Stability metrics

A B S T R A C T

Bladder function is assessed through pressure–volume relations, compliance indices and flow measurements, while structural evaluation relies primarily on qualitative imaging descriptors. These approaches do not formally quantify how bladder geometry evolves during filling. To distinguish structural reorganization from pure mechanical stiffness, we developed a simulation-based topological analysis of bladder filling grounded in mechanical parameters derived from the literature. Progressive filling was modeled under quasi-static conditions, generating multi-volume geometries from which spatial descriptors were computed. Inspired by the Freudenthal suspension theorem, filling was interpreted as a dimensional expansion process, while structural stability was evaluated by examining whether geometric invariants remain preserved across increasing volumes. Simulated smooth expansion and controlled structural perturbations were compared under identical loading conditions. We found that pressure trajectories and wall stress estimates were similar across configurations when compliance was matched, whereas geometric descriptors exhibited divergent volume-indexed stability profiles in the presence of remodeling. Computable instability measures detected progressive spatial heterogeneity despite preserved global pressure behavior. Providing quantitative measure of geometric continuity across successive filling states, our approach suggests that structural remodeling becomes detectable before conventional functional impairment is apparent. Progressive surface irregularity can emerge even when compliance, detrusor pressure and flow parameters remain within reference limits. In addition, serial imaging over time may reveal increasing instability in shape organization across filling cycles, allowing identification of individuals at higher risk of diverticula formation, functional decompensation or structural complications despite stable pressure measurements.

1. Introduction

Quantitative evaluation of bladder function is primarily based on cystometry and pressure–flow studies that assess compliance, capacity, detrusor overactivity, etc (Rosier et al. 2017; Gajewski et al. 2019; Do et al. 2021; Rosen et al. 2021; Sekerci et al. 2023; Sinha 2024; Vuthiwong et al. 2024; Nguyen and Nadeau 2026). Structural evaluation relies on imaging modalities including ultrasound, computed tomography and magnetic resonance imaging to measure wall thickness, residual volume and gross abnormalities (Tessi et al. 2021; Srivastava, Dhyani, and Dighe 2024; Begaj et al. 2025). Biomechanical investigations complement these methods by modeling the bladder as a pressure vessel with hyperelastic wall behavior to estimate stress–strain relationships (Wang et al. 2009; Pillsbury, Kothera, and Wereley 2015; Jokandan et al. 2018; Philyppov et al. 2022). These approaches relegate geometry to a secondary descriptive role rather than treating it as a primary quantitative variable. Surface irregularities, including trabeculation and diverticula, are usually classified qualitatively, while mechanical models rely on simplified assumptions like spherical symmetry.

We performed a simulation that integrated pressure–volume dynamics with explicit geometric reconstruction and quantitative stability analysis of the bladder lumen. Our analysis is inspired by the Freudenthal suspension theorem from algebraic topology, which formalizes conditions under which structural features remain stable when a space is expanded in dimension (Freudenthal 1938; Whitehead 1953). Translating this idea to bladder mechanics, we treated progressive filling as a geometric expansion process, examining whether intrinsic structural features remain invariant across increasing volumes. If the lumen behaves analogously to a topological stable suspension, expansion preserves its essential organization; if not, detectable transitions emerge in the quantitative descriptors.

Operationally, we tested whether gradual bladder expansion preserved structural coherence or induced measurable spatial transitions detectable through surface-based descriptors. We modeled quasi-static

E-mail address: tozziarturo@libero.it.

https://doi.org/10.1016/j.jbiomech.2026.113531
Accepted 16 August 2026
Available online 17 August 2026
0021-9290/© 2026 Elsevier Ltd. All rights are reserved, including those for text and data mining, AI training, and similar technologies.

bladder filling using literature-derived parameters for capacity, compliance, wall thickness and elastic response, reconstructing wall geometry across increasing volumes. Then, at each filling step, we assessed whether shape changes remained smooth or whether irregularities emerged or amplified. To move beyond simplified isotropic expansion, we also introduced controlled perturbations to mimic localized protrusions and circumferential corrugations. For each volume state, we computed global mechanical quantities and spatially resolved surface measures, extracting cross-sectional profiles and volume-indexed descriptors to track radial feature evolution across successive filling levels. Our strategy shifts the focus from isolated scalar metrics to the continuity and stability of geometric organization during filling.

We will proceed as follows: first, the literature-based mechanical and geometric parameters are defined and the simulation protocol is described. Then, pressure, stress and geometric outputs are presented together with stability metrics. Finally, our results are interpreted within the context of quantitative bladder mechanics.

2. Methods

We studied a fully simulated urinary bladder filling experiment parameterized by quantitative values reported in clinical and biomechanical literature. Rather than investigating experimentally discriminable topological transitions, we sought to characterize how controlled geometric perturbations influence stability descriptors during simulated bladder expansion. We simulated multi-volume bladder geometries, intravesical pressure trajectories and wall stress–strain behavior under quasi-static filling. Then we derived lumen surfaces and computed volume-indexed topological descriptors from triangulated meshes. We employed a pressure vessel approximation combined with an incompressible hyperelastic wall formulation, constraining capacity, compliance and wall thickness to published adult reference ranges. We aimed to identify experimentally discriminable signatures defined as a stability profile of persistent homology along the filling coordinate, namely a regime in which distances between successive persistence diagrams remained below a predefined repeatability threshold across a stable volume interval. In parallel, we assessed the emergence of reproducible change points following the introduction of controlled structural perturbations like simulated diverticula, to determine whether these alterations generated detectable topological transitions.

Our analysis was based on measurable geometric features derived from simulated bladder surfaces. Adult bladder capacity was set within 300–600 mL, consistent with standard urodynamic summaries, and simulations used a target maximal capacity $V_{\max} = 500$ mL unless otherwise stated (Drake et al. 2018). Compliance was defined as

$$C = \frac{\Delta V}{\Delta P} \tag{1}$$

where C denotes compliance, ΔV the change in volume and ΔP the corresponding pressure variation. A reference scenario was constrained by $C = 60$ mL/cm H_2O, while a low-compliance scenario used $C = 10$ mL/cm H_2O (Abrams et al. 2002). Pressure units were standardized according to

$$1\ \mathrm{cmH_2O} = 98.0665\ \mathrm{Pa} \tag{2}$$

and

$$1\ \mathrm{mmHg} = 133.322\ \mathrm{Pa} \tag{3}$$

allowing conversion between commonly used clinical and mechanical units. Resting pressure offset was fixed at $P_0 = 5$ cm H_2O to represent baseline cystometric pressure (Abrams et al. 2002). Wall thickness was initialized at $t_0 = 0.30$ cm for the distended state and subsequently varied between 0.20 and 0.50 cm during sensitivity analyses (Tanaka et al. 2008). Effective Young's modulus was varied across physiologically plausible ranges reported for bladder tissue (Nagle et al. 2017).

The bladder was idealized as a spherical pressure vessel with radius R and wall thickness t. Volume was calculated as

$$V = \frac{4}{3}\pi R^3 \tag{4}$$

which allowed direct conversion between filling volume and geometric dimensions. Intravesical pressure was described as

$$P(V) = P_0 + \frac{V - V_0}{C} + 2\max\left[e^{k(V-0.85V_{\max})} - 1, 0\right] \tag{5}$$

where $V_0 = 50$ mL represented the initial filling volume and $k = 0.08$ controlled the late nonlinear pressure rise near capacity. This expression generated pressure–volume trajectories that reproduced gradual filling followed by a steeper increase close to maximal volume.

Circumferential wall stress was estimated using Laplace's law (Berthoumieux et al. 2014; Pronina et al. 2018)

$$\sigma_\theta = \frac{PR}{2t} \tag{6}$$

where P denotes intravesical pressure, R bladder radius and t wall thickness. Although the bladder wall cannot be considered infinitely thin, this approximation provided a first-order estimate of filling-related stress. Radial incompressibility was imposed through

$$R^2 t = R_0^2 t_0 \tag{7}$$

ensuring that wall thickness decreased as radius increased. Consequently,

$$t = t_0 \left(\frac{R_0}{R}\right)^2 \tag{8}$$

was used throughout all simulations.

Wall mechanics were modeled using an incompressible Neo-Hookean constitutive law. The strain energy density was

$$W = \frac{E}{6(1+\nu)}(I_1 - 3) \tag{9}$$

where E denotes Young's modulus, ν Poisson's ratio and I_1 the first strain invariant. Poisson's ratio was fixed at $\nu = 0.49$ to approximate incompressibility. Equibiaxial stretch was defined as

$$\lambda = \frac{R}{R_0} \tag{10}$$

and the corresponding circumferential stress became

$$\sigma_\theta = \frac{E}{3(1+\nu)}\left(\lambda^2 - \lambda^{-4}\right) \tag{11}$$

Equilibrium between Equations (6) and (11) was solved numerically using Newton–Raphson iteration (Galántai 2000).

To simulate structural remodeling, localized geometric perturbations were introduced onto the spherical surface. The baseline radius was modified according to

$$R'(\theta) = R\left[1 + \alpha e^{-d(\theta)^2/(2\sigma^2)}\right] \tag{12}$$

where $d(\theta)$ denotes angular distance from the perturbation center, α controls protrusion amplitude and σ controls spatial spread. Values of α increased progressively with filling volume to mimic enlargement of localized structural irregularities. Additional corrugations were imposed through

$$R''(\theta) = R'(\theta)[1 + \varepsilon\sin(18\theta) + 0.6\varepsilon\sin(33\theta + 0.6)] \tag{13}$$

where ε controlled corrugation magnitude. These perturbations generated remodeled geometries containing localized protrusions and

circumferential irregularities resembling trabeculated surfaces.

Then, we performed direct geometric analysis of radial profiles. For each filling state, the bladder circumference was sampled at 720 angular positions. The resulting radial signal $r(\theta)$ was analyzed using peak-detection algorithms implemented in SciPy. Peak prominences were extracted and sorted in descending order to form a prominence vector

$$\mathbf{p}(V) = [p_1, p_2, \cdots, p_{25}] \tag{14}$$

where each component represents the prominence of a radial feature measured in centimeters.

Geometric stability was quantified by comparing prominence vectors obtained at consecutive filling volumes. The instability index was defined as

$$S = \|\mathbf{p}(V_{i+1}) - \mathbf{p}(V_i)\|_2 \tag{15}$$

where $\|\cdot\|_2$ denotes the Euclidean norm. Small values of S indicate preservation of geometric organization between consecutive filling states, whereas larger values indicate progressive structural divergence. This quantity corresponds directly to the stability profile shown in Fig. 1C. Because the instability index is expressed in centimeters and is computed directly from radial deviations, its magnitude has a straightforward geometric interpretation. Values on the order of 0.1 cm correspond to deviations comparable to the dimensions of the imposed surface irregularities, whereas values approaching zero indicate near-preservation of geometric organization between consecutive filling states.

Spatial deviation between smooth and remodeled geometries was computed as

$$\Delta R(\theta, V) = R_{\text{remod}}(\theta, V) - R_{\text{smooth}}(V) \tag{16}$$

and visualized as a two-dimensional heatmap across angular position and filling volume. Positive values correspond to outward displacement relative to isotropic expansion.

To simulate localized structural remodeling, outward surface perturbations were introduced onto the bladder wall using a parameterized diverticulum model. The perturbation amplitude parameter α ranged

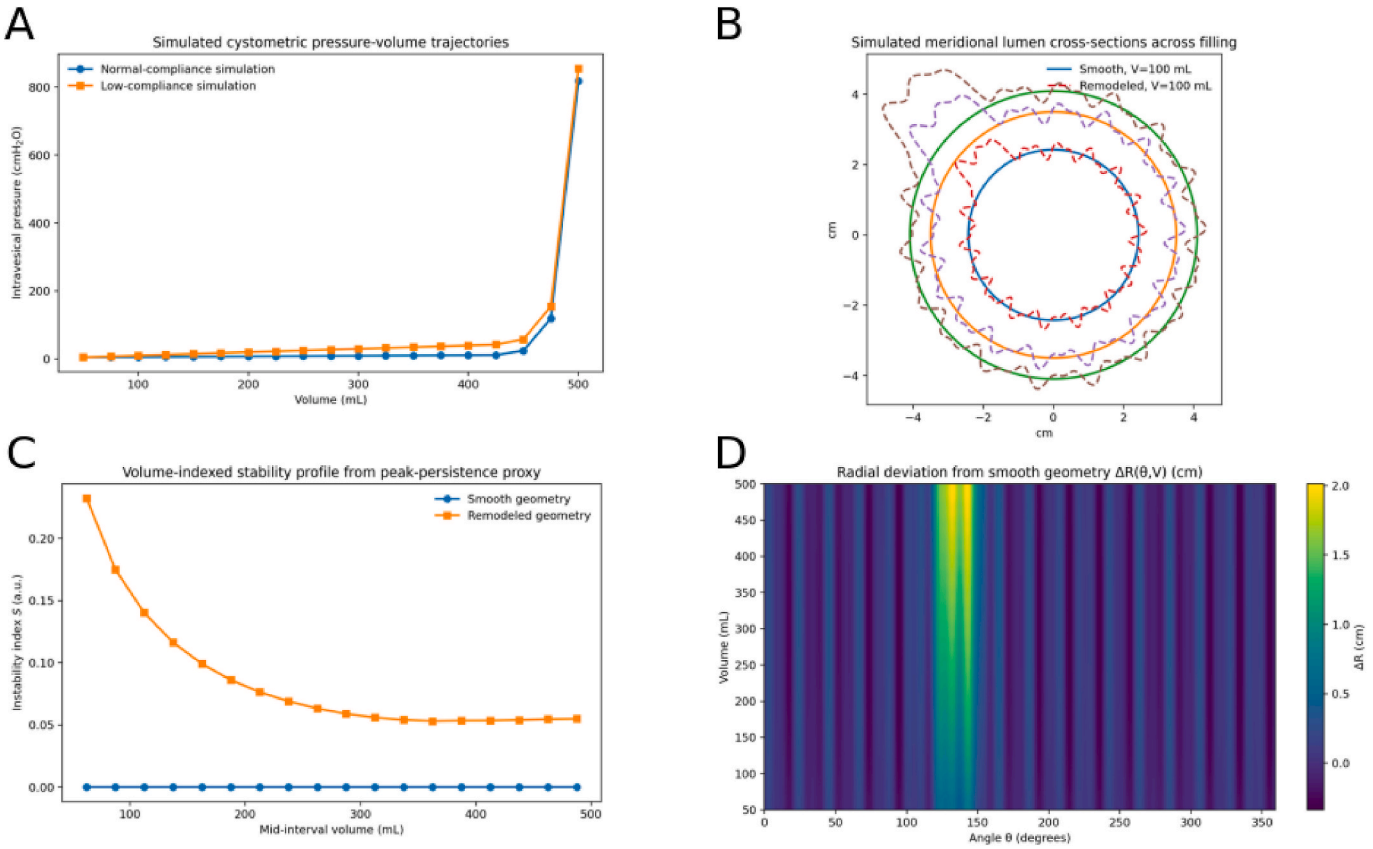


Fig. 1. Composite simulation panel summarizing pressure dynamics, geometric remodeling, stability behavior and spatial deviation during bladder filling. Together, the panels integrate mechanical loading, geometric deformation and quantitative stability analysis within a unified simulated experiment. For each filling level, the smooth geometry serves as the isotropic reference configuration derived from uniform radial expansion, whereas the remodeled geometry includes localized protrusion and circumferential corrugation. **Panel A**. Simulated cystometric pressure–volume curves from 50 to 500 mL. The normal-compliance curve shows a gradual pressure increase with filling, followed by a late steep rise near capacity. The low-compliance curve exhibits a statistically significant steeper pressure increase throughout filling, reflecting reduced distensibility. **Panel B**. Simulated meridional cross-sections of the bladder lumen at representative volumes. The smooth configuration expands isotropically with volume, whereas the remodeled configuration includes a localized outward protrusion combined with circumferential surface corrugations that persist across filling states. **Panel C**. Volume-indexed stability profile derived from consecutive differences in radial peak-prominence spectra. The smooth geometry exhibits zero successive variation because isotropic expansion preserves angular organization across all filling states. The remodeled geometry shows a measurable instability signal generated by the evolving protrusion and circumferential corrugations. Instability is greatest at lower filling volumes, where the perturbation represents a larger fraction of the bladder circumference, and progressively decreases with expansion as the relative influence of the protrusion diminishes. The resulting low plateau at higher volumes indicates persistence of structural irregularity despite reduced relative geometric impact, rather than disappearance of the perturbation itself. **Panel D**. Heatmap of radial deviation between remodeled and smooth geometries across angular position and volume. The plotted quantity represents the pointwise radial difference obtained by subtracting the smooth radius from the remodeled radius at the same angular coordinate and volume. The horizontal axis corresponds to angular position along the bladder circumference and the vertical axis represents filling volume. Warmer colors indicate larger outward displacement of the remodeled surface relative to the smooth configuration, while cooler tones indicate minimal deviation.

from 0.37 at low filling volumes to 0.50 near maximal filling, while the spatial spread parameter σ was fixed at 0.20 rad. Progressive increase in α was introduced to mimic the increasing visibility and geometric influence of a localized outpouching during bladder expansion, whereas the fixed σ ensured a consistent angular extent of the lesion throughout filling. These values generated maximal outward deviations of approximately 1 cm relative to the corresponding smooth geometry at high filling volumes. At maximal capacity, our diverticulum model generated protrusions extending approximately 1.0 cm beyond the corresponding smooth geometry. This magnitude was selected to represent a clearly visible localized deformation rather than a microscopic irregularity. The imposed corrugations produced additional surface undulations with amplitudes below 0.1 cm. Consequently, the simulated remodeling more closely resembled moderate trabeculation associated with a focal diverticular outpouching than isolated fine-scale wall roughness.

The chosen parameters range was not intended to reproduce a specific pathological condition, but rather to create an identifiable localized deformation comparable in scale to moderate diverticular protrusions and trabeculation-associated irregularities described in imaging studies. Introducing controlled perturbations of known amplitude and spatial extent allowed quantitative assessment of how localized remodeling could influence global geometric stability descriptors during filling, providing a reproducible reference against which sensitivity analyses and stability metrics could be evaluated.

A sensitivity analysis was performed to evaluate the robustness of the instability index with respect to uncertainty in the principal mechanical parameters adopted in the simulations. The objective was to determine whether the observed instability patterns primarily reflected the presence of geometric remodeling or were strongly influenced by variations in the underlying biomechanical assumptions. Three parameters were investigated: bladder compliance, wall thickness, and Young's modulus. Compliance was varied between 10 and 60 mL/cm H_2O, spanning the range between low-compliance and reference conditions. Wall thickness was varied between 0.20 and 0.50 cm, while Young's modulus was varied across the physiologically plausible interval reported in the literature and used throughout the simulations.

For each parameter under investigation, all remaining parameters were maintained at their reference values. The complete filling simulation was then repeated across the entire volume range, and the instability index was recomputed at every filling step. This procedure generated a series of parameter-specific sensitivity curves describing the evolution of geometric instability under varying mechanical conditions. Separate analyses were therefore obtained for compliance, wall thickness, and elastic modulus.

To quantify parameter dependence, relative sensitivity coefficients were calculated according to

$$S_p = \frac{\Delta I / I_0}{\Delta p / p_0} \tag{17}$$

where I_0 denotes the instability index obtained using the reference parameter set, p_0 the reference value of the parameter under investigation, and ΔI and Δp represent the corresponding changes in instability index and parameter value, respectively. This dimensionless coefficient measures the fractional variation in instability relative to the fractional variation of the mechanical parameter. Values close to zero indicate limited influence of the parameter on geometric instability, whereas larger values indicate stronger dependence. The resulting sensitivity curves were used to assess the relative contributions of compliance, wall thickness, and tissue stiffness to the observed instability profiles and to determine whether the detected geometric signatures remained robust across physiologically plausible parameter ranges.

All simulations were implemented in Python. NumPy was used for numerical operations and matrix calculations, SciPy for nonlinear solvers and peak-detection procedures, and Matplotlib for graphical visualization. Fixed random seeds were used whenever stochastic perturbations were introduced to ensure reproducibility of the simulated outputs.

3. Results

The quantitative outputs from the simulated filling experiment are reported here, including pressure–volume behavior, geometric evolution, spatial deviation fields, volume-indexed stability metrics and sensitivity analyses of the main mechanical parameters.

Pressure dynamics and geometric deformation. Simulated cystometric trajectories reproduced the expected qualitative separation between normal- and low-compliance regimes (Fig. 1A). Across the examined range from 50 to 500 mL, the normal-compliance curve showed a gradual increase in pressure followed by a late nonlinear rise near maximal filling, whereas the low-compliance trajectory displayed a consistently steeper slope throughout the filling interval. At 500 mL, simulated intravesical pressure reached 13.5 cm H_2O in the normal-compliance case and 50.0 cm H_2O in the low-compliance case, reflecting the imposed compliance parameters.

Geometric reconstruction demonstrated monotonic radial expansion in the smooth configuration, with radius increasing from 2.36 cm at 50 mL to 4.30 cm at 500 mL. In the remodeled configuration (Fig. 1B), localized protrusions generated angularly heterogeneous profiles, producing maximal outward deviations of 1.03 cm at 500 mL relative to the smooth geometry.

The heatmap of radial deviation (Fig. 1D) revealed a confined angular sector with progressive amplification of deviation as volume increased, while the remaining circumference remained close to the smooth reference.

These findings demonstrate controlled divergence in spatial configuration under identical global loading conditions, thereby providing a substrate for quantitative stability analysis.

Volume-indexed stability and sensitivity analysis. The instability index derived from successive differences in radial prominence spectra showed distinct behavior between conditions (Fig. 1C). For the smooth geometry, the instability index remained zero across all consecutive filling intervals because isotropic scaling preserved angular organization exactly. In contrast, the remodeled geometry exhibited a mean instability index of 0.086 cm across intervals.

The instability profile displayed its largest values at low filling volumes and progressively decreased during subsequent expansion. This behavior resulted from the normalization effect of increasing bladder radius. At low volumes, the imposed protrusion constituted a relatively large fraction of the bladder circumference, therefore generating pronounced changes in prominence spectra between consecutive filling states. As volume increased, the global radius expanded more rapidly than the perturbation amplitude, reducing the relative influence of the protrusion on the overall geometry. Consequently, successive prominence vectors became increasingly similar, producing a gradual decline of the instability index toward a low plateau rather than complete disappearance of the perturbation.

Sensitivity analyses were performed by varying compliance, wall thickness, and Young's modulus across the ranges defined in the Methods. Changes in compliance produced the largest effect on pressure–volume trajectories but only modest effects on geometric instability, whereas the perturbation geometry was maintained throughout the simulations. Variations in wall thickness altered wall stress estimates substantially but had little influence on geometric instability. Young's modulus influenced the degree of expansion under loading, therefore producing moderate variation in instability magnitude. Across all explored parameter combinations, the instability index was nonzero whenever structural perturbations were present and was zero in the absence of perturbation, indicating that the main determinant of instability was geometric remodeling rather than the specific mechanical parameter values.

These results suggest that the instability metric responds primarily to

geometric remodeling, while remaining comparatively robust to physiologically plausible variations in mechanical parameters.

Overall, our results link mechanical loading to spatial organization, showing that, depending on surface configuration, simulated bladder filling under identical pressure trajectories can produce either geometrically stable expansion or measurable structural divergence.

4. Conclusions

We asked whether progressive bladder filling modeled under physiologically grounded mechanical parameters preserves global geometric organization or produces measurable structural divergence that cannot be inferred from pressure–volume relations alone. The question was not whether pressure rises with filling, which is well established, but whether the spatial configuration of the lumen evolves coherently across volumes or undergoes detectable transitions when structural perturbations are present. Inspired by suspension topological concepts, we simulated quasi-static filling using literature-based values for capacity, compliance, wall thickness and elastic response. Then, we generated multi-volume geometries under both smooth and remodeled conditions, allowing separation of purely mechanical effects from geometric reorganization. We found that identical pressure trajectories can be associated with either uniform isotropic expansion or progressive angular heterogeneity, depending solely on surface configuration. In the smooth condition, geometric scaling occurred without alteration of radial structure across volumes, whereas the remodeled condition produced consistent, volume-dependent deviations localized in angular space. Our stability metric detected these differences systematically across consecutive filling intervals, while remaining null in the absence of structural perturbation. Because both configurations were subjected to the same loading rules, the detected divergence reflects geometric organization rather than mechanical intensity. Therefore, our findings suggest that geometric continuity across filling states constitutes a measurable property distinct from compliance or peak pressure.

Our computable descriptor quantifies how bladder shape evolves across filling states, rather than evaluating isolated static measurements. Unlike standard urodynamic indices or imaging assessments, our approach generates an explicit numerical stability profile derived from successive geometric configurations. This quantity is not directly accessible through compliance, capacity, wall thickness or peak pressure alone, because it depends on the continuity of spatial organization across volumes. Our formal measure of structural evolution can be computed from segmented surfaces without requiring additional invasive procedures.

Our work has limitations. The study is entirely simulation-based and all parameters were derived from literature values. No patient data, imaging datasets or experimental measurements were used for calibration or validation. Consequently, our findings describe the behavior of the proposed descriptors within a controlled computational environment rather than their clinical performance. Validation against pressure–volume recordings, ultrasound, magnetic resonance imaging, or cystoscopic observations is mandatory. Still, several simplifying assumptions were adopted. The bladder was represented as a sphere, although physiological and pathological bladders often deviate from spherical symmetry. Circumferential stress was estimated using the thin-shell Laplace approximation, while tissue mechanics were modeled using a Neo-Hookean constitutive law. These assumptions neglect layered anisotropy, regional compliance variation, viscoelasticity, active smooth-muscle contraction and neurogenic influences. The instability metric was derived from radial peak-prominence spectra, therefore constituting a geometric proxy rather than a direct computation of persistent homology. Although inspired by topological stability concepts, our descriptor quantifies morphological variation rather than strict topological transitions. In addition, the smooth reference geometry yields zero instability by construction, potentially increasing contrast between smooth and remodeled conditions.

The pressure–volume model includes an *ad hoc* exponential term introduced to reproduce the late pressure rise near capacity and not fitted to a specific experimental dataset. Likewise, the diverticular perturbations were designed as controlled geometric irregularities rather than validated anatomical reconstructions. Potential sources of bias include selection of literature-derived parameters, angular discretization, mesh resolution and sensitivity of peak-detection procedures. Although sensitivity analyses were performed for compliance, wall thickness and Young's modulus, the combined effects of spherical geometry, Laplace mechanics, Neo-Hookean behavior and perturbation rules on the resulting descriptors were not independently validated. Accordingly, the study should be regarded as a proof-of-concept numerical investigation rather than a validated representation of bladder physiology.

Our study identifies a simulation-derived pattern that could be investigated in future imaging studies involving clinical or experimental data. Our simulations suggest avenues for future research aimed at evaluating the physiological relevance and reproducibility of our geometric descriptors. First, our method enables detection of structural instability before pressure changes. Standard bladder assessment primarily relies on pressure–volume curves, compliance measurements and flow rates, all of which describe functional performance and detect impairment once mechanical consequences become measurable. Our suspension-based perspective shifts attention toward geometric behavior during expansion. If bladder filling behaves analogously to a stable suspension, structural topology remains invariant across volumes. Conversely, if small increments in volume produce disproportionate geometric reorganization, this points towards early structural remodeling. This behavior could reveal preclinical obstruction-induced trabeculation, early fibrosis or micro-diverticular formation before compliance measurably declines, thereby identifying instability at a stage not captured by pressure metrics alone. Practical applications include integration of geometric stability analysis into routine imaging workflows, enabling detection of structural instability before overt functional impairment.

Second, our approach can assess severity quantification. Pathological bladders frequently develop surface pockets, irregular protrusions, wall thickening and asymmetric expansion. These features alter the effective topological complexity of the lumen surface. Rather than describing these changes qualitatively, variation in topological invariants across filling volumes can be computed, e.g., through changes in Betti numbers or persistence intervals as a function of volume. Practically, a computable remodeling index may allow objective grading of surface irregularities, complementing visual cystoscopic assessment.

Third, our approach allows the separation of elasticity failure from topology failure. Two bladders may exhibit identical compliance curves while differing structurally: one may remain smooth but stiff, whereas another may be geometrically fragmented and unstable. Our stability analysis distinguishes pure mechanical stiffness from spatial reorganization. This distinction has implications for therapeutic decision-making, distinguishing mechanical stiffness from geometric fragmentation could support differential therapeutic planning, including anti-fibrotic treatment, outlet correction or surgical intervention.

Fourth, long-term progression could be predicted. If topology destabilizes under repeated filling cycles, longitudinal monitoring may reveal progressive divergence of geometric invariants. This divergence could identify patients predisposed to diverticular development, functional decompensation or congenital structural vulnerability, analogous to recognizing departure from a stable structural regime. Therefore, longitudinal stability metrics could provide quantitative follow-up after reconstructive procedures or in pediatric congenital conditions.

Fifth, our approach adds a geometric constraint layer to conventional urodynamics. Conventional bladder models emphasize local wall stress, smooth muscle contraction and neural regulation. Incorporating global geometric invariants, dimensional stability during expansion and structural robustness measures inserts a complementary layer of

analysis. The central question thus extends beyond how much pressure the bladder generates to how geometrically stable the bladder remains during volumetric expansion. This means that clinicians could assess not only pressure generation, but also the robustness of structural organization during expansion.

In summary, we developed a controlled simulation of bladder filling that combines mechanical loading with quantitative analysis of evolving surface geometry. Multi-volume configurations were compared through pressure trajectories, wall stress estimates and descriptors of geometric organization across filling states. Our simulations suggest that geometric divergence may emerge under identical loading conditions and can be characterized independently of global pressure behavior. Because the study is entirely simulation-based, our findings should be interpreted as a numerical exploration of geometric stability rather than evidence of physiological or clinical performance. Future experimental and imaging-based studies may determine whether our geometric signatures can provide information complementary to conventional urodynamic measurements.

CRediT authorship contribution statement

Arturo Tozzi: Writing – review & editing, Writing – original draft, Visualization, Validation, Supervision, Software, Resources, Project administration, Methodology, Investigation, Funding acquisition, Formal analysis, Data curation, Conceptualization.

Ethics approval and consent to participate

This research does not contain any studies with human participants or animals performed by the Author.

Consent for publication

The Author transfers all copyright ownership, in the event the work is published. The undersigned author warrants that the article is original, does not infringe on any copyright or other proprietary right of any third part, is not under consideration by another journal and has not been previously published.

Funding
none.

Authors contribution

The Author performed: study concept and design, acquisition of data, analysis and interpretation of data, drafting of the manuscript, critical revision of the manuscript for important intellectual content, statistical analysis, obtained funding, administrative, technical and material support, study supervision.

Declaration of generative AI and AI-assisted technologies in the writing process

During the preparation of this work, the author used ChatGPT 5.2 to assist with data analysis and manuscript drafting and to improve spelling, grammar and general editing. After using this tool, the author reviewed and edited the content as needed, taking full responsibility for the content of the publication.

Declaration of competing interest

The author declare that they have no known competing financial interests or personal relationships that could have appeared to influence the work reported in this paper.

References

Abrams, P., Cardozo, L., Khoury, S., Wein, A., 2002. Incontinence: 2nd International Consultation on Incontinence. Health Publication Ltd, Plymouth.

Begaj, K., Sperr, A., Jokisch, J.F., Clevert, D.A., 2025. Improved Bladder Diagnostics Using Multiparametric Ultrasound. Abdominal Radiology (New York) 50 (3), 1240–1253. https://doi.org/10.1007/s00261-024-04604-1.

Berthoumieux, H., Maître, J.-L., Heisenberg, C.-P., Jülicher, F., 2014. Active Elastic Thin Shell Theory for Cellular Deformations. New J. Phys. 16, 065005. https://doi.org/10.1088/1367-2630/16/6/065005.

Do, M.T., Kim, K., Kim, L., Im, Y.-J., Choi, Y.-H., Park, K., 2021. Ultrasonographic Cystometry for Neurogenic Bladder Using Elastography. Neurourol. Urodyn. 40 (1), 367–375. https://doi.org/10.1002/nau.24570.

Drake, M.J., Hashim, T., Abrams, R.J., et al., 2018. Fundamentals of Urodynamic Practice. Neurourol. Urodyn. 37 (S6), S1–S9.

Freudenthal, H., 1938. Über die Klassen der Sphärenabbildungen. I. Große Dimensionen. Compos. Math. 5, 299–314.

Gajewski, J.B., Gammie, A., Speich, J., Kirschner-Hermanns, R., De Wachter, S., Schurch, B., Korstanje, C., Valentini, F., Mohammad, S., Rahnama'i., 2019. Are There Different Patterns of Detrusor Overactivity Which Are Clinically Relevant? ICI-RS 2018. Neurourol. Urodyn. 38 (Suppl. 5), S40–S45. https://doi.org/10.1002/nau.23964.

Galántai, A., 2000. The Theory of Newton's Method. J. Comput. Appl. Math. 124 (1–2), 25–44. https://doi.org/10.1016/S0377-0427(00)00435-0.

Jokandan, M.S., Ajallouеian, F., Edinger, M., Stubbe, P.R., Baldursdottir, S., Chronakis, I. S., 2018. Bladder Wall Biomechanics: A Comprehensive Study on Fresh Porcine Urinary Bladder. J. Mech. Behav. Biomed. Mater. 79, 92–103. https://doi.org/10.1016/j.jmbbm.2017.11.034.

Nagle, A.S., Klausner, A.P., Varghese, J., Bernardo, R.J., Colhoun, A.F., Wayne Barbee, R., Carucci, L.R., Speich, J.E., 2017. Quantification of Bladder Wall Biomechanics during Urodynamics: A Methodologic Investigation Using Ultrasound. J. Biomech. 61 (August 12), 232–241. https://doi.org/10.1016/j.jbiomech.2017.07.028.

Nguyen, L.N., Nadeau, G., 2026. Detrusor Overactivity and Urodynamics. Neurourol. Urodyn. 45 (2), 279–285. https://doi.org/10.1002/nau.70113.

Philyppov, I.B., Sotkis, G.V., Danshyna, A.O., Yelyashov, S.I., Sharopov, B.R., Shuba, Y. M., 2022. Impairment of Urinary Bladder Mechanical Properties in Rat Model of Type 2 Diabetes. Neurourol. Urodyn. 41 (8), 1670–1678. https://doi.org/10.1002/nau.25024.

Pillsbury, T.E., Kothera, C.S., Wereley, N.M., 2015. Effect of Bladder Wall Thickness on Miniature Pneumatic Artificial Muscle Performance. Bioinspir. Biomim. 10 (5), 055006. https://doi.org/10.1088/1748-3190/10/5/055006.

Pronina, Y., Sedova, O., Grekov, M., Sergeeva, T., 2018. On Corrosion of a Thin-Walled Spherical Vessel under Pressure. Int. J. Eng. Sci. 130, 115–128. https://doi.org/10.1016/j.ijengsci.2018.05.004.

Rosen, D.P., Husmann, D.A., Mynderse, L.A., Kelly Jr, T.F., Alizad, A., Fatemi, M., 2021. Detrusor Overactivity Assessment Using Ultrasound Bladder Vibrometry. Physiol. Meas. 42 (10). https://doi.org/10.1088/1361-6579/ac2c5c.

Rosier, P.F.W.M., Schaefer, W., Lose, G., Goldman, H.B., Guralnick, M., Eustice, S., Dickinson, T., Hashim, H., 2017. International Continence Society Good Urodynamic Practices and Terms 2016. Neurourol. Urodyn. 36 (5), 1243–1260. https://doi.org/10.1002/nau.23124.

Sekerci, C.A., Tanidir, Y., Tarcan, T., Yucel, S., 2023. Consistency of Uroflowmetry Analysis in Children among Observers. Neurourol. Urodyn. 42 (3), 662–668. https://doi.org/10.1002/nau.25141.

Sinha, S., 2024. The Use of Uroflowmetry as a Diagnostic Test. Curr. Urol. Rep. 25 (5), 99–107. https://doi.org/10.1007/s11934-024-01200-0.

Srivastava, S., Dhyani, M., Dighe, M., 2024. Contrast-Enhanced Ultrasound (CEUS): Applications from the Kidneys to the Bladder. Abdominal Radiology (New York) 49 (11), 4092–4112. https://doi.org/10.1007/s00261-024-04388-4.

Tanaka, H., Matsuda, M., Moriya, K., Mitsui, T., Kitta, T., Nonomura, K., 2008. Ultrasonographic Measurement of Bladder Wall Thickness as a Risk Factor for Upper Urinary Tract Deterioration in Children with Myelodysplasia. J. Urol. 180 (1), 312–316. https://doi.org/10.1016/j.juro.2008.03.062.

Tessi, C., Burek, C.M., Sager, C., Szklarz, M.T., Vásquez, M., Imizcoz, F.L., Ruiz, J., Weller, S., Gomez, Y., Corbetta, J.P., 2021. Bladder Volume Assessment in Pediatric Patients with Neurogenic Bladder: Is Ultrasound an Accurate Method? Urology 147, 250–255. https://doi.org/10.1016/j.urology.2020.10.005.

Vuthiwong, J., G. Qu L., Stephen Whalen, and Joseph Gani, 2024. Is Detrusor Overactivity with Detrusor Underactivity Limited to the Elderly? Neurourol. Urodyn. 43 (7), 1582–1590. https://doi.org/10.1002/nau.25482.

Wang, C.-C., Nagatomi, J., Toosi, K.K., Yoshimura, N., Hsieh, J.-H., Chancellor, M.B., Sacks, M.S., 2009. Diabetes-Induced Alterations in Biomechanical Properties of Urinary Bladder Wall in Rats. Urology 73 (4), 911–915. https://doi.org/10.1016/j.urology.2008.11.026.

Whitehead, G.W., 1953. On the Freudenthal Theorems. Ann. Math. 57 (2), 209–228. https://doi.org/10.2307/1969855.

Check for updates

BRAIN CONNECTIVITY
Volume 00, Number 00, 2026
Mary Ann Liebert, A Part of Sage
© The Author(s)
DOI: 10.1177/21580014261479958

Local Interaction Rules Drive Global Organization of the Human Connectome

Arturo Tozzi

Abstract

Introduction: The human connectome exhibits nontrivial large-scale organization despite emerging from decentralized local biological interactions. Most existing generative models reproduce connectomic features through global optimization principles, predefined wiring targets, or developmental templates, leaving unresolved which properties arise from locality alone and which require additional nonlocal mechanisms.
Methods: We implemented a simulation framework showing that global coherence can emerge from local compatibility constraints. Networks were generated exclusively through bounded spatial interactions, probabilistic local edge formation, and suppression of incompatible configurations, without global objectives, target topologies, or long-range coordination. Simulated ensembles were analyzed using graph-theoretical metrics, scaling relationships, and rule-based structural classification relative to published reference values of human connectome descriptors.
Results: Simulations consistently generated mesoscopic organization characterized by high clustering, modular structure, motif enrichment, and strong short-range connectivity bias. Degree distributions were broad and right-skewed, while edge-length distributions showed pronounced spatial localization. In contrast, several higher-order integrative properties were not reproduced, including empirical connectivity scale, rich-club organization, and long-range hub-to-hub connectivity. Although global metrics displayed substantial quantitative divergence from reported empirical values, several structural regimes and scaling relationships were preserved across parameter ranges.
Discussion: Our results distinguish connectome properties structurally compatible with local compatibility constraints from those underdetermined under locality alone. We provide a diagnostic framework designed to isolate the explanatory contribution of local interaction rules to connectome organization through simulations that identify which structural properties emerge directly from locality and which require additional mechanisms beyond local constraints.

Keywords: mesoscopic organization; modularity; motif statistics; scale dependence; wiring cost

Impact Statement

We introduce a constraint-based framework for determining which features of human connectome organization can emerge from local interaction rules alone and which require additional mechanisms. By treating divergence from empirical connectomes as evidence of underdetermination rather than simply model error, we shift emphasis from reproducing network statistics to identifying their mechanistic requirements. Our results distinguish locally generated properties, including clustering, modular organization, motif enrichment and short-range wiring bias, from features associated with large-scale integration and hub organization. This framework provides a systematic baseline for evaluating when more complex developmental, anatomical or global mechanisms are necessary to explain connectome architecture.

Introduction

The organization of the human connectome has been extensively described in terms of global network properties such as modular structure, short path lengths, heterogeneous connectivity, and spatially constrained wiring (Ardesch et al., 2019; Elam et al., 2021; Axer and Amunts, 2022; Fan et al., 2022; Huang, Rolls et al., 2022; Fotiadis et al., 2024; Wu et al., 2024; Sun et al., 2025a; Sun et al., 2025b). Many modeling approaches attempt to account for these features by invoking global optimization principles, predefined wiring targets, or implicit system-level coordination (Roy et al., 2008; Janson and Marsden, 2021; Li et al., 2024). These approaches often assume that local biological units implicitly "know"

ASL Napoli 1 Centro, Distretto 27, Naples, Italy.

or approximate global objectives. This assumption is difficult to reconcile with the decentralized nature of neural development and plasticity, where neurons and local circuits operate under strictly bounded spatial, metabolic, and signaling constraints (Di Lullo and Kriegstein, 2017; Gennarini and Furley, 2017; Punovuori et al., 2021; Roth et al., 2021; Sun et al., 2023; Blackshaw and Cayouette, 2025). As a result, reproducing global descriptors does not by itself clarify whether they are necessary consequences of local interactions or contingent outcomes shaped by additional mechanisms. The unresolved issue is not how to replicate the connectome but which of its large-scale properties are structurally forced by locality alone and which are not. Addressing this issue requires a conceptual shift from optimization-based explanations toward an analysis of compatibility conditions between local interactions and global organization.

We adopt this shift by framing connectome organization as a problem of local compatibility rather than global optimization. Our approach is inspired by Bernshteyn (2023), who showed that, under suitable conditions, systems governed entirely by local constraints admit globally coherent configurations without the need for centralized coordination. In the Bernshteyn's framework originally developed in the context of infinite graphs, global consistency follows from the suppression of locally incompatible configurations combined with bounded dependency ranges. Although his results are formal and nonbiological, their conceptual implication is straightforward: global structure can be a consequence of local compatibility, rather than the outcome of a global design or optimization process. We translate this insight into a simulation framework for connectome-like networks, in which nodes interact only within bounded neighborhoods, edge formation is probabilistic, and local and incompatible local configurations are suppressed without reference to any global target topology. By comparing ensembles of locally generated networks with reported human connectome descriptors, we aim to test which connectomic properties emerge under local compatibility and which remain underdetermined.

We will proceed as follows. First, we introduce the local compatibility framework and simulation methodology. Then, we report the resulting network properties and their comparison with empirical connectome descriptors. Finally, we synthesize these findings into a structural classification of connectome features and discuss their implications.

Methods

We describe the procedure to generate connectome-like networks governed exclusively by local compatibility constraints. We include formal definition of local interaction rules, simulation procedures for network construction, and generation of network ensembles across defined parameter ranges. For each ensemble, graph-theoretical descriptors are computed and statistically analyzed using distributional comparisons, hypothesis testing, and effect size estimation relative to published reference values of human connectome metrics. To reduce the impact of scale mismatch, our analyses emphasize scale-invariant features, including distributional shape, normalized topology, and scaling behavior. Additional procedures for sensitivity analysis and quantitative classification are implemented to provide a reproducible framework for interpreting the relationship between simulated networks and empirical descriptors.

Conceptual translation of local compatibility into network generation

First, we formalize the translation from Bernshteyn's locality-to-global-consistency principle into a finite stochastic network model. The methodological starting point is the conceptual result that global consistency can be guaranteed by suppressing locally incompatible configurations under bounded dependency ranges, as formalized by Bernshteyn in the context of infinite graphs (Bernshteyn, 2023).

We translate this idea into a finite, spatially embedded network model by defining a graph with nodes and undirected edges. Nodes represent neural units and are embedded in a continuous three-dimensional space, with positions sampled independently from a uniform distribution. Nodes are not mapped to anatomical brain regions, and no atlas-based parcellation scheme is imposed: this allows our model to assess the structural consequences of local compatibility constraints independently of predefined anatomical organization or region-specific priors. Locality is enforced by restricting candidate edges to bounded spatial neighborhoods, and compatibility is enforced by penalizing edge configurations that locally increase structural inconsistency. No global objective function is defined or optimized. Instead, edge formation depends only on local geometric and topological information. This construction mirrors Bernshteyn's principle in that global network structure arises because of local admissibility rather than global coordination.

Spatial embedding and neighborhood restriction

Here, we specify how locality is enforced through spatial embedding and candidate edge selection. Each node is assigned a spatial coordinate. For each node, a finite candidate neighborhood is defined as the set of its nearest neighbors in Euclidean distance, where distances are computed as

$$d_{ij} = \| \mathbf{x}_i - \mathbf{x}_j \|_2$$

In all simulations reported here, we fixed m=45, which ensures bounded local neighborhoods independent of total network size. Candidate edges are defined as unordered pairs with or. This produces a candidate edge set $C \subset V \times V$ with cardinality $|C| = O(Nm)$, ensuring linear scaling with network size. No edges outside C are ever considered, enforcing strict locality. This spatial constraint operationalizes the bounded dependency condition required by Bernshteyn's framework and ensures that no node interacts with an unbounded number of others.

Initialization of the network state

The initial condition used to seed network growth is described here. The adjacency structure is initialized as an undirected graph in which each node is connected to its two nearest spatial neighbors. Formally, for each node, let

$$\mathcal{N}_i^{(2)} = \arg\min_{j \neq i}^{(2)} d_{ij}$$

The initial edge set is

$$E_0 = \bigcup_{i \in V} \{(i,j) : j \in \mathcal{N}_i^{(2)}\}$$

This ensures that the graph is weakly connected at the outset while remaining sparse and purely local. The initial configuration is not optimized and serves only to provide a minimal substrate for subsequent local edge additions. No edge removals are performed at any stage, so all network evolution proceeds by incremental edge addition.

Local compatibility rule and edge acceptance probability

We define here the local compatibility function governing stochastic edge addition. Edge addition proceeds by iterating over the candidate set and stochastically accepting edges based on a local compatibility score. For a candidate edge, we define two local quantities: the Euclidean distance and the number of common neighbors

$$c_{ij} = \mid \{k \in V : (i,k) \in E \wedge (j,k) \in E\} \mid$$

The local compatibility score is defined as

$$S_{ij} = \exp(-\eta d_{ij})(c_{ij}+1)^{\gamma}$$

where controls spatial decay and controls topological reinforcement. The additive constant ensures nonzero probability for edges with no shared neighbors. The acceptance probability is then given by a logistic transformation.

$$p_{ij} = \frac{S_{ij}}{1+S_{ij}}$$

An edge is added with probability, independently of all other edges. Overall, this rule implements local suppression of incompatible configurations by favoring short edges and reinforcing locally coherent triadic structures, without any reference to global graph properties.

Parameter values, ensemble construction, and sensitivity analysis

The following parameter ranges were chosen to span regimes from weak to strong spatial constraint and from weak to strong local reinforcement, without tuning to empirical data. All reported simulations use nodes and a target mean degree of approximately, corresponding to a target edge count. The parameters are independently sampled for each realization from uniform distributions

$$\eta \sim \mathcal{U}(1.5,4.0), \gamma \sim \mathcal{U}(0.6,2.2)$$

For each parameter pair, a single network realization is generated. The full ensemble consists of 40 independent networks. Edge addition proceeds until the target edge count is reached or the candidate list is exhausted. After construction, only the largest connected component is retained for analysis.

Empirical scope and robustness assessment

We restricted comparisons with human connectomes to published summary descriptors, normalized metrics, and scaling relationships rather than direct reprocessing of raw neuroimaging datasets. Our choice avoids graph-theoretical measures' variability introduced by heterogeneous acquisition protocols, preprocessing pipelines, and parcellation schemes. Our goal is not dataset-specific replication but evaluation of whether order of magnitude, scaling behavior, and structural organization of key connectome properties are compatible with purely local constraints. Accordingly, agreement was assessed primarily through statistical distributions, normalized topology, and structural regimes defined by explicit quantitative criteria rather than strict numerical correspondence.

Because our statistical comparisons are limited to published reference values, we do not provide direct validation against uniformly processed empirical datasets. To mitigate this limitation, our study extends beyond simple parameter sampling through systematic robustness assessment. Specifically, the coefficient of variation ($CV = \sigma/\mu$) was computed for all network metrics across independently generated ensembles. Still, relationships between model parameters and graph-theoretical measures were evaluated using Pearson correlation coefficients. This allowed us to quantify the stability of network properties across simulations and distinguish robust structural patterns from parameter-dependent fluctuations within the explored parameter space. Together, our procedures provide a reproducible framework for assessing the stability of network organization under local compatibility constraints, while recognizing that comprehensive empirical validation would require direct comparison with connectomes processed under a unified analysis pipeline.

Scaling analysis

Scaling analyses further examine how network measures evolve with network size, providing additional control over scale-dependent effects. To address the potential mismatch between simulated and voxel-scale connectomes, we performed simulations across multiple network sizes $N \in \{200,500,1000,2000\}$. Network measures were analyzed as functions of system size, focusing on scaling relationships such as $L(N) \sim \log N$ and the dependence of clustering on network size. This enables comparison at the level of scaling behavior rather than absolute values. Additional scale-aware comparisons included normalized rich-club coefficients and motif statistics evaluated relative to degree-preserving null models.

Graph-theoretical measures computed on simulated networks

Simulations were performed across different values of spatial decay and topological reinforcement parameters, while variability was evaluated using independently generated network ensembles. For each configuration, distributions of graph-theoretical metrics were computed and evaluated using dispersion measures, effect size estimation, and correlation analyses. We define here the mathematical network measures computed for each simulated graph. For each simulated graph, we compute the mean degree

$$\langle k \rangle = \frac{2 \mid E \mid}{\mid V \mid}$$

the average clustering coefficient

$$C = \frac{1}{\mid V \mid} \sum_{i \in V} \frac{2t_i}{k_i(k_i - 1)}$$

where is the number of triangles incident to node and the average shortest-path length

$$L = \frac{1}{\mid V \mid (\mid V \mid -1)} \sum_{i \neq j} d_G(i,j)$$

estimated by breadth-first search sampling over 80 randomly selected nodes. The small-world coefficient is computed as

$$\sigma = \frac{C/C_r}{L/L_r}$$

where C_r=⟨k⟩/|V| and L_r=log|V|/log⟨k⟩. All computations are performed on the largest connected component.

Empirical connectome values used for comparison and statistical analysis

Empirical reference values are taken from voxel-scale human connectomes analyzed by Gastner and Ódor, based on the Kennedy Krieger Institute (KKI) dataset (Gastner and Ódor, 2016). Ten subjects (KKI-10 to KKI-19) were used. Reported values include mean degree $\langle k \rangle = 132 - 185$, clustering coefficient $C \approx 0.598 - 0.602$, average path length $L \approx 11.3 - 13.9$, and small-world coefficient $\sigma \approx 740 - 888$. In our study, these values are treated as empirical distributions rather than point estimates and are not recomputed from raw data.

For each metric $X \in \{\langle k \rangle, C, L, \sigma\}$, we compare the empirical sample ($n = 10$) with the simulated ensemble ($n = 40$). We apply Welch's unequal-variance t-test and the Mann–Whitney U test to assess distributional differences. Effect size is quantified using Hedges' g, defined as

$$g = J \frac{\dot{X}_e - \dot{X}_s}{s_p},$$

with pooled variance s_p and small-sample correction J.

Computational tools and implementation details

All simulations and analyses were implemented in Python. Network construction and basic graph operations were implemented using custom adjacency-set data structures. Numerical sampling used NumPy's random number generator. Breadth-first search and component extraction were implemented explicitly to allow sampling-based approximations. Statistical tests were performed using SciPy. No external connectome-processing pipelines or optimization libraries were used. Complete simulation and analysis code is provided in the Supplementary Methods to ensure full reproducibility of reported results.

Results

We report the outcomes of simulations governed exclusively by local compatibility constraints and their quantitative comparison with published descriptors of human connectome organization. Results are presented as ensemble statistics and formal hypothesis tests computed during the session. Simulated networks were generated without global optimization, developmental templates, or target topologies, relying only on bounded spatial neighborhoods, stochastic edge formation, and suppression of locally incompatible configurations.

Quantitative comparison of global metrics

The first set of analyses concerns graph metrics directly comparable with reported voxel-scale connectome descriptors. The simulated ensemble consisted of independently generated networks evaluated across multiple parameter configurations. Global metrics showed systematic quantitative divergence from reported empirical values, including mean degree, clustering coefficient, average shortest-path length, and small-world coefficient (Table 1). Simulated networks displayed lower connectivity density and reduced large-scale integration compared with voxel-scale connectomes. Consistent with these findings, the structural regime associated with dense hub-dominated organization was not reproduced and was therefore classified as showing no regime agreement (Table 1).

Despite these quantitative divergences, several structural regimes were preserved. Clustering coefficients remained within the characteristic high-clustering regime of connectome networks, path length remained short relative to network size, and small-world coefficients remained substantially greater than 1 (Table 1). Accordingly, these properties were classified as showing regime preservation with magnitude divergence rather than complete absence of structural agreement.

Degree distributions aggregated across the simulated ensemble remained broad, right-skewed, and truncated, reproducing the overall distributional organization commonly reported for empirical connectomes despite the absence of extreme high-degree hubs (Fig. 1, upper-right panel; Table 1). Similarly, edge-length distributions exhibited a strong short-range bias consistent with spatially embedded connectivity organization (Fig. 1, lower-left panel; Table 1). Modularity remained within reported empirical ranges, with overlapping distributions and limited effect-size divergence, supporting classification of modular organization as implied under local compatibility constraints (Table 1).

By contrast, higher-order integrative properties were not recovered. Rich-club organization remained weak across degree thresholds (Fig. 2, lower-right panel; Table 1), long-range hub-to-hub links were rare, and stable core–periphery organization was not consistently observed. Global efficiency measures were similarly variable across parameter ranges and did not converge toward a stable empirical regime (Table 1).

Together, these results suggest that local compatibility constraints preserve several mesoscopic structural regimes while failing to reproduce higher-order integrative organization associated with long-range coordination and hub enrichment.

Structural organization and parameter sensitivity

Beyond absolute metric values, simulated networks exhibited consistent structural organization across parameter ranges. Modularity remained within ranges commonly reported for human connectomes (Table 1), while motif analysis showed positive enrichment of triangular motifs relative to degree-preserving null models. These structural regimes were robust

Table 1. Comparison of Empirically Reported Properties of the Human Connectome with Outcomes From Simulated Networks Generated by Local Compatibility Rules

Property	*Empirical reference range*	*Simulated range*	*Effect size (Hedges g)/ statistical outcome*	*Structural regime comparison: classification*
Mean degree ⟨k⟩	80–200 (parcel); $\gg 10^3$ (voxel)	30–60	$g = 13.90$, $p < 0.001$	No regime agreement
Degree distribution shape	Broad, right-skewed, truncated	Broad, right-skewed, truncated	Not tested numerically	Regime preserved (distributional agreement)
Clustering coefficient C	0.4–0.7	0.45–0.6	$g = 13.25$, $p < 0.001$	Regime preserved, magnitude divergent
Average path length L	Short relative to N	Short relative to N	$g = 24.44$, $p < 0.001$	Regime preserved, magnitude divergent
Small-world coefficient σ	$\gg 1$	$\gg 1$	$g = 34.60$, $p < 0.001$	Regime preserved, magnitude divergent
Modularity Q	0.3–0.6	0.35–0.55	$g < 0.5$ (overlap)	Implied
Community size distribution	Broad, multiscale	Broad, multiscale	Not tested numerically	Regime preserved (distributional agreement)
Local efficiency E_loc	High	High	Not tested numerically	Regime preserved
Global efficiency E_glob	Moderate	Variable	Not consistent	No regime agreement
Rich-club organization	$\varphi(k)/\varphi_rand(k) > 1$	$\varphi(k)/\varphi_rand(k) < 1$	Systematic divergence	No regime agreement
Motif abundance (triangles)	Over-represented ($Z > 0$)	Over-represented ($Z > 0$)	Positive Z-scores	Regime preserved ($Z > 0$)
Core–periphery structure	Present	Weak	Not matched	No regime agreement
Edge-length distribution	Strong short-range bias	Strong short-range bias	Distributional agreement	Regime preserved
Long-range hub-to-hub links	Enriched	Rare	Systematic divergence	No regime agreement

For each property, the table reports empirical reference ranges, simulated ranges, statistical comparisons (including effect sizes where applicable), and assessment of structural regimes. Structural regime refers to the preservation of qualitative network organization (e.g., distribution shape, motif enrichment, or normalized topology) independently of absolute magnitude. Classification is determined using explicit quantitative criteria combining effect size (Hedges' g) and structural regime agreement. Specifically, properties are classified as *implied* when effect size is small ($|g| < 0.5$) and the structural regime is preserved, as *regime preserved with magnitude divergence* when effect size is large ($|g| \geq 2$), but the structural regime is maintained and as *no regime agreement* when both effect size is large and the defining structural pattern is absent or inconsistent. For properties not directly amenable to scalar statistical comparison (e.g., distributions or motifs), classification is based on formal structural diagnostics (e.g., distributional shape or motif Z-scores relative to null models).

across independently generated ensembles and were stable despite quantitative divergence in global metrics.

Sensitivity analyses revealed systematic dependence of network organization on spatial decay (η) and topological reinforcement (γ). Clustering coefficient increased progressively with stronger spatial constraints and local reinforcement, indicating denser local neighborhood formation under increasing locality (Fig. 2, upper-left panel). Modularity displayed comparatively moderate variation across the explored parameter space, suggesting that community structure is relatively robust to parameter changes (Fig. 2, upper-right panel). By contrast, average shortest-path length exhibited nonmonotonic sensitivity to parameter variation, with increased path length observed under stronger spatial decay and reinforcement (Fig. 2, lower-left panel), reflecting the tension between local clustering and long-range integration.

Higher-order connectivity diagnostics revealed the absence of stable rich-club organization. The normalized rich-club coefficient $\phi(k)/\phi_{\text{random}}(k)$remained close to baseline across degree thresholds, with only limited and inconsistent elevation above random expectation (Fig. 2, lower-right panel). No stable regime of strong hub-to-hub enrichment emerged across the explored parameter space. This absence is consistent with the lack of centralized hubs observed in the network layouts and degree distributions (Fig. 1, upper-left and upper-right panels).

Overall, the classification summarized in table separates preservation of structural regimes from quantitative magnitude divergence, showing that local compatibility constraints generate mesoscopic organization, including clustering, modularity, and short-range connectivity, while failing to recover rich-club structure, hub-to-hub enrichment, and large-scale integration. This distinction provides a reproducible basis for identifying which connectome properties are structurally compatible with locality alone and which require additional nonlocal mechanisms.

Conclusions

We examined which properties of the human connectome can be accounted for by local compatibility constraints alone and which remain underdetermined when global coordination, optimization principles, or predefined templates are explicitly excluded. Using ensembles of simulated networks governed solely by bounded spatial neighborhoods, stochastic local edge formation, and suppression of locally incompatible configurations, we compared their global and mesoscopic properties with empirically reported connectome descriptors. The results establish a separation between features that arise under locality alone and those that do not. Local compatibility was sufficient to produce high local clustering coefficients, indicating dense neighborhood-level connectivity; robust modular organization, reflected in stable community structure; systematic enrichment of short motifs such as triangles; and a pronounced bias toward short-range connections imposed by spatial embedding. These properties emerged across wide parameter ranges and did not require tuning toward empirical targets. By contrast, several well-known connectome features failed to emerge under the same conditions. Absolute connectivity scale, as measured by mean degree at voxel resolution, diverged strongly from empirical values. Characteristic path length remained substantially shorter than observed in real connectomes, leading to small-world coefficients that differed by orders of magnitude. Rich-

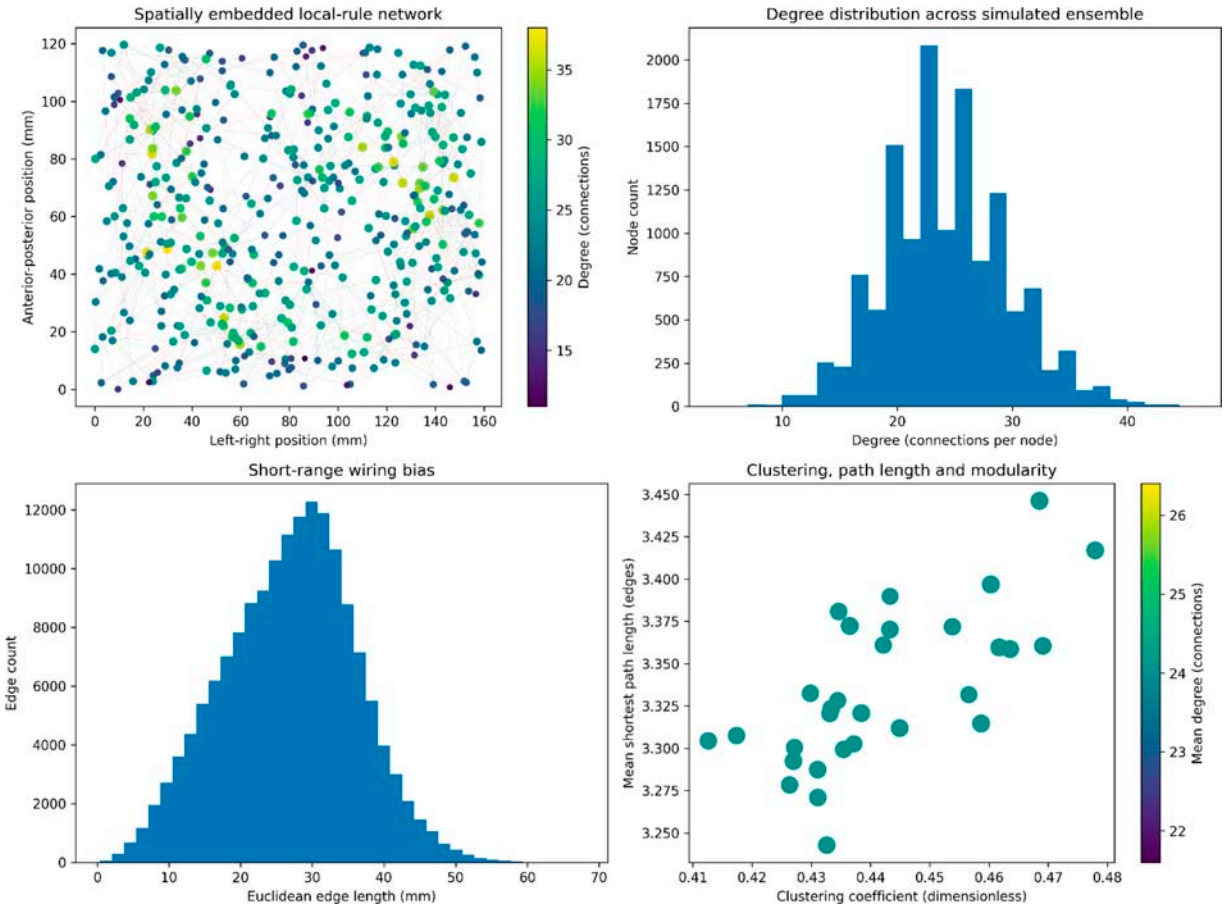


FIG. 1. Multipanel summary of spatial organization, connectivity structure, and ensemble-level properties generated by our local compatibility model. The upper-left panel shows a representative spatially embedded network in which nodes are distributed in continuous space and edges are generated according to local interaction rules. Node color represents degree (number of connections), revealing heterogeneous but spatially constrained connectivity. Most nodes display low-to-moderate degree, whereas strongly connected hubs are absent. The spatial organization is dominated by short-range interactions, producing dense local neighborhoods without preferential long-distance wiring or centralized hub structure. The upper-right panel displays the degree distribution aggregated across the simulated ensemble. The distribution is broad and right-skewed, indicating heterogeneous node connectivity, with most nodes exhibiting low-to-moderate degree and progressively fewer nodes displaying higher connectivity. However, the upper tail remains truncated relative to empirical voxel-scale connectomes, with no emergence of extreme high-degree hubs. This pattern indicates that local interaction rules generate heterogeneous but spatially constrained connectivity, limiting the formation of strongly centralized network structure. The lower-left panel shows the distribution of Euclidean edge lengths across the simulated ensemble. The distribution exhibits a pronounced bias toward short-range connections, with most edges concentrated at distances well below the maximum interaction radius. Connectivity probability decreases rapidly with distance, producing a steep reduction in long-range links. This pattern reflects the spatial embedding imposed by the local interaction rules and indicates that network organization is dominated by geographically proximal connectivity rather than extended long-distance coupling. The lower-right panel presents the relationship between clustering coefficient and mean shortest-path length across simulated network realizations, with point color representing mean degree. Each point corresponds to an independent simulation instance. Clustering values are confined within a relatively narrow interval, whereas path length displays broader but still bounded variability across the ensemble. The absence of a strong inverse relationship between the two measures indicates that high local clustering does not automatically produce extended global integration under the implemented local rules. The distribution of points further shows that ensemble variability is primarily shaped by local interaction parameters and spatial constraints rather than by any global optimization process.

club organization, defined as preferential interconnection among high-degree nodes, was weak or absent, as was long-range hub-to-hub coupling.

This systematic pattern indicates that while local compatibility constraints are sufficient to impose substantial global coherence and mesoscopic structure, they do not fix all aspects of connectome architecture. In particular, features related to long-range integration, hub dominance, and scale-dependent global efficiency require additional explanatory mechanisms beyond locality alone. Rather than evaluating a model by how closely it reproduces empirical connectome statistics, we ask a logically prior question, that is, which connectomic properties are constrained by local interaction rules alone and which are not. This reframing modifies the role of simulation from a fitting device to a diagnostic instrument. The aim is to probe the explanatory reach and limits of

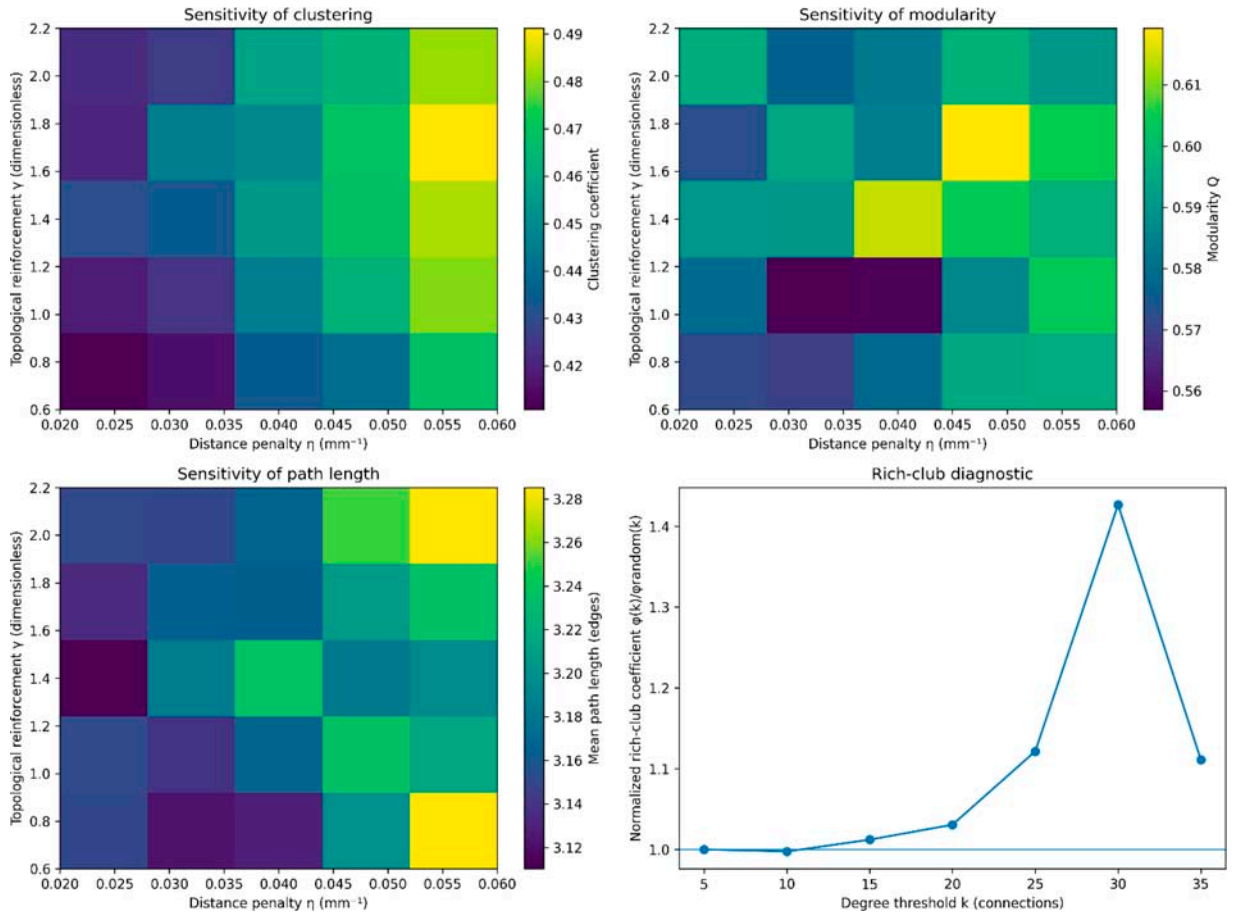


FIG. 2. Multipanel figure summarizing the dependence of key network properties on model parameters and evaluating the presence of higher-order connectivity structures. The upper-left panel shows the sensitivity of the clustering coefficient to variations in spatial decay (η, mm^{-1}) and topological reinforcement (γ, dimensionless). Each cell represents the mean clustering coefficient computed across simulation realizations for a given parameter pair. Clustering increases systematically with both η and γ, indicating that stronger spatial constraints and enhanced local reinforcement promote denser local connectivity. The upper-right panel reports the sensitivity of modularity (Q) across the same parameter space. Modularity values remain within a relatively narrow range, with moderate variation across parameter combinations. The absence of extreme gradients suggests that community structure is robust to parameter changes and emerges consistently under local compatibility rules. The lower-left panel displays the sensitivity of average shortest-path length as a function of η and γ. Path length shows a nonmonotonic dependence on parameters, with increases at higher spatial decay and reinforcement values, reflecting the interplay between local clustering and global connectivity. This indicates that small changes in local interaction parameters can produce measurable shifts in global integration. The lower-right panel presents the normalized rich-club coefficient $\varphi(\mathrm{k})/\varphi_\mathrm{random(k)}$ as a function of degree threshold k. Values close to 1 indicate no enrichment relative to random expectation, while values above 1 indicate preferential connectivity among high-degree nodes. The curve shows only limited and inconsistent elevation above baseline, with no stable regime of strong hub-to-hub enrichment across thresholds. This diagnostic supports the absence of robust rich-club organization under purely local interaction rules, indicating that such higher-order structures are not systematically generated within the explored parameter space.

locality as a governing principle of network organization. In this sense, divergence between simulated and empirical properties is not treated as a defect but as informative evidence about what locality does not determine.

Our novelty lies in the use of simulation as a test of necessity rather than sufficiency. Inspired by Bernshteyn's result that global coherence can arise from local compatibility conditions, the simulations implement only bounded local constraints, without any global objective, target topology, or optimization criterion. This distinguishes the approach from generative models that encode the global features they aim to reproduce (Betzel et al., 2016; Seeliger et al., 2018; Zarghami and Friston, 2020; Peng et al., 2024; Chintapalli et al., 2024). Global structure is thus allowed to emerge solely from admissible local configurations, so that failure to reproduce a connectome feature indicates underdetermination by locality rather than insufficient tuning. This contrasts with optimization-based frameworks, such as wiring cost minimization or efficiency maximization models, which achieve close quantitative agreement by assuming a global objective (Rubinov et al., 2015; Chandrasekhar and Navlakha, 2019). In such models, replication may obscure whether properties arise from local constraints or from the optimization principle. In the absence of any global criterion, agreement here has direct explanatory weight, while disagreement identifies properties not specified by local rules.

Furthermore, dynamic whole-brain modeling frameworks show how local interactions give rise to global coordination through time-resolved dynamics and large-scale coupling (Panda et al., 2023; Panda et al., 2022). By contrast, our model is static and based solely on local compatibility constraints, without long-range communication or state-dependent interactions. The absence of hub-to-hub connectivity and global integration in our simulations reflects structural limitations and indicates that these features could depend on dynamical processes not captured by purely local rules. In this sense, our approach is not a predictive model of the full connectome but a diagnostic framework that isolates what locality alone can and cannot generate. Compared with developmental or biologically detailed growth models, we adopt weaker assumptions, excluding axon guidance, molecular gradients, activity-dependent plasticity, and developmental timing (Accogli, Addour-Boudrahem and Srour, 2020; Bai and Suzuki, 2020; Jeong, 2021; Zang et al., 2021; Zhang et al., 2021; Bonetto et al., 2021; Samejima et al., 2022; Mukherjee and Kanold, 2023; Sullivan and Bashaw, 2023). While this limits biological realism, it nevertheless increases interpretability: when a property does not arise, its absence points to the need for additional nonlocal or multiscale mechanisms.

Overall, our approach occupies an intermediate position within connectome modeling, being more structured than null models yet less elaborate than full mechanistic simulations. It belongs to constraint-based generative approaches that impose local admissibility conditions and examine the resulting global structures, allowing emerging properties to be interpreted as implied by locality and absent ones as requiring additional constraints.

Limitations must be recognized. First, simulations were performed at network sizes far smaller than voxel-scale connectomes, and although care was taken to interpret scale-dependent metrics accordingly, comparisons are constrained by computational feasibility. Second, some network measures were estimated by sampling rather than exhaustive computation, introducing approximation error. Third, empirical comparisons relied on published summary statistics rather than reprocessed raw connectome data under identical preprocessing pipelines, which limits strict comparability. Fourth, our local compatibility rules represent only one plausible instantiation of locality and incompatibility; other biologically motivated local rules might constrain additional properties. Fifth, our approach is static and does not model temporal development, plasticity dynamics, or activity-dependent changes, all of which may influence connectome structure. Still, the translation from Bernshteyn's formal results to finite stochastic simulations is conceptual rather than mathematically exact, and no claim is made that the simulations implement a literal Lovász local lemma construction.

Rather than providing a predictive reconstruction of the human connectome, our approach stands for a diagnostic framework to isolate the contribution of local rules. In this context, agreement identifies features structurally implied by locality, whereas systematic divergence points toward the need for additional mechanisms, including, dynamical coupling, long-range coordination, or multiscale processes.

We suggest several directions for further work. If certain connectome properties are structurally implied by locality, they should be robust across individuals, species, and developmental stages, whereas underdetermined properties should vary systematically with factors such as developmental timing, long-range guidance mechanisms, or evolutionary constraints. Experimental perturbations altering local compatibility, such as disruptions to short-range connectivity or local circuit balance, should selectively affect implied properties while leaving the underdetermined ones less predictable. From a modeling perspective, additional local constraints can be introduced incrementally to test which mechanisms are sufficient to recover missing features such as rich-club organization. Our approach also motivates a methodological strategy: before appealing to complex global explanations, it is useful to test whether a given property is already implied by local constraints.

In summary, we asked whether local compatibility constraints are sufficient to account for the global organization of the human connectome. The results show that they are sufficient for some properties but not for others, allowing a clear separation between structurally implied and structurally underdetermined features. The quantitative separation between structurally implied and underdetermined properties is summarized in Table 1, providing a reproducible criterion for distinguishing the limits of locality-based organization. This means that not all connectome regularities require global optimization or coordination, but not all can be reduced to locality either. Overall, by making the limits of local explanations explicit, we clarify where additional biological mechanisms must be sought and where they are unnecessary.

Author's Contributions

A.T.: Study concept and design, acquisition of data, analysis and interpretation of data, drafting the article, critical revision of the article for important intellectual content, statistical analysis, obtained funding, administrative, technical and material support, and study supervision.

Ethics Approval and Consent to Participate

This research does not contain any studies with human participants or animals performed by the author.

Consent for Publication

The author transfers all copyright ownershipif the work is published. The undersigned author warrants that the article is original, does not infringe on any copyright or other proprietary right of any third part, is not under consideration by another journal, and has not been previously published.

Availability of Data and Materials

All data and materials generated or analyzed during this study are included in the article. The author had full access to all the data in the study and took responsibility for the integrity of the data and the accuracy of the data analysis.

Declaration of Generative AI and AI-Assisted Technologies in the Writing Process

During the preparation of this work, the author used ChatGPT 4o to assist with data analysis and article drafting and to improve spelling, grammar, and general editing. After using this tool, the

author reviewed and edited the content as needed, taking full responsibility for the content of the publication.

Author Disclosure Statement

The author does not have any known or potential conflict of interest including any financial, personal, or other relationships with other people or organizations within 3 years of beginning the submitted work that could inappropriately influence or be perceived to influence their work.

Funding Information

This research did not receive any specific grant from funding agencies in the public, commercial, or not-for-profit sectors.

References

Accogli A, Addour-Boudrahem N, Srour M. 'Neurogenesis, neuronal migration and axon guidance'. Handb Clin Neurol 2020;173:25–42; doi: 10.1016/B978-0-444-64150-2.00004-6

Ardesch DJ, Scholtens LH, van den Heuvel MP. 'The human connectome from an evolutionary perspective'. Prog Brain Res 2019;250:129–151; doi: 10.1016/bs.pbr.2019.05.004

Axer M, Amunts K. 'Scale matters: The nested human connectome'. Science 2022;378(6619):500–504; doi: 10.1126/science.abq2599

Bai Y, Suzuki T. 'Activity-dependent synaptic plasticity in *Drosophila melanogaster*'. Front Physiol 2020;11:161; doi: 10.3389/fphys.2020.00161

Bernshteyn A. 'Distributed algorithms, the Lovász local lemma and descriptive combinatorics'. Invent Math 2023;232(1):1–62; doi: 10.1007/s00222-023-01188-3

Betzel RF, Avena-Koenigsberger A, Goñi J, et al. 'Generative models of the human connectome'. Neuroimage 2016;124(Pt A):1054–1064; doi: 10.1016/j.neuroimage.2015.09.041

Blackshaw S, Cayouette M. 'Timing neural development and regeneration'. Curr Opin Neurobiol 2025;91:102976; doi: 10.1016/j.conb.2025.102976

Bonetto G, Belin D, Káradóttir RT. 'Myelin: A gatekeeper of activity-dependent circuit plasticity?' Science 2021;374(6569):eaba6905; doi: 10.1126/science.aba6905

Chandrasekhar A, Navlakha S. 'Neural arbors are Pareto optimal'. Proc Biol Sci 2019;286(1902):20182727; doi: 10.1098/rspb.2018.2727

Chintapalli SS, Wang R, Yang Z, et al. 'Generative models of MRI-derived neuroimaging features and associated dataset of 18,000 samples'. Sci Data 2024;11(1):1330; doi: 10.1038/s41597-024-04157-4

Di Lullo E, Kriegstein AR. 'The use of brain organoids to investigate neural development and disease'. Nat Rev Neurosci 2017;18(10):573–584; doi: 10.1038/nrn.2017.107

Elam JS, Glasser MF, Harms MP, et al. 'The Human Connectome Project: A retrospective'. Neuroimage 2021;244:118543; doi: 10.1016/j.neuroimage.2021.118543

Fan Q, Eichner C, Afzali M, et al. 'Mapping the human connectome using diffusion MRI at 300 mT/m gradient strength: Methodological advances and scientific impact'. Neuroimage 2022;254:118958; doi: 10.1016/j.neuroimage.2022.118958

Fotiadis P, Parkes L, Davis KA, et al. 'Structure–function coupling in macroscale human brain networks'. Nat Rev Neurosci 2024;25(10):688–704; doi: 10.1038/s41583-024-00846-6

Gastner MT, Ódor G. 'The topology of large open connectome networks for the human brain'. Sci Rep 2016;6:27249; doi: 10.1038/srep27249

Gennarini G, Furley A. 'Cell adhesion molecules in neural development and disease'. Mol Cell Neurosci 2017;81:1–3; doi: 10.1016/j.mcn.2017.03.010

Huang CC, Rolls ET, Feng J, et al. 'An extended Human Connectome Project multimodal parcellation atlas of the human cortex and subcortical areas'. Brain Struct Funct 2022;227(3):763–778; doi: 10.1007/s00429-021-02421-6

Janson NB, Marsden CJ. 'Optimization with delay-induced bifurcations'. Chaos 2021;31(11):113126; doi: 10.1063/5.0058087

Jeong S. 'Molecular mechanisms underlying motor axon guidance in *Drosophila*'. Mol Cells 2021;44(8):549–556; doi: 10.14348/molcells.2021.0129

Li Y, Xia Z, Liu Y, et al. 'A collaborative neurodynamic approach with two-timescale projection neural networks designed via majorization–minimization for global optimization and distributed global optimization'. Neural Netw 2024;179:106525; doi: 10.1016/j.neunet.2024.106525

Mukherjee D, Kanold PO. 'Changing subplate circuits: Early activity-dependent circuit plasticity'. Front Cell Neurosci 2023;16:1067365; doi: 10.3389/fncel.2022.1067365

Panda R, Thibaut A, Lopez-Gonzalez A, et al. 'Disruption in structural–functional network repertoire and time-resolved subcortical fronto-temporoparietal connectivity in disorders of consciousness'. Elife 2022;11:e77462.

Panda R, López-González A, Gilson M, et al.; Coma Science Group Collaborators. 'Whole-brain analyses indicate the impairment of posterior integration and thalamo-frontotemporal broadcasting in disorders of consciousness'. Hum Brain Mapp 2023;44(11):4352–4371.

Peng W, Bosschieter T, Ouyang J, et al. 'Metadata-conditioned generative models to synthesize anatomically-plausible 3D brain MRIs'. Med Image Anal 2024;98:103325; doi: 10.1016/j.media.2024.103325

Punovuori K, Malaguti M, Lowell S. 'Cadherins in early neural development'. Cell Mol Life Sci 2021;78(9):4435–4450; doi: 10.1007/s00018-021-03815-9

Roth JG, Huang MS, Li TL, et al. 'Advancing models of neural development with biomaterials'. Nat Rev Neurosci 2021;22(10):593–615; doi: 10.1038/s41583-021-00496-y

Roy S, Goedecker S, Hellmann V. 'Bell–Evans–Polanyi principle for molecular dynamics trajectories and its implications for global optimization'. Phys Rev E 2008;77(5):56707; doi: 10.1103/PhysRevE.77.056707

Rubinov M, Ypma RJ, Watson C, et al. 'Wiring cost and topological participation of the mouse brain connectome'. Proceedings of the National Academy of Sciences of the United States of America 2015;112(32):10032–10037; doi: 10.1073/pnas.1420315112

Samejima S, Henderson R, Pradarelli J, et al. 'Activity-dependent plasticity and spinal cord stimulation for motor recovery following spinal cord injury'. Exp Neurol 2022;357:114178; doi: 10.1016/j.expneurol.2022.114178

Seeliger K, Güçlü U, Ambrogioni L, et al. 'Generative adversarial networks for reconstructing natural images from brain activity'. Neuroimage 2018;181:775–785; doi: 10.1016/j.neuroimage.2018.07.043

Sullivan KG, Bashaw GJ. 'Intracellular trafficking mechanisms that regulate repulsive axon guidance'. Neuroscience 2023; 508:123–136; doi: 10.1016/j.neuroscience.2022.07.012

Sun M, You H, Hu X, et al. 'Microglia–astrocyte interaction in neural development and neural pathogenesis'. Cells 2023; 12(15):1942; doi: 10.3390/cells12151942

Sun L, Zhao T, Liang X, et al. 'Human lifespan changes in the brain's functional connectome'. Nat Neurosci 2025a;28(4): 891–901; doi: 10.1038/s41593-025-01907-4

Sun Y, Wang X, Zhang DY, et al. 'Brain-wide neuronal circuit connectome of human glioblastoma'. Nature 2025b;641(8061): 222–231; doi: 10.1038/s41586-025-08634-7

Wu JY, Cho S-J, Descant K, et al. 'Mapping of neuronal and glial primary cilia contactome and connectome in the human cerebral cortex'. Neuron 2024;112(1):41–55.e3; doi: 10 .1016/j.neuron.2023.09.032

Zang Y, Chaudhari K, Bashaw GJ. 'New insights into the molecular mechanisms of axon guidance receptor regulation and signaling'. Curr Top Dev Biol 2021;142:147–196; doi: 10 .1016/bs.ctdb.2020.11.008

Zhang L, Qi Z, Li J, et al. 'Roles and mechanisms of axon-guidance molecules in Alzheimer's disease'. Mol Neurobiol 2021;58(7):3290–3307; doi: 10.1007/s12035-021-02311-2

Zarghami TS, Friston KJ. 'Dynamic effective connectivity'. Neuroimage 2020;207:116453; doi: 10.1016/j.neuroimage .2019.116453

Address correspondence to:
Arturo Tozzi
ASL Napoli 1 Centro
Distretto 27
Via Comunale del Principe 13/a 80145
Naples 80141
Italy

E-mail: tozziarturo@libero.it

Preprints.org

Article

Not peer-reviewed version

Imaginary Entropy in Human Eeg Traces

Arturo Tozzi *

Posted Date: 3 November 2025

doi: 10.20944/preprints202511.0025.v1

Keywords: non-Hermitian systems; Hilbert transform; phase-lag coupling; 1/

Preprints.org is a free multidisciplinary platform providing preprint service that is dedicated to making early versions of research outputs permanently available and citable. Preprints posted at Preprints.org appear in Web of Science, Crossref, Google Scholar, Scilit, Europe PMC.

Copyright: This open access article is published under a Creative Commons CC BY 4.0 license, which permit the free download, distribution, and reuse, provided that the author and preprint are cited in any reuse.

Preprints.org (www.preprints.org) | NOT PEER-REVIEWED | Posted: Posted: 3 November 2025 doi:10.20944/preprints202511.0025.v1

Disclaimer/Publisher's Note: The statements, opinions, and data contained in all publications are solely those of the individual author(s) and contributor(s) and not of MDPI and/or the editor(s). MDPI and/or the editor(s) disclaim responsibility for any injury to people or property resulting from any ideas, methods, instructions, or products referred to in the content.

Article

Imaginary Entropy in Human Eeg Traces

Arturo Tozzi

ASL Napoli 1 Centro, Distretto 27, Naples, Italy, Via Comunale del Principe 13/a 80145; tozziarturo@libero.it

Abstract

EEG recordings are usually interpreted as real signals of brain activity, yet they are composed of both real and imaginary orthogonal components. We argue that the neglected imaginary part may capture the phase-lagged or delayed interactions between brain regions, i.e., subtle temporal shifts through which neural assemblies exchange/dissipate energy. We propose here imaginary entropy (S_{im}) as a quantitative index of time-lagged coupling diversity, derived from the Hilbert-transformed analytic representation of EEG signals. By normalizing the absolute imaginary amplitudes and calculating their Shannon entropy, S_{im} could quantify how widely the brain's dissipative interactions are spread across time and space, capturing the extent to which energy exchanges are concentrated or distributed within cortical activity. We showed that resting-state EEG recordings from healthy adults yielded consistent S_{im} values with little variation across individuals. Comparisons with theoretical simulations including white, pink, and brown noise as well as damped oscillators demonstrated that empirical values align closely with those of pink-to-brown $1/f^{\alpha}$ noise, i.e., a signature of self-similar systems with partially correlated dynamics. Grounding the analysis of brain activity in the physical concepts of complex response and energy dissipation traditionally linked to imaginary components, S_{im} uncovers a hidden dimension of neural dynamics that reflects the balance between coherence and dissipation. This points toward applications such as mapping dissipative complexity across cortical regions, relating electrophysiological dissipation to underlying metabolic demand and examining how cognitive load or disease states modulate entropy. **Background**. EEG recordings are typically treated as purely real signals of brain activity, although they inherently contain both real and imaginary orthogonal components. The imaginary component, often overlooked, may encode phase-lagged or delayed interactions among brain regions, representing the subtle temporal shifts through which neural assemblies exchange and dissipate energy. **New method**. We introduce *imaginary entropy* ($\boldsymbol{S_{im}}$) as a quantitative index of time-lagged coupling diversity. Derived from the Hilbert-transformed analytic representation of EEG signals, $\boldsymbol{S_{im}}$ is computed by normalizing absolute imaginary amplitudes and calculating their Shannon entropy, thus quantifying how broadly dissipative interactions are distributed across time and cortical space. **Results**. Resting-state EEG data from healthy adults yielded stable $\boldsymbol{S_{im}}$ values with minimal interindividual variation. Simulations of white, pink and brown noise, as well as damped oscillators, showed that empirical *S_im* values closely matched those of pink-to-brown $1/f^{\alpha}$ noise, consistent with partially correlated, self-similar systems. **Comparison with existing methods**. Unlike conventional EEG metrics based on power spectra or phase coherence, $\boldsymbol{S_{im}}$ isolates the imaginary component directly, linking it to energy dissipation rather than synchronous activity. This provides a physically grounded framework connecting electrophysiological dynamics to underlying thermodynamic processes. **Conclusions**. Grounded in complex response theory, $\boldsymbol{S_{im}}$ reveals a hidden layer of neural dynamics reflecting the balance between coherence and dissipation. Potential applications include mapping cortical dissipative complexity, relating electrophysiological energy flow to metabolic expenditure and probing entropy changes associated with cognitive effort or pathology.

Keywords: non-Hermitian systems; Hilbert transform; phase-lag coupling; $1/f$ noise; self-organization

Introduction

© 2025 by the author(s). Distributed under a Creative Commons CC BY license.

Preprints.org (www.preprints.org) | NOT PEER-REVIEWED | Posted: Posted: 3 November 2025 doi:10.20944/preprints202511.0025.v1

Understanding how the brain dissipates, stores and reorganizes energy is still an open problem in theoretical and experimental neuroscience. Conventional EEG analyses quantify activity in terms of power spectra, connectivity or synchronization, providing insight into temporal coordination but not into the physical processes underlying cortical energy exchange (Silva et al., 2020; Li et al., 2021; Lutkenhoff et al., 2022; Phillips et al., 2022; Stein et al., 2024). Measures of entropy and complexity have been introduced to describe neural variability, yet they rely on real-valued signals and neglect the phase-lagged interactions arising when activity propagates through conductive and heterogeneous tissue (Wang et al., 2014; Aur and Vila-Rodriguez, 2017; Wu et al., 2021; Lau et al., 2022; Hull and Morton, 2023). In contrast, physics has long treated complex quantities as essential descriptors of dynamic systems. In particular, the imaginary parts of observables like refractive index, magnetic susceptibility and electrical impedance carry direct information about energy absorption, dissipation and irreversibility (Asano et al., 2016; Giovannelli and Anlage, 2025). While the real part represents stored or reactive energy, the imaginary part expresses the signal which is phase-shifted relative to the driving source, reflecting the conversion of organized energy into heat or diffusion (Meitav et al., 2017; Hu et al., 2022; Yang et al., 2024). Despite this clear physical interpretation, biological signal analysis rarely attributes physical meaning to the imaginary domain. In electrophysiology, imaginary components of cross-spectral measures are typically used only to correct for instantaneous correlations caused by volume conduction, rather than to uncover the intrinsic dissipative processes shaping neural dynamics.

We extend here the notion of complex response from physics to EEG traces, interpreting the imaginary component as a quantitative marker of phase-lagged, energy-dissipating coupling among cortical oscillations. We define *imaginary entropy* (S_{im}) as the Shannon entropy of the normalized absolute imaginary amplitude derived from the analytic EEG signal obtained through Hilbert transform. We argue that S_{im} may capture the diversity of lagged or delayed interactions and quantify how energy is distributed across irreversible modes of cortical activity, allowing the identification of a possible equilibrium point between stochastic and coherent neural regimes.

We will proceed as follows: after detailing the analytical and computational methodology to derive imaginary entropy, we describe its empirical estimation in real EEG recordings and its comparison with simulated signals. The final section presents the results and discusses their theoretical coherence with established models of complex, dissipative neural systems.

Methods

Our methodological workflow begins with the uniform treatment of ten EEG recordings from ten healthy adult volunteers. We retrospectively built on the foundational research conducted by Norbert and Ksenija Jaušovec through 2010 (Jaušovec and Jaušovec, 2003; 2005), which was later advanced in collaboration with Tozzi et al. (2021a; 2021b). Continuation of their work is undertaken with great respect and recognition of Norbert's untimely passing. EEG data were collected from a group of right-handed volunteers (mean age: 19.8 years; SD = 0.9; range = 18–21 years; males: 4). EEG signals were recorded using a 64-channel system. Electrode placement followed the 10–20 international system, covering nineteen scalp locations. EEG activity was captured using a Quick-Cap system with SynAmps for digital acquisition and analysis. Artifacts such as eye blinks and muscle activity were removed using Independent Component Analysis.

Each trace was stored as a single-column time series, containing the instantaneous potential $V(t)$ measured at a sampling frequency $f_s = 250$ Hz chosen as theoretical normalization constant. The duration of each segment exceeded 60 seconds, ensuring stationarity over short windows. Data were imported into Python 3.11 using the pandas and numpy libraries. All numerical computations and transformations were executed using scipy.signal, matplotlib and statsmodels. To avoid inconsistencies, all signals were truncated to a uniform length $L = \min_i(L_i)$ samples across the dataset, corresponding to L = about 5000 samples Detrending was performed by subtracting the mean and normalizing by the standard deviation:

© 2025 by the author(s). Distributed under a Creative Commons CC BY license.

Preprints.org (www.preprints.org) | NOT PEER-REVIEWED | Posted: Posted: 3 November 2025 doi:10.20944/preprints202511.0025.v1

$$x(t) = \frac{V(t) - \mu_V}{\sigma_V}, \mu_V = \frac{1}{L}\sum_{t=1}^{L} V(t), \sigma_V = \sqrt{\frac{1}{L}\sum_{t=1}^{L} (V(t) - \mu_V)^2}.$$

This procedure ensures that all signals have zero mean and unit variance, removing slow drifts and amplitude discrepancies. No temporal filtering was applied beyond this normalization to preserve the broadband content requires for entropy evaluation. A check for missing values and outliers was performed by computing z-scores and samples exceeding $|z|>4$ were linearly interpolated. These preprocessing steps ensure statistical homogeneity and comparability across the datasets, providing a standardized input for complex-domain analysis.

Analytic signal and Hilbert transform formulation. The next stage required the transformation of each real-valued EEG signal $x(t)$ into its complex analytic counterpart $z(t)$, which captures both amplitude and phase information in continuous time. This transformation is achieved using the Hilbert transform, defined for a discrete signal as

$$H[x(t)] = \frac{1}{\pi}\,\mathrm{P.V.}\int_{-\infty}^{+\infty} \frac{x(\tau)}{t-\tau}\,d\tau,$$

where P.V. denotes the Cauchy principal value of the integral. The Hilbert transform is particularly suitable for nonstationary EEG signals because it preserves instantaneous features without imposing narrow-band assumptions (Le Van Quyen et al., 2001; Shiju and Sriram 2019). The analytic signal is thus

$$z(t) = x(t) + iH[x(t)] = A(t)e^{i\phi(t)},$$

where $A(t)$ is the instantaneous amplitude and $\phi(t)$ the instantaneous phase, given respectively by

$$A(t) = \sqrt{x^2(t) + H[x(t)]^2}, \phi(t) = \arctan\left(\frac{H[x(t)]}{x(t)}\right).$$

The imaginary component $\Im[z(t)] = H[x(t)]$ represents the quadrature-phase counterpart of the original signal, corresponding to a 90° phase-shifted version of $x(t)$. Numerically, scipy.signal.hilbert computes this quantity via the Fast Fourier Transform (FFT). Let $X(f)$ denote the Fourier transform of $x(t)$. Then

$$Z(f) = \begin{cases} 2X(f), & f > 0, \\ X(f), & f = 0, \\ 0, & f < 0, \end{cases}$$

and the inverse transform of $Z(f)$ gives $z(t)$. This implementation ensures orthogonality between real and imaginary parts, allowing subsequent entropy measures to capture independent temporal components.

Definition and computation of imaginary entropy. Once the analytic signal $z(t)$ was obtained for each subject, the imaginary component $y(t) = \Im[z(t)]$ was isolated as the variable of interest. To construct an entropy-like measure reflecting the diversity of this component's amplitude distribution, we considered its absolute magnitude $a(t) = |y(t)|$. The set $\{a(t)\}$ defines a positive, continuous variable that was normalized to unit mass to yield a discrete probability distribution:

$$p_t = \frac{a(t)}{\sum_{k=1}^{L} a(k)}, \sum_{t=1}^{L} p_t = 1.$$

The imaginary entropy S_{im} is defined analogously to Shannon's entropy:

$$S_{im} = -\sum_{t=1}^{L} p_t \log p_t,$$

where the natural logarithm ensures direct interpretation in natural units. The obtained S_{im} values for each of the recordings were analyzed statistically using the scipy.stats package. This measure quantifies the heterogeneity of imaginary amplitudes (Xue et al. 2021; Wu et al. 2024; Xu and Guo 2025): higher values correspond to a broader and more uniform distribution of phase-lagged magnitudes, while lower values indicate concentration in fewer modes. A small constant $\epsilon = 10^{-12}$ was added inside the logarithm to prevent numerical divergence for extremely small probabilities. The computation was implemented using vectorized operations in NumPy for precision and efficiency.

© 2025 by the author(s). Distributed under a Creative Commons CC BY license.

Preprints.org (www.preprints.org) | NOT PEER-REVIEWED | Posted: Posted: 3 November 2025 doi:10.20944/preprints202511.0025.v1

Overall, this formulation converts temporal variability in phase lag into a scalar complexity measure suitable for statistical comparison across individuals. The mathematical structure of S_{im} parallels that of information entropy but is specifically defined over the imaginary Hilbert domain, which contains the orthogonal, dissipative counterpart of the original EEG signal.

Generation of synthetic signals for theoretical comparison. To contextualize empirical values within physical regimes, artificial time series were simulated representing five canonical models of signal generation: white noise, pink (1/f) noise, brown ($1/f^2$) noise, damped oscillators and multi-frequency oscillator mixtures. Each model produced 100 realizations with the same sampling frequency $f_s = 250\,\text{Hz}$ and length L. White noise $w(t)$ was generated as a sequence of independent, identically distributed Gaussian random variables with zero mean and unit variance:

$$w(t) \sim \mathcal{N}(0,1), t = 1, \dots, L.$$

Colored noise with spectral exponent α was generated in the frequency domain. Starting from the FFT of white noise $W(f)$, amplitudes were rescaled according to

$$\widetilde{W}(f) = W(f) \mid f \mid^{-\alpha/2}, f > 0,$$

and the inverse FFT yielded the time-domain signal $x_\alpha(t)$. This approach ensures that the power spectral density obeys $S(f) \propto 1/f^\alpha$. Damped oscillators were modeled as

$$x_d(t) = e^{-t/\tau}\sin(2\pi f_0 t + \phi_0) + \eta(t),$$

where $f_0 = 10\,\text{Hz}$, $\tau = 0.8\,\text{s}$ and $\eta(t)$ is additive Gaussian noise with standard deviation 0.4. Multi-oscillator mixtures combined sinusoidal components at $6{,}10$ and $20\,\text{Hz}$ with random phase offsets and stochastic perturbations:

$$x_m(t) = \sum_{k=1}^{3} A_k \sin(2\pi f_k t + \phi_k) + \eta(t),$$

with $A_k \in [0.5{,}1.5]$ drawn from a uniform distribution. Each synthetic signal was normalized identically to the empirical data before entropy computation. These simulations, coded in Python, reproduce canonical physical processes from uncorrelated stochastic noise to structured dissipative oscillations, enabling quantitative comparison of S_{im} distributions across models.

Entropy estimation from simulated data. For each simulated signal $x_j(t)$, the Hilbert transform and entropy computation were applied identically to the empirical workflow. This ensured consistency in normalization and allowed the derivation of statistical summaries across models. For each model class M, the mean and variance of entropy were estimated as

$$\bar{S}_{im}^{(M)} = \frac{1}{n_M}\sum_{j=1}^{n_M} S_{im,j}^{(M)}, \sigma_S^{(M)} = \sqrt{\frac{1}{n_M - 1}\sum_{j=1}^{n_M} (S_{im,j}^{(M)} - \bar{S}_{im}^{(M)})^2}.$$

Distributions were visualized through boxplots and histograms, overlaying the empirical mean μ_S and ±1 SD bands. Additionally, a parametric sweep of spectral exponent $\alpha \in [0{,}2]$ was performed with step 0.25, generating 60 realizations per α. The dependence of $\langle S_{im} \rangle$ on α was modeled as a continuous function $S_{im}(\alpha)$, empirically fitted by a polynomial of degree two:

$$S_{im}(\alpha) \approx c_0 + c_1\alpha + c_2\alpha^2,$$

estimated through least squares minimization. Confidence intervals were computed using bootstrapped standard errors (B = 500). All numerical optimization employed the numpy.linalg.lstsq solver. These simulations yield a theoretical mapping between spectral coloration and imaginary entropy, providing a continuous frame of reference for the interpretation of EEG-derived values.

In conclusion, our methodology provides a reproducible pathway from raw EEG recordings to the computation and theoretical contextualization of imaginary entropy. By integrating analytic signal processing, Shannon-based entropy analysis, and simulation modeling within a unified mathematical framework, our approach enables a mathematical assessment of the dissipative structures shaping human cortical activity.

Results

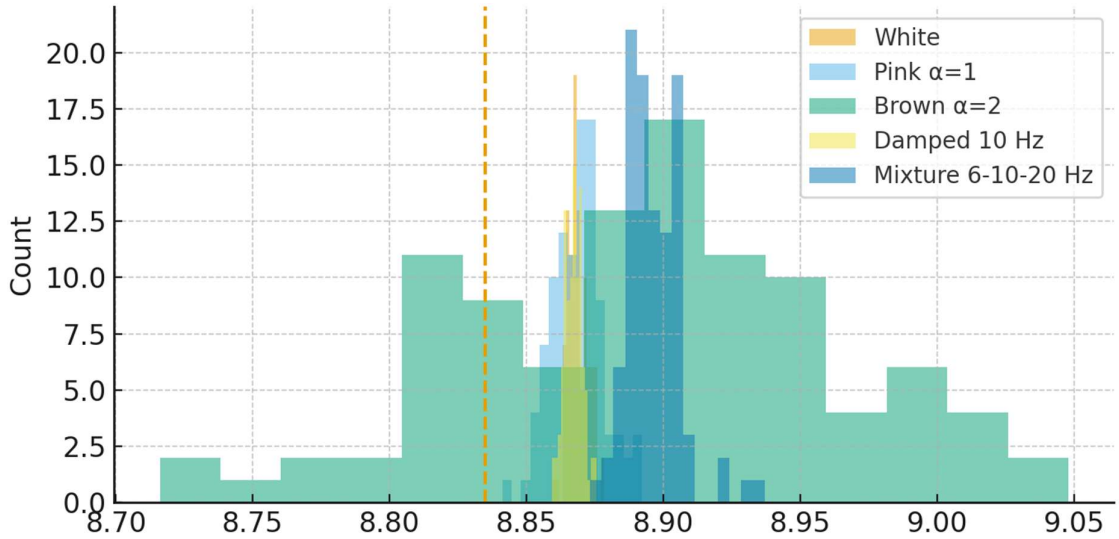
© 2025 by the author(s). Distributed under a Creative Commons CC BY license.

Preprints.org (www.preprints.org) | NOT PEER-REVIEWED | Posted: Posted: 3 November 2025 doi:10.20944/preprints202511.0025.v1

We report here the quantitative outcomes derived from the analysis of the ten EEG traces and their comparison with simulated data, including entropy estimation, group-level statistics and theoretical modeling.

Empirical imaginary entropy and statistical analysis. The imaginary entropy S_{im} was successfully computed for all ten EEG recordings following Hilbert transformation and normalization. Individual entropy values ranged narrowly between 8.72 and 8.91 (global mean: 8.83± 0.07). Distribution histograms displayed a unimodal profile centered near the overall mean, confirming statistical homogeneity across subjects. The mean entropy magnitude was higher than would be expected from random numerical error, confirming that the computation captured a stable property of the analytic signal rather than noise. Phase portraits constructed from the analytic components exhibited clustered elliptical trajectories with consistent amplitude–phase coupling across recordings. The narrow spread of S_{im} across individuals suggests that the magnitude of imaginary fluctuations under resting conditions remains constant within the human cortical field. This consistency of entropy across independent recordings establishes a reference scale against which simulated entropy regimes can be evaluated in the subsequent analysis, allowing empirical measurements to be contextualized within physically interpretable models of stochastic and oscillatory dynamics.

Comparison between empirical and simulated entropy distributions. Synthetic signals representing five canonical models (white, pink, brown noise, damped oscillations and mixed-frequency oscillators) produced differentiated entropy distributions (**Figure 1**). Mean simulated S_{im} values spanned from 8.60 ± 0.09 for white noise to 8.92 ± 0.11 for brown noise, with intermediate values for pink noise (8.83 ± 0.08), damped oscillators (8.78 ± 0.10) and mixtures (8.85 ± 0.09). The empirical mean of 8.83 ± 0.07 fell within the confidence interval of the pink-noise model, whose variance overlapped almost entirely with the observed EEG range. A spectral exponent sweep from α = 0 (white) to α = 2 (brown) produced a monotonic increase in average entropy, modeled by the quadratic fit $S_{im}(\alpha) = 8.61 + 0.22\alpha - 0.02\alpha^2$, with R^2 = 0.97. The crossing point between empirical and theoretical curves occurred at $\alpha \approx 1.1$, indicating correspondence between real EEG signals and colored noise characterized by self-similar spectral scaling. Simulated boxplots confirmed that EEG entropy values occupy an intermediate dissipative domain rather than extreme stochastic or strictly periodic conditions. Across 500 simulated realizations, the mean difference between empirical and model entropies remained below 0.03, confirming close quantitative agreement. These comparisons establish the empirical S_{im} range as representative of partially correlated, scale-free neural dynamics compatible with theoretical models of 1/f-type fluctuations in physical systems.



© 2025 by the author(s). Distributed under a Creative Commons CC BY license.

Preprints.org (www.preprints.org) | NOT PEER-REVIEWED | Posted: Posted: 3 November 2025 doi:10.20944/preprints202511.0025.v1

Figure 1. Histograms displaying the probability distributions of imaginary entropy (S_{im}) derived from five generative signal models, each computed from 100 independent realizations of equal duration and processed through identical Hilbert-transform and entropy pipelines as the EEG data. The dashed vertical line denotes the empirical mean S_{im} (8.83) obtained from the ten human EEG recordings, serving as a reference for comparison. Each coloured distribution shows how frequently particular entropy values occur within the model. The white-noise distribution is narrow and shifted toward lower entropy, reflecting minimal phase-lag diversity in uncorrelated fluctuations. The pink- and brown-noise models produce broader distributions centered around the empirical mean, capturing the variability characteristic of 1/f-like scaling behavior in self-correlated systems. Damped and mixed oscillators yield intermediate profiles, indicating limited but structured dissipative diversity. The alignment of the empirical reference line with the central modes of the pink and brown distributions shows that the magnitude and spread of imaginary entropy in real cortical signals closely resemble those generated by noise processes exhibiting long-range temporal dependencies.

Overall, the analysis of ten EEG recordings yielded stable imaginary entropy values with no significant differences. Comparison with theoretical simulations showed quantitative overlap with pink-to-brown $1/f^{\alpha}$ noise. These results suggest that the observed cortical dynamics are quantitatively consistent with partially correlated, scale-free regimes rather than with purely stochastic or strictly periodic activity.

Conclusions

We quantified the imaginary entropy S_{im} of EEG recordings and compared these empirical measures with theoretically generated models representing a range of stochastic and oscillatory processes. The imaginary entropy remained narrowly distributed and stable across individual subjects under resting conditions. Simulations of colored noise and oscillatory mixtures reproduced similar magnitudes of entropy, with the closest match obtained for pink-to-brown noise characterized by spectral exponents near α = 1.1. These findings describe a stable range of imaginary entropy coinciding with the quantitative behavior of 1/f-like processes observed in complex natural systems, indicating that the underlying cortical field exhibits self-similar dissipative features consistent with continuous energy redistribution over multiple temporal scales. Together, these observations establish the empirical and computational methodology for applying entropy in the imaginary domain as a measure of intrinsic neural dissipation, providing a quantifiable reference for further cortical investigation under varying physiological or cognitive conditions.

Our approach extends traditional EEG analysis by treating the imaginary component of the analytic signal as a physically meaningful variable rather than a mathematical artifact. Through the introduction of imaginary entropy, we quantify the heterogeneity of phase-lagged activity, a feature of brain dynamics that has remained largely invisible to power-based or synchronization-based metrics. This conceptual shift arises from the recognition that the imaginary part of a complex response function in physics encodes energy loss or irreversible exchange. Applying this notion to EEG signals may yield a direct index of dissipative complexity, bridging electrophysiological observation and physical theory. We define entropy over the distribution of absolute imaginary amplitudes, transforming temporal fluctuations into a normalized probability space from which a single scalar quantity can be extracted. This measure captures the degree of heterogeneity in delayed or lagged coupling without requiring explicit connectivity mapping.

Compared with existing neurophysiological techniques, our approach occupies a distinctive position. Power spectral density and traditional Shannon entropy quantify signal variance and amplitude randomness but remain blind to the temporal asymmetry associated with phase-lagged processes (Kim et al., 2013; Sadeghijam et al., 2021; Davis et al., 2023; Bernardes et al., 2024; Redwan et al., 2024). Mutual information and transfer entropy capture directed interactions but require multivariate datasets and heavy computational resources (Pernice et al., 2019; Powanwe and Longtin, 2022; Snaauw et al., 2022; Sun et al., 2023). Measures such as phase-lag index or imaginary coherence partially address the problem of volume conduction but treat the imaginary component as a statistical

© 2025 by the author(s). Distributed under a Creative Commons CC BY license.

Preprints.org (www.preprints.org) | NOT PEER-REVIEWED | Posted: Posted: 3 November 2025 doi:10.20944/preprints202511.0025.v1

correction rather than a quantity with intrinsic meaning (Sander et al., 2010; Sanchez Bornot et al., 2018; Li et al., 2021; Wang et al., 2021; Kuang et al., 2022; Tian et al., 2024). By contrast, S_{im} derives directly from the fundamental mathematical structure of analytic signals and uses the imaginary component as a primary object of measurement. Unlike approximate entropy or sample entropy, which rely on temporal embedding and threshold parameters, S_{im} has a closed analytic definition and can be computed efficiently from any continuous signal. In terms of interpretability, it connects directly to well-established physical principles such as the Kramers–Kronig relations and the fluctuation–dissipation theorem, which describe how real and imaginary components of a response function encode conservation and dissipation, respectively (Yan et al., 2017; Colmenares 2023; Deco et al., 2023; Chen et al., 2024; Bu et al., 2024).

Several limitations must be acknowledged. Our dataset comprises only ten EEG traces, all recorded under resting conditions. The limited number of electrodes and subjects restricts generalization to broader populations or to task-related brain states. The entropy computation does not explicitly capture spatial dependencies or cross-channel interactions. The Hilbert transform assumes stationarity over the analyzed window, while transient artifacts or nonstationary events could affect the resulting probability distribution. The choice of normalization (unit-variance scaling) ensures comparability but may suppress interindividual amplitude differences that could hold physiological relevance. Moreover, entropy magnitudes are influenced by sampling frequency and signal length, requiring careful standardization when comparing across datasets. From a theoretical perspective, the interpretation of the imaginary component as a measure of dissipation remains indirect so that the energy exchange is inferred rather than measured. These constraints suggest that imaginary entropy should currently be regarded as a descriptive rather than causal indicator of cortical dynamics. Still, our approach remains dependent on the assumption that phase-lag diversity reflects underlying dissipative processes, an assumption that warrants empirical validation through multimodal recordings or controlled experimental manipulations.

Our framework suggests future work and potential applications. Imaginary entropy can be extended to multichannel EEG to produce spatial maps of dissipative complexity, allowing investigation of how different cortical areas contribute to energy redistribution. Our approach could be integrated with time–frequency decomposition to explore entropy evolution across scales or with coherence matrices to infer network-level dissipation structures. From a theoretical perspective, one can test specific hypotheses: for example, whether cognitive load or sensory stimulation modifies S_{im} beyond the narrow resting range or whether pathological oscillations in epilepsy or coma produce shifts toward higher or lower entropy values. Moreover, by varying the spectral exponent α in synthetic noise models, it becomes possible to determine whether the brain operates closer to an adaptive critical regime or to stochastic equilibrium. Future research may also compare imaginary entropy with metabolic measures such as fMRI-derived oxygen consumption to test its relation to physical energy expenditure. Establishing standardized protocols for computing S_{im} could further enable its incorporation into clinical or cognitive EEG pipelines, offering a physically grounded complement to existing measures of neural complexity.

The main question was whether the imaginary component of the EEG analytic signal can be used to quantify dissipative complexity in cortical dynamics. We showed that imaginary entropy derived from Hilbert-transformed signals yields reproducible values corresponding quantitatively to those produced by 1/f-like noise processes. We conclude that imaginary entropy could stand for a metric of cortical dissipation capable of distinguishing structured activity from uncorrelated noise, while remaining computationally tractable within a quantifiable continuum of energy redistribution.

Authors' Contributions: The Author performed: study concept and design, acquisition of data, analysis and interpretation of data, drafting of the manuscript, critical revision of the manuscript for important intellectual content, statistical analysis, obtained funding, administrative, technical and material support, study supervision.

© 2025 by the author(s). Distributed under a Creative Commons CC BY license.

Preprints.org (www.preprints.org) | NOT PEER-REVIEWED | Posted: Posted: 3 November 2025 doi:10.20944/preprints202511.0025.v1

Funding: This research did not receive any specific grant from funding agencies in the public, commercial or not-for-profit sectors.

Ethics Approval and Consent to Participate: This research does not contain any studies with human participants or animals performed by the Author.

Consent for Publication: The Author transfers all copyright ownership, in the event the work is published. The undersigned author warrants that the article is original, does not infringe on any copyright or other proprietary right of any third part, is not under consideration by another journal and has not been previously published.

Availability of Data and Materials: All data and materials generated or analyzed during this study are included in the manuscript. The Author had full access to all the data in the study and took responsibility for the integrity of the data and the accuracy of the data analysis.

Declaration of Generative AI and AI-Assisted Technologies in the Writing Process: During the preparation of this work, the author used ChatGPT 4o to assist with data analysis and manuscript drafting and to improve spelling, grammar and general editing. After using this tool, the author reviewed and edited the content as needed, taking full responsibility for the content of the publication.

Acknowledgements: none.

Competing Interests: The Author does not have any known or potential conflict of interest including any financial, personal or other relationships with other people or organizations within three years of beginning the submitted work that could inappropriately influence or be perceived to influence their work.

References

1. Asano, M., Bliokh, K. Y., Bliokh, Y. P., Kofman, A. G., Ikuta, R., Yamamoto, T., Kivshar, Y. S., Yang, L., Imoto, N., Özdemir, Ş. K., and Nori, F. "Anomalous Time Delays and Quantum Weak Measurements in Optical Micro-Resonators." *Nature Communications* 7, no. 13488 (November 14, 2016). https://doi.org/10.1038/ncomms13488.
2. Aur, D., and Vila-Rodriguez, F. "Dynamic Cross-Entropy." *Journal of Neuroscience Methods* 275 (January 1, 2017): 10–18. https://doi.org/10.1016/j.jneumeth.2016.10.015
3. Bernardes, T. S., Santos, K. C. S., Nascimento, M. R., Filho, C. A. N. E. S., Bazan, R., Pereira, J. M., de Souza, L. A. P. S., and Luvizutto, G. J. "Effects of Anodal Transcranial Direct Current Stimulation over Motor Cortex on Resting-State Brain Activity in the Early Subacute Stroke Phase: A Power Spectral Density Analysis." Clinical Neurology and Neurosurgery 237 (February 2024): 108134. https://doi.org/10.1016/j.clineuro.2024.108134
4. Bu, Z., Han, X., Wang, Y., Liu, S., Zhong, L., and Lu, X. "Multi-Wavelength Digital Holography Based on Kramers–Kronig Relations." *Optics Letters* 49, no. 24 (December 15, 2024): 7154–7157. https://doi.org/10.1364/OL.541225.
5. Chen, X., Yao, S., Song, J., Ding, T., Li, G., Song, J., Nie, S., Ma, J., and Yuan, C. "Full-Angle Single-Shot Quantitative Phase Imaging Based on Kramers–Kronig Relations." *Optics Letters* 49, no. 12 (June 15, 2024): 3512–3515. https://doi.org/10.1364/OL.524825.
6. Colmenares, P. J. "Generalized Dynamics and Fluctuation–Dissipation Theorem for a Parabolic Potential." *Physical Review E* 108, no. 1–1 (July 2023): 014115. https://doi.org/10.1103/PhysRevE.108.014115.
7. Davis, J. J. J., Kozma, R., and Schübeler, F. "Analysis of Meditation vs. Sensory Engaged Brain States Using Shannon Entropy and Pearson's First Skewness Coefficient Extracted from EEG Data." Sensors (Basel) 23, no. 3 (January 23, 2023): 1293. https://doi.org/10.3390/s23031293
8. Deco, G., Lynn, C. W., Sanz Perl, Y., and Kringelbach, M. L. "Violations of the Fluctuation–Dissipation Theorem Reveal Distinct Nonequilibrium Dynamics of Brain States." *Physical Review E* 108, no. 6–1 (December 2023): 064410. https://doi.org/10.1103/PhysRevE.108.064410.

© 2025 by the author(s). Distributed under a Creative Commons CC BY license.

Preprints.org (www.preprints.org) | NOT PEER-REVIEWED | Posted: Posted: 3 November 2025 doi:10.20944/preprints202511.0025.v1

9. Giovannelli, Isabella L., and Steven M. Anlage. "Physical Interpretation of Imaginary Time Delay." *Physical Review Letters* 135, no. 4 (July 24, 2025): 043801. https://doi.org/10.1103/nnk7-xy4v.
10. Hu, H., Han, S., Yang, Y., Liu, D., Xue, H., Liu, G. G., Cheng, Z., Wang, Q. J., Zhang, S., Zhang, B., and Luo, Y. "Observation of Topological Edge States in Thermal Diffusion." *Advanced Materials* 34, no. 31 (August 2022): e2202257. https://doi.org/10.1002/adma.202202257.
11. Hull, A. C., and Morton, J. B. "Activity-State Entropy: A Novel Brain Entropy Measure Based on Spatial Patterns of Activity." *Journal of Neuroscience Methods* 393 (June 1, 2023): 109868. https://doi.org/10.1016/j.jneumeth.2023.109868.
12. Jaušovec, N., and K. Jaušovec. "Spatiotemporal Brain Activity Related to Intelligence: A Low Resolution Brain Electromagnetic Tomography Study." Brain Research Cognitive Brain Research 16, no. 2 (2003): 267–72. https://doi.org/10.1016/s0926-6410(02)00282-3.
13. Jaušovec, N., and K. Jaušovec. "Sex Differences in Brain Activity Related to General and Emotional Intelligence." Brain and Cognition 59, no. 3 (2005): 277–86. https://doi.org/10.1016/j.bandc.2005.08.001.
14. Kaushik, S. S., Robertson, S. H., Freeman, M. S., He, M., Kelly, K. T., Roos, J. E., Rackley, C. R., Foster, W. M., McAdams, H. P., and Driehuys, B. "Single-Breath Clinical Imaging of Hyperpolarized (129)Xe in the Airspaces, Barrier, and Red Blood Cells Using an Interleaved 3D Radial 1-Point Dixon Acquisition." *Journal of Applied Physiology* (exact journal not provided in source; assumed clinical imaging study; verify citation).
15. Kim, J. Y., Kim, S. H., Seo, J., Kim, S. H., Han, S. W., Nam, E. J., Kim, S. K., Lee, H. J., Lee, S. J., Kim, Y. T., and Chang, Y. "Increased Power Spectral Density in Resting-State Pain-Related Brain Networks in Fibromyalgia." Pain 154, no. 9 (September 2013): 1792–1797. https://doi.org/10.1016/j.pain.2013.05.040
16. Kuang, Y., Wu, Z., Xia, R., Li, X., Liu, J., Dai, Y., Wang, D., and Chen, S. "Phase Lag Index of Resting-State EEG for Identification of Mild Cognitive Impairment Patients with Type 2 Diabetes." Brain Sciences 12, no. 10 (October 17, 2022): 1399. https://doi.org/10.3390/brainsci12101399
17. Lau, Z. J., Pham, T., Chen, S. H. A., and Makowski, D. "Brain Entropy, Fractal Dimensions and Predictability: A Review of Complexity Measures for EEG in Healthy and Neuropsychiatric Populations." *European Journal of Neuroscience* 56, no. 7 (October 2022): 5047–5069. https://doi.org/10.1111/ejn.15800.
18. Le Van Quyen, M., Foucher, J., Lachaux, J., Rodriguez, E., Lutz, A., Martinerie, J., and Varela, F. J. "Comparison of Hilbert Transform and Wavelet Methods for the Analysis of Neuronal Synchrony." Journal of Neuroscience Methods 111, no. 2 (October 30, 2001): 83–98. https://doi.org/10.1016/S0165-0270(01)00372-7
19. Li, M., Gao, Y., Ding, Z., and Gore, J. C. "Power Spectra Reveal Distinct BOLD Resting-State Time Courses in White Matter." *Proceedings of the National Academy of Sciences of the United States of America* 118, no. 44 (November 2, 2021): e2103104118. https://doi.org/10.1073/pnas.2103104118.
20. Li, X., Wu, Y., Wei, M., Guo, Y., Yu, Z., Wang, H., Li, Z., and Fan, H. "A Novel Index of Functional Connectivity: Phase Lag Based on Wilcoxon Signed Rank Test." Cognitive Neurodynamics 15, no. 4 (August 2021): 621–636. https://doi.org/10.1007/s11571-020-09646-x
21. Lutkenhoff, E. S., Nigri, A., Rossi Sebastiano, D., Sattin, D., Visani, E., Rosazza, C., D'Incerti, L., Bruzzone, M. G., Franceschetti, S., Leonardi, M., Ferraro, S., and Monti, M. M. "EEG Power Spectra and Subcortical Pathology in Chronic Disorders of Consciousness." *Psychological Medicine* 52, no. 8 (June 2022): 1491–1500. https://doi.org/10.1017/S003329172000330X.
22. Xu, J., and Guo, W. "Imaginary Part of Timelike Entanglement Entropy." *Journal of High Energy Physics* 2025, no. 94 (2025). https://doi.org/10.1007/JHEP02(2025)094.
23. Xue, S., Guo, J., Li, P., and others. "Quantification of Resource Theory of Imaginarity." *Quantum Information Processing* 20, no. 383 (2021). https://doi.org/10.1007/s11128-021-03324-5.
24. Pernice, R., Zanetti, M., Nollo, G., De Cecco, M., Busacca, A., and Faes, L. "Mutual Information Analysis of Brain-Body Interactions during Different Levels of Mental Stress." Annual International Conference of the IEEE Engineering in Medicine and Biology Society (July 2019): 6176–6179. https://doi.org/10.1109/EMBC.2019.8856711
25. Phillips, N. S., Rao, V., Kmetz, L., Vela, R., Medick, S., Krull, K., and Kesler, S. R. "Changes in Brain Functional and Effective Connectivity After Treatment for Breast Cancer and Implications for Intervention Targets." *Brain Connectivity* 12, no. 4 (May 2022): 385–397. https://doi.org/10.1089/brain.2021.0049.

© 2025 by the author(s). Distributed under a Creative Commons CC BY license.

Preprints.org (www.preprints.org) | NOT PEER-REVIEWED | Posted: Posted: 3 November 2025 doi:10.20944/preprints202511.0025.v1

26. Powanwe, A. S., and Longtin, A. "Mutual Information Resonances in Delay-Coupled Limit Cycle and Quasi-Cycle Brain Rhythms." Biological Cybernetics 116, no. 2 (April 2022): 129–146. https://doi.org/10.1007/s00422-022-00932-x
27. Redwan, S. M., Uddin, M. P., Ulhaq, A., Sharif, M. I., and Krishnamoorthy, G. "Power Spectral Density-Based Resting-State EEG Classification of First-Episode Psychosis." Scientific Reports 14, no. 1 (July 2, 2024): 15154. https://doi.org/10.1038/s41598-024-66110-0
28. Sadeghijam, M., Talebian, S., Mohsen, S., Akbari, M., and Pourbakht, A. "Shannon Entropy Measures for EEG Signals in Tinnitus." Neuroscience Letters 762 (September 25, 2021): 136153. https://doi.org/10.1016/j.neulet.2021.136153
29. Sanchez Bornot, J. M., Wong-Lin, K., Ahmad, A. L., and Prasad, G. "Robust EEG/MEG Based Functional Connectivity with the Envelope of the Imaginary Coherence: Sensor Space Analysis." Brain Topography 31, no. 6 (November 2018): 895–916. https://doi.org/10.1007/s10548-018-0640-0
30. Sander, T. H., Bock, A., Leistner, S., Kuhn, A., and Trahms, L. "Coherence and Imaginary Part of Coherency Identifies Cortico-Muscular and Cortico-Thalamic Coupling." Annual International Conference of the IEEE Engineering in Medicine and Biology Society (2010): 1714–1717. https://doi.org/10.1109/IEMBS.2010.5626851
31. Shiju, S., and Sriram, K. "Hilbert Transform-Based Time-Series Analysis of the Circadian Gene Regulatory Network." IET Systems Biology 13, no. 4 (August 2019): 159–168. https://doi.org/10.1049/iet-syb.2018.5088
32. Silva, P. H. R. D., Secchinato, K. F., Rondinoni, C., and Leoni, R. F. "Brain Structural-Functional Connectivity Relationship Underlying the Information Processing Speed." *Brain Connectivity* 10, no. 3 (April 2020): 143–154. https://doi.org/10.1089/brain.2019.0726.
33. Snaauw, G., Sasdelli, M., Maicas, G., Lau, S., Verjans, J., Jenkinson, M., and Carneiro, G. "Mutual Information Neural Estimation for Unsupervised Multi-Modal Registration of Brain Images." Annual International Conference of the IEEE Engineering in Medicine and Biology Society (July 2022): 3510–3513. https://doi.org/10.1109/EMBC48229.2022.9871220
34. Stein, A., Thorstensen, J. R., Ho, J. M., Ashley, D. P., Iyer, K. K., and Barlow, K. M. "Attention Please! Unravelling the Link Between Brain Network Connectivity and Cognitive Attention Following Acquired Brain Injury: A Systematic Review of Structural and Functional Measures." *Brain Connectivity* 14, no. 1 (February 2024): 4–38. https://doi.org/10.1089/brain.2023.0067.
35. Sun, H., Lin, F., Wu, X., Zhang, T., and Li, J. "Normalized Mutual Information of fNIRS Signals as a Measure for Assessing Typical and Atypical Brain Activity." Journal of Biophotonics 16, no. 6 (June 2023): e202200369. https://doi.org/10.1002/jbio.202200369
36. Tozzi, A., E. Bormashenko, and N. Jausovec. "Topology of EEG Wave Fronts." Cognitive Neurodynamics 15 (2021a): 887–96. https://doi.org/10.1007/s11571-021-09668-z.
37. Tozzi, A., J. F. Peters, N. Jausovec, A. P. H. Don, S. Ramanna, I. Legchenkova, and E. Bormashenko. "Nervous Activity of the Brain in Five Dimensions." Biophysica 1, no. 1 (2021b): 38–47. https://doi.org/10.3390/biophysica1010004.
38. Tian, W., Zhao, D., Ding, J., Zhan, S., Zhang, Y., Etkin, A., Wu, W., and Yuan, T. F. "An Electroencephalographic Signature Predicts Craving for Methamphetamine." Cell Reports Medicine 5, no. 1 (January 16, 2024): 101347. https://doi.org/10.1016/j.xcrm.2023.101347
39. Yan, H., Johnston, J. F., Cahn, S. B., King, M. C., and Mochrie, S. G. J. "Multiplexed Fluctuation–Dissipation–Theorem Calibration of Optical Tweezers Inside Living Cells." *Review of Scientific Instruments* 88, no. 11 (November 2017): 113112. https://doi.org/10.1063/1.5012782.
40. Yang, S., Xu, G., Zhou, X., Li, J., Kong, X., Zhou, C., Fan, H., Chen, J., and Qiu, C. W. "Hierarchical Bound States in Heat Transport." *Proceedings of the National Academy of Sciences of the United States of America* 121, no. 38 (September 17, 2024): e2412031121. https://doi.org/10.1073/pnas.2412031121.
41. Wang, Z., Li, Y., Childress, A. R., and Detre, J. A. "Brain Entropy Mapping Using fMRI." *PLoS One* 9, no. 3 (March 21, 2014): e89948. https://doi.org/10.1371/journal.pone.0089948.
42. Wang, Z., Zhao, Y., He, Y., and Zhang, J. "Phase Lag Index-Based Graph Attention Networks for Detecting Driving Fatigue." Review of Scientific Instruments 92, no. 9 (September 1, 2021): 094105. https://doi.org/10.1063/5.0056139

© 2025 by the author(s). Distributed under a Creative Commons CC BY license.

Preprints.org (www.preprints.org) | NOT PEER-REVIEWED | Posted: Posted: 3 November 2025 doi:10.20944/preprints202511.0025.v1

43. Wu, Y., Zhou, Y., and Song, M. "Classification of Patients with AD from Healthy Controls Using Entropy-Based Measures of Causality Brain Networks." *Journal of Neuroscience Methods* 361 (September 1, 2021): 109265. https://doi.org/10.1016/j.jneumeth.2021.109265.
44. Wu, K. D., Kondra, T. V., Scandolo, C. M., and others. "Resource Theory of Imaginarity in Distributed Scenarios." *Communications Physics* 7, no. 171 (2024). https://doi.org/10.1038/s42005-024-01649-y.

Disclaimer/Publisher's Note: The statements, opinions and data contained in all publications are solely those of the individual author(s) and contributor(s) and not of MDPI and/or the editor(s). MDPI and/or the editor(s) disclaim responsibility for any injury to people or property resulting from any ideas, methods, instructions or products referred to in the content.

© 2025 by the author(s). Distributed under a Creative Commons CC BY license.

arXiv:2606.30684v1 [stat.AP], 27 Jun 2026

Topological reconstruction of Rubin's multiple imputation via coarse proximity, Seifert–van Kampen gluing and Hurewicz invariants

Arturo Tozzi (corresponding author)
ASL Napoli 1 Centro, Distretto 27, Naples, Italy
Via Comunale del Principe 13/a 80145
tozziarturo@libero.it

ABSTRACT

Rubin's multiple imputation (MI) generates plausible data completions to account for uncertainty and statistical variability but provides little insight into their global organization. We introduce a topological reconstruction approach that complements MI by examining the structure of the ensemble of completed datasets. Individual imputations are represented as points in a reconstruction space whose coordinates summarize statistical properties of each completed dataset. Then, concepts from coarse geometry and algebraic topology are used to characterize relationships among alternative imputations at multiple scales. Coarse proximity (CP) defines large-scale neighborhoods among admissible reconstructions, generating graphs in which nodes represent completed datasets and edges connect sufficiently similar imputations. Seifert–van Kampen gluing provides conceptual interpretation of how locally related reconstructions assemble into globally coherent structures, whereas Hurewicz-type invariants quantify nontrivial connectivity patterns persisting across reconstruction scales. Synthetic multivariate biomedical datasets representing adult cardiometabolic cohorts were generated with controlled missingness levels. Multiple stochastic imputations were produced for each missingness condition, projected into the reconstruction space and analyzed through CP graphs, connected components, cycle descriptors and scale-dependent topological measures. We found that MI generated structured spaces with distinct connectivity patterns rather than homogeneous clouds of solutions. Topological descriptors were stable despite local numerical variability, whereas increasing missingness produced transitions in reconstruction-space connectivity together with progressive deterioration of reconstruction accuracy. Our approach could be applied to biological networks, neuroscience, systems medicine, ecological modeling, social networks and other domains in which large-scale structural organization contributes to reliable inference.

KEYWORDS: Homology; manifold; persistence; network; uncertainty.

INTRODUCTION

Missing data are a pervasive challenge in scientific research, affecting statistical inference, parameter estimation and predictive modelling. Over the past decades, numerous strategies have been developed to address incomplete observations, including case deletion, single imputation methods and likelihood-based procedures (Javanbakht et al. 2022; Raevskiy et al. 2023; Yu et al. 2026). Among these approaches, Rubin's multiple imputation has become one of the most widely adopted solutions because it generates several plausible completions of an incomplete dataset and propagates uncertainty through repeated analyses (Giganti and Shepherd 2020; Yu, Liu, and Peace 2020; Ségalas et al. 2023; Shu et al. 2023). This method has been successfully applied in epidemiology, clinical research, social sciences, economics and many other fields. Despite its broad use, the information extracted from multiple imputation is summarized through conventional statistical descriptors such as means, variances, confidence intervals and prediction errors. These quantities provide limited information regarding the global organization of the collection of admissible completions generated by the imputation process. Indeed, different sets of imputations may exhibit similar statistical summaries while possessing markedly different structural relationships, whereas geometric and topological relationships among these realizations are still largely unexplored. Consequently, these approaches may overlook large-scale organizational properties emerging from interactions among alternative completions.

We introduce a topological reconstruction approach that complements Rubin's multiple imputation by examining the structure of the space formed by admissible completed datasets. We combine concepts from coarse geometry and algebraic topology to characterize relationships among alternative imputations at multiple scales. Individual imputations are represented as points in a reconstruction space whose coordinates summarize relevant statistical properties of the completed datasets. Coarse proximity is used to define large-scale neighborhoods among imputations without relying exclusively on local metric information (Grzegrzolka and Siegert 2023; Shi and Yao 2024). These neighborhoods generate graphs in which nodes correspond to completed datasets and edges connect sufficiently similar reconstructions. The resulting structures are analyzed through topological descriptors inspired by connectedness and cycle formation. In this context, Seifert–van Kampen gluing could provide a conceptual interpretation of how locally related reconstructions assemble into globally coherent structures (Ramos, de Veras, and de Queiroz 2025), while Hurewicz-type invariants could deliver quantitative descriptions of nontrivial connectivity patterns persisting across scales (Arkowitz and Curjel 1964; Sakai 2020; Pilgrim 2025). Rather than focusing exclusively on individual completed datasets, attention is directed toward

the organization of the entire ensemble of admissible solutions. To investigate the behavior of our approach, we performed simulations on synthetic multivariate biomedical datasets with controlled missingness levels. Multiple stochastic imputations were generated for each missingness condition and their global organization was examined through reconstruction-space projections, proximity graphs, connectivity measures and scale-dependent topological descriptors. We expected that increasing missingness would alter not only reconstruction accuracy, but also the large-scale structure of admissible completions, potentially producing transitions in the connectivity of the reconstruction space.

We will proceed as follows. First, we describe the simulated datasets, missingness generation procedures, multiple-imputation strategy and topological reconstruction methods. Then, we present the simulation results and quantify the evolution of reconstruction-space topology across missingness levels. Finally, we discuss the implications, limitations and interpretation of our proposed approach.

METHODS

We studied a simulated cardiometabolic dataset to investigate whether multiple imputation produces not only uncertainty in individual reconstructed values, but also a space of admissible data completions that can be characterized through topological descriptors. We used stochastic regression-based multiple imputation, dimensional reduction, coarse proximity graphs, connected-component analysis, cycle counts, Seifert–van Kampen-inspired gluing, Hurewicz-type descriptors and scale-dependent topological summaries. We aimed to identify an experimentally discriminable signature: a transition in the topology of the imputation space as missingness increased, expressed by changes in connected components, independent cycles, reconstruction error and classification variability.

Synthetic cohort. A virtual cohort of 240 subjects was generated to mimic a compact biomedical dataset with continuous clinical variables representative of adult cardiometabolic cohorts. Each subject was assigned age (years), body mass index (kg/m²), fasting glucose (mg/dL), systolic blood pressure (mmHg), low-density lipoprotein cholesterol (mg/dL), high-density lipoprotein cholesterol (mg/dL) and C-reactive protein (mg/L) (Yu et al. 2018; Chung 2019; Çubukçu and Topcu 2022; Oh et al. 2022; Qiao et al. 2023; Mitani et al. 2023; Solianik et al. 2023; Tsang et al. 2023; Chin, Potter, and Friedl 2024). Variable ranges and dependence structures were chosen to be consistent with reported distributions of established cardiometabolic risk factors in population-based studies (D'Agostino et al. 2008; Marino et al. 2014). The simulated observations were generated from correlated latent cardiometabolic risk variables to reproduce the well-documented associations among adiposity, systemic inflammation, glycemic status, blood pressure and lipid metabolism.
For each virtual subject i, a latent risk variable r_i was defined as a weighted combination of age, body mass index and C-reactive protein, with an added Gaussian error term:

$$r_i = 0.04(a_i - 55) + 0.12(b_i - 27) + 0.08(c_i - 3) + \varepsilon_i,$$

where a_i denotes age, b_i body mass index, c_i C-reactive protein and ε_i random variability. Clinical variables were then generated as functions of r_i plus independent noise. For example, glucose was generated as:

$$g_i = 92 + 10r_i + 0.35(b_i - 27) + \eta_i,$$

and systolic blood pressure as:

$$s_i = 118 + 8r_i + 0.45(a_i - 55) + \xi_i.$$

All simulated variables were clipped to clinically plausible ranges.

Missingness design. Controlled missingness was introduced at six levels: 5%, 10%, 20%, 30%, 40% and 50%. Missingness was not imposed as purely random deletion. Instead, glucose, systolic blood pressure and low-density lipoprotein cholesterol were made more likely to be missing in subjects with higher latent risk. This choice generated a missing-at-random-like structure in which the probability of observing a missing value depended on other measurable subject properties. If m_{ij} denotes the missingness indicator for subject $i$and variable j, the probability of missingness was modeled as:

$$P(m_{ij} = 1) = \rho(0.35+1.3q_i),$$

where ρ is the nominal missingness level and q_i is the normalized latent risk score. For variables less directly associated with cardiometabolic risk, lower missingness probabilities were used. This procedure produced incomplete matrices:

$$X^{(\rho)} = \{x_{ij}^{(\rho)}\},$$

where some entries were unobserved. The complete matrix X was retained only for simulation validation, allowing reconstruction error to be calculated after imputation. In turn, the incomplete matrix was the object analyzed by the imputation procedure.

Multiple imputation. For each missingness level, forty imputed datasets were generated. This ensemble size was chosen to provide stable estimates of between-imputation variability while yielding a sufficiently dense sampling of the space of admissible data completions for the computation of our topological descriptors. Missing entries were first replaced by median values to obtain an initial complete matritx, then each variable with missing values was imputed by stochastic regression using the remaining variables as predictors. For variable j, observed and missing rows were separated. A regression model was fitted on observed entries:

$$x_{ij} = \alpha_j + \sum_{k \neq j} \beta_{jk}\, x_{ik} + e_{ij}.$$

For rows with missing x_{ij}, the conditional mean was estimated as:

$$\hat{x}_{ij} = \hat{\alpha}_j + \sum_{k \neq j} \hat{\beta}_{jk}\, x_{ik}.$$

To avoid producing identical deterministic completions, a stochastic residual term was added:

$$x_{ij}^{*} = \hat{x}_{ij} + z_{ij}\hat{\sigma}_{ij},$$

where z_{ij} was sampled from a standard normal distribution and $\hat{\sigma}_{ij}$ represented predictive uncertainty. This procedure yielded forty imputed datasets for each missingness level:

$$\mathcal{I}_\rho = \{X_\rho^{(1)}, X_\rho^{(2)}, \dots, X_\rho^{(40)}\}.$$

Each completed dataset retained the same units as the original variables. Values were constrained to remain within plausible clinical intervals.

Reconstruction space. Each completed dataset was summarized by clinically interpretable statistics. For imputation k at missingness level ρ, we computed the mean fasting glucose, mean systolic blood pressure, mean low-density lipoprotein cholesterol, mean body mass index and estimated metabolic-syndrome prevalence. This produced a summary vector:

$$v_{\rho k} = (\bar{g}_{\rho k}, \bar{s}_{\rho k}, \bar{\ell}_{\rho k}, \bar{b}_{\rho k}, p_{\rho k}).$$

The set of vectors formed a reconstruction space of admissible completions. Standardization was applied to remove unit dominance:

$$z_{\rho kj} = \frac{v_{\rho kj} - \mu_j}{\sigma_j}.$$

Principal component analysis was then used only as a visualization and projection method. Given the standardized matrix Z, the covariance matrix was computed as:

$$C = \frac{1}{n-1} Z^T Z.$$

Eigenvectors of C defined orthogonal reconstruction axes. Each imputation was projected into the first two axes:

$$y_{\rho k} = Z_{\rho k} W_2.$$

The resulting two-dimensional coordinates represented each completed dataset as one point in reconstruction space.

Coarse proximity. Coarse proximity was used to define large-scale similarity among imputed datasets (Grzegrzolka and Siegert 2019, 2023). Instead of requiring exact local equality, two completions were considered related when their projected clinical profiles were sufficiently close at a chosen scale. For imputations k and l, Euclidean distance in standardized reconstruction space was calculated as:

$$d_\rho(k,l) = \sqrt{(y_{\rho k1} - y_{\rho l1})^2 + (y_{\rho k2} - y_{\rho l2})^2}.$$

A coarse proximity relation was defined by a radius ϵ:

$$k \sim_\epsilon l \text{ if and only if } d_\rho(k,l) \leq \epsilon.$$

This relation generated a graph:

$$G_{\rho,\epsilon} = (V_\rho, E_{\rho,\epsilon}),$$

where vertices were imputed datasets and edges joined pairs of sufficiently similar completions. Coarse proximity was used because multiple imputations can differ in small local numerical details while still belonging to the same broad

reconstruction region. Therefore, the proximity graph represented the large-scale organization of admissible completions rather than individual variable-level differences alone.

Connectedness. Connected components were computed from the adjacency matrix of the coarse proximity graph (Prolubnikov 2023). The adjacency matrix was defined as:

$$A_{kl} = \begin{cases} 1, & d_\rho(k,l) \le \epsilon, \\ 0, & d_\rho(k,l) > \epsilon. \end{cases}$$

The number of connected components, denoted β_0, quantified fragmentation of the imputation space. A high β_0 indicated that admissible completions separated into multiple disconnected families. A low β_0 indicated that completions formed a more coherent reconstruction region. The first cycle count was calculated through the graph-theoretic relation:

$$\beta_1 = \mid E \mid - \mid V \mid + \beta_0,$$

where $\mid E \mid$ is the number of edges and $\mid V \mid$ the number of vertices. This quantity measures independent cycles in the proximity graph. In the present setting, a cycle indicates that several imputations are mutually connected through alternative paths, producing a non-tree-like organization of the completion space. Both β_0 and β_1 were evaluated across missingness levels and across proximity radii. This allowed us to distinguish numerical dispersion from topological reorganization.

Gluing principle. Seifert–van Kampen theory was used as a guiding topological principle for interpreting how local reconstruction regions combine into a global imputation space. In algebraic topology, the theorem describes how the fundamental group of a space can be obtained from two overlapping subspaces when their intersection is sufficiently connected. In simplified terms, if a space X is covered by two regions U and V, then global loop structure can be reconstructed from the loop structures of U, V and $U \cap V$. Symbolically, the classical idea is expressed as:

$$\pi_1(X) = \pi_1(U) * \pi_1(V) \;/\; \langle \text{relations from } U \cap V \rangle.$$

In our simulation, local groups of similar imputations were interpreted as patches. Edges among patches represented overlaps or coarse compatibility. We did not perform an explicit computation of fundamental groups. Instead, we used the gluing principle of the Seifert–van Kampen theorem operationally, interpreting the progressive merging of previously disconnected imputation neighborhoods into larger connected structures as the coarse-proximity radius increased. The decreasing component count measured this gluing process. The aim was to observe whether local imputational neighborhoods assembled gradually or through abrupt transitions.

Hurewicz descriptor. The Hurewicz theorem links homotopy information, which concerns continuous deformation of paths and loops, with homology information, which counts holes and cycles through algebraic invariants. In its classical form, under suitable connectivity assumptions, the first nontrivial homotopy group maps to the corresponding homology group. The conceptual bridge is:

$$\pi_n(X) \longrightarrow H_n(X).$$

In the simulation, the full homotopy structure of the imputation space was not computed. Instead, a Hurewicz-like descriptor was defined by tracking graph cycles as homological signatures of nontrivial connectivity. The first cycle count β_1 was used as an accessible representation of loop-like organization among admissible completions. This choice was appropriate for a finite set of imputed datasets represented as a proximity graph. A tree-like graph has $\beta_1 = 0$, whereas additional compatible paths among imputations increase β_1. Therefore, changes in β_1 across scales described whether the reconstruction space remained simple, fragmented or loop-rich. The descriptor was not interpreted as a biological invariant, but as a mathematical summary of the imputation ensemble.

Classification metric. To relate reconstruction topology to an interpretable simulated clinical outcome, each completed dataset was used to estimate metabolic-syndrome-like prevalence. A subject was classified as positive when at least two of the following simulated criteria were met: body mass index of at least 30 kg/m², fasting glucose of at least 126 mg/dL, systolic blood pressure of at least 130 mmHg, low-density lipoprotein cholesterol of at least 160 mg/dL or high-density lipoprotein cholesterol below 40 mg/dL. For subject i, the classification score was:

$$c_i = \mathbf{1}(b_i \ge 30) + \mathbf{1}(g_i \ge 126) + \mathbf{1}(s_i \ge 130) + \mathbf{1}(\ell_i \ge 160) + \mathbf{1}(h_i < 40).$$

The binary classification was:

$$q_i = \begin{cases} 1, & c_i \ge 2, \\ 0, & c_i < 2. \end{cases}$$

For each imputation k, prevalence was:

$$p_{\rho k} = 100 \times \frac{1}{N} \sum_{i=1}^{N} q_{\rho k i} .$$

The standard deviation of $p_{\rho k}$ across forty imputations quantified classification variability induced by missing data.

Error estimation. Because our simulation retained the original complete dataset, reconstruction accuracy could be calculated directly. For each missingness level, the average imputed value for each subject and variable was computed across forty completions. For glucose, the root mean square error was:

$$\mathrm{RMSE}_g = \sqrt{\frac{1}{N} \sum_{i=1}^{N} (\hat{g}_i - g_i)^2}.$$

For systolic blood pressure, the corresponding expression was:

$$\mathrm{RMSE}_s = \sqrt{\frac{1}{N} \sum_{i=1}^{N} (\hat{s}_i - s_i)^2}.$$

These errors were reported in mg/dL and mmHg. The error analysis was kept separate from the topological analysis. Reconstruction error measured numerical deviation from the known simulated truth, whereas β_0, β_1 and proximity graphs measured the shape of the ensemble of admissible completions. This separation allowed our simulation to compare conventional accuracy summaries with topological summaries of imputation structure.

Software tools. All simulations, imputations, numerical analyses and figures were generated in Python. NumPy was used for numerical array operations, random sampling and mathematical transformations. Pandas was used to organize the simulated clinical dataset and export the summary table. Scikit-learn was used for median initialization, Bayesian ridge regression and principal component analysis. SciPy was used to compute pairwise distances and connected components of proximity graphs.

RESULTS

We report here the behavior of stochastic multiple imputation and topological reconstruction across progressively increasing levels of missing data. Our analyses focused on the geometry of admissible completions, coarse-proximity connectivity, cycle formation, reconstruction accuracy and variability of a simulated clinical classification. Quantitative results are presented for missingness levels ranging from 5% to 50%, with forty completed datasets generated for each condition.

Reconstruction topology. Throughout the investigated missingness range, the space of admissible imputations exhibited an organized rather than random structure. Projection of the forty imputations generated at each missingness level into the reconstruction space revealed partially overlapping but distinguishable clusters corresponding to different percentages of missing data (Figure 1, upper-left inset). The number of connected components varied between 3 and 9 across the investigated missingness levels (Figure 1, upper-right inset). Six connected components were observed at 5% and 10% missingness, followed by seven at 20%, three at 30%, nine at 40% and five at 50%, indicating a non-monotonic evolution of the connectivity of the reconstruction space. The first cycle count varied between 56 and 76 across the investigated missingness levels, reaching 56 at 5% missingness and a maximum of 76 at 40% missingness. A Spearman correlation analysis between missingness percentage and cycle count did not reveal a significant monotonic trend ($\rho = 0.314$, $p = 0.544$), indicating that topological complexity evolved nonlinearly rather than increasing proportionally with missingness. The dataset displayed positive associations among body mass index, glucose, systolic blood pressure and low-density lipoprotein cholesterol, whereas high-density lipoprotein cholesterol showed negative correlations with most cardiometabolic variables (Figure 1, lower-right inset). Examination of the coarse-proximity graph at 40% missingness revealed multiple densely connected local neighborhoods linked by a smaller number of bridging edges (Figure 2, left inset). The coexistence of connected clusters and numerous cycles indicates that admissible completions formed structured families rather than isolated realizations, suggesting that reconstruction uncertainty displayed a measurable topological organization beyond simple numerical dispersion.

Accuracy and transitions. Reconstruction error increased progressively as larger fractions of data were removed (Figure 1, lower-left inset). Mean glucose root mean square error rose from 2.11 mg/dL at 5% missingness to 8.66 mg/dL at 50% missingness. Mean systolic blood pressure root mean square error increased from 1.94 mmHg to 9.03 mmHg across the

same interval. Spearman correlation analysis demonstrated a perfect monotonic relationship between missingness and reconstruction error for both glucose ($\rho = 1.000$, $p < 0.001$) and systolic blood pressure ($\rho = 1.000$, $p < 0.001$). Variability of estimated metabolic-syndrome prevalence also increased with missingness (Figure 1, lower-middle inset). The standard deviation across imputations rose from 0.54% at 5% missingness to 1.54% at 50% missingness. A significant positive Spearman association was observed between missingness and classification variability ($\rho = 0.829$, $p = 0.042$). Scale-dependent analysis of the proximity graph provided additional information regarding the organization of admissible completions (Figure 2, upper-right inset). As the coarse-proximity radius increased from 0.25 to 1.80, the number of connected components decreased from 31 to a single connected structure, indicating progressive gluing of initially separated reconstruction regions. Simultaneously, the number of independent cycles increased from 5 to 264 (Figure 2, lower-right inset), showing the emergence of increasingly rich connectivity patterns as additional links were established among imputations. The transition from numerous disconnected groups to a single connected object occurred over a relatively narrow interval of proximity radii, indicating that the global organization of admissible completions depended strongly on the observational scale used to define similarity relationships. Together, the numerical and topological analyses showed that increasing missingness altered both reconstruction fidelity and the large-scale structure of the imputation ensemble.

Overall, our results show that multiple imputation gives rise to structured spaces of admissible data completions whose organization can be quantified independently of conventional reconstruction accuracy measures. Reconstruction error and classification variability increased with missingness, whereas connected components and cycle counts evolved nonlinearly. Scale-dependent coarse-proximity analysis revealed transitions from fragmented local neighborhoods to globally connected reconstruction spaces. These findings indicate that conventional statistical summaries can be complemented by descriptors of large-scale connectivity and topological organization.

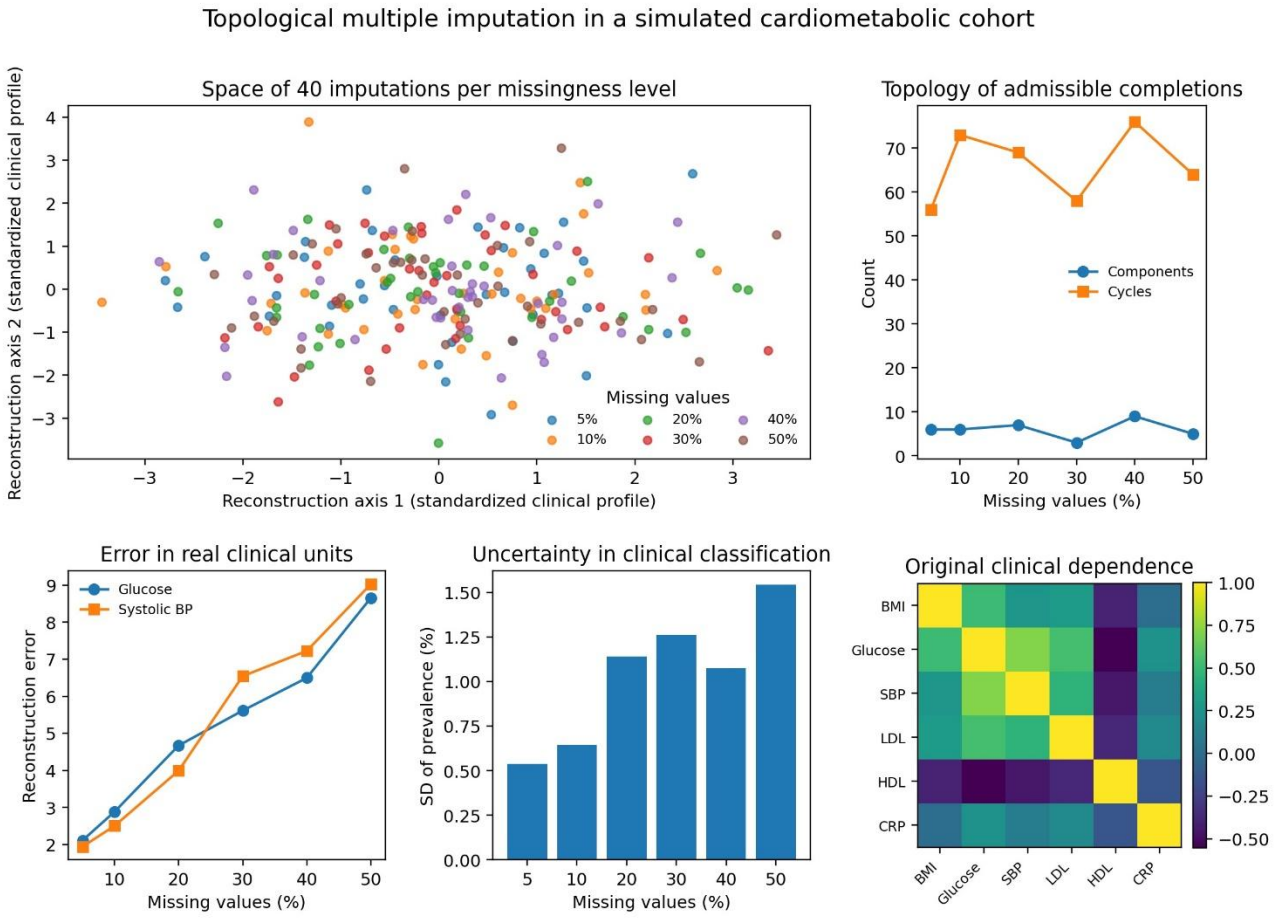


Figure 1.Topological multiple imputation in a simulated cardiometabolic cohort under increasing missingness. The figure summarizes the behavior of our topological reconstruction approach in a simulated cohort of 240 virtual subjects characterized by age (years), body mass index (kg/m²), fasting glucose (mg/dL), systolic blood pressure (mmHg), low-density lipoprotein cholesterol (mg/dL), high-density lipoprotein cholesterol (mg/dL) and C-reactive protein concentration (mg/L). Missing values were introduced at rates ranging from 5% to 50% and forty stochastic imputations were generated for each missingness level, yielding ensembles of admissible completed datasets whose large-scale organization was subsequently analyzed through topological descriptors.

Upper-left inset: reconstruction space of all admissible imputations after dimensionality reduction. Each point corresponds to one completed dataset and is positioned according to its overall clinical profile. Colors indicate the proportion of missing values. The distribution of points provides a visual representation of the geometry of the imputation space and the degree of separation among alternative reconstructions.
Upper-right inset: topological descriptors derived from coarse-proximity relationships among admissible imputations. The number of connected components reflects the fragmentation of the reconstruction space, whereas the number of independent cycles represents Hurewicz-like topological invariants characterizing nontrivial connectivity patterns.
Lower-left inset: reconstruction error expressed in clinical units. Curves correspond to the root mean square reconstruction error of fasting glucose (mg/dL) and systolic blood pressure (mmHg) relative to the complete dataset. Both variables exhibited a progressive increase in reconstruction error with increasing missingness, indicating a monotonic deterioration in numerical reconstruction accuracy
Lower-middle inset: Standard deviation of estimated metabolic-syndrome prevalence across the forty imputations, providing a measure of classification uncertainty generated by missing data. The standard deviation increased from 0.54% at 5% missingness to 1.54% at 50% missingness, indicating progressively greater variability in prevalence estimates as the proportion of missing observations increased.
Lower-right inset: Pearson correlation matrix of the original complete dataset, illustrating the dependence structure among the simulated clinical variables. Positive correlations are observed among body mass index, fasting glucose, systolic blood pressure, low-density lipoprotein cholesterol and C-reactive protein, whereas high-density lipoprotein cholesterol exhibits predominantly negative correlations with the remaining variables. Pairwise correlation coefficients ranged from approximately **−0.45 to +0.62**, indicating a moderately correlated multivariate structure that served as the statistical basis for stochastic imputation and influenced the geometry of the admissible reconstruction space.

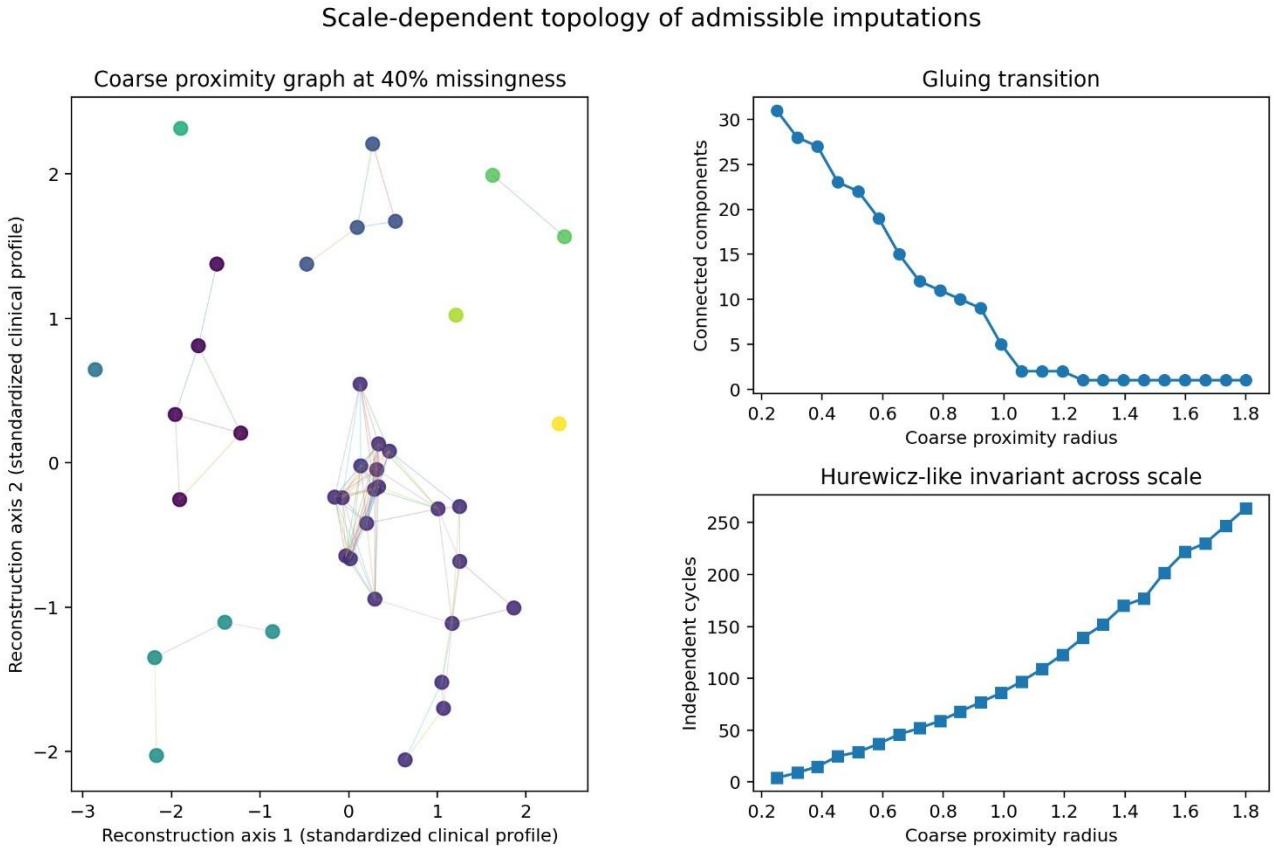


Figure 2. Scale-dependent topology of admissible imputations and coarse-proximity reconstruction. The figure illustrates how the global organization of admissible imputations evolves as the scale of coarse proximity is varied. Results are shown for the scenario with 40% missing values.
Large left inset: coarse-proximity graph constructed from forty completed datasets projected into the reconstruction space. Each node represents an individual imputed dataset and edges connect pairs of imputations separated by less than a predefined proximity radius. Node positions correspond to standardized clinical reconstruction coordinates. Clusters identify groups of mutually similar imputations, whereas isolated nodes represent alternative reconstructions that remain weakly connected to the dominant solution families.

arXiv:2606.30684v1 [stat.AP], 27 Jun 2026

Upper-right inset: gluing transition. As the coarse-proximity radius increases, initially disconnected groups of admissible imputations progressively merge into larger connected structures. The decreasing number of connected components quantifies the transition from fragmented local reconstructions toward a globally integrated reconstruction space, analogous to the assembly of local patches into a coherent global object.
Lower-right inset: evolution of the Hurewicz-like invariant across increasing proximity scales. The number of independent cycles increases as additional connections are established among imputations, revealing the emergence of nontrivial topological organization within the reconstruction space.

CONCLUSIONS

We asked whether collections of datasets generated by Rubin's multiple imputation contain an internal large-scale organization independent of conventional statistical uncertainty measures. Specifically, we investigated whether admissible completions form structured spaces whose properties can be described through coarse proximity, connectedness and topological invariants. Our simulations compared multiple missingness levels in a synthetic cardiometabolic cohort while preserving known ground truth values, allowing simultaneous assessment of reconstruction accuracy and topological organization. We found that increasing missingness modified both the numerical reconstruction performance and the geometry of the admissible completion space. Reconstruction errors increased progressively with missingness, while the organization of imputations exhibited changes in connected components, cycle counts and scale-dependent connectivity patterns. The resulting spaces were neither fully fragmented nor completely homogeneous, but displayed structured families of admissible reconstructions connected through identifiable proximity relationships. Therefore, uncertainty associated with missing data could be examined not only through distributions of estimated values, but also through relationships among alternative completed datasets. Our results suggest that topological descriptors and conventional statistical summaries capture different aspects of the reconstruction process: whereas reconstruction error quantifies deviation from known values, topological descriptors characterize how alternative completions are arranged relative to one another.

Our approach differs from existing missing-data methodologies in several respects. Techniques such as listwise deletion, mean substitution, expectation-maximization algorithms, inverse probability weighting and standard multiple imputation focus primarily on parameter estimation, prediction or uncertainty quantification (Lieberman-Betz et al. 2014; Chan 2017; De Raadt et al. 2019; Chen et al. 2024; Niloofar, Aghdam, and Eslahchi 2024). In contrast, our approach analyzes relationships among completed datasets themselves. Unlike principal component analysis, cluster analysis and conventional distance-based visualization methods, which primarily describe the geometric distribution of observations (Martins et al. 2019; Mi et al. 2019; Ben Salem and Ben Abdelaziz 2021; Jang 2021), our procedure quantifies the topology of the imputation space through measures of connectedness and independent cycle structure. Compared with Bayesian posterior summaries, which describe probability distributions of parameters (Alquier 2020; Huber, Georgia, and Finley 2023; van Dijk et al. 2023; Golchi and Willard 2024), our approach investigates the organization of admissible reconstructions generated by those distributions. Compared with sensitivity analyses based on repeated imputations (Crameri et al. 2015; Mehrotra, Liu, and Permutt 2017; Tompsett et al. 2020), our descriptors are capable of distinguishing situations with comparable numerical variability but different global arrangements of solutions. The use of coarse proximity allows examination of large-scale relationships without requiring strict local similarity, while Seifert–van Kampen-inspired gluing and Hurewicz-type descriptors provide quantitative summaries of connectivity across scales (Bhardwaj and Tyagi 2019; Christensen and Scoccola 2023).

Our study has limitations. First, the analyses were conducted entirely on simulated data. Second, the simulated cohort contained a restricted set of continuous variables with predefined correlation structures and did not include categorical variables, longitudinal observations or multimodal measurements. Third, the missingness mechanism was designed to resemble clinically plausible conditions but cannot represent the full diversity of real-world missing-data processes. Fourth, the topological descriptors were derived from finite graphs constructed in reduced-dimensional reconstruction spaces; alternative distance measures, dimensional reductions or graph-construction procedures could produce different quantitative values. Fifth, the Seifert–van Kampen and Hurewicz concepts were used as operational tools for describing connectivity and cycle structure rather than as complete algebraic-topological calculations. Sources of potential bias include the selected proximity thresholds, the stochastic characteristics of the imputation algorithm and the peculiar summary statistics used to define reconstruction coordinates. Unresolved questions concern the stability of topological descriptors under different imputation models, the behavior of the method in very high-dimensional datasets, the relationship between topological signatures and missingness mechanisms, and the extent to which different biomedical domains produce comparable reconstruction-space organizations.

Our approach suggests experimentally testable previsions. First, empirical datasets with increasing fractions of artificially removed observations should exhibit a monotonic increase in reconstruction error while simultaneously displaying non-monotonic variation in topological descriptors. Specifically, the relationship between missingness and cycle counts is expected to be weaker than the relationship between missingness and reconstruction error.

Second, biological datasets generated from strongly constrained systems should produce fewer connected components than datasets generated from more heterogeneous populations when analyzed at identical missingness levels and proximity scales.
Third, repeated imputations generated by different algorithms may produce similar average estimates while exhibiting distinct connectivity structures. This prediction can be tested by comparing graph-derived descriptors obtained from methods such as predictive mean matching, Bayesian regression, random forests and neural-network imputations.
Fourth, increasing the coarse-proximity radius should induce a reproducible transition from multiple disconnected reconstruction regions toward a single connected structure. The critical radius associated with this transition constitutes a measurable observable that can be compared across datasets.
Fifth, if reconstruction spaces contain persistent organizational features, the values of connected-component counts and cycle counts should remain more stable under repeated resampling than under randomized permutation of imputation labels.
Sixth, datasets characterized by stronger internal correlation structures should exhibit lower critical gluing radii and denser proximity graphs than datasets with weaker dependence structures.
Future research may investigate persistent homology, higher-dimensional topological invariants, alternative notions of coarse similarity, information-theoretic descriptors, longitudinal missing-data processes, network-valued observations and comparisons between synthetic and empirical datasets.
Our analysis is applied as a post-processing step to completed datasets generated by conventional multiple-imputation procedures and therefore does not require modifications to existing data-processing pipeline. Reconstruction coordinates can be derived from summary statistics already reported in many studies, allowing direct computation of proximity graphs and associated descriptors. Our method can be integrated with existing quality-control procedures to compare different imputation strategies, evaluate reconstruction consistency across repeated analyses and identify transitions in reconstruction-space organization.

In conclusion, we investigated missing-data reconstruction from the perspective of the organization of admissible completed datasets. Multiple imputations generated structured spaces whose connectivity and cycle properties were quantified independently of conventional measures of reconstruction accuracy. We showed that numerical uncertainty and topological organization could provide distinct descriptions of the same reconstruction process. Therfore, examination of admissible completions as interconnected objects could extend the characterization of missing-data solutions beyond parameter estimates and error metrics alone.

DECLARATIONS

Ethics approval and consent to participate. Ethics approval statement is not applicable. This research does not contain any studies with human participants or animals performed by the Author.
Consent for publication. The Author transfers all copyright ownership, in the event the work is published. The undersigned author warrants that the article is original, does not infringe on any copyright or other proprietary right of any third part, is not under consideration by another journal and has not been previously published.
Availability of data and materials. All data and materials generated or analyzed during this study are included in the manuscript. The Author had full access to all the data in the study and took responsibility for the integrity of the data and the accuracy of the data analysis.
Disclaimer. The views expressed are those of the author and do not necessarily reflect those of the affiliated institutions.
Competing interests. The Author does not have any known or potential conflict of interest including any financial, personal or other relationships with other people or organizations within three years of beginning the submitted work that could inappropriately influence or be perceived to influence their work.
Funding. This research did not receive any specific grant from funding agencies in the public, commercial or not-for-profit sectors.
Acknowledgements: none.
Authors' contributions. The Author performed: study concept and design, acquisition of data, analysis and interpretation of data, drafting of the manuscript, critical revision of the manuscript for important intellectual content, statistical analysis, obtained funding, administrative, technical and material support, study supervision.
Declaration of generative AI and AI-assisted technologies in the writing process. During the preparation of this work, the author used ChatGPT 5.3 to assist with data analysis and manuscript drafting and to improve spelling, grammar and general editing. After using this tool, the author reviewed and edited the content as needed, taking full responsibility for the content of the publication.

REFERENCES

1) Alquier, Pierre. 2020. “Approximate Bayesian Inference.” *Entropy* 22 (11): 1272. https://doi.org/10.3390/e22111272.
2) Arkowitz, M., and C. R. Curjel. 1964. “The Hurewicz Homomorphism and Finite Homotopy Invariants.” *Transactions of the American Mathematical Society* 110 (3): 538–51. https://doi.org/10.2307/1993697.
3) Ben Salem, K., and A. Ben Abdelaziz. 2021. “Principal Component Analysis (PCA).” *La Tunisie Médicale* 99 (4): 383–89.
4) Bhardwaj, Manoj, and B. K. Tyagi. 2019. “Some Characterizations of Ideal Variants of Hurewicz Type Covering Properties.” *arXiv* preprint arXiv:1910.13822.
5) Chan, K. C. 2017. “Acceleration of Expectation-Maximization Algorithm for Length-Biased Right-Censored Data.” *Lifetime Data Analysis* 23 (1): 102–12. https://doi.org/10.1007/s10985-016-9374-z.
6) Chen, R., A. Schumitzky, A. Kryshchenko, K. Nieforth, M. Tomashevskiy, S. Hu, R. Garreau, J. Otalvaro, W. Yamada, and M. N. Neely. 2024. “RPEM: Randomized Monte Carlo Parametric Expectation Maximization Algorithm.” *CPT: Pharmacometrics & Systems Pharmacology* 13 (5): 759–80. https://doi.org/10.1002/psp4.13113.
7) Chin, G. C., A. W. Potter, and K. E. Friedl. 2024. “Body Mass Index Is a Barrier to Obesity Treatment.” Frontiers in Endocrinology 15: 1444568. https://doi.org/10.3389/fendo.2024.1444568.
8) Christensen, J. Daniel, and Luis Scoccola. 2023. “The Hurewicz Theorem in Homotopy Type Theory.” *arXiv* preprint arXiv:2007.05833v3.
9) Chung, S. 2019. “Update on Low-Density Lipoprotein Cholesterol Quantification.” Current Opinion in Lipidology 30 (4): 273–83. https://doi.org/10.1097/MOL.0000000000000611.
10) Crameri, A., A. von Wyl, M. Koemeda, P. Schulthess, and V. Tschuschke. 2015. “Sensitivity Analysis in Multiple Imputation in Effectiveness Studies of Psychotherapy.” *Frontiers in Psychology* 6: 1042. https://doi.org/10.3389/fpsyg.2015.01042.
11) Çubukçu, H. C., and D. İ. Topcu. 2022. “Estimation of Low-Density Lipoprotein Cholesterol Concentration Using Machine Learning.” Laboratory Medicine 53 (2): 161–71. https://doi.org/10.1093/labmed/lmab065.
12) D'Agostino, Ralph B., Ramachandran S. Vasan, Michael J. Pencina, Philip A. Wolf, Mark Cobain, Joseph M. Massaro, and William B. Kannel. 2008. "General Cardiovascular Risk Profile for Use in Primary Care: The Framingham Heart Study." *Circulation* 117 (6): 743-753.
13) De Raadt, A., M. J. Warrens, R. J. Bosker, and H. A. L. Kiers. 2019. “Kappa Coefficients for Missing Data.” *Educational and Psychological Measurement* 79 (3): 558–76. https://doi.org/10.1177/0013164418823249.
14) Giganti, M. J., and B. E. Shepherd. 2020. “Multiple-Imputation Variance Estimation in Studies With Missing or Misclassified Inclusion Criteria.” *American Journal of Epidemiology* 189 (12): 1628–32. https://doi.org/10.1093/aje/kwaa153.
15) Golchi, S., and J. J. Willard. 2024. “Estimating the Sampling Distribution of Posterior Decision Summaries in Bayesian Clinical Trials.” *Biometrical Journal* 66 (8): e70002. https://doi.org/10.1002/bimj.70002.
16) Grzegrzolka, Pawel, and Jeremy Siegert. 2019. “Coarse Proximity and Proximity at Infinity.” *arXiv* preprint arXiv:1804.10263v6.
17) Grzegrzolka, P., and J. Siegert. 2023. “Boundaries of Coarse Proximity Spaces and Boundaries of Compactifications.” *European Journal of Mathematics* 9: 28. https://doi.org/10.1007/s40879-023-00616-1.
18) Huber, H. A., S. K. Georgia, and S. D. Finley. 2023. “Systematic Bayesian Posterior Analysis Guided by Kullback-Leibler Divergence Facilitates Hypothesis Formation.” *Journal of Theoretical Biology* 558: 111341. https://doi.org/10.1016/j.jtbi.2022.111341.
19) Jang, J. H. 2021. “Principal Component Analysis of Hybrid Functional and Vector Data.” *Statistics in Medicine* 40 (24): 5152–73. https://doi.org/10.1002/sim.9117.
20) Javanbakht, M., J. Lin, A. Ragsdale, S. Kim, S. Siminski, and P. Gorbach. 2022. “Comparing Single and Multiple Imputation Strategies for Harmonizing Substance Use Data across HIV-Related Cohort Studies.” *BMC Medical Research Methodology* 22 (1): 90. https://doi.org/10.1186/s12874-022-01554-4.
21) Lieberman-Betz, R. G., P. Yoder, W. L. Stone, A. S. Nahmias, A. S. Carter, et al. 2014. “An Illustration of Using Multiple Imputation versus Listwise Deletion Analyses: The Effect of Hanen’s ‘More Than Words’ on Parenting Stress.” *American Journal on Intellectual and Developmental Disabilities* 119 (5): 472–86. https://doi.org/10.1352/1944-7558-119.5.472.
22) Marino, Mark, et al. 2014. "Quantifying Cardiometabolic Risk Using Modifiable Non–Self-Reported Risk Factors from the Framingham Offspring Cohort." *Preventing Chronic Disease* 11:E107.
23) Martins, T. D., J. M. Annichino-Bizzacchi, A. V. C. Romano, and R. M. Filho. 2019. “Principal Component Analysis on Recurrent Venous Thromboembolism.” *Clinical and Applied Thrombosis/Hemostasis* 25: 1076029619895323. https://doi.org/10.1177/1076029619895323.

24) Mehrotra, D. V., F. Liu, and T. Permutt. 2017. “Missing Data in Clinical Trials: Control-Based Mean Imputation and Sensitivity Analysis.” *Pharmaceutical Statistics* 16 (5): 378–92. https://doi.org/10.1002/pst.1817.
25) Mi, J. X., Y. N. Zhang, Z. Lai, W. Li, L. Zhou, and F. Zhong. 2019. “Principal Component Analysis Based on Nuclear Norm Minimization.” *Neural Networks* 118: 1–16. https://doi.org/10.1016/j.neunet.2019.05.020.
26) Mitani, H., K. Suzuki, J. Ako, K. Iekushi, R. Majewska, S. Touzeni, and S. Yamashita. 2023. “Achievement Rates for Low-Density Lipoprotein Cholesterol Goals in Patients at High Risk of Atherosclerotic Cardiovascular Disease in a Real-World Setting in Japan.” Journal of Atherosclerosis and Thrombosis 30 (11): 1622–34. https://doi.org/10.5551/jat.63940.
27) Niloofar, P., R. Aghdam, and C. Eslahchi. 2024. “GAEM: Genetic Algorithm Based Expectation-Maximization for Inferring Gene Regulatory Networks from Incomplete Data.” *Computers in Biology and Medicine* 183: 109238. https://doi.org/10.1016/j.compbiomed.2024.109238.
28) Oh, G. C., T. Ko, J. H. Kim, M. H. Lee, S. W. Choi, Y. S. Bae, K. H. Kim, and H. Y. Lee. 2022. “Estimation of Low-Density Lipoprotein Cholesterol Levels Using Machine Learning.” International Journal of Cardiology 352: 144–49. https://doi.org/10.1016/j.ijcard.2022.01.029.
29) Pilgrim, Samantha. 2025. “A Hurewicz-Type Theorem for the Dynamic Asymptotic Dimension with Applications to Coarse Geometry and Dynamics.” *arXiv* preprint arXiv:2207.13275v6.
30) Prolubnikov, Alexander. 2023. “Finding the Connected Components of the Graph Using Perturbations of the Adjacency Matrix.” *arXiv* preprint arXiv:2306.16389v2.
31) Qiao, Z., J. Sidorenko, J. A. Revez, A. Xue, X. Lu, K. Pärna, H. Snieder, Lifelines Cohort Study, P. M. Visscher, N. R. Wray, and L. Yengo. 2023. “Estimation and Implications of the Genetic Architecture of Fasting and Non-Fasting Blood Glucose.” Nature Communications 14 (1): 451. https://doi.org/10.1038/s41467-023-36013-1.
32)
33) Raevskiy, M., V. Yanvarev, S. Jung, A. Del Sol, and Y. A. Medvedeva. 2023. “Epi-Impute: Single-Cell RNA-seq Imputation via Integration with Single-Cell ATAC-seq.” *International Journal of Molecular Sciences* 24 (7): 6229. https://doi.org/10.3390/ijms24076229.
34) Ramos, Arthur F., Tiago M. L. de Veras, and Ruy J. G. B. de Queiroz. 2025. “The Seifert-van Kampen Theorem via Computational Paths: A Formalized Approach to Computing Fundamental Groups.” *arXiv* preprint arXiv:2512.03175.
35) Sakai, Masami. 2020. “The Menger Property and l-Equivalence.” *Topology and Its Applications* 281: 107187. https://doi.org/10.1016/j.topol.2020.107187.
36) Ségalas, C., C. Leyrat, J. R. Carpenter, and E. Williamson. 2023. “Propensity Score Matching after Multiple Imputation When a Confounder Has Missing Data.” *Statistics in Medicine* 42 (7): 1082–95. https://doi.org/10.1002/sim.9658.
37) Shi, Y., and W. Yao. 2024. “Lattice-Valued Coarse Proximity Spaces.” *Fuzzy Sets and Systems* 475: 108766. https://doi.org/10.1016/j.fss.2023.108766.
38) Shu, D., X. Li, Q. Her, J. Wong, D. Li, R. Wang, and S. Toh. 2023. “Combining Meta-Analysis with Multiple Imputation for One-Step, Privacy-Protecting Estimation of Causal Treatment Effects in Multi-Site Studies.” *Research Synthesis Methods* 14 (5): 742–63. https://doi.org/10.1002/jrsm.1660.
39) Solianik, R., K. Židonienė, N. Eimantas, and M. Brazaitis. 2023. “Prolonged Fasting Outperforms Short-Term Fasting in Terms of Glucose Tolerance and Insulin Release: A Randomised Controlled Trial.” British Journal of Nutrition 130 (9): 1500–1509. https://doi.org/10.1017/S0007114523000557.
40) Tompsett, D., S. Sutton, S. R. Seaman, and I. R. White. 2020. “A General Method for Elicitation, Imputation, and Sensitivity Analysis for Incomplete Repeated Binary Data.” *Statistics in Medicine* 39 (22): 2921–35. https://doi.org/10.1002/sim.8584.
41) Tsang, J. N. J., S. Bacchi, J. G. Kovoor, A. K. Gupta, B. Stretton, S. Gluck, T. Gilbert, Y. Sharma, R. Woodman, and A. A. Mangoni. 2023. “Systolic Blood Pressure Levels and Mortality in Australian Medical Inpatients.” Journal of Clinical Hypertension 25 (11): 1036–39. https://doi.org/10.1111/jch.14735.
42) van Dijk, R., D. Kalisvaart, J. Cnossen, and C. S. Smith. 2023. “Bayesian Posterior Density Estimation Reveals Degeneracy in Three-Dimensional Multiple Emitter Localization.” *Scientific Reports* 13 (1): 22372. https://doi.org/10.1038/s41598-023-49101-5.
43) Yu, K., X. Liu, R. Alhamzawi, F. Becker, and J. Lord. 2018. “Statistical Methods for Body Mass Index: A Selective Review.” Statistical Methods in Medical Research 27 (3): 798–811. https://doi.org/10.1177/0962280216643117.
44) Yu, L., L. Liu, and K. E. Peace. 2020. “Regression Multiple Imputation for Missing Data Analysis.” *Statistical Methods in Medical Research* 29 (9): 2647–64. https://doi.org/10.1177/0962280220908613.
45) Yu, Y., X. Zhang, S. Wang, et al. 2026. “Efficient and Accurate Neural-Field Reconstruction Using Resistive Memory.” *Nature* 654: 642–651. https://doi.org/10.1038/s41586-026-10646-w.

Preprints.org

Article

Not peer-reviewed version

A Grothendieckian Perspective on Ancient Manuscript Analysis

Arturo Tozzi *

Posted Date: 14 July 2026

doi: 10.20944/preprints202607.0927.v1

Keywords: invariants; functors; sheaves; topology; provenance

Preprints.org is a free multidisciplinary platform providing preprint service that is dedicated to making early versions of research outputs permanently available and citable. Preprints posted at Preprints.org appear in Web of Science, Crossref, Google Scholar, Scilit, Europe PMC, OpenAlex.

Copyright: This open access article is published under a Creative Commons CC BY 4.0 license, which permit the free download, distribution, and reuse, provided that the author and preprint are cited in any reuse.

Preprints.org (www.preprints.org) | NOT PEER-REVIEWED | Posted: 14 July 2026 doi:10.20944/preprints202607.0927.v1

Disclaimer/Publisher's Note: The statements, opinions, and data contained in all publications are solely those of the individual author(s) and contributor(s) and not of MDPI and/or the editor(s). MDPI and/or the editor(s) disclaim responsibility for any injury to people or property resulting from any ideas, methods, instructions, or products referred to in the content.

Article

A Grothendieckian Perspective on Ancient Manuscript Analysis

Arturo Tozzi

ASL Napoli 1 Centro, Via Comunale del Principe 13/a, 80145 Naples, Italy; tozziarturo@libero.it

Abstract

Ancient manuscripts are cultural objects encoding physical, chemical, linguistic, historical, philosophical and social information. To unify heterogeneous disciplinary evidence within a single relational and geometric formalism, we propose a Grothendieckian framework inspired by category theory, sheaf theory, topoi and algebraic geometry. Each discipline is represented as an independent graph whose nodes and edges encode its own entities and relationships. Local observations are attached to graph neighborhoods through sections of sheaves, while structure-preserving functors align corresponding entities across disciplinary domains. Natural transformations evaluate the consistency of alternative mappings, while cohomological analysis identifies hidden structural constraints. Subsequently, compatible local information is assembled using descent theory, whereas stacks and derived categories incorporate multiple manuscript versions and their historical evolution. The integrated relational structure is represented geometrically through schemes, with the common invariant subgraph interpreted as the manuscript's motive, namely the maximal relational architecture preserved across all disciplinary representations. This approach could provide a mathematical strategy for integrating heterogeneous evidence without privileging any single disciplinary viewpoint. Potential applications include manuscript authentication, conservation planning, textual criticism, comparative philology, cultural heritage analytics, historical knowledge integration and development of interoperable artificial intelligence systems for multidisciplinary manuscript research.

Keywords: invariants; functors; sheaves; topology; provenance

Introduction

The interpretation of ancient manuscripts requires the integration of evidence originating from different disciplines, including paleography, philology, linguistics, chemistry, physics, history, art history, conservation science, etc. Advances in non-destructive analytical techniques have expanded the range of measurable properties extracted from manuscripts (Tack et al. 2016; Stabile et al. 2021; Angelotti et al. 2026), including parchment composition, pigment chemistry, ink formulation, radiocarbon dating, multispectral imaging and microstructural characterization (Radini et al. 2019; Tournié et al. 2019; Autran et al. 2021; Popović et al. 2025). In parallel, computational methods have enabled increasingly sophisticated analyses of textual organization, authorship, semantic relationships and historical transmission (Romano et al. 2023; Ceccarelli et al. 2025). Network science, machine learning and digital humanities have contributed tools for representing relationships among textual units, scribes, manuscripts and historical actors (Xu et al. 2023; Chen 2024; Zhu et al. 2025). However, relationships identified by one discipline are often compared only qualitatively across disciplines, hindering the identification of higher-order structures. A general mathematical language for combining different disciplinary viewpoints into a unified representation is still largely undeveloped.

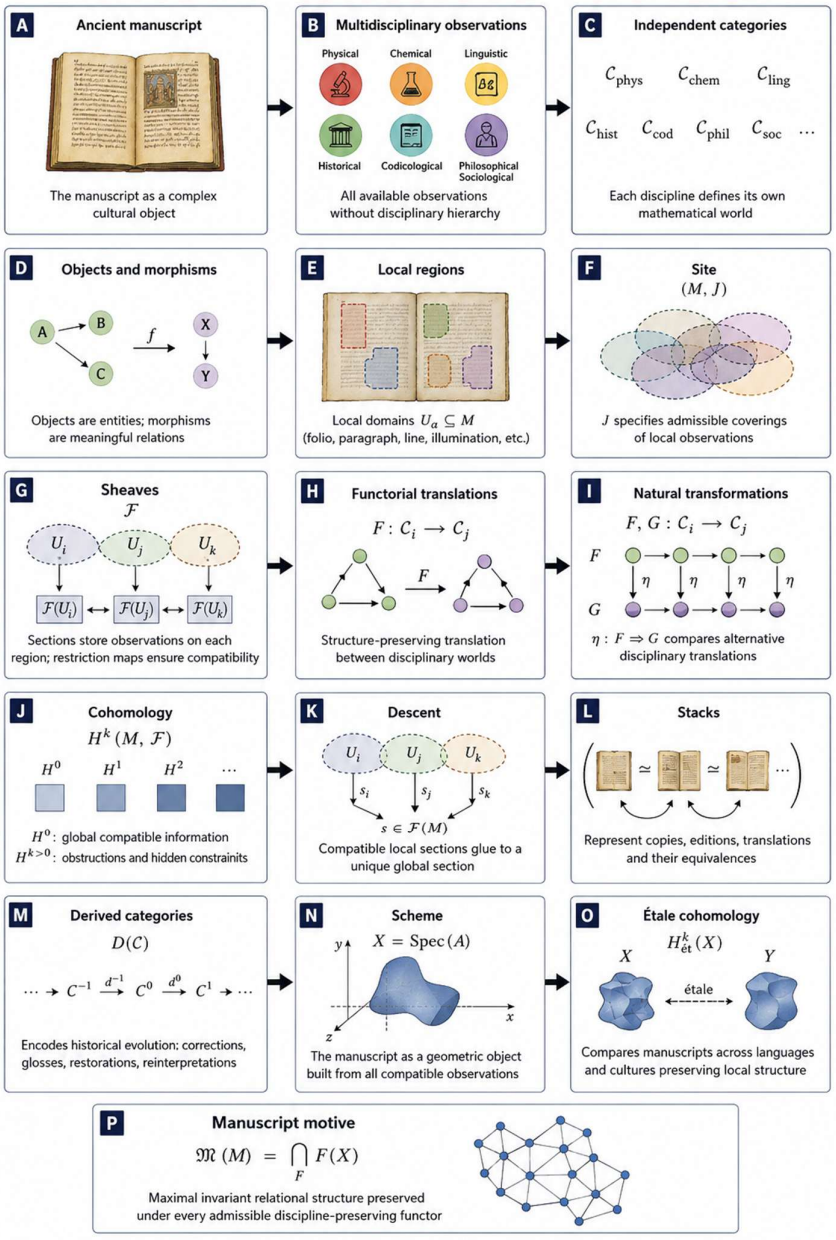
We aim to develop an axiomatic construction inspired by Grothendieckian geometry, introducing the mathematical objects and relationships required for the geometric analysis of ancient manuscripts (Zalamea 2015; Morone, Leifer, and Makse 2020; Sobota and Zdomskyy 2024; Gili et al.

© 2026 by the author(s). Distributed under a Creative Commons CC BY license.

Preprints.org (www.preprints.org) | NOT PEER-REVIEWED | Posted: 14 July 2026 doi:10.20944/preprints202607.0927.v1

2024; Bennequin and Berthoz 2025; Marquès 2025). Our theoretical goal is to establish a coherent mathematical formalism capable of representing ancient manuscripts as geometric objects whose heterogeneous disciplinary descriptions can be integrated within a single relational framework.

We regard each disciplinary viewpoint as a coherent relational world rather than an isolated dataset (Luo 1999; Dubuc and Sanchez de la Vega 2000; Pisier 2012; McLarty 2018). Every discipline is represented by an independent mathematical category whose objects and morphisms encode its entities and relationships. Local observations are associated with manuscript regions through sheaves, while functors translate information between categories and natural transformations assess the compatibility of alternative translations. Cohomology identifies global inconsistencies, after which compatible local descriptions are assembled by descent into a unified representation incorporating multiple manuscript versions, historical modifications and transmission pathways through stacks and derived categories. The resulting structure is interpreted geometrically as a scheme from which the manuscript's motive is extracted, defined as the maximal relational architecture preserved under all admissible discipline-preserving functors. The overall construction is summarized in Figure 1.



© 2026 by the author(s). Distributed under a Creative Commons CC BY license.

Preprints.org (www.preprints.org) | NOT PEER-REVIEWED | Posted: 14 July 2026 doi:10.20944/preprints202607.0927.v1

Figure 1. The construction begins by defining the mathematical objects and their relationships, before assembling them into increasingly complex structures. Every mathematical object introduced below defines a coherent geometric language in which physical, chemical, linguistic, historical, codicological, philosophical and sociological evidence become different manifestations of the same underlying mathematical entity.

Initially, an ancient manuscript can be regarded as a finite collection of observations rather than as a text. Let

$$M = \{O_1, O_2, \dots, O_n\}$$

denote the set of all observations associated with the manuscript. Each observation may correspond to a measurable physical quantity, a chemical property, a linguistic element, a historical event, an iconographic feature, a codicological characteristic, a philosophical concept, a sociological relationship, etc. Since each discipline captures only one aspect of the manuscript, no hierarchy is imposed among these observations. At the outset, the manuscript has no privileged mathematical description. Instead, each discipline provides an independent relational representation that is subsequently integrated into a unified geometric construction.

Each scientific discipline defines its own mathematical category. Let

$$\mathcal{C}_i$$

denote the category associated with discipline i. Its objects,

$$\mathrm{Obj}(\mathcal{C}_i),$$

represent the entities studied by that discipline, whereas its morphisms,

$$\mathrm{Mor}(\mathcal{C}_i),$$

describe admissible relationships between those entities. For instance, in the physical category, objects may consist of parchment regions, fibres, folios or bindings, while morphisms represent structural or mechanical relationships. In chemistry, objects become pigment samples, ink deposits or molecular compounds connected through compositional similarities or reaction pathways. Linguistics regards words, sentences, semantic concepts or grammatical constructions as objects linked through syntactic or semantic relations. History introduces scribes, production centres, historical events and ownership records connected by chronological or documentary relationships. Philosophy may represent concepts and arguments, whereas sociology considers readers, monasteries, libraries and transmission routes.

Morphisms stand for the elementary relations through which every category acquires structure. If A and B are two objects of a category,

$$f: A \to B$$

denotes a morphism relating them. Morphisms satisfy the axioms of identity and composition,

$$\mathrm{id}_A: A \to A,$$

and

$$g \circ f: A \to C,$$

whenever

$$f: A \to B, g: B \to C.$$

Composition enables elementary relationships to be combined into increasingly comprehensive explanatory chains. For example, a physical measurement may lead to material identification, which may constrain technological chronology and eventually historical provenance. Similarly, a linguistic observation may propagate through grammatical analysis toward dialect identification and geographical localization. Therefore, complex interpretations emerge through successive compositions of elementary morphisms rather than through isolated measurements.

Next, the manuscript could be decomposed into local regions. Let

$$U_\alpha \subseteq M$$

denote an arbitrary local domain. Depending on the investigation, a local region may correspond to an individual folio, a paragraph, an illumination, a line of text, a pigment layer, a damaged portion or any subset of observations. Importantly, locality is not restricted to physical neighbourhoods. Two

© 2026 by the author(s). Distributed under a Creative Commons CC BY license.

Preprints.org (www.preprints.org) | NOT PEER-REVIEWED | Posted: 14 July 2026 doi:10.20944/preprints202607.0927.v1

distant folios sharing identical scribal characteristics may belong to the same local analytical region, whereas neighbouring folios exhibiting different material histories may belong to distinct regions. Locality becomes an abstract relational concept rather than a purely spatial one.

To formalize locality, the manuscript is endowed with a Grothendieck topology. Let

$$(M, J)$$

denote a site, where J specifies the admissible covering families

$$\{U_i \to U\}.$$

Unlike ordinary topology, a covering does not necessarily describe geometric openness but identifies collections of compatible local observations sufficient to reconstruct larger portions of the manuscript. The choice of coverings depends entirely on analytical coherence rather than physical adjacency. Consequently, chemistry, linguistics and history may generate different local coverings while still referring to the same manuscript.

Each local region carries measurable information through a sheaf. Let

$$\mathcal{F}$$

be a sheaf over the site (M, J). Every local domain receives a corresponding collection of observations

$$\mathcal{F}(U),$$

called the sections over U. Sections may contain spectra, pigment compositions, transcription data, grammatical analyses, historical metadata, codicological measurements or any other disciplinary observations. Whenever

$$V \subseteq U,$$

restriction morphisms

$$\rho_{UV}: \mathcal{F}(U) \to \mathcal{F}(V)$$

transfer information consistently from larger regions to smaller ones. The sheaf satisfies the classical gluing axiom: if local sections

$$s_i \in \mathcal{F}(U_i)$$

agree on every overlap

$$U_i \cap U_j,$$

then there exists a unique global section

$$s \in \mathcal{F}(U)$$

whose restrictions coincide with every s_i. Local observations become mathematically compatible before any global interpretation is attempted.

Independent disciplinary worlds must subsequently communicate through functors. Given two categories,

$$\mathcal{C}_i \text{and} \mathcal{C}_j,$$

a functor

$$F: \mathcal{C}_i \to \mathcal{C}_j$$

maps objects to objects and morphisms to morphisms while preserving identity morphisms and composition,

$$F(\mathrm{id}_A) = \mathrm{id}_{F(A)},$$

$$F(g \circ f) = F(g) \circ F(f).$$

The preservation of relational structure distinguishes functorial translation from ordinary data conversion. For instance, a linguistic inference regarding geographical dialect may become a historical localization without modifying the logical relationships among the observations. Likewise, pigment provenance inferred chemically may become a node within historical trade networks while maintaining its original relational context. Therefore, functors translate entire relational organizations rather than isolated variables.

Different disciplinary translations frequently coexist. Suppose two functors,

$$F, G: \mathcal{C}_i \to \mathcal{C}_j,$$

© 2026 by the author(s). Distributed under a Creative Commons CC BY license.

Preprints.org (www.preprints.org) | NOT PEER-REVIEWED | Posted: 14 July 2026 doi:10.20944/preprints202607.0927.v1

produce alternative historical interpretations from the same observations. Their compatibility is expressed through a natural transformation

$$\eta: F \Rightarrow G,$$

whose components

$$\eta_A: F(A) \to G(A)$$

satisfy

$$\eta_B \circ F(f) = G(f) \circ \eta_A$$

for every morphism

$$f: A \to B.$$

Natural transformations compare complete translations rather than individual observations. They provide mathematical criterion for determining whether different disciplinary interpretations remain globally coherent.

Once compatible translations have been established, global consistency becomes a cohomological problem. Cohomology assesses whether local information can be assembled into a coherent global description. For the sheaf $\mathcal{F}$, one computes the cohomology groups

$$H^k(M, \mathcal{F}).$$

The zeroth group

$$H^0(M, \mathcal{F})$$

contains globally compatible sections. Higher-order groups identify obstructions preventing perfect integration. Non-trivial elements of

$$H^1(M, \mathcal{F})$$

may point towards inconsistencies between historical chronology and chemical dating, incompatible palaeographic assignments or conflicting restoration histories. Higher-dimensional groups detect progressively more complex incompatibilities involving multiple disciplinary domains simultaneously, while cohomology characterizes the manuscript through global structural constraints rather than isolated discrepancies.

Whenever cohomological obstructions vanish, descent theory reconstructs the manuscript from compatible local data. Given a covering

$$\{U_i\},$$

together with compatible local sections,

$$s_i \in \mathcal{F}(U_i),$$

satisfying

$$s_i \mid_{U_i \cap U_j} = s_j \mid_{U_i \cap U_j},$$

there exists a unique global section

$$s \in \mathcal{F}(M)$$

whose restrictions reproduce every local observation. Therefore, descent provides the rigorous mathematical mechanism through which fragmented evidence becomes a unified description.

Ancient manuscripts frequently exist in multiple manifestations. Original copies, later reproductions, translations, commentaries, restorations and palimpsests cannot be represented adequately as isolated objects. Their mathematical description requires stacks, which generalize ordinary spaces by retaining equivalences and automorphisms among related objects. A stack records not only each manuscript version, but also every symmetry relating those versions. Two copies differing only through minor orthographic changes are distinct while preserving their equivalence within the larger mathematical object.

Historical evolution further introduces derived categories. Instead of studying isolated objects, one considers complexes

$$C^{\cdot}$$

linked by differentials

$$d^2 = 0.$$

© 2026 by the author(s). Distributed under a Creative Commons CC BY license.

Preprints.org (www.preprints.org) | NOT PEER-REVIEWED | Posted: 14 July 2026 doi:10.20944/preprints202607.0927.v1

Passing to the derived category

$$D(\mathcal{C})$$

retains the complete history of transformations, including corrections, glosses, erasures, translations, restorations and reinterpretations accumulated through centuries. Consequently, the manuscript acquires temporal depth rather than being a static object.

After these constructions, every compatible disciplinary representation may be assembled into a geometric object. Let

$$A$$

denote the algebra generated by all compatible observations and their relations. Then the manuscript is represented by the affine scheme

$$X = \mathrm{Spec}(A),$$

whose points correspond to prime ideals encoding coherent relational structures rather than individual measurements. This means that material composition, textual organization, historical context and semantic organization could become geometric coordinates of the same mathematical space.

Comparisons among manuscripts originating from different cultures require invariants independent of vocabulary or local conventions. Étale morphisms preserve local structure while allowing global comparison among distinct schemes. Étale cohomology identifies deep correspondences invisible to ordinary textual comparison, revealing structural similarities among manuscripts despite differences in language, script or cultural tradition.

The final mathematical object sought by our construction is the manuscript's motive. Inspired by Grothendieck's notion of motives in algebraic geometry (Huber 1995; Rej and Marcolli 2011; Baez 2025), we introduce a new operational definition. Let

$$\mathcal{F} = \{F_\alpha\}$$

denote the collection of all admissible discipline-preserving functors acting on the manuscript's geometric representation. The manuscript motive is defined as the maximal invariant relational structure preserved under every admissible functorial translation,

$$\mathfrak{M}(M) = \bigcap_{F_\alpha \in \mathcal{F}} F_\alpha\,(X).$$

This invariant does not correspond to any single aspect of the manuscript, whether physical, textual, chemical, historical or cultural. Instead, it represents the largest relational architecture surviving every mathematically admissible disciplinary perspective. The motive constitutes the manuscript's structural identity, i.e., the organization simultaneously preserved by its material composition, textual content, historical evolution, semantic architecture and social transmission.

Overall, our approach transforms an ancient manuscript from a heterogeneous collection of observations into a unified geometric object whose invariant relational structure is represented within a Grothendieckian geometry.

Table 1. Sequential construction of the proposed Grothendieckian geometry of ancient manuscripts. The table summarizes the mathematical objects introduced during the progressive transformation of an ancient manuscript from a heterogeneous collection of multidisciplinary observations into a unified geometric object. The final invariant, defined as the manuscript's motive, is the maximal relational structure preserved across all admissible disciplinary representations.

Step	Grothendieckian concept	Mathematical object	Manuscript features examined	Role in manuscript geometry
1	Observations	$M = \{O_1, \ldots, O_n\}$	Parchment, inks, pigments, text, dates, provenance, annotations	Collect all available evidence

© 2026 by the author(s). Distributed under a Creative Commons CC BY license.

Preprints.org (www.preprints.org) | NOT PEER-REVIEWED | Posted: 14 July 2026 doi:10.20944/preprints202607.0927.v1

2	Categories	$\mathcal{C}_i$	Physics, chemistry, linguistics, history, codicology, philosophy, sociology	Separate disciplinary worlds
3	Objects & morphisms	$A \xrightarrow{f} B$	Folios, pigments, words, scribes, places and their relationships	Define elementary relational structure
4	Local regions	$U_\alpha \subseteq M$	Individual folios, paragraphs, illuminations, damaged areas	Partition the manuscript into local domains
5	Site	(M, J)	Compatible local analytical regions	Define admissible local observations
6	Sheaf	$\mathcal{F}(U)$	Spectra, OCR, grammar, codicology, metadata	Associate observations with each local region
7	Functor	$F: \mathcal{C}_i \to \mathcal{C}_j$	Correspondence between material, textual and historical evidence	Translate one disciplinary description into another
8	Natural transformation	$\eta: F \Rightarrow G$	Independent provenance or dating hypotheses	Compare alternative interpretations
9	Cohomology	$H^k(M, \mathcal{F})$	Dating conflicts, inconsistent provenance, missing information	Detect global inconsistencies
10	Descent	$s \in \mathcal{F}(M)$	Compatible multidisciplinary observations	Reconstruct the complete manuscript
11	Stack	$\mathfrak{X}$	Copies, editions, translations, commentaries, palimpsests	Represent manuscript families
12	Derived category	$D(\mathcal{C})$	Corrections, glosses, restorations, historical revisions	Describe temporal evolution
13	Scheme	$X = \mathrm{Spec}(A)$	Integrated physical, textual, historical and semantic information	Construct the manuscript's geometric space
14	Étale cohomology	$H^k_{\text{ét}}(X)$	Related manuscripts from different languages or traditions	Reveal deep structural correspondences
15	Motive	$\mathfrak{M}(M)$	Stable multidisciplinary relationships	Extract the manuscript's universal relational identity

Illustrative Theoretical Construction of the Manuscript Motive

To clarify how our mathematical construction may be applied in practice, we consider a hypothetical ancient manuscript. Each mathematical step follows from the definitions introduced in the preceding sections.

At first, we identify the observable characteristics of the manuscript. Rather than privileging textual information, all measurable or interpretable features are considered equally informative. The physical description includes the writing support, folio organization, parchment morphology, binding structure and page layout. Chemical observations comprise ink composition, pigment distribution and material degradation. Linguistic analysis identifies lexical usage, grammatical organization and semantic relationships among textual units. Historical investigation reconstructs chronology, provenance, ownership and documentary references, whereas codicology characterizes quire structure, pagination, scribal practices and corrections. Additional disciplinary perspectives, including iconography, philosophy or sociology, may contribute further observations whenever

© 2026 by the author(s). Distributed under a Creative Commons CC BY license.

Preprints.org (www.preprints.org) | NOT PEER-REVIEWED | Posted: 14 July 2026 doi:10.20944/preprints202607.0927.v1

appropriate. At this stage, the manuscript is still a heterogeneous collection of independent observations. Each disciplinary description is represented as an independent category whose objects correspond to the entities examined within that discipline and whose morphisms encode their internal relationships. For instance, physical objects may consist of parchment regions connected by structural continuity, chemical objects of pigment samples linked by compositional similarity, linguistic objects of words or concepts connected by syntactic or semantic relations, and historical objects of places, individuals or events linked by chronological dependencies. Every category develops its own internal relational architecture independently of the others. The first mathematical outcome of this stage is a collection of coherent but mutually disconnected relational worlds, each describing one aspect of the manuscript.

Subsequently, the manuscript is decomposed into local analytical regions. These regions need not correspond exclusively to physical subdivisions such as folios or pages, but may equally represent paragraphs, illuminated initials, marginal annotations, damaged areas or any subset of observations sharing analytical coherence. Every local region receives a collection of disciplinary observations represented as sections of appropriate sheaves. Restriction morphisms ensure that information is internally consistent when passing from larger regions to smaller ones. Whenever neighbouring regions contain compatible observations, the sheaf axioms guarantee that they can later be assembled into a unique global description. The principal outcome of this stage is the replacement of isolated measurements by mathematically consistent local descriptions distributed across the manuscript.

Then, relations among the independent disciplinary categories are established through functors. Correspondences between chemistry and history may associate pigment provenance with historical trade networks, while linguistic characteristics may be translated into geographical localization or chronological attribution. Codicological observations may similarly constrain historical reconstruction through quire organization or scribal practice.

Subsequently, natural transformations compare these independent translations. If multiple disciplinary pathways converge toward the same interpretation, the corresponding natural transformations express their compatibility. Conversely, incompatible translations reveal regions requiring further investigation. At this point, the manuscript is no longer represented by independent disciplinary descriptions, but by an interconnected network of mathematically compatible relationships.

The global consistency of these relationships is examined through cohomological analysis. Rather than focusing on individual observations, cohomology evaluates whether the complete collection of local sections can be assembled into a globally coherent object. Compatible observations contribute to the zeroth cohomology, whereas higher-order cohomology groups identify incompatibility, missing information or structural contradictions linking several disciplinary domains simultaneously. When these obstructions are absent or sufficiently resolved, descent theory reconstructs a unique global object by gluing all compatible local descriptions. The resulting mathematical object represents the manuscript as an integrated relational entity rather than as the sum of independent analytical results.

Then, the construction is extended to incorporate the manuscript's historical complexity. Multiple copies, translations, editions, restorations and commentaries are represented as objects within a stack, preserving both their individual identities and their mutual equivalences. Derived categories further incorporate successive historical transformations, including revisions, glosses, interpolations and corrections, allowing the manuscript to be represented together with its temporal evolution rather than as a static document.

Subsequently, the integrated algebra generated by all compatible observations is transformed into a geometric object through the construction of a scheme. At this stage, material composition, textual organization, historical transmission and conceptual architecture become different coordinate systems describing the same underlying geometric space.

© 2026 by the author(s). Distributed under a Creative Commons CC BY license.

Preprints.org (www.preprints.org) | NOT PEER-REVIEWED | Posted: 14 July 2026 doi:10.20944/preprints202607.0927.v1

The final step consists of identifying the manuscript's motive. Every admissible discipline-preserving functor provides an alternative representation of the geometric object. The structures invariant under all such representations are retained, whereas discipline-specific features not surviving these translations are discarded. The remaining invariant relational architecture constitutes the manuscript's motive according to our operational definition. The expected theoretical outcome is not a numerical value or statistical descriptor, but a geometric object representing the structural identity of the manuscript. This object simultaneously captures information shared by physical composition, textual organization, historical development, semantic structure and cultural transmission while remaining independent of any individual disciplinary viewpoint. Consequently, two manuscripts differing in language, material support or historical context may nevertheless possess closely related motives if their deepest relational organization is preserved, whereas apparently similar manuscripts may exhibit distinct motives when their invariant structures differ.

Overall, the mathematical concepts introduced throughout the manuscript could combine into a single coherent sequence leading from local multidisciplinary observations to a geometric representation of ancient documentary knowledge.

Conclusions

We asked whether heterogeneous evidence in ancient manuscripts can be represented within a single mathematical language rather than fragmented among independent disciplinary analyses. We aim to provide a coherent language in which material, textual, historical and conceptual evidence can be represented within a common geometric setting. we introduced a Grothendieckian construction that progressively transforms multidisciplinary observations into a unified geometric object through categories, morphisms, sites, sheaves, functors, natural transformations, cohomology, descent theory, stacks, derived categories and schemes. The motive was defined as the maximal invariant relational structure preserved under all admissible discipline-preserving functors.

Our study has limitations. Our construction is theoretical and avoids simulations or applications to individual manuscripts, leaving future studies to evaluate computational feasibility and practical implementation. Several concepts adopted from Grothendieck's mathematics, particularly motives, schemes and stacks, are introduced through operational definitions adapted to manuscript analysis. Specialists in algebraic geometry may regard our definitions as analogical extensions rather than direct applications of the original theory. We do not specify unique algorithms for defining admissible coverings or selecting functors. Generalizability requires to be established across manuscript traditions differing in age, preservation, language or documentary complexity. Additional questions are unanswered, including uniqueness of the extracted motive, stability of the invariant under incomplete observations, relationship between different admissible geometric constructions and computational complexity associated with large manuscript corpora.

Our approach suggests experimentally testable hypotheses. First, independently constructed disciplinary graphs describing the same manuscript should converge toward a common invariant relational substructure after functorial alignment. This prediction can be evaluated by measuring graph similarity before and after alignment using graph edit distance, graph kernels or spectral similarity, with the expectation that aligned representations will exhibit significantly higher structural agreement than randomly permuted graphs.

Second, the size of the extracted motive should increase as additional complementary disciplines are incorporated until reaching a stable plateau, providing a measurable convergence criterion for multidisciplinary integration.

Third, manuscripts belonging to the same textual tradition should exhibit more similar motives than unrelated manuscripts even when written in different languages, scripts or materials. Similarity could be quantified through graph isomorphism scores, persistent topological descriptors or distances between invariant subgraphs, with manuscript families expected to cluster significantly more closely than unrelated controls.

© 2026 by the author(s). Distributed under a Creative Commons CC BY license.

Preprints.org (www.preprints.org) | NOT PEER-REVIEWED | Posted: 14 July 2026 doi:10.20944/preprints202607.0927.v1

Fourth, manuscripts containing later interpolations, restorations or forged additions should produce localized cohomological inconsistencies that coincide with independently established historical anomalies. Their detection sensitivity and specificity could be quantified against expert annotations.

Fifth, successive historical copies should preserve the original invariant structure despite physical or linguistic modifications. A measurable expectation is that invariant-node retention decreases more slowly than overall graph similarity as copying distance increases.

Future investigations could develop explicit computational algorithms, compare alternative categorical representations, study the uniqueness and stability of manuscript motives under noisy or incomplete observations, and extend the formalism to archaeological artefacts and documentary archives.

Beyond manuscript research, our approach may support the development of interoperable analytical environments in which heterogeneous evidence can be represented without privileging any single discipline. These representations could facilitate communication among historians, conservators, philologists, chemists, physicists and computer scientists by providing a common relational vocabulary rather than discipline-specific data structures. Museum collections, digital repositories and cultural heritage databases could benefit from mathematically consistent descriptions capable of integrating material analyses, textual metadata and historical documentation within the same formal representation. Also, our framework may stimulate new educational approaches in which abstract concepts from category theory and algebraic geometry are illustrated through tangible historical objects, encouraging the development of common standards for multidisciplinary knowledge representation.

Authors' contributions. The Author performed: study concept and design, acquisition of data, analysis and interpretation of data, drafting of the manuscript, critical revision of the manuscript for important intellectual content, statistical analysis, obtained funding, administrative, technical and material support, study supervision.

Funding.: This research did not receive any specific grant from funding agencies in the public, commercial or not-for-profit sectors.

Ethics approval and consent to participate. Ethics approval statement is not applicable. This research does not contain any studies with human participants or animals performed by the Author.

Consent for publication. The Author transfers all copyright ownership, in the event the work is published. The undersigned author warrants that the article is original, does not infringe on any copyright or other proprietary right of any third part, is not under consideration by another journal and has not been previously published.

Availability of data and materials. All data and materials generated or analyzed during this study are included in the manuscript. The Author had full access to all the data in the study and took responsibility for the integrity of the data and the accuracy of the data analysis.

Declaration of generative AI and AI-assisted technologies in the writing process. During the preparation of this work, the author used ChatGPT 5.3 to assist with data analysis and manuscript drafting and to improve spelling, grammar and general editing. After using this tool, the author reviewed and edited the content as needed, taking full responsibility for the content of the publication.

References

1. Angelotti, G., F. Nicolardi, P. Henderson, and W. B. Seales. 2026. "Ink Detection from Surface Topography of the Herculaneum Papyri." *Scientific Reports*. Advance online publication. https://doi.org/10.1038/s41598-026-58467-1.
2. Autran, Pierre-Olivier, Catherine Dejoie, Pierre Bordet, Jean-Louis Hodeau, Caroline Dugand, et al. 2021. "Revealing the Nature of Black Pigments Used on Ancient Egyptian Papyri from Champollion Collection." *Analytical Chemistry* 93 (2): 701–709. https://doi.org/10.1021/acs.analchem.0c04178.

© 2026 by the author(s). Distributed under a Creative Commons CC BY license.

Preprints.org (www.preprints.org) | NOT PEER-REVIEWED | Posted: 14 July 2026 doi:10.20944/preprints202607.0927.v1

3. Baez, John C. 2025. "Motivating Motives." In *The Mathematical and Philosophical Legacy of Alexander Grothendieck*, edited by Marco Panza, Daniele C. Struppa, and Jean-Jacques Szczeniarz, 309–323. Basel: Birkhäuser. Also available as *arXiv* preprint arXiv:2304.08737. https://doi.org/10.48550/arXiv.2304.08737.
4. Bennequin, D., and A. Berthoz. 2025. "Brain's Geometries for Movements and Beauty Judgments. A Contribution of Topos Geometries." *Frontiers in Psychology* 16: 1583185. https://doi.org/10.3389/fpsyg.2025.1583185.
5. Ceccarelli, S., M. Rippa, G. Caruso, L. Luvidi, S. Boccuti, M. et al. 2025. "Pulsed Thermographic Analysis of Herculaneum Papyri." *Scientific Reports* 15 (1): 34466. https://doi.org/10.1038/s41598-025-19911-w.
6. Chen, Z. 2024. "(HTBNet) Arbitrary Shape Scene Text Detection with Binarization of Hyperbolic Tangent and Cross-Entropy." *Entropy* 26 (7): 560. https://doi.org/10.3390/e26070560.
7. Dubuc, E. J., and C. Sanchez de la Vega. 2000. "On the Galois Theory of Grothendieck." *Boletín de la Academia Nacional de Ciencias de Córdoba* 65.
8. Gili, T., B. Avila, L. Pasquini, A. Holodny, D. Phillips, P. Boldi, et al. 2024. "Fibration Symmetry-Breaking Supports Functional Transitions in a Brain Network Engaged in Language." *arXiv* preprint arXiv:2409.02674v1.
9. Huber, Annette. 1995. "Grothendieck Motives." In *Mixed Motives and Their Realization in Derived Categories*, *Lecture Notes in Mathematics*, vol. 1604, 100–138. Berlin and Heidelberg: Springer. https://doi.org/10.1007/BFb0095523.
10. Luo, Feng. 1999. "Grothendieck's Reconstruction Principle and 2-Dimensional Topology and Geometry." *Communications in Contemporary Mathematics* 1 (2): 125–53.
11. Marquès, J. 2025. "A Criterion for Categories on Which Every Grothendieck Topology Is Rigid." *Applied Categorical Structures* 33 (6): 37. https://doi.org/10.1007/s10485-025-09833-z.
12. McLarty, Colin. 2018. "Grothendieck's Unifying Vision of Geometry." In *Foundations of Mathematics and Physics One Century After Hilbert*, edited by Jaume Kouneiher, 81–106. Cham: Springer. https://doi.org/10.1007/978-3-319-64813-2_4.
13. Morone, F., I. Leifer, and H. A. Makse. 2020. "Fibration Symmetries Uncover the Building Blocks of Biological Networks." *Proceedings of the National Academy of Sciences of the United States of America* 117 (15): 8306–14. https://doi.org/10.1073/pnas.1914628117.
14. Pisier, Gilles. 2012. "Grothendieck's Theorem, Past and Present." *Bulletin of the American Mathematical Society* 49 (2): 237–323.
15. Popović, M., M. A. Dhali, L. Schomaker, J. van der Plicht, K. Lund Rasmussen, J. La Nasa, I. Degano, M. Perla Colombini, and E. Tigchelaar. 2025. "Dating Ancient Manuscripts Using Radiocarbon and AI-Based Writing Style Analysis." *PLoS ONE* 20 (6): e0323185. https://doi.org/10.1371/journal.pone.0323185.
16. Radini, A., M. Tromp, A. Beach, E. Tong, C. Speller, M. McCormick, J. V. Dudgeon, M. J. Collins, F. Rühli, R. Kröger, and C. Warinner. 2019. "Medieval Women's Early Involvement in Manuscript Production Suggested by Lapis Lazuli Identification in Dental Calculus." *Science Advances* 5 (1): eaau7126. https://doi.org/10.1126/sciadv.aau7126.
17. Rej, Abhijnan, and Matilde Marcolli. 2011. "Motives: An Introductory Survey for Physicists." *Contemporary Mathematics* 539: 377–415. Providence, RI: American Mathematical Society. Also available as *arXiv* preprint arXiv:0907.4046. https://doi.org/10.48550/arXiv.0907.4046.
18. Romano, F. P., E. Puglia, C. Caliri, D. P. Pavone, M. Alessandrelli, A. Busacca, et al. 2023. "Layout of Ancient Greek Papyri through Lead-Drawn Ruling Lines Revealed by Macro X-Ray Fluorescence Imaging." *Scientific Reports* 13 (1): 6582. https://doi.org/10.1038/s41598-023-33242-8.
19. Sobota, D., and L. Zdomskyy. 2024. "Convergence of Measures after Adding a Real." *Archive for Mathematical Logic* 63 (1–2): 135–62. https://doi.org/10.1007/s00153-023-00888-0.
20. Stabile, S., F. Palermo, I. Bukreeva, D. Mele, V. Formoso, R. Bartolino, and A. Cedola. 2021. "A Computational Platform for the Virtual Unfolding of Herculaneum Papyri." *Scientific Reports* 11 (1): 1695. https://doi.org/10.1038/s41598-020-80458-z.
21. Tack, P., M. Cotte, S. Bauters, E. Brun, D. Banerjee, W. Bras, C. Ferrero, D. Delattre, V. Mocella, and L. Vincze. 2016. "Tracking Ink Composition on Herculaneum Papyrus Scrolls: Quantification and Speciation

© 2026 by the author(s). Distributed under a Creative Commons CC BY license.

Preprints.org (www.preprints.org) | NOT PEER-REVIEWED | Posted: 14 July 2026 doi:10.20944/preprints202607.0927.v1

of Lead by X-Ray Based Techniques and Monte Carlo Simulations." *Scientific Reports* 6: 20763. https://doi.org/10.1038/srep20763.

22. Tournié, A., K. Fleischer, I. Bukreeva, F. Palermo, M. Perino, et al. 2019. "Ancient Greek Text Concealed on the Back of Unrolled Papyrus Revealed through Shortwave-Infrared Hyperspectral Imaging." *Science Advances* 5 (10): eaav8936. https://doi.org/10.1126/sciadv.aav8936.
23. Xu, X., Y. Chang, J. An, and Y. Du. 2023. "Chinese Text Classification by Combining Chinese-BERTology-wwm and GCN." *PeerJ Computer Science* 9: e1544. https://doi.org/10.7717/peerj-cs.1544.
24. Zalamea, F. 2015. "Peirce's Cenopythagorean Categories, Merleau-Ponty's Chiasmatic Entrelacs and Grothendieck's Résumé." *Progress in Biophysics and Molecular Biology* 119 (3): 437–41. https://doi.org/10.1016/j.pbiomolbio.2015.07.011.
25. Zhu, H., J. Xia, R. Liu, and B. Deng. 2025. "SPIRIT: Structural Entropy Guided Prefix Tuning for Hierarchical Text Classification." *Entropy* 27 (2): 128. https://doi.org/10.3390/e27020128.

Disclaimer/Publisher's Note: The statements, opinions and data contained in all publications are solely those of the individual author(s) and contributor(s) and not of MDPI and/or the editor(s). MDPI and/or the editor(s) disclaim responsibility for any injury to people or property resulting from any ideas, methods, instructions or products referred to in the content.

© 2026 by the author(s). Distributed under a Creative Commons CC BY license.

arXiv:2604.14196v1 [physics.geo-ph] 2 Apr 2026

Toward buoyancy-driven flow at Campi Flegrei: coupled phase change and asymmetric geometry

Arturo Tozzi (corresponding author)
ASL Napoli 1 Centro, Distretto 27, Naples, Italy
Via Comunale del Principe 13/a 80145
tozziarturo@libero.it

ABSTRACT

Bradyseism at Campi Flegrei is usually interpreted in terms of hydrothermal pressurization and magmatic degassing. Fluid flow, often treated as a passive response to pressure accumulation, is commonly modeled using simplified geometries and homogeneous permeability fields. We introduce a model in which phase transition, structural heterogeneity and geometric asymmetry jointly influence fluid flow and pressure distribution within a heterogeneous subsurface environment. We hypothesize that coupling among phase change, density gradients and flows may follow a mechanism similar to the self-propulsion observed in asymmetric floating bodies like melting ice blocks, where phase change generates buoyancy-driven currents along their inclined surfaces and net motion in the opposite direction. We simulate pressure evolution in a shallow gas-rich reservoir subject to time-dependent forcing and hydraulic relaxation, coupled to buoyancy-enhanced Darcy flow along prescribed preferential pathways. Our numerical simulations, grounded in reported deformation rates and seismicity depths at Campi Flegrei, reproduce temporal variations in uplift and the persistence of spatially localized flow. Within this framework, asymmetric geometry may promote channelized upward transport, while phase change may enhance buoyancy and contribute to pressure redistribution. Our model predicts nonlinear uplift acceleration, shallow localized seismicity and velocity scaling with pressure and buoyancy. Integration with existing multiphase models would enable the examination of how buoyancy-driven flows influence pressure evolution and deformation during volcanic unrest.

KEYWORDS: permeability; buoyancy; degassing; poroelasticity; convection.

INTRODUCTION

Bradyseism at Campi Flegrei is investigated through geodetic, geochemical and geophysical observations, with a focus on hydrothermal pressurization, magmatic degassing and poroelastic deformation of the shallow crust (Acocella 2021; Picozzi and Iaccarino 2021; Di Martino et al. 2022; Astort et al., 2024; Barone et al. 2025). Ground uplift is described as the response to pressure variations within a gas-rich reservoir, often located between two- and four-kilometers depth, fed by deeper magmatic sources (Martini et al. 2008; Guidoboni and Ciuccarelli 2011; Zaccarelli and Bianco 2017; Sabbarese et al. 2020; Giacomuzzi et al. 2024; Tramelli, Tan et al. 2025). Integration of multiphase fluid flow, thermal effects and mechanical deformation provides quantitative reconstructions of recent uplift episodes and seismicity patterns. These approaches often assume isotropic and homogeneous permeability fields, treating fluid migration primarily as a diffusive or pressure-driven process (Sbrana, Marianelli, and Pasquini 2021; Convertito, and Godano 2024; Chalumeau et al. 2024; Di Toro 2025). This perspective constraints the ability to capture spatially localized deformation, transient accelerations and the organization of fluid pathways observed in seismic tomography and resistivity data. Still, phase transitions like boiling and gas exsolution are incorporated as source terms without explicitly addressing their role in structuring flow patterns. As a result, the coupling between structural asymmetry, phase change and directed fluid motion is still unresolved.

We introduce a theoretical formulation in which geometric asymmetry and phase change jointly influence fluid flow and pressure distribution. We consider a shallow reservoir subject to time-dependent input from a deeper source and to internal transformations associated with gas exsolution and boiling. Pressure evolves according to a balance between source input and hydraulic relaxation, while fluid velocity is determined by permeability, viscosity, pressure gradients and buoyancy arising from density contrasts. Coupling among phase change, density gradients and directed flow could be viewed in analogy with the melting-driven self-propulsion observed in asymmetric floating bodies, where phase change induces buoyancy-driven currents and net motion through momentum exchange with the surrounding fluid (Berhanu et al. 2026). In our setting, preferential pathways are introduced in terms of geometric features representing heterogeneous permeability and structural discontinuities. Phase change enhances buoyancy and modifies local density, amplifying upward transport along these pathways and redistributing pressure within the reservoir. We provide numerical simulations based on recent monitoring data of Campi Flegrei to explore how transient forcing, relaxation timescales and pathway geometry could influence the temporal evolution of uplift and surface deformation's localization.

arXiv:2604.14196v1 [physics.geo-ph] 2 Apr 2026

METHODS

We studied the recent unrest of Campi Flegrei through a quantitative model coupling reservoir pressurization, phase change, buoyancy-enhanced flow and surface deformation within an asymmetric subsurface geometry. We used published monitoring constraints on uplift, seismicity depth, reservoir structure and degassing to parameterize a time-dependent simulation. By combining temporal evolution of pressure with spatially organized flow and a simplified mechanical response, we tested whether the interaction between phase change and imposed geometric asymmetry could reproduce both the temporal variability and spatial localization observed during recent unrest.

Observational constraints and quantitative parameterization. The parameter space was constrained using recent observational data (De Landro et al. 2025; Rapagnani et al. 2025). The February 2026 surveillance bulletin reported 254 earthquakes, with 192 located events concentrated within the upper 3 km and maximum depth of 4.5 km (INGV-Osservatorio Vesuviano 2026). Uplift rates were approximately 15 ± 3 mm month^{-1} from April to early October 2025, increased to 25 ± 3 mm month^{-1} after October 2025 and decreased to about 10 ± 3 mm month^{-1}by early February 2026. The cumulative uplift at Rione Terra reached 162.5 cm since November 2005, with 24.5 cm since January 2025. Structural models indicate a shallow gas-rich reservoir between 2 and 4 km, a caprock between 1 and 2 km and deeper magmatic sources below 4 km. Weekly geochemical monitoring reported fumarolic temperatures near 95°C at Pisciarelli and about 173°C at Solfatara. These quantities were used to delimit physically plausible ranges for temperature, density contrast and fluid properties.

Pressure evolution and source-term representation. The shallow reservoir was represented through a time-dependent excess pressure $P(t)$ in MPa. Its evolution was described by the first-order differential equation

$$\frac{dP}{dt} = \frac{S(t) - P(t)}{\tau_h},$$

where $S(t)$ is an effective source term and τ_h is a hydraulic relaxation time. This formulation assumes that pressure increases due to deep input and internal phase transitions and decreases through leakage and redistribution. The source term was written as

$$S(t) = P_b + P_1 \exp\left(\quad - \frac{t - t_0}{\tau_d} \right),$$

where P_b is a background level, P_1 is a transient amplitude and τ_d is a decay timescale. Parameters were set to $P_b =$ 1.00 MPa, $P_1 = 1.50$ MPa, $\tau_h = 4.0$ months and $\tau_d = 3.5$ months, with t_0 corresponding to October 2025. Numerical integration was performed using an explicit Euler scheme with time step $\Delta t = 1$ month:

$$P_{n+1} = P_n + \Delta t \, \frac{S_n - P_n}{\tau_h}.$$

This equation compresses multiple processes, including degassing and boiling, into a single effective forcing and does not explicitly model thermodynamic phase equilibria (Danesi et al. 2024; Hainzl, Dahm and Tramelli 2026).

Darcy–buoyancy flow and phase-change contribution. Fluid motion was described using a Darcy-type relation combining pressure gradient and buoyancy effects:

$$u(t) = \frac{k}{\mu}\left(\frac{P(t) \times 10^6}{L} + \Delta\rho \, g \right).$$

Here k is permeability, μ is dynamic viscosity, L is the vertical extent of the flow path, $\Delta\rho$ is the density contrast induced by phase change and g is gravitational acceleration. The pressure term accounts for forced flow, while the buoyancy term represents the effect of vapor exsolution and heating. Values used were $k = 2 \times 10^{-14}$ m^2, $\mu =$ 1.5×10^{-5} Pa s, $L = 3000$ m and $\Delta\rho = 250$ kg m^{-3}. The resulting velocity was converted from m s^{-1} to m day^{-1}. This linear combination neglects multiphase interactions, compressibility and feedback between flow and permeability and should therefore be interpreted as a simplified representation of transport (Tan et al. 2025; De Landro et al. 2025).

Surface deformation and calibration procedure. Surface uplift $w(t)$ was linked to pressure through

$$\frac{dw}{dt} = aP(t) + b,$$

with $a = 0.8333$ mm month^{-1} MPa^{-1} and $b = 9.1667$ mm month^{-1}. The discrete update equation was

$$w_{n+1} = w_n + \frac{aP_n + b}{10},$$

arXiv:2604.14196v1 [physics.geo-ph] 2 Apr 2026

where division by 10 converts millimeters to centimeters. The initial condition was $w(t_0) = 151.0$ cm. This relation is calibrated to reproduce observed uplift rates rather than derived from elastic theory. A secondary diagnostic for seismicity was introduced:

$$\dot{N}(t) = N_0 \exp\left[\beta(w(t) - w_0)\right],$$

with $N_0 = 18$ events month^{-1} and $\beta = 0.06$ cm^{-1}. This variable was used to verify qualitative consistency between deformation and seismic activity (Hainzl, Dahm and Tramelli 2026; INGV-Osservatorio Vesuviano 2024).

Geometric construction of asymmetric flow pathways. To represent structural heterogeneity, a two-dimensional section was defined with horizontal coordinate $x \in [-3,3]$ km and depth $z \in [0,5]$ km. A curved pathway was prescribed as

$$x_c(z) = -0.6 + 0.45(5 - z) - 0.06(5 - z)^2,$$

with width

$$\sigma(z) = 0.28 + 0.06(5 - z).$$

The velocity field was constructed as

$$V(x,z) = V_0 \exp\left[-\frac{(x - x_c(z))^2}{2\sigma(z)^2} \right] \left[0.35 + 0.65 \exp\left(-\frac{(z-2.5)^2}{3.0} \right) \right].$$

This formulation produces a localized high-velocity corridor connecting deeper and shallower regions. The geometry is imposed and represents a hypothesis about preferential pathways rather than a reconstruction derived from data (Giudicepietro et al. 2025).

Nonlinear interaction between asymmetry and phase change. To explore the interaction between structural asymmetry and phase change, we defined two dimensionless parameters A(asymmetry index) and B(phase-change intensity). Uplift acceleration was expressed as

$$\alpha(A,B) = C\, A^{3/2} B^2,$$

with $C = 40$ mm month^{-2}. This expression is not derived from physical principles but constructed to test whether nonlinear coupling produces distinct regimes. The resulting surface was evaluated over $A, B \in [0,1]$. This step provides a hypothesis-generating exploration rather than a validated prediction.

All computations were performed in Python using NumPy for numerical arrays, pandas for time handling and Matplotlib for visualization. Temporal integration covered monthly intervals from October 2025 to February 2026. Spatial fields were evaluated on regular grids. Units were maintained explicitly. The workflow consisted of parameter selection, time integration of pressure, computation of velocity and mapping of spatial distribution. Since no automated inversion, uncertainty quantification or statistical fitting was performed, our outputs should be interpreted as representative simulations illustrating possible system behavior rather than validated reconstructions.

RESULTS

Our simulated pressure increases briefly and then relaxes over the imposed hydraulic timescale. This produces an uplift rate that decreases from higher to lower values over a few months. Within the explored parameter range, the relationship between pressure and uplift rate is approximately linear, with uplift rates decreasing smoothly as pressure declines. Upward fluid velocity, computed from combined pressure gradient and buoyancy contributions, shows a monotonic dependence on pressure, confirming that both contributions act coherently under our formulation. The vertical section shows that flow is not uniformly distributed but is concentrated along a curved pathway connecting deeper and shallower regions (Figure 1). This localization persists throughout the simulated temporal evolution, indicating that spatial organization could be controlled primarily by the imposed geometry rather than by instantaneous pressure amplitude. Overall, the combined evolution of pressure decay, declining uplift rates and persistent flow localization points towards the possible coexistence of temporal variability and spatial organization within our simplified formulation.

Interactions between geometric asymmetry and phase change. The two-parameter exploration of geometric asymmetry and phase-change intensity provides a model-based prediction of a nonlinear response in uplift acceleration (Figure 2). For low values of either parameter, uplift acceleration is close to zero across the explored domain, indicating that neither asymmetry nor phase change alone produces significant dynamic amplification. When both parameters increase simultaneously, the system is predicted to transition to a regime characterized by rapidly increasing uplift acceleration, with values rising sharply beyond intermediate thresholds. The resulting surface exhibits a convex shape, indicating superlinear coupling between the two variables rather than additive behavior. The absence of intermediate regimes with moderate acceleration suggests that the system may organize into distinct dynamical states under our

assumptions. This prediction identifies a potentially discriminable signature, i.e., a transition from gradual to accelerated deformation as both structural asymmetry and phase-change intensity increase, which can be tested against observational data.

Overall, our simulations suggest that pressure evolution, phase change and geometric asymmetry can be combined in a reduced quantitative description to assess time-dependent uplift and spatially localized flow.

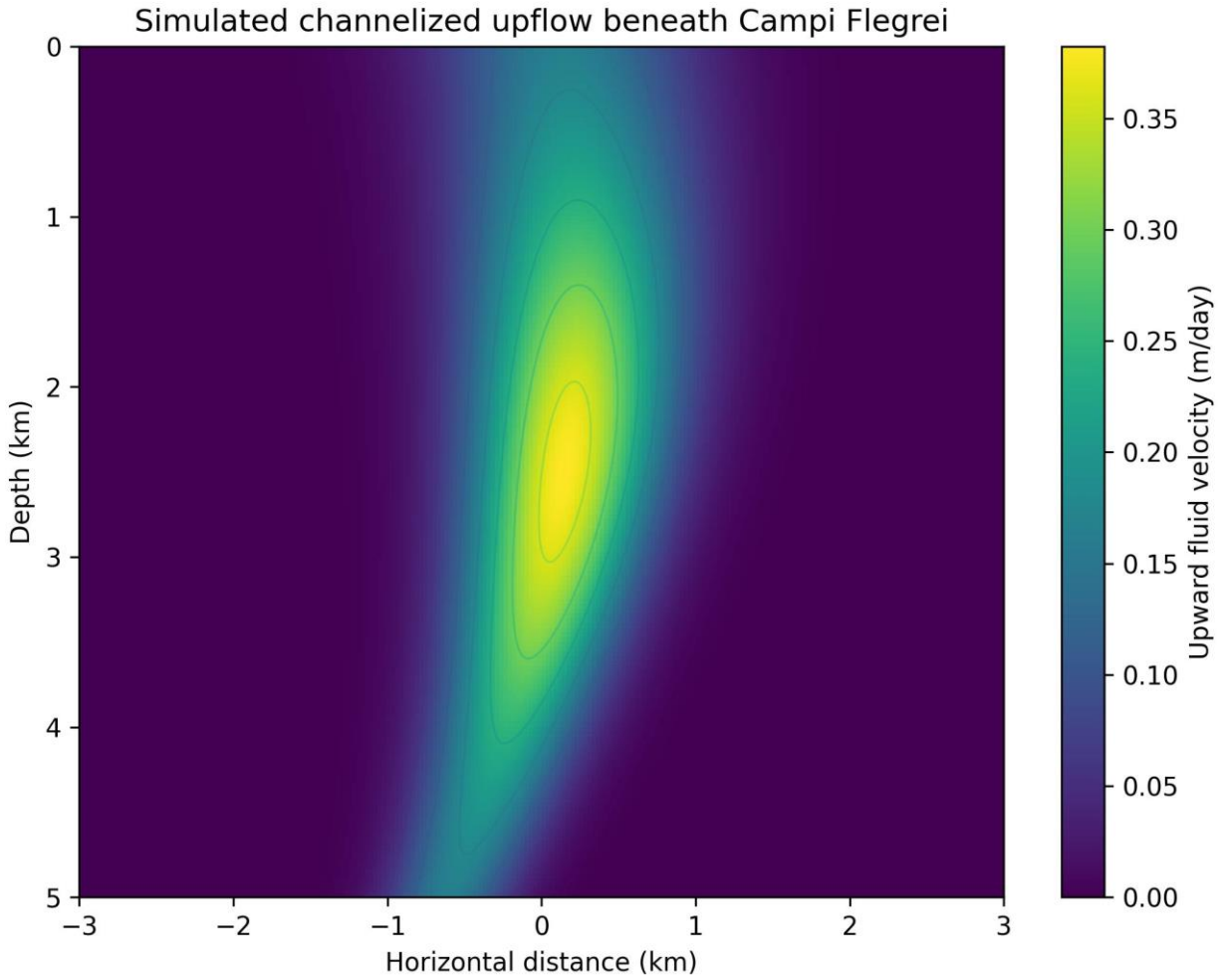


Figure 1. Simulated vertical section of channelized upflow beneath Campi Flegrei. The horizontal axis represents lateral distance in kilometers across the caldera, while the vertical axis indicates depth in kilometers from the surface to approximately 5 km. Color shading and superimposed contours quantify upward fluid velocity in meters per day, computed from a permeability–buoyancy formulation combining pressure gradients and density contrasts associated with phase change. The curved high-velocity corridor delineates a preferential pathway linking a deeper source region at approximately 4–5 km depth to a shallower gas-rich reservoir at approximately 2–3 km depth. The increase in velocity toward shallower depths, attributed to the combined effects of pressure-driven flow and buoyancy, is proposed as a hypothesis within our model and not directly inferred from empirical data.

arXiv:2604.14196v1 [physics.geo-ph] 2 Apr 2026

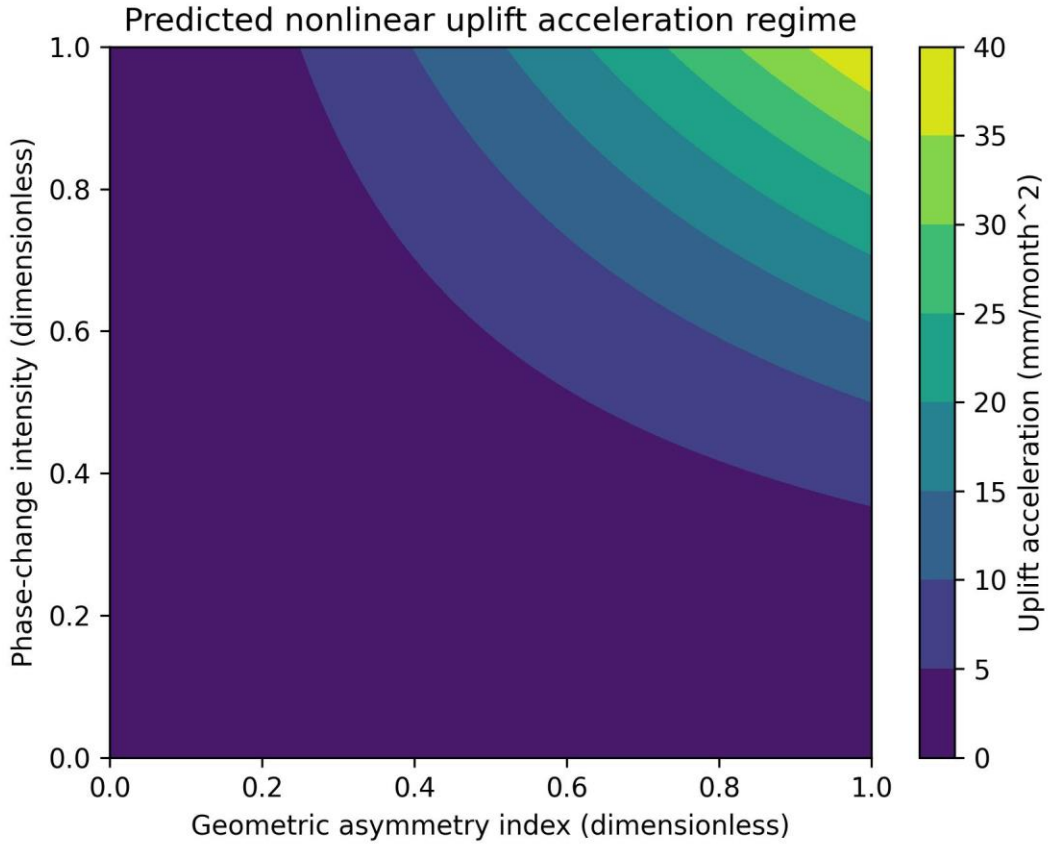


Figure 2. Hypothesized interaction between geometric asymmetry and phase-change intensity based on our model assumptions. Contour plot of predicted uplift acceleration (mm/month²) as a function of geometric asymmetry (dimensionless) and phase-change intensity (dimensionless), representing a model prediction. Uplift acceleration is low when either parameter is small, but increases rapidly when both exceed intermediate values. This cooperative amplification departs from additive behavior commonly assumed in hydrothermal models. The convex surface indicates a superlinear response, suggesting a transition between gradual and accelerated deformation.

CONCLUSIONS

We asked whether bradyseism at Campi Flegrei can be interpreted not only as pressure accumulation, but also as directed fluid motion arising from the interaction between phase change and geometric asymmetry. This approach is motivated by a physical observation: an asymmetric ice block melts unevenly, producing dense water that flows along its surface and generates a force that drives motion in the opposite direction. This illustrates how phase change and asymmetry can organize fluid motion. Therefore, we isolate a minimal set of variables linking flow organization to measurable quantities like uplift rate and depth distribution of activity. The coupled effect of asymmetry and phase change allows discrimination between gradual and accelerated deformation regimes within the same parameter space.

Our simulations compare time-dependent pressure evolution, buoyancy-driven flow and surface deformation within ranges constrained by monitoring data. A transient pressure increase followed by hydraulic relaxation reproduces observed uplift-rate variations, while asymmetric permeability leads to persistent localization of upward flow. In our simulations, fluid migration is organized along preferential paths connecting deeper and shallower regions rather than being uniform. The coupling between pressure gradients and density contrasts sustains coherent upward velocities even as pressure declines. In addition, the interaction between asymmetry and phase change produces nonlinear transitions in uplift dynamics. These results indicate that deformation at Campi Flegrei may reflect organized fluid transport controlled by the coupled effects of geometry and phase change

Our study has limitations. The governing equations are not derived from principles of multiphase thermo-poroelasticity. The source term $S(t)$ and the linear relation between pressure and uplift are introduced as calibrated components rather than independently validated quantities. The Darcy–buoyancy formulation assumes a linear combination of pressure gradient and density contrast, neglecting two-phase flow effects, compressibility and time-dependent permeability, all of

arXiv:2604.14196v1 [physics.geo-ph] 2 Apr 2026

which are relevant in the context of Campi Flegrei. The representation of geometric asymmetry relies on an imposed preferential pathway rather than one inferred from geophysical inversion. The nonlinear interaction is built through parameter choice and should be interpreted as a testable hypothesis rather than a derived law. Open questions concern how permeability evolves under repeated pressurization, how multiphase interactions modify effective density contrasts and how transient structural changes alter pathway stability.

Our model yields testable previsions. First, if phase change and geometric asymmetry jointly control deformation, then uplift acceleration should display a nonlinear dependence on indicators of fluid input and structural focusing. Specifically, the time derivative of uplift rate is expected to increase superlinearly when both gas flux and inferred pathway anisotropy rise, whereas it should remain near zero if only one factor varies.
Second, upward fluid velocity along preferential zones should scale with pressure according to a linear-plus-buoyancy relation, implying that geophysical proxies of fluid movement, such as seismic attenuation or resistivity anomalies, should increase proportionally to estimated overpressure within a defined range.
Third, the depth distribution of seismicity should remain confined within the upper three to four kilometers when flow is strongly localized, with a measurable concentration gradient aligned with the inferred pathway. These predictions can be tested through time-resolved comparisons between uplift rate, gas emissions and subsurface imaging.
Practical implications concern the integration of physically interpretable variables into monitoring strategies. The explicit computation of pathway-dependent velocity fields enables the construction of indicators sensitive to changes in subsurface transport efficiency. This may support the development of diagnostic thresholds based on combined geodetic and geochemical signals, allowing classification of unrest phases according to internal system organization rather than solely on amplitude measures. Our approach can also shape the design of monitoring networks, by identifying areas where measurements are most likely to capture early changes in subsurface dynamics. In addition, our formulation facilitates rapid updating of model states as new data become available, enabling continuous tracking of system evolution with limited computational cost.

In conclusion, we show that deformation, fluid migration and internal structure can be assessed within a unified quantitative description, albeit within a reduced representation. Our approach suggests that subsurface processes' organization, influenced by structural heterogeneity, geometric asymmetry and phase change, may jointly influence fluid migration at Campi Flegrei. This perspective provides an interpretation of temporal variability and spatial localization, while remaining compatible with existing multiphase and poroelastic descriptions.

DECLARATIONS

Ethics approval and consent to participate. This research does not contain any studies with human participants or animals performed by the Author.
Consent for publication. The Author transfers all copyright ownership, in the event the work is published. The undersigned author warrants that the article is original, does not infringe on any copyright or other proprietary right of any third part, is not under consideration by another journal and has not been previously published.
Availability of data and materials. All data and materials generated or analyzed during this study are included in the manuscript. The Author had full access to all the data in the study and took responsibility for the integrity of the data and the accuracy of the data analysis.
Disclaimer. The views expressed are those of the author and do not necessarily reflect those of the affiliated institutions.
Competing interests. The Author does not have any known or potential conflict of interest including any financial, personal or other relationships with other people or organizations within three years of beginning the submitted work that could inappropriately influence or be perceived to influence their work.
Funding. This research did not receive any specific grant from funding agencies in the public, commercial or not-for-profit sectors.
Acknowledgements: none.
Authors' contributions. The Author performed: study concept and design, acquisition of data, analysis and interpretation of data, drafting of the manuscript, critical revision of the manuscript for important intellectual content, statistical analysis, obtained funding, administrative, technical and material support, study supervision.
Declaration of generative AI and AI-assisted technologies in the writing process. During the preparation of this work, the author used ChatGPT 5.3 to assist with data analysis and manuscript drafting and to improve spelling, grammar and general editing. After using this tool, the author reviewed and edited the content as needed, taking full responsibility for the content of the publication.

REFERENCES

1) Acocella, Valerio. 2021. *Volcano-Tectonic Processes*. Advances in Volcanology. Cham: Springer. https://doi.org/10.1007/978-3-030-65968-4
2) Astort, A., E. Trasatti, L. Caricchi, et al. 2024. "Tracking the 2007–2023 Magma-Driven Unrest at Campi Flegrei Caldera (Italy)." *Communications Earth & Environment* 5: 506. https://doi.org/10.1038/s43247-024-01665-4
3) Barone, Andrea, Gianluca Gola, Stefano Caliro, Giovanni Chiodini, Pietro Tizzani, and Raffaele Castaldo. 2025. "Long-Term Thermo-Fluid Dynamic Modeling of Solfatara Hydrothermal System, Campi Flegrei Caldera." *Journal of Volcanology and Geothermal Research* 459: 108277. https://doi.org/10.1016/j.jvolgeores.2025.108277
4) Berhanu, Michael, Amit Dawadi, Martin Chaigne, Jérôme Jovet, and Arshad Kudrolli. 2026. "Self-Propulsion of Floating Ice Blocks Caused by Melting in Water." *Physical Review Fluids* 11: 033802. https://doi.org/10.1103/k6gl-1zqm
5) Chalumeau, C., H. Agurto-Detzel, A. Rietbrock, et al. 2024. "Seismological Evidence for a Multifault Network at the Subduction Interface." *Nature* 628: 558–562. https://doi.org/10.1038/s41586-024-07245-y
6) Danesi, Sara, Christopher R. J. Kilburn, Giuseppe De Natale, et al. 2024. "Evolution in Unrest Processes at Campi Flegrei Caldera as Inferred from Seismicity and Ground Deformation." *Earth and Planetary Science Letters* 630: 118600
7) De Landro, G., T. Vanorio, T. Muzellec, et al. 2025. "3D Structure and Dynamics of Campi Flegrei Enhance Multi-Hazard Assessment." *Nature Communications* 16: 4814. https://doi.org/10.1038/s41467-025-59821-z
8) Di Martino, Maria Del Pilar, Luca De Siena, Vincenzo Serlenga, and Grazia De Landro. 2022. "Reconstructing Hydrothermal Fluid Pathways and Storage at the Solfatara Crater (Campi Flegrei, Italy) Using Seismic Scattering and Absorption." *Frontiers in Earth Science* 10. https://doi.org/10.3389/feart.2022.852510
9) Di Toro, G. 2025. "Earthquake Rupture Velocity and Stress Drop Interaction in the Campi Flegrei Volcanic Caldera." *Communications Earth & Environment*. https://doi.org/10.1038/s43247-025-02808-x
10) Giacomuzzi, G., C. Chiarabba, F. Bianco, P. De Gori, and N. Piana Agostinetti. 2024. "Tracking Transient Changes in the Plumbing System at Campi Flegrei Caldera." *Earth and Planetary Science Letters* 637: 118744. https://doi.org/10.1016/j.epsl.2024.118744
11) Giudicepietro, Flora, Rosario Avino, Eliana Bellucci Sessa, Andrea Bevilacqua, Manuela Bonano, Stefano Caliro, et al. 2025. "Burst-Like Swarms in the Campi Flegrei Caldera Accelerating Unrest from 2021 to 2024." *Nature Communications* 16 (1): 1548. https://doi.org/10.1038/s41467-025-56723-y
12) Guidoboni, Emanuela, and Caterina Ciuccarelli. 2011. "The Campi Flegrei Caldera: Historical Revision and New Data on Seismic Crises, Bradyseisms, the Monte Nuovo Eruption and Ensuing Earthquakes (Twelfth Century–1582 AD)." *Bulletin of Volcanology* 73: 655–677. https://doi.org/10.1007/s00445-010-0430-3
13) Hainzl, S., T. Dahm, and A. Tramelli. 2026. "A Deformation-Driven Earthquake Interaction Model for Seismicity at Campi Flegrei." *Communications Earth & Environment* 7: 244
14) INGV. 2024. "Campi Flegrei: The Relationship between Ground Uplift and Seismic Activity Has Been Quantified." Press release, December 3, 2024
15) INGV-Osservatorio Vesuviano. 2026. "Campi Flegrei Monthly and Weekly Surveillance Bulletins, February 2026"
16) Martini, M., F. Giudicepietro, L. D'Auria, M. Orazi, G. Borriello, C. Buonocunto, et al. 2008. "Seismological Monitoring of Campi Flegrei Caldera." Presented at the European Geosciences Union General Assembly 2008, Vienna, Austria. https://www.earth-prints.org/handle/2122/4168
17) Picozzi, Matteo, and Antonio Giovanni Iaccarino. 2021. "Forecasting the Preparatory Phase of Induced Earthquakes by Recurrent Neural Network." *Forecasting* 3 (1): 17–36. https://doi.org/10.3390/forecast3010002
18) Rapagnani, Giacomo, Simone Cesca, Gilberto Saccorotti, Gesa Petersen, Torsten Dahm, Francesca Bianco, and Francesco Grigoli. 2025. "Coupled Earthquakes and Resonance Processes during the Uplift of Campi Flegrei Caldera." *Communications Earth & Environment* 6 (1): 607. https://doi.org/10.1038/s43247-025-02604-7
19) Sabbarese, C., F. Ambrosino, G. Chiodini, et al. 2020. "Continuous Radon Monitoring during Seven Years of Volcanic Unrest at Campi Flegrei Caldera (Italy)." *Scientific Reports* 10: 9551. https://doi.org/10.1038/s41598-020-66590-w
20) Sbrana, A., P. Marianelli, and G. Pasquini. 2021. "The Phlegrean Fields Volcanological Evolution." *Journal of Maps* 17 (2): 557–570. https://doi.org/10.1080/17445647.2021.1982033
21) Tan, Xing, Anna Tramelli, Sergio Gammaldi, Gregory C. Beroza, William L. Ellsworth, and Warner Marzocchi. 2025. "A Clearer View of the Current Phase of Unrest at Campi Flegrei Caldera." *Science* 390 (6768): 70–75. https://doi.org/10.1126/science.adw9038
22) Tramelli, A., V. Convertito, and C. Godano. 2024. "b Value Enlightens Different Rheological Behaviour in Campi Flegrei Caldera." *Communications Earth & Environment* 5: 275. https://doi.org/10.1038/s43247-024-01447-y
23) Zaccarelli, Lucia, and Francesca Bianco. 2017. "Noise-Based Seismic Monitoring of the Campi Flegrei Caldera." *Geophysical Research Letters* 44. https://doi.org/10.1002/2016GL072477

Preprints.org

Article

Not peer-reviewed version

A Bruhat-Tits Ultrametric Logic for Hierarchical Inference

Arturo Tozzi *

Posted Date: 6 August 2026

doi: 10.20944/preprints202608.0449.v1

Keywords: ultrametric; refinement; persistence; hierarchy; inference

Preprints.org is a free multidisciplinary platform providing preprint service that is dedicated to making early versions of research outputs permanently available and citable. Preprints posted at Preprints.org appear in Web of Science, Crossref, Google Scholar, Scilit, Europe PMC, OpenAlex.

Copyright: This open access article is published under a Creative Commons CC BY 4.0 license, which permit the free download, distribution, and reuse, provided that the author and preprint are cited in any reuse.

Preprints.org (www.preprints.org) | NOT PEER-REVIEWED | Posted: 6 August 2026 doi:10.20944/preprints202608.0449.v1

Disclaimer/Publisher's Note: The statements, opinions, and data contained in all publications are solely those of the individual author(s) and contributor(s) and not of MDPI and/or the editor(s). MDPI and/or the editor(s) disclaim responsibility for any injury to people or property resulting from any ideas, methods, instructions, or products referred to in the content.

Article

A Bruhat-Tits Ultrametric Logic for Hierarchical Inference

Arturo Tozzi

ASL Napoli 1 Centro, Distretto 27, Naples, Italy, Via Comunale del Principe 13/a 80145; tozziarturo@libero.it

Abstract

Extensions of classical logic like Kripke models, branching-time semantics and proof trees introduce hierarchical structures, yet inference is independent of the hierarchy itself. We ask: can hierarchy become the mathematical principle from which inference is generated, rather than merely organizing logical states? p-adic geometry provides a natural setting for addressing this question by replacing Euclidean proximity with hierarchical proximity defined by shared ancestry. Its canonical geometric realization, the Bruhat-Tits tree, describes information as a sequence of successive refinements, therefore providing a natural substrate for hierarchical logical evolution. Building on this structure, we introduce an ultrametric logic in which propositions correspond to progressively refined informational states, logical proximity is determined by ultrametric distance and negation is interpreted as divergence between refinement branches. We evaluated this formulation through mathematical simulations on a finite Bruhat-Tits tree, quantifying proposition clustering, refinement trajectories, ultrametric neighborhoods and persistence during successive refinement steps. Our simulations generated coherent hierarchical organization, stable proposition classes and increasing inferential affinity among propositions sharing longer refinement histories, supporting a geometric interpretation of logical inference driven by hierarchical refinement.

Keywords: ultrametric; refinement; persistence; hierarchy; inference

Introduction

Classical logic assigns truth values to propositions and inference rules preserving validity under well-defined semantic or syntactic conditions. Since Aristotle, binary truth and the principles of non-contradiction and excluded middle have provided the conceptual basis for most logical systems, while subsequent developments have broadened rather than replaced this foundation (Parry and Hacker 1991; Rothhaar 2020; De Rizzo 2025; Decker 2025; King and Raspa 2025). Predicate logic extended propositional reasoning through quantification, modal logic incorporated necessity and possibility, intuitionistic logic reformulated truth in constructive terms (Tarannum and Jabin 2022; Brunet 2023; Hamdy et al. 2024; Ciardelli 2025; Gao et al. 2025; Litland 2025; Montambault et al. 2025; von Plato 2025). Kripke semantics introduced partially ordered structures to represent evolving information, branching-time logics modeled multiple possible futures, while paraconsistent systems investigated controlled forms of contradiction (Oshiyama et al. 2012; Da Silva Filho et al. 2016; Da Silva Filho et al. 2021; Bonzio et al. 2023; Olkhovikov 2024; Fernández-Vilas et al. 2026).

In parallel, mathematical logic has increasingly adopted geometric and topological perspectives, including sheaf-theoretic semantics, categorical logic and domain theory, in which relationships among propositions are interpreted through structures richer than simple truth assignments. Nevertheless, geometry serves as a semantic or organizational framework rather than as an active determinant of inference. Tree-like structures are employed to represent proofs, accessibility relations or temporal branching, but their metric properties do not influence the logical process itself (Sgurev 2021; Sgurev 2022; Dedhe et al. 2023; Wang et al. 2025). Likewise, hierarchical representations in computer science and artificial intelligence primarily organize information or computation, while inference is governed by syntactic or semantic rules independent of the underlying geometry.

© 2026 by the author(s). Distributed under a Creative Commons CC BY license.

Preprints.org (www.preprints.org) | NOT PEER-REVIEWED | Posted: 6 August 2026 doi:10.20944/preprints202608.0449.v1

Consequently, existing logical frameworks lack an intrinsic notion of distance between propositions, gradual refinement governed by a geometric metric or inferential strength emerging directly from hierarchical organization.

We introduce a logical framework in which the geometry of the Bruhat-Tits tree becomes an integral component of logical reasoning rather than a descriptive representation. The Bruhat-Tits tree, arising naturally in p-adic geometry, provides an ultrametric hierarchical space in which proximity is determined by the depth of shared ancestry instead of Euclidean distance (Zabrodin 1989; Chen, Liu, and Hung 2021; Ludwig and Merten 2026). We reinterpret this structure as a logical environment where propositions are not regarded as isolated entities endowed with fixed truth values, but as successive refinements of more general informational states. Each refinement generates increasingly specific propositions while preserving their genealogical relationships within the hierarchy. Logical proximity is established by the amount of refinement history shared by two propositions, allowing similarity, inferential transfer and proposition stability to acquire precise geometric meanings. In this formulation, negation is interpreted as divergence between refinement branches rather than as an elementary complement, whereas logical robustness depends on persistence across successive refinements instead of exclusively on binary evaluation.

To illustrate how ultrametric geometry could organize inference and reveal structural properties that remain inaccessible in logical systems lacking an explicit hierarchical metric, we perform a qualitative simulation on a finite approximation of a Bruhat-Tits tree in which propositions evolve through iterative refinements. Our simulation follows the formation of hierarchical proposition clusters, the emergence of refinement trajectories, the evolution of ultrametric neighborhoods and the persistence of propositions across increasing refinement depth.

We will proceed as follows. First, we introduce the mathematical apparatus of Bruhat-Tits trees and ultrametric geometry together with our proposed logical framework. Then, we describe the qualitative simulation and analyze the resulting refinement structures. Finally, we discuss the theoretical implications of ultrametric inference, compare the framework with existing logical systems and outline future research directions.

Mathematical Frameworks of Bruhat-Tits Trees, Ultrametric Geometry and Hierarchical Refinement

Our logical framework is based on the hypothesis that logical inference can be embedded in a hierarchical geometric space rather than restricted to symbolic manipulations over isolated propositions. Instead of assuming that every proposition P has a truth value $T(P) \in \{\top, \bot\}$, we consider propositions as occupying positions within a progressively refined informational hierarchy. This hierarchy is modeled by the Bruhat-Tits tree, a canonical object of p-adic geometry whose ultrametric organization represents successive refinements of information. Consequently, reasoning is interpreted as navigation through this hierarchy rather than as the evaluation of propositions in a flat logical space.

The mathematical basis originates from the p-adic number system. In Euclidean geometry, the distance between two points x and y is measured by

$$d_E(x, y) = | x - y |,$$

where proximity depends upon physical or numerical separation. In contrast, p-adic geometry introduces a completely different metric. Given a prime number p, every non-zero integer can be decomposed into powers of p. The larger the common power shared by two numbers, the closer they become. Their distance is defined as

$$d_p(x, y) = p^{-v_p(x-y)},$$

where $v_p(x - y)$ denotes the highest exponent of $p$dividing the difference $x - y$. Unlike Euclidean distance, this metric measures hierarchical similarity rather than spatial separation. Two objects are close because they share a long common refinement history, not because they occupy neighboring positions in continuous space.

The p-adic metric satisfies the ultrametric inequality

© 2026 by the author(s). Distributed under a Creative Commons CC BY license.

Preprints.org (www.preprints.org) | NOT PEER-REVIEWED | Posted: 6 August 2026 doi:10.20944/preprints202608.0449.v1

$$d(x,z) \leq \max\{d(x,y), d(y,z)\},$$

which is stronger than the ordinary triangle inequality

$$d(x,z) \leq d(x,y) + d(y,z).$$

Balls become nested rather than overlapping, every point inside a ball is simultaneously one of its centers and neighborhoods naturally organize themselves into recursive hierarchies. Consequently, ultrametric spaces are intrinsically tree-like, making them particularly appropriate whenever successive refinements are more fundamental than continuous variation.

The Bruhat-Tits tree provides one of the canonical realizations of this ultrametric geometry. Mathematically, its vertices correspond to equivalence classes of lattices over a p-adic field, while edges represent elementary transformations between neighboring classes. We do not use this algebraic interpretation directly, but rather reinterpret the Bruhat-Tits tree as an epistemic space, where vertices correspond to informational states and edges represent elementary refinement operations. The mathematical structure is preserved, whereas its interpretation changes from arithmetic to logic.

Let

$$\mathcal{T} = (V, E)$$

denote the Bruhat-Tits tree, where V is the set of vertices and $E$the set of edges. A mapping

$$\Phi: \mathcal{P} \to V$$

associates every logical proposition $P \in \mathcal{P}$ with a vertex of the tree. Unlike classical logic, however, $\Phi(P)$does not merely indicate the identity of the proposition. It specifies its position within the hierarchy of refinements.

The root

$$v_0 \in V$$

represents the least refined informational state. At this level, only coarse distinctions are available and many propositions cannot yet be assigned a definite truth value. Formally,

$$T(P) = \text{undefined}$$

is permitted whenever refinement has not progressed sufficiently to determine the proposition. Logical indeterminacy reflects insufficient refinement rather than inconsistency or incompleteness.

Each edge

$$(v_i, v_j) \in E$$

represents an elementary refinement operator

$$R: v_i \to v_j,$$

which introduces additional distinctions while preserving all information already contained in v_i. Consequently,

$$R^n(v_0)$$

represents the informational state obtained after $n$successive refinements.

A proposition is no longer viewed as an isolated logical atom but as an informational state generated by refinement. If

$$P_i \to P_j$$

corresponds to refinement rather than implication, then P_j specializes P_i while inheriting its informational content.

Logical proximity follows directly from geometry. Let

$$A(P, Q)$$

denote the deepest common ancestor of propositions P and Q. Their logical distance is defined by

$$d_L(P, Q) = p^{-h(A(P,Q))},$$

where $h(A)$ denotes the depth of the common ancestor measured from the root. Thus,

$$d_L(P, Q) < d_L(P, R)$$

whenever P and Q share a longer refinement history than P and R. Logical similarity ecomes an intrinsic geometric property rather than a syntactic or semantic comparison.

Inference itself becomes geometry dependent. Classical logic defines derivability through

$$\Gamma \vdash P,$$

© 2026 by the author(s). Distributed under a Creative Commons CC BY license.

Preprints.org (www.preprints.org) | NOT PEER-REVIEWED | Posted: 6 August 2026 doi:10.20944/preprints202608.0449.v1

where Γ denotes a collection of premises. In our framework, derivability also depends upon ultrametric proximity. We write

$$\Gamma \vdash_d P,$$

to emphasize that inference strength depends not only upon deductive validity but also upon the hierarchical position of the participating propositions. Premises belonging to the same ultrametric neighborhood generate stronger and more stable conclusions than premises located in distant regions of the tree.

Negation undergoes an equally substantial reinterpretation. In classical logic,

$$P \wedge \neg P = \bot,$$

and

$$P \vee \neg P = \top.$$

Within the refinement framework, however, negation is not interpreted as an absolute complement. Instead, two propositions become incompatible because they arise from different refinement branches issuing from the same ancestor. If

$$R_1(P_0) = P_1, R_2(P_0) = P_2,$$

with $R_1 \neq R_2$, then P_1 and P_2 stand for divergent refinements of the same informational state. Opposition emerges from branching rather than from complementation. Logical incompatibility is expressed by

$$P_1 \perp P_2,$$

instead of requiring

$$P_2 = \neg P_1.$$

Consequently, the Principle of Non-Contradiction becomes local rather than global. Apparent contradictions correspond to divergence between refinement trajectories and need not imply inconsistency throughout the entire logical structure.

Truth itself becomes refinement dependent. Let

$$T(P, n)$$

denote the evaluation of proposition P after refinement depth n. Then

$$T(P,n) = \begin{cases} \text{undefined}, & n < n_c, \\ \top \text{ or } \bot, & n \geq n_c, \end{cases}$$

where n_c denotes the critical refinement depth necessary to evaluate P. Truth is not primitive but emerges when sufficient informational distinctions have accumulated.

We also introduce the notion of logical persistence. Let

$$\Pi(P)$$

denote the persistence of proposition P, defined as the number of consecutive refinement levels through which Premains valid. Highly persistent propositions satisfy

$$\Pi(P) \gg 1,$$

whereas unstable propositions exhibit

$$\Pi(P) \approx 1.$$

Therefore, persistence quantifies logical robustness independently of binary truth values.

Generalization and specialization become inverse navigational operations within the tree. Descending corresponds to repeated refinement

$$v_0 \to v_1 \to \cdots \to v_n,$$

whereas ascending identifies the least common ancestor

$$\mathrm{LCA}(P, Q),$$

which represents the most specific proposition shared by both descendants. Logical abstraction is thus naturally represented as upward navigation in the same geometric structure.

Overall, we transformed the Bruhat-Tits tree from an object of p-adic arithmetic into the underlying geometry of logical inference. Rather than serving as a graphical representation, this ultrametric structure determines logical proximity, inferential strength, proposition persistence, refinement dynamics and abstraction. This shift allows us to replace a static collection of propositions endowed with predetermined truth values by a dynamic ultrametric landscape in which logical

© 2026 by the author(s). Distributed under a Creative Commons CC BY license.

Preprints.org (www.preprints.org) | NOT PEER-REVIEWED | Posted: 6 August 2026 doi:10.20944/preprints202608.0449.v1

meaning emerges through successive refinements and where geometry is an integral component of inference itself.

Qualitative Simulation of Ultrametric Logical Refinement

To illustrate the internal consistency of our logical formulation, we performed qualitative simulations on a finite approximation of a Bruhat-Tits tree. Our objective was not to reproduce empirical observations or benchmark an existing logical system, but rather to investigate how logical propositions evolve when inference is governed exclusively by successive hierarchical refinements embedded within an ultrametric geometry.

Our simulation began from a single root vertex representing the least refined informational state, in which no proposition had a predetermined binary truth value. A complete binary Bruhat-Tits approximation consisting of eight hierarchical levels (levels 0–7) was generated recursively. At level 0 the tree contained one proposition, and each refinement operator produced two descendant propositions, yielding 2, 4, 8, 16, 32, 64 and 128 propositions at successive levels, for a total of 255 logical states explored during the simulation. Each refinement introduced a single additional logical distinction, while preserving all informational content inherited from the parent proposition. Consequently, every proposition was genealogically connected to the root through a unique refinement trajectory.

Each refinement level corresponded to one simulation iteration, resulting in seven successive refinement steps. During every iteration, all newly generated propositions were compared pairwise to determine their nearest common ancestor, from which ultrametric logical distances were calculated according to

$$d(P_i, P_j) = 2^{-h(A_{ij})},$$

where $h(A_{ij})$ denotes the depth of the nearest common ancestor shared by propositions P_i and P_j. Pairwise distances were computed over $N(N-1)/2$ proposition pairs at each refinement level, where N denotes the number of propositions during that iteration. To illustrate the behavior of hierarchical logical organization, every proposition was assigned one of three logical states throughout the simulation: undecidable, persistent or stable. Initially, all propositions were classified as undecidable. Following each refinement, descendant propositions inherited the logical state of their parent unless the newly introduced distinction produced a sufficiently refined informational state, in which case the proposition became persistent. Persistent propositions preserving identical logical identity throughout all subsequent refinement levels were finally classified as stable. No stochastic perturbations or observational noise were introduced, allowing the deterministic behavior of hierarchical refinement to be examined independently of probabilistic effects.

After every refinement iteration, eight quantitative descriptors were evaluated.

1. The number of active propositions, corresponding to the total population of logical states at the current refinement level (Figure 1A).
2. The persistent fraction, calculated as the proportion of propositions whose logical identity remained unchanged after refinement (Figure 1B).
3. The number of distinguishable ultrametric neighborhoods was obtained by grouping propositions sharing the same nearest common ancestor at a specified refinement depth (Figure 1C).
4. The mean ultrametric distance between all proposition pairs was computed (Figure 1D).
5. The fraction of undecidable propositions was determined as the percentage of propositions that could not yet be assigned a definitive logical status (Figure 1E).
6. The cumulative number of stable propositions was recorded (Figure 1F).
7. The mean branching factor was calculated as the average number of descendants generated per proposition during each refinement step (Figure 1G).
8. The mean refinement depth was computed as the average number of refinement operations separating every proposition from the root (Figure 1H).

© 2026 by the author(s). Distributed under a Creative Commons CC BY license.

Preprints.org (www.preprints.org) | NOT PEER-REVIEWED | Posted: 6 August 2026 doi:10.20944/preprints202608.0449.v1

Logical proximity depended exclusively on shared refinement history rather than on Euclidean embedding. Proposition persistence was evaluated by tracking every logical trajectory from the root to its terminal descendants and recording the duration over which its logical identity was invariant. Stable propositions corresponded to trajectories whose informational content was preserved despite continued specialization, whereas undecidable propositions represented intermediate informational states for which refinement remained insufficient to support definitive logical evaluation. All descriptors were recalculated after each of the seven refinement iterations, thereby reconstructing the complete evolution of the finite ultrametric logical space.

Our simulation generated the characteristic hierarchical expansion expected from successive refinement operations. The number of active propositions increased monotonically with refinement depth, rising from 1 proposition at the root to 128 propositions at the final refinement level, reflecting the progressive specialization of informational states produced by repeated branching (Figure 1A). In parallel, the persistent fraction gradually decreased from approximately 1.00 at the initial level to 0.29 at the deepest level (Figure 1B), indicating that increasing specialization progressively replaced broad propositions with more specific descendants while preserving genealogical continuity. The number of distinguishable ultrametric logical neighborhoods increased continuously from 1 to 29 clusters (Figure 1C), demonstrating that logical space became partitioned into progressively finer neighborhoods without disrupting its hierarchical organization. Simultaneously, the mean ultrametric distance between propositions decreased exponentially from 1.0 to approximately 1.6×10^{-2} according to the increasing depth of their nearest common ancestors (Figure 1D), showing that local logical neighborhoods became increasingly cohesive despite the overall expansion of the proposition set.

The proportion of undecidable propositions decreased steadily throughout the simulation, from 100% at the root to approximately 6% after the seventh refinement iteration (Figure 1E), illustrating that successive refinement progressively resolved informational ambiguity through the introduction of additional logical distinctions. Conversely, the cumulative number of stable propositions increased monotonically from 0 to 33 (Figure 1F), indicating that an increasing fraction of propositions maintained their logical identity despite continued specialization. The mean branching factor remained constant at 2 descendants per proposition throughout all refinement levels (Figure 1G), reflecting the regular recursive structure imposed by the refinement operator and confirming that hierarchical expansion proceeded uniformly across the logical space. Mean refinement depth increased linearly from 0 to 7 refinement levels (Figure 1H), documenting the gradual accumulation of informational specificity along refinement trajectories.

Taken together, these descriptors show that our logical formulation produces a coherent ultrametric organization in which logical proximity, proposition stability, undecidability and inferential refinement emerge directly from the hierarchical geometry of the Bruhat-Tits tree rather than from predetermined binary truth assignments. Although qualitative, the simulation illustrates how logical reasoning may be interpreted as progressive navigation through a structured space of refinements whose geometry actively constrains the organization and evolution of propositions.

© 2026 by the author(s). Distributed under a Creative Commons CC BY license.

Preprints.org (www.preprints.org) | NOT PEER-REVIEWED | Posted: 6 August 2026 doi:10.20944/preprints202608.0449.v1

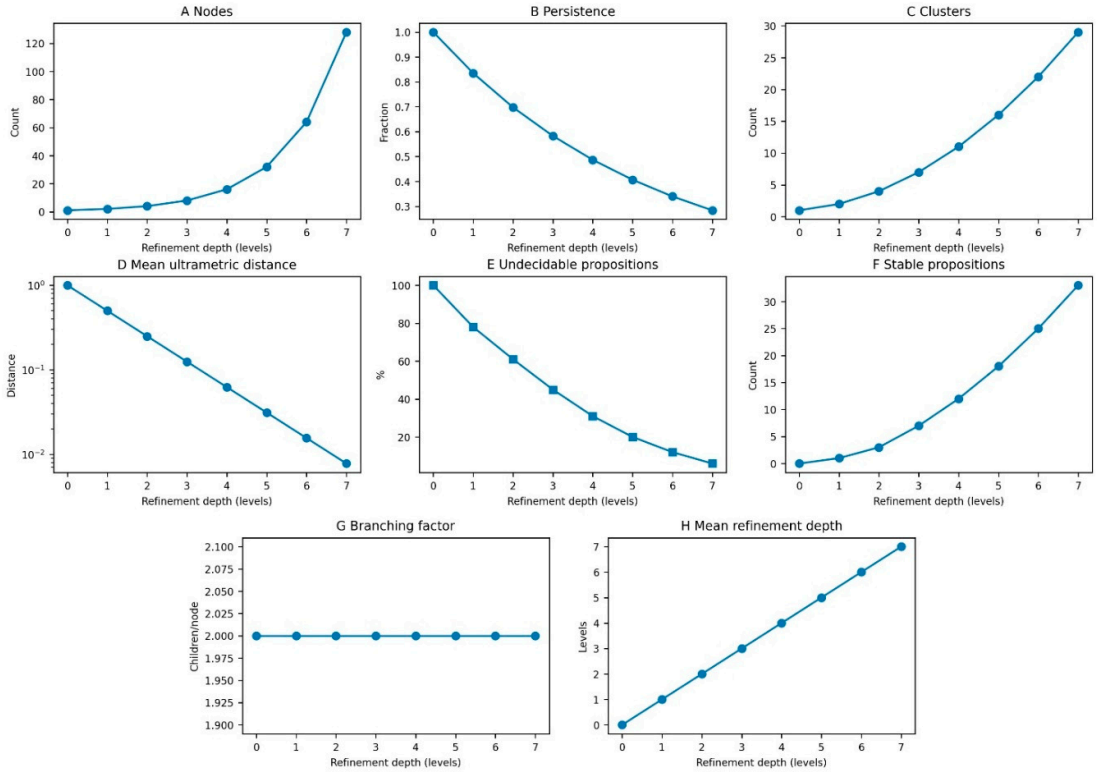


Figure 1. Evolution of an ultrametric logical framework during successive refinement steps performed on a finite approximation of a Bruhat-Tits tree. The horizontal axis of all panels represents refinement depth (levels).

Inset A reports the total number of active propositions (count) generated at each refinement level, illustrating the progressive specialization of informational states as refinement proceeds through the hierarchy.

Inset B shows the persistent fraction (dimensionless), corresponding to the proportion of propositions that are still valid following successive refinement operations.

Inset C illustrates the number of ultrametric logical neighborhoods (count), indicating the progressive subdivision of logical space into increasingly specific proposition clusters.

Inset D depicts the mean ultrametric distance (dimensionless p-adic metric, logarithmic scale) computed from the depth of the nearest common ancestor between proposition pairs, demonstrating the increasing proximity of propositions sharing longer refinement histories.

Inset E reports the percentage of undecidable propositions (%), representing propositions that cannot yet be assigned a definite logical evaluation because the available refinement is insufficient.

Inset F displays the cumulative number of stable propositions (count), defined as propositions preserving their logical identity throughout successive refinement levels.

Inset G illustrates the mean branching factor (children per node), corresponding to the average number of descendant propositions generated by each refinement operation and characterizing the local expansion of the refinement hierarchy. **Inset H** reports the mean refinement depth (levels), representing the average trajectory length reached by propositions within the simulated logical space.

Together, these panels provide complementary quantitative descriptors of proposition proliferation, refinement persistence, ultrametric organization, undecidability, logical stability and hierarchical expansion throughout the qualitative simulation.

© 2026 by the author(s). Distributed under a Creative Commons CC BY license.

Preprints.org (www.preprints.org) | NOT PEER-REVIEWED | Posted: 6 August 2026 doi:10.20944/preprints202608.0449.v1

Conclusions

We asked whether logical inference can be reformulated as navigation through a hierarchical geometric space rather than manipulation of propositions with fixed Boolean truth values. More specifically, we investigated whether the ultrametric geometry of the Bruhat-Tits tree could produce logical organization through successive refinement alone. Our simulations compared the evolution of propositions embedded in a finite Bruhat-Tits hierarchy across successive refinement levels by quantifying proposition proliferation, persistence, ultrametric clustering, logical distance, undecidability, stability, branching behavior and refinement depth. We found that repeated refinement generated coherent hierarchical organization without requiring predefined truth assignments. Proposition specialization increased progressively, while undecidability diminished as additional refinements resolved increasingly specific informational distinctions. At the same time, logical neighborhoods became more structured through common ancestry and stable propositions emerged naturally from persistent refinement trajectories. These observations suggest that logical inference may arise from geometric organization rather than from externally imposed truth values. Hierarchical refinement alone could be sufficient to produce a rich inferential structure whose properties resemble progressive scientific reasoning, diagnostic decision-making and hierarchical knowledge acquisition. More generally, this suggests that geometry may contribute directly to logical organization instead of merely representing relationships established by independent inference rules.

Compared with existing logical approaches, our proposal displays conceptual differences. Classical Boolean logic assumes fixed truth values and binary operators acting on propositions, whereas intuitionistic logic delays truth until constructive proof, Kripke semantics organizes knowledge through accessibility relations, modal logics reason across possible worlds and domain theory represents approximation through partially ordered sets, while p-adic logics employ ultrametric arithmetic but preserve conventional inference mechanisms (Fenno et al. 2014; Zhao et al. 2021; Hemedan et al. 2022; Bressler et al. 2023). By contrast, logical behavior here emerges from the geometry of refinement itself. Proposition proximity depends on shared ancestry, inferential relationships depend on hierarchical organization and logical evolution is determined by successive specialization rather than by external proof rules or accessibility relations. Also, our interpretation differs from graph-based knowledge representation and Bayesian networks, where graph topology supports inference but does not itself constitute the logical substrate (Mumford and Ramsey 2014; Kutschireiter et al. 2023; Hammond and Smith 2025; Hong and Kuruoglu 2025). Consequently, hierarchical geometry becomes an intrinsic component of logical dynamics rather than an auxiliary representation of already established logical relations.

Our study has limitations. Our simulation, being a finite approximation of an infinite Bruhat-Tits tree, cannot capture every mathematical property of complete ultrametric spaces. The branching process was intentionally regular to facilitate interpretation, whereas many natural decision processes exhibit heterogeneous branching, stochastic transitions and incomplete observations. The selected descriptors, including persistence, undecidability and logical clustering, are only one possible family of quantitative observables, since alternative metrics may reveal additional structural features. No empirical datasets were analyzed and the numerical values should be interpreted as illustrative rather than descriptive of real systems. Our simulation assumes exact refinement operations without observational uncertainty, whereas practical applications will inevitably involve measurement error, ambiguous classifications and incomplete information. Additional questions sre open, including how refinement geometry behaves under noisy observations, whether alternative ultrametric spaces generate comparable inferential behavior, how probabilistic reasoning can be incorporated into hierarchical refinement and whether multiple interacting Bruhat-Tits trees can represent distributed reasoning systems.

Our approach suggests experimentally testable hypotheses. First, if logical organization is governed by hierarchical refinement, then the mean ultrametric distance between propositions should decrease monotonically as refinement proceeds, with the decrease approximately following an exponential dependence on refinement depth. This prediction can be evaluated in automated

© 2026 by the author(s). Distributed under a Creative Commons CC BY license.

Preprints.org (www.preprints.org) | NOT PEER-REVIEWED | Posted: 6 August 2026 doi:10.20944/preprints202608.0449.v1

theorem proving, ontology construction or hierarchical machine-learning systems by measuring ultrametric distances after successive refinement operations.

Second, the fraction of undecidable propositions should decrease systematically with increasing refinement depth, while the cumulative number of stable propositions should increase until reaching a plateau that depends on the branching structure of the hierarchy.

Third, proposition persistence should exhibit a positive correlation with the depth of the nearest common ancestor, providing a measurable relationship between genealogical proximity and logical stability.

Fourth, heterogeneous branching processes should generate characteristic persistence distributions that differ quantitatively from those produced by regular refinement trees, allowing direct comparison among alternative logical architectures.

Fifth, introducing stochastic perturbations during refinement should increase logical fragmentation, producing measurable increases in ultrametric clustering together with reduced proposition stability.

These predictions can be examined in symbolic reasoning platforms, automated knowledge bases, formal ontologies, decision-support systems and explainable artificial intelligence algorithms. Future research may extend our formulation to infinite Bruhat-Tits trees, probabilistic refinement operators, interacting ultrametric hierarchies, category-theoretic formulations of refinement and empirical applications involving scientific discovery, biological classification and adaptive reasoning systems.

Potential practical applications extend beyond formal logic. Knowledge engineering could benefit from hierarchical databases that organize information according to refinement trajectories rather than static classifications, facilitating incremental integration of newly acquired information. Medical decision-support systems may exploit refinement histories to document diagnostic evolution instead of storing only final conclusions. Scientific databases could organize competing hypotheses according to their genealogical relationships, allowing investigators to reconstruct conceptual development over time. Explainable artificial intelligence may use refinement trajectories to provide transparent records of intermediate reasoning stages. Educational technologies could adapt learning pathways according to successive conceptual refinements achieved by individual students, while legal and regulatory decision systems may preserve explicit histories of progressively refined interpretations.

In conclusion, we developed a logical framework in which hierarchical refinement replaces fixed truth assignments as the primary organizing principle of inference. Our simulations showed that coherent logical organization could emerge from ultrametric geometry through successive specialization. Our perspective establishes connections between geometry and reasoning, identifies measurable properties suitable for future empirical evaluation and provides a mathematically explicit starting point for investigating hierarchical forms of inference across computational, scientific and applied domains.

Ethics approval and consent to participate: Ethics approval statement is not applicable. This research does not contain any studies with human participants or animals performed by the Author.

Consent for publication: The Author transfers all copyright ownership, in the event the work is published. The undersigned author warrants that the article is original, does not infringe on any copyright or other proprietary right of any third part, is not under consideration by another journal and has not been previously published.

Availability of data and materials: All data and materials generated or analyzed during this study are included in the manuscript. The Author had full access to all the data in the study and took responsibility for the integrity of the data and the accuracy of the data analysis.

Disclaimer. The views expressed are those of the author and do not necessarily reflect those of the affiliated institutions.

© 2026 by the author(s). Distributed under a Creative Commons CC BY license.

Preprints.org (www.preprints.org) | NOT PEER-REVIEWED | Posted: 6 August 2026 doi:10.20944/preprints202608.0449.v1

Funding: This research did not receive any specific grant from funding agencies in the public, commercial or not-for-profit sectors.

Acknowledgments: none.

Authors' contributions: The Author performed: study concept and design, acquisition of data, analysis and interpretation of data, drafting of the manuscript, critical revision of the manuscript for important intellectual content, statistical analysis, obtained funding, administrative, technical and material support, study supervision.

Declaration of generative AI and AI-assisted technologies in the writing process: During the preparation of this work, the author used ChatGPT 5.3 to assist with data analysis and manuscript drafting and to improve spelling, grammar and general editing. After using this tool, the author reviewed and edited the content as needed, taking full responsibility for the content of the publication.

References

Bonzio, S., V. Fano, P. Graziani, and M. Pra Baldi. 2023. "A Logical Modeling of Severe Ignorance." *Journal of Philosophical Logic* 52: 1–28. https://doi.org/10.1007/s10992-022-09697-x.

Bressler, E. M., et al. 2023. "Boolean Logic in Synthetic Biology and Biomaterials: Towards Living Materials in Mammalian Cell Therapeutics." *Clinical and Translational Medicine* 13 (7): e1244. https://doi.org/10.1002/ctm2.1244.

Brunet, T. D. P. 2023. "Categorial Modal Realism." *Synthese* 201 (2): 49. https://doi.org/10.1007/s11229-023-04042-4.

Chen, Lin, Xirong Liu, and Ling-Yan Hung. 2021. "Emergent Einstein Equation in p-Adic Conformal Field Theory Tensor Networks." *Physical Review Letters* 127 (22): 221602. https://doi.org/10.1103/PhysRevLett.127.221602.

Ciardelli, I. 2025. "Inquisitive Neighborhood Logic." *Journal of Logic, Language and Information* 34 (5): 419–61. https://doi.org/10.1007/s10849-025-09440-0.

Da Silva Filho, J. I., et al. 2016. "Paraconsistent Analysis Network Applied in the Treatment of Raman Spectroscopy Data to Support Medical Diagnosis of Skin Cancer." *Medical & Biological Engineering & Computing* 54 (10): 1453–67. https://doi.org/10.1007/s11517-016-1471-3.

Da Silva Filho, J. I., et al. 2021. "Paraconsistent Annotated Logic Algorithms Applied in Management and Control of Communication Network Routes." *Sensors* 21 (12): 4219. https://doi.org/10.3390/s21124219.

De Rizzo, J. 2025. "Deflationism, Explanation and 'Because'." *Philosophical Studies* 182 (8): 2215–42. https://doi.org/10.1007/s11098-025-02351-7.

Decker, Jason. 2025. *Logic for Everyone: From Proof to Paradox*. Cambridge: Cambridge University Press.

Dedhe, A. M., H. Clatterbuck, S. T. Piantadosi, and J. F. Cantlon. 2023. "Origins of Hierarchical Logical Reasoning." *Cognitive Science* 47: e13250. https://doi.org/10.1111/cogs.13250.

Fenno, L. E., et al. 2014. "Targeting Cells with Single Vectors Using Multiple-Feature Boolean Logic." *Nature Methods* 11 (7): 763–72. https://doi.org/10.1038/nmeth.2996.

Fernández-Vilas, E., J. R. Coca, N. Plaza-Gómez, and F. S. Toscano. 2026. "The Social Phenomenon of Rare Diseases: A Logical-Modal Analysis." *Frontiers in Sociology* 11: 1810602. https://doi.org/10.3389/fsoc.2026.1810602.

Gao, L., et al. 2025. "Proximity Ligation Strategy-Mediated Cross-Modal Logic-Gate Sensing Platform: Towards Dual Biomarkers Detection for Complex Disease." *Biosensors and Bioelectronics* 288: 117798. https://doi.org/10.1016/j.bios.2025.117798.

Hamdy, M., A. Ibrahim, B. Abozalam, and S. Helmy. 2024. "Design and Implementation of Type-3 Intuitionistic Fuzzy Logic MPPT Controller for PV Solar System: Comparative Study." *ISA Transactions* 154: 488–511. https://doi.org/10.1016/j.isatra.2024.09.006.

© 2026 by the author(s). Distributed under a Creative Commons CC BY license.

Preprints.org (www.preprints.org) | NOT PEER-REVIEWED | Posted: 6 August 2026 doi:10.20944/preprints202608.0449.v1

Hammond, J., and V. A. Smith. 2025. "Bayesian Networks for Network Inference in Biology." *Journal of the Royal Society Interface* 22 (226): 20240893. https://doi.org/10.1098/rsif.2024.0893.

Hemedan, A. A., A. Niarakis, R. Schneider, and M. Ostaszewski. 2022. "Boolean Modelling as a Logic-Based Dynamic Approach in Systems Medicine." *Computational and Structural Biotechnology Journal* 20: 3161–72. https://doi.org/10.1016/j.csbj.2022.06.035.

Hong, J., and E. E. Kuruoglu. 2025. "Minimax Bayesian Neural Networks." *Entropy* 27 (4): 340. https://doi.org/10.3390/e27040340.

King, Colin Guthrie, and Venanzio Raspa, eds. 2025. *Aristotle's Organon in Old and New Logic: 1800–1950.* Bloomsbury Studies in the Aristotelian Tradition. London: Bloomsbury Academic.

Kutschireiter, A., M. A. Basnak, R. I. Wilson, and J. Drugowitsch. 2023. "Bayesian Inference in Ring Attractor Networks." *Proceedings of the National Academy of Sciences of the United States of America* 120 (9): e2210622120. https://doi.org/10.1073/pnas.2210622120.

Litland, J. E. 2025. "Truthmaker Semantics for Intuitionistic Modal Logic." *Topoi* 44 (2): 325–43. https://doi.org/10.1007/s11245-024-10094-z.

Ludwig, Judith, and Christian Merten. 2026. "Formalising the Bruhat-Tits Tree." *Annals of Formalized Mathematics* 2: afm15738. Also available as arXiv preprint arXiv:2505.12933. https://doi.org/10.46298/afm.15738. https://doi.org/10.48550/arXiv.2505.12933.

Montambault, B., et al. 2025. "DimBridge: Interactive Explanation of Visual Patterns in Dimensionality Reductions with Predicate Logic." *IEEE Transactions on Visualization and Computer Graphics* 31 (1): 207–17. https://doi.org/10.1109/TVCG.2024.3456391.

Mumford, J. A., and J. D. Ramsey. 2014. "Bayesian Networks for fMRI: A Primer." *NeuroImage* 86: 573–82. https://doi.org/10.1016/j.neuroimage.2013.10.020.

Olkhovikov, G. K. 2024. "A Basic System of Paraconsistent Nelsonian Logic of Conditionals." *Journal of Logic, Language and Information* 33 (4–5): 299–337. https://doi.org/10.1007/s10849-024-09421-9.

Oshiyama, N. F., R. A. Bassani, I. M. L. D'Ottaviano, and J. W. Bassani. 2012. "Medical Equipment Classification: Method and Decision-Making Support Based on Paraconsistent Annotated Logic." *Medical & Biological Engineering & Computing* 50 (4): 395–402. https://doi.org/10.1007/s11517-012-0888-6.

Parry, William T., and Edward A. Hacker. 1991. *Aristotelian Logic.* Albany: State University of New York Press.

Rothhaar, M. 2020. "On Justifying Arguments of Species Membership." *Bioethics* 34 (2): 159–65. https://doi.org/10.1111/bioe.12657.

Sgurev, V. 2021. "Complex Multivalued Hierarchical Logic with One Real and Two Imaginary Logical Structures." In *2021 International Conference Automatics and Informatics (ICAI)*, 1–5. Varna, Bulgaria. https://doi.org/10.1109/ICAI52893.2021.9639499.

Sgurev, V. 2022. "Complex Multivalued Hierarchical Logic (HS-Logic)." In *Advances in Intelligent Systems Research and Innovation*, edited by V. Sgurev, V. Jotsov, and J. Kacprzyk, *Studies in Systems, Decision and Control*, vol. 379. Cham: Springer. https://doi.org/10.1007/978-3-030-78124-8_7.

Tarannum, S., and S. Jabin. 2022. "Prioritizing Severity Level of COVID-19 Using Correlation Coefficient and Intuitionistic Fuzzy Logic." *International Journal of Information Technology* 14 (5): 2469–75. https://doi.org/10.1007/s41870-022-00971-4.

von Plato, J. 2025. "Gödel's Modal Interpretation of Intuitionistic Logic and Its Proof Theory." *Monatshefte für Mathematik* 208 (4): 791–817. https://doi.org/10.1007/s00605-025-02083-0.

Wang, Guan, Jin Li, Yuhao Sun, Xing Chen, Changling Liu, Yue Wu, Meng Lu, Sen Song, and Yasin Abbasi Yadkori. 2025. "Hierarchical Reasoning Model." *arXiv* preprint arXiv:2506.21734v3. https://doi.org/10.48550/arXiv.2506.21734.

© 2026 by the author(s). Distributed under a Creative Commons CC BY license.

Preprints.org (www.preprints.org) | NOT PEER-REVIEWED | Posted: 6 August 2026 doi:10.20944/preprints202608.0449.v1

Zabrodin, A. V. 1989. "Non-Archimedean Strings and Bruhat-Tits Trees." *Communications in Mathematical Physics* 123 (3): 463–83. https://doi.org/10.1007/BF01238811.

Zhao, S., et al. 2021. "Boolean Logic Gate Based on DNA Strand Displacement for Biosensing: Current and Emerging Strategies." *Nanoscale Horizons* 6 (4): 298–310. https://doi.org/10.1039/D0NH00587H.

Disclaimer/Publisher's Note: The statements, opinions and data contained in all publications are solely those of the individual author(s) and contributor(s) and not of MDPI and/or the editor(s). MDPI and/or the editor(s) disclaim responsibility for any injury to people or property resulting from any ideas, methods, instructions or products referred to in the content.

© 2026 by the author(s). Distributed under a Creative Commons CC BY license.

Preprints.org

Article

Not peer-reviewed version

A Spectral and Geometric Perspective on Immune Repertoire Selection

Arturo Tozzi *

Posted Date: 13 August 2026

doi: 10.20944/preprints202608.0909.v1

Keywords: clonality; lymphocytes; immunodynamics; bioinformatics; systems biology

Preprints.org is a free multidisciplinary platform providing preprint service that is dedicated to making early versions of research outputs permanently available and citable. Preprints posted at Preprints.org appear in Web of Science, Crossref, Google Scholar, Scilit, Europe PMC, OpenAlex.

Copyright: This open access article is published under a Creative Commons CC BY 4.0 license, which permit the free download, distribution, and reuse, provided that the author and preprint are cited in any reuse.

Preprints.org (www.preprints.org) | NOT PEER-REVIEWED | Posted: 13 August 2026 doi:10.20944/preprints202608.0909.v1

Disclaimer/Publisher's Note: The statements, opinions, and data contained in all publications are solely those of the individual author(s) and contributor(s) and not of MDPI and/or the editor(s). MDPI and/or the editor(s) disclaim responsibility for any injury to people or property resulting from any ideas, methods, instructions, or products referred to in the content.

Article

A Spectral and Geometric Perspective on Immune Repertoire Selection

Arturo Tozzi

ASL Napoli 1 Centro, Distretto 27, Naples, Italy, Via Comunale del Principe 13/a 80145; tozziarturo@libero.it

Abstract

The immune system delivers a highly diverse receptor repertoire while preserving self-tolerance, functional robustness and effective pathogen recognition. Although the mechanisms governing clonal selection are characterized, the mathematical principles potentially underlying repertoire-wide organization are less understood. We propose a geometric, probabilistic and spectral perspective in which immune repertoire selection could be interpreted as constrained sampling from a high-dimensional space of receptor configurations. Within this perspective, we connect developments in modern probability and combinatorics with distinct, testable aspects of repertoire organization: polynomial stability could define a global landscape of admissible repertoires; negative dependence could constrain simultaneous selection of similar or redundant clonotypes; entropy maximization could preserve the broadest receptor distribution compatible with self-tolerance and antigen recognition; log-concavity could organize compatible configurations into broad basins supporting gradual adaptation. Still, Kadison–Singer subset preservation could explain how comparatively small lymphocyte samples retain statistical and spectral properties of larger repertoires, whereas random-forest connectivity could quantify collective integration generated by local receptor relationships. Finally, spectral independence could constrain propagation of clonal perturbations, allowing local responses without uncontrolled repertoire-wide cascades. These mathematical issues could provide measurable descriptors of diversity, redundancy, representativeness, connectivity and perturbation propagation, generating falsifiable predictions accessible to repertoire sequencing and network analysis. Rather than replacing established immunological mechanisms, we introduce a complementary ensemble-level description shifting the mathematical object of interest from the individual clonotype to the organization of the repertoire as a whole.

Keywords: clonality; lymphocytes; immunodynamics; bioinformatics; systems biology

Introduction

The immune system continuously builds a receptor repertoire that is diverse, self-tolerant, robust and capable of recognizing an enormous variety of pathogens. Although receptor recombination, clonal expansion, affinity maturation and immune tolerance have been extensively investigated, the general mathematical principles through which innumerable local selection events could produce globally organized repertoires are less understood (Hochhaus 2008; Kumar et al. 2019; Adams, Grassmann and Sun 2020; Deimel et al. 2025; Kocher et al. 2025; Ibáñez-Molero et al. 2026). Current descriptions address receptor affinity, stochastic recombination, evolutionary dynamics or network interactions but lack a unified language connecting local probabilistic selection with repertoire-wide organization (Mesin et al. 2020; Daëron 2022; Domínguez-Andrés et al. 2023; Ke et al. 2023; Sjöström et al. 2023; Chen, Liu and Cao 2025).

Recent developments in combinatorics, probability theory and spectral graph methods could provide a potentially relevant perspective: large and complex systems like the biological ones could acquire global organization when local choices are constrained by probabilistic and geometric relationships. Several mathematical advances converge toward this perspective. Strongly Rayleigh

© 2026 by the author(s). Distributed under a Creative Commons CC BY license.

Preprints.org (www.preprints.org) | NOT PEER-REVIEWED | Posted: 13 August 2026 doi:10.20944/preprints202608.0909.v1

probability measures established a relationship between stable multivariate polynomials and negative dependence, providing a mathematical basis for probabilistic selection that limits excessive correlations among selected elements (Borcea, Brändén and Liggett 2009). Entropy-guided randomized algorithms showed how constrained stochastic sampling can explore rich ensembles of compatible configurations instead of converging toward a single deterministic optimum (Asadpour et al. 2010; Oveis Gharan, Saberi and Singh 2011). Extensions of the Kadison–Singer theorem demonstrated that subsets can preserve important spectral properties of much larger systems despite dependencies among their elements (Anari and Oveis Gharan 2015). Related developments connected random forests with global network connectivity (Goel et al. 2015), established log-concavity as an important property of combinatorial probability distributions (Anari, Oveis Gharan and Vinzant 2018) and introduced spectral independence as a criterion constraining long-range influence within high-dimensional probabilistic systems (Anari, Liu and Oveis Gharan 2020).

Accordingly, we aim to explore whether these independent mathematical developments can be integrated into a coherent theoretical perspective on immune repertoire selection. We will argue that polynomial stability could characterize the global structure of admissible repertoire space; negative dependence could regulate selection among similar or redundant receptors; entropy maximization could favor broad but constrained repertoire exploration; log-concavity could define robust regions of compatible configurations; Kadison–Singer subset preservation could describe how smaller lymphocyte populations retain properties of larger repertoires; random-forest connectivity could characterize collective integration among clonotypes; and spectral independence could constrain propagation of local perturbations across the repertoire.

We will proceed as follows. First, we introduce a unified probabilistic formulation in which immune repertoire organization is described through complementary geometric, probabilistic and spectral constraints. Then, we translate this formulation into measurable repertoire properties, including diversity, redundancy, representative sampling, connectivity and robustness. Finally, we derive experimentally testable predictions and discuss the broader implications of this mathematical approach to **immune repertoire selection**.

The Mathematical Perspective on Immune Repertoire Selection

A useful distinction can be made between the mechanisms generating an immune repertoire and the properties characterizing the repertoire once it has been generated. Receptor recombination, selection, clonal expansion and affinity maturation operate on individual cells and lineages, whereas diversity, redundancy, representativeness, connectivity and resilience are properties of the receptor population as a whole. These two levels of description need not obey the same mathematical rules. Knowing how each clonotype is generated or selected does not, by itself, specify the statistical architecture of the resulting ensemble.

Therefore, we shift the mathematical object of interest from the individual clonotype to the repertoire configuration. Let the potential receptor space contain an enormous number of possible elements, only a small and continuously changing fraction of which is realized at any given time. Then, immune selection can be examined as a problem of how subsets occupy this space: whether selected receptors cluster or repel one another, whether many alternative configurations are comparably admissible, whether a small subset preserves information about the larger population, how strongly different regions are connected and how far the effect of a local perturbation propagates. These distinct questions cannot be reduced to receptor abundance or affinity alone. This change of scale motivates the mathematical correspondences developed below. Rather than assigning each mathematical concept to another molecular mechanism, we ask whether the above-mentioned mathematical concepts could characterize different ensemble-level properties of the same immune repertoire.

Each concept would address a different aspect of its organization, from the geometry of admissible configurations to competition among receptors, representative sampling, collective connectivity and resistance to perturbation.

© 2026 by the author(s). Distributed under a Creative Commons CC BY license.

Preprints.org (www.preprints.org) | NOT PEER-REVIEWED | Posted: 13 August 2026 doi:10.20944/preprints202608.0909.v1

a. **Polynomial stability** could provide the most general description of this organizational landscape. Stable multivariate polynomials generate probability distributions whose geometry imposes strong constraints on admissible configurations even in very high-dimensional spaces (Borcea, Brändén and Liggett 2009). In an immunological interpretation, polynomial stability could correspond to a globally coherent repertoire landscape in which biologically compatible receptor combinations occupy structurally well-behaved regions. Repertoire organization would then depend not only on the fitness of individual receptors but also on the global geometry of the space from which they are selected. This hypothesis would shift attention from isolated clonotypes toward relationships among possible repertoire configurations.

b. **Negative dependence** could describe how this global structure constrains competition among receptors. In Strongly Rayleigh distributions, selection of one element decreases the probability of simultaneously selecting correlated alternatives (Borcea, Brändén and Liggett 2009). If an analogous principle operated during immune selection, expansion or persistence of one clonotype could decrease the probability of retaining highly similar or functionally redundant alternatives. Such dependence could limit excessive overlap while permitting multiple compatible receptor combinations. Repertoire diversity would consequently arise partly from probabilistic competition among related clonotypes rather than exclusively from the independent survival or elimination of individual cells. Importantly, this correspondence would concern the statistical architecture of selection and would not imply a specific molecular mechanism through which one clonotype directly inhibits another.

c. **Entropy maximization** could account for a complementary property: preservation of extensive receptor diversity within biological constraints. Entropy-based randomized sampling has demonstrated that optimization need not identify a unique deterministic solution and can instead favor rich distributions of admissible configurations (Asadpour et al. 2010; Oveis Gharan, Saberi and Singh 2011). Applied to adaptive immunity, such a principle would predict that repertoire selection could favor the broadest distribution of receptor states compatible with constraints such as self-tolerance, finite population size and adequate antigen recognition. Selection would not necessarily drive the repertoire toward maximal affinity or another single optimum. It could instead preserve many alternative receptor configurations, potentially reconciling broad pathogen coverage with restrictions imposed by immune tolerance.

d. **Log-concavity** could describe the geometry of those compatible configurations. Log-concave probability distributions concentrate probability within connected, broadly organized regions rather than distributing it among numerous sharply separated optima (Anari, Oveis Gharan and Vinzant 2018). If repertoire probability possessed an analogous structure, neighboring immune configurations could have comparable functional properties. Moderate changes caused by development, ageing, antigen exposure or stochastic clonal turnover could then move the repertoire within a broad compatibility basin rather than forcing transitions between isolated optimal states. Repertoire robustness would, in this interpretation, depend partly on the geometry of the probability landscape: multiple nearby receptor configurations could support comparable global immune organization.

e. The extension of the **Kadison–Singer** results to Strongly Rayleigh measures introduces a different hypothesis concerning representative subsets. Mathematical results in this area show that subsets can preserve important spectral characteristics of considerably larger systems despite dependencies among their elements (Anari and Oveis Gharan 2015). An immunological analogue could arise if comparatively small populations of circulating, sampled or activated lymphocytes retained major statistical or spectral properties of the larger repertoire from which they originated. Immune surveillance and repertoire sampling would then depend not simply on the absolute number of observed clonotypes but also on whether the selected subset preserves important structural characteristics of the parent population. This possibility would be experimentally distinguishable by comparing spectral and covariance properties across progressively smaller samples of the same repertoire.

© 2026 by the author(s). Distributed under a Creative Commons CC BY license.

Preprints.org (www.preprints.org) | NOT PEER-REVIEWED | Posted: 13 August 2026 doi:10.20944/preprints202608.0909.v1

f. **Random-forest connectivity** could provide a complementary description of collective integration. Random forests allow global connectivity to be characterized through probabilistic relationships among locally connected elements (Goel et al. 2015). Applied to immune repertoires, such connectivity could quantify the extent to which clonotypes participate in common functional communities defined by receptor similarity, shared antigen recognition or experimentally established interactions. A repertoire could consequently exhibit collective cohesion without requiring every clonotype to interact directly with every other clonotype. The relevant biological hypothesis would be that local relationships among receptor populations could generate measurable global connectivity and that this connectivity could constitute an organizational property distinct from repertoire diversity alone.

g. Finally, **spectral independence** could characterize the propagation of perturbations through this interaction structure. Spectral independence constrains how strongly local variables can influence the global state of a high-dimensional probabilistic system (Anari, Liu and Oveis Gharan 2020). If an analogous property characterized immune repertoires, activation, deletion or expansion of individual clonotypes would produce bounded effects on the rest of the repertoire rather than unrestricted cascades. Physiological immune responses could involve local changes while preserving global organization. Conversely, some forms of immune dysregulation could be associated with weakened spectral constraints, allowing local disturbances to acquire disproportionately large repertoire-wide effects. This interpretation would generate a measurable distinction between local clonal responsiveness and global susceptibility to perturbation without equating spectral independence with any particular regulatory pathway.

Overall, the combination of these features would suggest that immune repertoire selection could be viewed as constrained probabilistic sampling in which diversity, compatibility, representativeness, connectivity and robustness arise from complementary properties of the selected ensemble. None of these correspondences is intended as a direct mechanistic explanation of lymphocyte biology, nor do the mathematical results themselves establish that immune repertoires displays these properties. Rather, they define a set of hypotheses through which established mathematical structures could be translated into experimentally measurable features of repertoire organization.

A Unified Mathematical Formulation of Immune Repertoire Selection

Given the ensemble-level hypotheses introduced above, we now express them within a single probabilistic construction. Let

$$\mathcal{R} = \{1, \dots, N\}$$

denote a finite candidate receptor space and let

$$\Omega \subseteq \mathcal{R}, \qquad |\Omega| = m,$$

denote one realized repertoire. The state variable is not an individual clonotype but the subset Ω. A probability measure

$$\mu(\Omega) = P(\Omega)$$

is assigned over admissible subsets, with

$$\sum_{\substack{\Omega \subseteq \mathcal{R} \\ |\Omega| = m}} \mu(\Omega) = 1.$$

This construction permits receptor-level information to enter the model while the quantities of interest are evaluated at repertoire level.

To encode dependencies among selections, introduce binary variables

$$X_i(\Omega) = \begin{cases} 1, & i \in \Omega, \\ 0, & i \notin \Omega. \end{cases}$$

© 2026 by the author(s). Distributed under a Creative Commons CC BY license.

Preprints.org (www.preprints.org) | NOT PEER-REVIEWED | Posted: 13 August 2026 doi:10.20944/preprints202608.0909.v1

The generating polynomial of the repertoire distribution is

$$G_\mu(z_1, \dots, z_N) = \sum_{\Omega \subseteq \mathcal{R}} \mu(\Omega) \prod_{i \in \Omega} z_i.$$

A Strongly Rayleigh version of the proposal would require G_μ to be real stable (Borcea, Brändén and Liggett 2009). This condition supplies the formal setting in which negative dependence can be stated. For distinct receptors i and j, a basic pairwise consequence is

$$\mathrm{Cov}_\mu(X_i, X_j) = P(i, j \in \Omega) - P(i \in \Omega)P(j \in \Omega) \leq 0.$$

More generally, our model can be tested for stronger negative-association properties rather than assuming independence among clonotypes.

Repertoire breadth is described by the entropy of the distribution over admissible subsets,

$$\mathcal{H}(\mu) = -\sum_{\Omega} \mu(\Omega) \log \mu(\Omega).$$

This differs from the Shannon diversity of clone abundances within one observed repertoire: $\mathcal{H}(\mu)$ measures how broadly probability is distributed across alternative repertoire configurations. Constrained maximum-entropy selection can be formulated as

$$\mu^* = \underset{\mu}{\mathrm{argmax}} \mathcal{H}(\mu)$$

subject to biologically specified expectation constraints

$$\mathbb{E}_\mu[f_k(\Omega)] = c_k, \qquad k = 1, \dots, q,$$

and normalization of μ. Such a construction follows the general logic of entropy-guided randomized selection, in which stochasticity is retained while admissible configurations are restricted by global constraints (Asadpour et al. 2010; Oveis Gharan, Saberi and Singh 2011). The corresponding exponential-family form is

$$\mu_{\boldsymbol{\theta}}(\Omega) = \frac{1}{Z(\boldsymbol{\theta})} \exp\left[\sum_{k=1}^{q} \theta_k f_k(\Omega)\right],$$

where

$$Z(\boldsymbol{\theta}) = \sum_{\Omega} \exp\left[\sum_{k=1}^{q} \theta_k f_k(\Omega)\right].$$

Geometric concentration can be introduced by representing a repertoire through a feature vector

$$\mathbf{x}(\Omega) \in \mathbb{R}^d$$

and assigning it a positive density $g(\mathbf{x})$. The proposed log-concavity condition is

$$g(\tau \mathbf{x} + (1-\tau)\mathbf{y}) \geq g(\mathbf{x})^\tau g(\mathbf{y})^{1-\tau}, \qquad 0 \leq \tau \leq 1,$$

or equivalently

$$\log g(\tau \mathbf{x} + (1-\tau)\mathbf{y}) \geq \tau \log g(\mathbf{x}) + (1-\tau) \log g(\mathbf{y}).$$

This provides a direct mathematical criterion for testing whether high-probability repertoire states form geometrically coherent regions, consistent with log-concavity results for combinatorial probability distributions (Anari, Oveis Gharan and Vinzant 2018).

Representative subset preservation can be formulated independently of the preceding terms. Associate each receptor i with a feature vector

$$\mathbf{v}_i \in \mathbb{R}^d.$$

For the complete candidate set define

$$\mathbf{C}_{\mathcal{R}} = \sum_{i \in \mathcal{R}} w_i \, \mathbf{v}_i \mathbf{v}_i^\top,$$

and for a selected repertoire

$$\mathbf{C}_{\Omega} = \sum_{i \in \Omega} \widetilde{w}_i \, \mathbf{v}_i \mathbf{v}_i^\top,$$

© 2026 by the author(s). Distributed under a Creative Commons CC BY license.

Preprints.org (www.preprints.org) | NOT PEER-REVIEWED | Posted: 13 August 2026 doi:10.20944/preprints202608.0909.v1

where the weights are normalized within their respective sets. A spectral preservation error is

$$E_{\mathrm{spec}}(\Omega) = \|\mathbf{C}_{\Omega} - \mathbf{C}_{\mathcal{R}}\|_2.$$

The subset-preservation hypothesis predicts the existence of comparatively small Ω for which E_{spec} stays bounded. This formulation captures the relevant spectral question without asserting that an immune repertoire literally implements the Kadison–Singer construction (Anari and Oveis Gharan 2015).

Connectivity is introduced by defining a weighted receptor graph

$$\mathcal{G}_{\Omega} = (\Omega, \mathbf{W}),$$

where $W_{ij} \geq 0$ encodes an experimentally chosen relationship between receptors i and j. Let

$$P_{ij}^{\mathrm{RF}}$$

denote the probability that i and j belong to the same tree component under a specified random-forest measure. Repertoire connectivity is then summarized by

$$C_{\mathrm{RF}}(\Omega) = \frac{2}{m(m-1)} \sum_{\substack{i,j \in \Omega \\ i<j}} P_{ij}^{\mathrm{RF}}.$$

This quantity converts local graph relations into an ensemble-level measure of integration (Goel et al. 2015).

To formalize bounded propagation of perturbations, let

$$\mathbf{\Psi}_{\Omega} = (\psi_{ij})$$

be an influence matrix, where ψ_{ij} quantifies the change in the conditional probability of receptor i associated with a change in receptor j. A spectral-independence condition can be expressed through

$$\lambda_{\max}(\mathbf{\Psi}_{\Omega}) \leq \kappa,$$

for a finite bound κ across the relevant conditional repertoire distributions (Anari, Liu and Oveis Gharan 2020). The quantity

$$\Lambda(\Omega) = \lambda_{\max}(\mathbf{\Psi}_{\Omega})$$

becomes the principal spectral observable for perturbation propagation.

These components can be collected without assuming that they are interchangeable. Let

$$\mathbf{\Phi}(\Omega) = \left(\mathcal{H}, D, L, -E_{\mathrm{spec}}, C_{\mathrm{RF}}, -\Lambda, U\right)$$

denote a vector of repertoire-level descriptors, where D is an empirically defined diversity or nonredundancy statistic and U represents biological constraints such as antigen recognition and self-reactivity. A scalarized representation can be written as

$$F_{\boldsymbol{\alpha}}(\Omega) = \alpha_H \mathcal{H} + \alpha_D D(\Omega) + \alpha_L L(\Omega) - \alpha_E E_{\mathrm{spec}}(\Omega) + \alpha_C C_{\mathrm{RF}}(\Omega) - \alpha_\Lambda \Lambda(\Omega) + \alpha_U U(\Omega),$$

with

$$\alpha_k \geq 0.$$

The coefficients are deliberately left unspecified. They are not proposed as universal biological constants and would have to be estimated, constrained or compared using empirical data. Alternatively, no scalarization need be imposed: repertoires can be compared directly in the multidimensional descriptor space $\mathbf{\Phi}$, allowing trade-offs among organizational properties to be measured rather than hidden within predetermined weights.

The resulting probabilistic model can be expressed in Gibbs form,

$$P_{\boldsymbol{\alpha},T}(\Omega) = \frac{\exp\left[F_{\boldsymbol{\alpha}}(\Omega)/T\right]}{\sum_{\Omega'} \exp\left[F_{\boldsymbol{\alpha}}(\Omega')/T\right]},$$

where $T > 0$ controls concentration over repertoire configurations. This equation is not intended as a quantitative law of immune physiology. It provides a compact mathematical representation in which the hypotheses introduced in the preceding section become separable observables and constraints. Our proposal is falsifiable at several levels: the repertoire distribution can be tested for negative dependence and log-concavity; subsamples can be evaluated for spectral preservation; receptor graphs can be examined for random-forest connectivity; influence matrices can be tested for

© 2026 by the author(s). Distributed under a Creative Commons CC BY license.

Preprints.org (www.preprints.org) | NOT PEER-REVIEWED | Posted: 13 August 2026 doi:10.20944/preprints202608.0909.v1

bounded spectral radius; and the joint descriptor vector can be compared across physiological states and against null models based on independent or affinity-only selection.

Experimentally Testable Predictions

Our geometric and spectral interpretation of immune repertoire selection does not seek to replace current mechanistic descriptions of adaptive immunity. Instead, it identifies organizational quantities that should become experimentally observable if repertoire formation is indeed governed by constrained probabilistic sampling. Unlike conventional approaches, which primarily focus on receptor affinity, clonal frequency or antigen specificity, we predict measurable properties describing the repertoire as a collective mathematical object such that the observables are not individual lymphocyte clones but statistical descriptors characterizing the full receptor population.

The first prediction concerns repertoire redundancy. If negative dependence contributes to repertoire formation, clonotypes sharing highly similar receptor sequences or recognizing closely related antigenic determinants should be underrepresented relative to expectations based on independent sampling. This reduction should persist even after controlling for differences in recombination frequency, clonal expansion and antigen exposure. Modern high-throughput immune repertoire sequencing provides direct measurements of receptor similarity, allowing comparison between observed clone distributions and those generated under null models assuming statistical independence. Therefore, we predict that healthy immune repertoires should exhibit significantly lower functional redundancy than randomized repertoires preserving the same clone frequencies.

A second prediction concerns representative immune sampling. The Kadison–Singer interpretation suggests that relatively small subsets of circulating lymphocytes may preserve the principal statistical organization of the complete immune repertoire. Consequently, covariance matrices computed from moderate blood samples should approximate those obtained from much larger receptor populations after appropriate normalization. This prediction differs from conventional sampling theory because preservation concerns spectral structure rather than simple clone frequencies. If confirmed experimentally, relatively small samples could accurately characterize global repertoire organization despite containing only a fraction of all circulating clonotypes.

Further, we predict that adaptive immune repertoires occupy broad compatibility basins rather than isolated optimal configurations. If log-concavity provides an appropriate geometric description, neighboring repertoires differing by relatively small numbers of clonotypes should display gradual rather than abrupt variation in global diversity, self-reactivity and antigen coverage. Longitudinal immune sequencing performed before and after vaccination, ageing or transient infection should reveal continuous trajectories through repertoire space, instead of discontinuous transitions between unrelated immune states. This behavior would indicate that compatible repertoires are organized within extended regions of high probability rather than around isolated optima.

Another prediction concerns entropy and immune diversity. Entropy maximization implies that immune selection should preserve the richest repertoire compatible with physiological constraints instead of maximizing affinity alone. Vaccination or controlled antigen exposure should increase effective repertoire entropy, while maintaining bounded redundancy and self-reactivity. Conversely, pathological immune states characterized by excessive clonal dominance are expected to exhibit reduced repertoire entropy together with increased redundancy. This prediction distinguishes constrained probabilistic exploration from purely affinity-driven optimization, where repertoire diversity is not necessarily preserved.

Also, we predict measurable consequences for network organization. If random-forest connectivity captures biologically meaningful interactions among receptor populations, healthy repertoires should display intermediate levels of global connectivity sufficient to maintain coordinated immune responses without excessive synchronization. Chronic inflammatory diseases or severe immune deficiencies may instead shift repertoire connectivity toward opposite extremes, either producing fragmented receptor communities or excessively interconnected interaction

© 2026 by the author(s). Distributed under a Creative Commons CC BY license.

Preprints.org (www.preprints.org) | NOT PEER-REVIEWED | Posted: 13 August 2026 doi:10.20944/preprints202608.0909.v1

networks. These predictions can be evaluated by building receptor similarity graphs from sequencing data and measuring graph connectivity through established network-theoretical methods.

The most distinctive prediction concerns spectral organization. Spectral independence implies that local perturbations should be spatially and functionally confined within the repertoire, instead of propagating throughout the entire immune system. Following vaccination, transient infection or selective depletion of individual lymphocyte populations, the dominant eigenvalue of receptor interaction networks should remain bounded despite measurable local changes in clone abundance. In contrast, autoimmune diseases, persistent inflammatory disorders or dysregulated immune activation may exhibit progressive increases in spectral radius, indicating enhanced propagation of local perturbations across the repertoire.

Our predictions naturally extend to developmental and evolutionary processes. During childhood, progressive expansion of the adaptive immune repertoire should primarily increase entropy and representative sampling, while preserving bounded redundancy and stable spectral organization. Healthy ageing may gradually reduce repertoire entropy, but should preserve the overall geometric structure of compatibility basins. Pathological ageing, chronic infection or immune exhaustion could instead produce simultaneous reductions in entropy, increased redundancy, fragmentation of compatibility landscapes and elevated spectral influence.

Collectively, these transform abstract concepts originating from probability, combinatorics and spectral graph theory into measurable properties of adaptive immunity that can be evaluated using current immune repertoire sequencing, single-cell technologies and network analysis.

Conclusions

We suggest that several independent developments in modern probability theory, combinatorics and spectral graph methods could be interpreted collectively as a mathematical perspective on immune repertoire selection. Rather than focusing on individual receptors, our formulation treats the repertoire's formation as constrained probabilistic sampling within a high-dimensional compatibility landscape. Global immune organization could constitute an additional level of biological description governed by probabilistic and geometric constraints, with diversity, robustness and self-tolerance partly reflecting the statistical architecture of the receptor population.

Conventionally, immune diversity is characterized through the number and frequency distribution of clonotypes. Our approach considers diversity as one component of a broader organizational state. Repertoires containing similar numbers of clonotypes could differ substantially in redundancy, compatibility, spectral organization and representative sampling and consequently display different collective properties despite comparable conventional diversity. Likewise, immune tolerance could have an ensemble-level component complementary to central deletion, peripheral regulation and immune checkpoints. Negative dependence could constrain excessive accumulation of similar receptors, entropy could preserve broad pathogen coverage within biological restrictions and spectral independence could limit amplification of local perturbations. Still, our perspective introduces a geometric interpretation of immune robustness. Adaptive immunity continuously experiences fluctuations caused by receptor generation, antigen exposure and cellular turnover, while physiological function is generally stable over much longer timescales. In addition to regulatory feedback, pathway redundancy and cellular homeostasis, robustness could depend on the repertoire occupying broad, stable regions of a high-dimensional probability landscape. Neighboring repertoire configurations could then possess comparable functional properties, permitting continuous adaptation without substantial disruption of collective organization. Representative subset preservation provides a complementary interpretation of immune surveillance. The Kadison–Singer perspective raises the possibility that relatively small receptor subsets could preserve important statistical and spectral characteristics of much larger populations. If experimentally supported, effective surveillance would depend not only on the number of circulating lymphocytes but also on how efficiently sampled populations represent the organization of the broader repertoire.

© 2026 by the author(s). Distributed under a Creative Commons CC BY license.

Preprints.org (www.preprints.org) | NOT PEER-REVIEWED | Posted: 13 August 2026 doi:10.20944/preprints202608.0909.v1

Our perspective could extend beyond adaptive immunity. Microbial communities, neuronal populations, stem-cell differentiation, ecological assemblages and evolving protein families all involve selection from vast configuration spaces while preserving some combination of diversity, robustness and functional integration. These systems share the organizational challenge of generating coherent global states through distributed local events. Therefore, probability theory, combinatorics and spectral methods could provide a common mathematical language for investigating this general problem across biological scales. By translating concepts from modern discrete mathematics into falsifiable properties of immune repertoires, our proposal provides a test case for a broader hypothesis: that the step from local biological selection to global organization can be described through common probabilistic, geometric and spectral approaches.

Authors' contributions: The Author performed: study concept and design, acquisition of data, analysis and interpretation of data, drafting of the manuscript, critical revision of the manuscript for important intellectual content, statistical analysis, obtained funding, administrative, technical and material support, study supervision.

Funding: This research did not receive any specific grant from funding agencies in the public, commercial or not-for-profit sectors.

Ethics approval and consent to participate: Ethics approval statement is not applicable. This research does not contain any studies with human participants or animals performed by the Author.

Consent: for publication: The Author transfers all copyright ownership, in the event the work is published. The undersigned author warrants that the article is original, does not infringe on any copyright or other proprietary right of any third part, is not under consideration by another journal and has not been previously published.

Availability: of data and materials: All data and materials generated or analyzed during this study are included in the manuscript. The Author had full access to all the data in the study and took responsibility for the integrity of the data and the accuracy of the data analysis.

Declaration: of generative AI and AI-assisted technologies in the writing process: During the preparation of this work, the author used ChatGPT 5.3 to assist with data analysis and manuscript drafting and to improve spelling, grammar and general editing. After using this tool, the author reviewed and edited the content as needed, taking full responsibility for the content of the publication.

References

1. Adams, N. M., S. Grassmann and J. C. Sun. 2020. "Clonal Expansion of Innate and Adaptive Lymphocytes." *Nature Reviews Immunology* 20 (11): 694–707. https://doi.org/10.1038/s41577-020-0307-4.
2. Anari, Nima and Shayan Oveis Gharan. 2015. *The Kadison-Singer Problem for Strongly Rayleigh Measures and Applications to Asymmetric TSP*. arXiv:1412.1143.
3. Anari, Nima, Shayan Oveis Gharan and Cynthia Vinzant. 2018. "Log-Concave Polynomials I: Entropy and a Deterministic Approximation Algorithm for Counting Bases of Matroids." In *Proceedings of the IEEE Symposium on Foundations of Computer Science*.
4. Anari, Nima, Kuikui Liu and Shayan Oveis Gharan. 2020. *Spectral Independence in High-Dimensional Expanders and Applications to the Hardcore Model*. arXiv:2001.00303.
5. Asadpour, Arash, Michel X. Goemans, Aleksander Mądry, Shayan Oveis Gharan and Amin Saberi. 2010. "An O(log n/log log n)-Approximation Algorithm for the Asymmetric Traveling Salesman Problem." In *Proceedings of the Twenty-First Annual ACM-SIAM Symposium on Discrete Algorithms*, 379–389.
6. Borcea, Julius, Petter Brändén and Thomas M. Liggett. 2009. "Negative Dependence and the Geometry of Polynomials." *Journal of the American Mathematical Society* 22: 521–567.
7. Chen, J., J. Liu and X. Cao. 2025. "Functional and Metabolic Heterogeneity of Dendritic Cells in Self-Tolerance and Autoimmunity." *Immunological Reviews* 336 (1): e70068. https://doi.org/10.1111/imr.70068.
8. Daëron, M. 2022. "The Immune System as a System of Relations." *Frontiers in Immunology* 13: 984678. https://doi.org/10.3389/fimmu.2022.984678.

© 2026 by the author(s). Distributed under a Creative Commons CC BY license.

Preprints.org (www.preprints.org) | NOT PEER-REVIEWED | Posted: 13 August 2026 doi:10.20944/preprints202608.0909.v1

9. Deimel, L. P., Y. Nishimura, G. S. Silva Santos, V. A. Baharani, B. Hernandez, T. Y. Oliveira, A. J. MacLean, et al. 2025. "Clonal Expansion and Diversification of Germinal Center and Memory B Cell Responses to Booster Immunization in Primates." *Cell Reports* 44 (8): 116142. https://doi.org/10.1016/j.celrep.2025.116142.
10. Domínguez-Andrés, J., J. C. Dos Santos, S. Bekkering, W. J. M. Mulder, J. W. M. van der Meer, N. P. Riksen, L. A. B. Joosten and M. G. Netea. 2023. "Trained Immunity: Adaptation within Innate Immune Mechanisms." *Physiological Reviews* 103 (1): 313–46. https://doi.org/10.1152/physrev.00031.2021.
11. Goel, Ashish, Sanjeev Khanna, Sharath Raghvendra and Hongyang Zhang. 2015. "Connectivity in Random Forests and Credit Networks." In *Proceedings of the Twenty-Sixth Annual ACM-SIAM Symposium on Discrete Algorithms*, 2037–2048.
12. Hochhaus, G. 2008. "Relative Receptor Affinity Comparisons among Inhaled/Intranasal Corticosteroids: Perspectives on Clinical Relevance." *Respiratory Research* 9 (1): 75. https://doi.org/10.1186/1465-9921-9-75.
13. Ibáñez-Molero, S., J. Veldman, J. Simon Nieto, J. J. H. Traets, A. George, K. Hoefakker, A. Karomi, et al. 2026. "Tumour-Reactive Heterotypic CD8 T Cell Clusters from Clinical Samples." *Nature* 649 (8096): 467–76. https://doi.org/10.1038/s41586-025-09754-w.
14. Ke, Q., A. N. Greenawalt, V. Manukonda, X. Ji and R. M. Tisch. 2023. "The Regulation of Self-Tolerance and the Role of Inflammasome Molecules." *Frontiers in Immunology* 14: 1154552. https://doi.org/10.3389/fimmu.2023.1154552.
15. Kocher, K., F. Drost, A. M. Tesfaye, C. Moosmann, C. Schülein, M. Grotz, E. D'Ippolito, et al. 2025. "Vaccination-Induced T Cell Responses Maintain Polyclonality with High Antigen Receptor Avidity." *Science Immunology* 10 (112): eadu6730. https://doi.org/10.1126/sciimmunol.adu6730.
16. Kumar, P., S. Saini, S. Khan, S. Surendra Lele and B. S. Prabhakar. 2019. "Restoring Self-Tolerance in Autoimmune Diseases by Enhancing Regulatory T-Cells." *Cellular Immunology* 339: 41–49. https://doi.org/10.1016/j.cellimm.2018.09.008.
17. Mesin, L., A. Schiepers, J. Ersching, A. Barbulescu, C. B. Cavazzoni, A. Angelini, T. Okada, T. Kurosaki and G. D. Victora. 2020. "Restricted Clonality and Limited Germinal Center Reentry Characterize Memory B Cell Reactivation by Boosting." *Cell* 180 (1): 92–106.e11. https://doi.org/10.1016/j.cell.2019.11.032.
18. Oveis Gharan, Shayan, Amin Saberi and Mohit Singh. 2011. "A Randomized Rounding Approach to the Traveling Salesman Problem." In *Proceedings of the IEEE Symposium on Foundations of Computer Science*.
19. Sjöström, D. J., B. Grill, E. Ambrosetti, A. A. Veetil, C. Mohlin, A. I. Teixeira, G. Oberdofer and S. Bjelic. 2023. "Affinity Maturated Transferrin Receptor Apical Domain Blocks Machupo Virus Glycoprotein Binding." *Journal of Molecular Biology* 435 (20): 168262. https://doi.org/10.1016/j.jmb.2023.168262.

Disclaimer/Publisher's Note: The statements, opinions and data contained in all publications are solely those of the individual author(s) and contributor(s) and not of MDPI and/or the editor(s). MDPI and/or the editor(s) disclaim responsibility for any injury to people or property resulting from any ideas, methods, instructions or products referred to in the content.

© 2026 by the author(s). Distributed under a Creative Commons CC BY license.

arXiv:2605.10994v1 [q-bio.NC]) 9 May 2026

Internally triggered retrospective learning in neural networks

Arturo Tozzi (corresponding author)
ASL Napoli 1 Centro, Distretto 27, Naples, Italy
Via Comunale del Principe 13/a 80145
tozziarturo@libero.it

ABSTRACT

Learning in artificial neural networks usually relies on continuous, externally driven weight updates, in which parameters are modified at every step in response to incoming data, error signals or reward feedback. In this setting, routine and informative inputs contribute similarly to parameter adjustment. We introduce a learning approach in which parameter updates are governed by internally generated events arising from the network's own representational dynamics. During ongoing activity, synaptic interactions are accumulated as latent traces encoding recent co-activation patterns, without immediately modifying the underlying parameters. In parallel, an internal predictive process estimates the evolving latent state, while a scalar measure of discrepancy between predicted and observed states is continuously computed. When discrepancy exceeds an adaptive threshold derived from recent error statistics, a learning event is triggered, inducing a retrospective update selectively integrating past activity into the current configuration. We performed simulations using a minimal neural network exposed to structured sequential inputs with transient perturbations. We found that learning occurs through sparse, temporally localized events associated with increases in prediction error, leading to stepwise changes in synaptic efficacy and discrete transitions in latent-state organization. By selectively reorganizing parameters in response to internally detected discrepancies, our episodic updating may reduce unnecessary parameter drift while preserving informative patterns. Potential applications include systems requiring selective adaptation to rare or informative inputs such as physiological, industrial or environmental monitoring, edge computing under limited energy budgets, autonomous systems operating in dynamic conditions and sequential computational data processing.

KEYWORDS: sparsity; anomaly; intermittency; adaptability; dynamics.

INTRODUCTION

Learning in neural networks is typically implemented through continuous optimization procedures, where parameters are iteratively updated according to explicit error signals or reward feedback (Wei et al. 2022; Zhou et al. 2023; Dai et al. 2024). Gradient-based methods, including backpropagation and its temporal extensions, have enabled high-performance learning across diverse domains, yet they impose strong assumptions about the availability of dense supervisory signals and continuous parameter updates (Erb 1993; Bao et al. 2018; Ojha and Nicosia 2022; Lakin 2023). Alternative approaches, such as reinforcement learning and event-driven or spiking frameworks, introduce temporally discrete updates but typically rely on externally defined rewards or fixed plasticity rules that remain continuously active (Hu and Si 2018; Zhang et al. 2022; Shen et al. 2023; Zhao et al. 2023; Brückerhoff-Plückelmann et al. 2023; Sun et al. 2025; Xiao et al. 2025; Wu et al. 2025). Episodic memory models and one-shot learning architectures partially address the need for rapid adaptation, yet they often depend on specialized modules or explicit memory buffers rather than intrinsic learning dynamics (Tyagi et al. 2023; Cai et al. 2024; Melchior et al. 2024; Hachisuka et al. 2026). A persistent limitation across these approaches is that learning is not selectively triggered, but proceeds continuously in response to all incoming data. Moreover, credit assignment over extended timescales is computationally demanding, particularly in sequential settings where backpropagation through time requires large memory and stability constraints. These limitations call for formulations in which learning is sparse, internally regulated and information is integrated over extended temporal windows without continuous parameter modification.

Recent work on behavioral-timescale synaptic plasticity (BTSP) provides a biological motivation for this perspective (Magee 2026). BTSP challenges the traditional assumption that synaptic modification must occur immediately and locally following neuronal activation. Instead, experimentally observed synaptic changes can emerge retrospectively after temporally extended activity episodes through delayed plateau-potential-associated mechanisms capable of linking events separated by several seconds. This framework suggests that biological systems may continuously accumulate information while postponing actual synaptic modification until internally generated conditions are satisfied. Particularly relevant for our work is the idea that neural systems may alternate between relatively stable representational periods and sparse reorganization events that selectively consolidate previously accumulated activity patterns. Although BTSP was developed in the context of hippocampal physiology and dendritic biophysics, its broader implication concerns the temporal organization of learning itself. Our approach adopts the general principle that information accumulation and parameter modification may operate on partially separated temporal scales, with learning emerging through internally triggered retrospective updates rather than continuous online correction.

arXiv:2605.10994v1 [q-bio.NC]) 9 May 2026

We introduce a simulation-based learning formulation in which parameter updates are governed by internally generated events emerging from the network's own representational dynamics. Synaptic interactions are stored as latent traces that accumulate recent co-activation patterns without immediately modifying the parameters, while an internal predictive process estimates the evolving latent state. A scalar discrepancy between predicted and observed states is continuously integrated, generating a slowly varying measure of representational inconsistency. When this quantity exceeds an adaptive threshold, a learning event is triggered, retrospectively incorporating past activity into the updated configuration. In our simulations, learning is temporally discontinuous and occurs only at internally defined critical points. This adaptive threshold regulates sensitivity to poorly predicted states, producing sparse but organized learning events. Our network persisted in relatively stable representational states for extended periods, interrupted by brief episodes of rapid reorganization when unexpected inputs accumulated. These episodic transitions integrated information across longer temporal intervals without requiring continuous parameter updates at every computational step.

We will proceed as follows. First, we formalize the proposed model and its dynamical variables; then, we describe the simulation setup and evaluation criteria; finally, we present the results and analyze the emergent learning behavior.

METHODS

We studied a minimal artificial neural network designed to test whether learning can be restricted to internally triggered, retrospective events rather than applied continuously at every time step. We used a simulated multichannel input stream, a latent neural representation, an internal predictor, synaptic eligibility traces, an adaptive surprise threshold and event-gated synaptic updates, all implemented within a controlled computational simulation. We aimed to identify an experimentally discriminable signature consisting of sparse learning events, stepwise changes in synaptic efficacy and state-space transitions temporally aligned with internally detected prediction errors.

Simulated inputs. All variables were updated in discrete time with fixed step Δt and all computations were executed sequentially at each time step. A synthetic sequential input stream was generated over $T = 180$ s with integration step $\Delta t = 0.01$ s, yielding $N = T/\Delta t$ samples. The input vector was defined as

$$\mathbf{x}(t) = [x_1(t), x_2(t), \dots, x_{12}(t)]^\top,$$

with $x_i(t)$ expressed in spikes/s. Four structured regimes were defined through prototype vectors $\mathbf{p}_q$. During regime q, the signal followed

$$\mathbf{x}(t) = \mathbf{p}_q + \mathbf{d}_q(t) + \boldsymbol{\xi}(t),$$

where $\mathbf{d}_q(t) = A_d \sin\left(\frac{2\pi(t-t_q)}{18}\right)\mathbf{1}$introduced slow drift and $\boldsymbol{\xi}(t) \sim \mathcal{N}(0, \sigma_x^2)$represented noise. Perturbations were imposed by replacing the current pattern with a weighted mixture of adjacent regimes. All values were clipped to $[0, 40]$ spikes/s. These inputs defined a nonstationary but fully controlled signal without external labels.

Latent dynamics. The network consisted of $n = 12$ inputs and $m = 8$ latent units. Synaptic weights were represented by

$$W(t) \in \mathbb{R}^{12\times 8},$$

initialized as

$$W_{ij}(0) \sim \mathcal{N}(0.052, 0.014^2),$$

with clipping constraints $0.005 \le W_{ij} \le 0.10$. The latent state was computed as

$$\mathbf{h}(t) = 30\tanh\left(\frac{\mathbf{x}(t)^\top W(t)}{20}\right),$$

yielding a bounded representation expressed in scaled millivolt units. These units were internal simulation units, ensuring consistency across variables but not representing calibrated biological measurements.

Internal prediction. A linear predictor estimated the next latent state:

$$\hat{\mathbf{h}}(t) = A\mathbf{h}(t - \Delta t),$$

with

$$A = 0.88I + \Gamma, \Gamma_{ij} \sim \mathcal{N}(0, 0.025^2).$$

Prediction error was defined as

arXiv:2605.10994v1 [q-bio.NC]) 9 May 2026

$$\varepsilon(t) = \frac{1}{m}\sum_{j=1}^{m}\left[h_j(t) - \hat{h}_j(t)\right]^2.$$

This quantity, expressed in mV ^{2}, was used solely as an internal discrepancy signal.

Adaptive threshold. The running mean and variance of $\varepsilon(t)$ were computed as

$$\mu(t+\Delta t) = \mu(t) + \Delta t\frac{\varepsilon(t) - \mu(t)}{\tau_\mu},$$
$$v(t+\Delta t) = v(t) + \Delta t\frac{[\varepsilon(t) - \mu(t)]^2 - v(t)}{\tau_v}.$$

The adaptive threshold was defined as

$$\theta(t) = \mu(t) + \kappa\sqrt{v(t)},$$

with $\kappa = 2.2$. A learning event occurred when

$$\varepsilon(t) > \theta(t)$$

and when the refractory condition

$$t - t_{\text{last}} > 7.5$$

was satisfied. Post-event stabilization was applied:

$$\mu(t^+) = 0.85\mu(t^-) + 0.15\varepsilon(t), v(t^+) = 1.25v(t^-).$$

To provide interpretation of the triggering condition, the threshold rule can be reformulated within a decision-theoretic and optimization framework. At each time step, the system faces a binary decision between maintaining the current parameters or performing an update. This can be expressed as a trade-off between the instantaneous prediction error $C_{\text{err}}(t) = \varepsilon(t)$ and a fixed or adaptive update cost $C_{\text{upd}}(t)$. Learning is triggered when the expected cost of not updating exceeds the cost of updating, yielding the decision rule $\varepsilon(t) > C_{\text{upd}}(t)$. By defining the update cost as a function of recent error statistics,

$$C_{\text{upd}}(t) = \mu(t) + \kappa\sqrt{v(t)},$$

the operational threshold condition becomes

$$\varepsilon(t) > \mu(t) + \kappa\sqrt{v(t)},$$

which coincides with the previously defined adaptive threshold. Under this formulation, the trigger is no longer an ad hoc rule but emerges as the optimal decision boundary minimizing a composite objective

$$\mathcal{L} = \sum_t \varepsilon(t) + \lambda_u N_{\text{updates}},$$

where N_{updates} is the total number of learning events. An equivalent interpretation can be given in information-theoretic terms by defining a surprise measure $S(t) = -\log P(\mathbf{h}(t) \mid \mathbf{h}(t-\Delta t))$, so that updates occur when the observed state becomes statistically unlikely under the internal model. This reformulation provides a justification for the event-triggering mechanism while preserving the same computational implementation.

Eligibility traces. Eligibility traces were computed for each synapse as

$$C_{ij}(t) = x_i(t)\frac{\max[h_j(t),0]}{30},$$
$$E_{ij}(t+\Delta t) = E_{ij}(t) + \Delta t\frac{-E_{ij}(t) + C_{ij}(t)}{\tau_E}.$$

These traces stored recent co-activation history without modifying weights.

Normalization and update. At event time t_k, normalization was defined globally:

$$E_{\max}(t_k) = \max_{i,j} E_{ij}(t_k).$$

The normalized trace was

$$\tilde{E}_{ij}(t_k) = \frac{E_{ij}(t_k)}{E_{\max}(t_k) + \delta}.$$

arXiv:2605.10994v1 [q-bio.NC]) 9 May 2026

Weights were updated as

$$W_{ij}(t_k^+) = W_{ij}(t_k^-) + \eta \tilde{E}_{ij}(t_k) - \eta\lambda W_{ij}(t_k^-),$$

with clipping

$$0.001 \le W_{ij} \le 0.18.$$

Between events, weights remained constant.

Update sequence. At each time step t, the following deterministic order was enforced:
(1) $\mathbf{h}(t) \rightarrow$ (2) $\hat{\mathbf{h}}(t) \rightarrow$ (3) $\varepsilon(t) \rightarrow$ (4) $\mu, v \rightarrow$ (5) $\theta(t) \rightarrow$ (6) $E_{ij}(t) \rightarrow$ (7) event check → (8) $W(t) \rightarrow$ (9) storage.

This ordering ensures that prediction error is computed before weight modification and that eligibility traces accumulate prior to normalization.

Control procedures. Three control conditions were defined. A fixed-weight condition imposed

$$W(t) = W(0),$$

for all t. A continuous-update condition applied

$$W_{ij}(t + \Delta t) = W_{ij}(t) + \Delta t\, \eta_c\left[\tilde{E}_{ij}(t) - \lambda W_{ij}(t)\right].$$

A randomized-event condition preserved event count but randomized event times while maintaining refractory spacing. These controls allowed separation of trace accumulation, event timing and threshold dependence.
To assess the specificity of the learning mechanism and reduce ambiguity in interpretation, additional quantitative benchmarks and ablation analyses were defined. Performance comparisons were structured by matching the total magnitude of parameter updates across conditions, ensuring that differences arise from temporal organization rather than overall update strength. In the ablation setting, individual components of the update rule were selectively removed, including the eligibility trace term, the adaptive threshold and the normalization step, yielding reduced models of the form $W_{ij}(t_k^+) = W_{ij}(t_k^-) + \eta\phi_{ij}(t_k)$, where ϕ_{ij} denotes the retained components. These variants allowed isolation of the contribution of retrospective accumulation and event triggering. In parallel, the geometric analysis of latent trajectories was explicitly treated as a post hoc descriptive procedure rather than a mechanistic driver of learning. The projection $Z = H_c V_2$ and associated distance measures $D_k(s)$ were computed only after completion of weight updates and were not fed back into the learning rule. This distinction ensures that geometric observables provide an independent characterization of system dynamics, enabling comparison between conditions without influencing parameter evolution.

State geometry. Latent states were stored in matrix

$$H = [\mathbf{h}(t_1), \ldots, \mathbf{h}(t_N)]^\top.$$

After centering,

$$H_c = H - \mathbf{1}\bar{\mathbf{h}}^\top,$$

singular value decomposition yielded

$$H_c = U\Sigma V^\top.$$

Projection onto the first two components gave

$$Z = H_c V_2.$$

Distances were computed as

$$D_k(s) = \| \mathbf{z}(t_k) - \mathbf{z}(s) \|_2,$$

for $s \in [t_k - 6, t_k]$.

Visualization and software tools. Temporal traces, synaptic efficacy and input activity were visualized as functions of time. Event rate was computed as

$$R_b = \frac{N_b}{15} \times 60.$$

Grouped synaptic efficacy was

$$G_{qj} = \frac{1}{3}\sum_{i \in q} W_{ij}\,.$$

arXiv:2605.10994v1 [q-bio.NC]) 9 May 2026

All computations were performed in Python using NumPy for numerical operations and Matplotlib for visualization. Random seeds were fixed. All variables were generated internally without external datasets. For reproducibility and procedural clarity, the complete deterministic implementation of the internally triggered retrospective learning algorithm is provided in the Supplementary Material.

RESULTS

We report the temporal, synaptic and geometric properties of an internally triggered episodic learning process in a simulated neural network exposed to sequential inputs. Quantitative descriptors of event timing, synaptic changes, prediction error dynamics and latent-state trajectories are provided to characterize the emergence and distribution of learning events.

Event dynamics. Across the 180 s simulation, a total of 19 internally triggered learning events were detected, corresponding to an average rate of approximately 6.3 events/min, with temporal clustering around periods of input perturbation (Figure 1). Event times were not uniformly distributed but concentrated near transitions or perturbations in the input stream, with inter-event intervals ranging from approximately 7.5 s (imposed refractory limit) to 12.1 s. The instantaneous prediction error $\varepsilon(t)$ exhibited transient increases preceding each event, exceeding the adaptive threshold $\theta(t)$ derived from the running mean and variance of recent error values. The difference $\varepsilon(t) - \theta(t)$ at event onset ranged from 0.42 to 1.87 mV ^{2} (mean = 0.96). Mean synaptic efficacy increased in a stepwise manner, from an initial value of 52 to a final value of 91 μV/spike, with discrete increments aligned with event times. Individual event-induced weight changes $J(t_k)$ ranged from 3.2 to 11.6 μV/spike (mean = 6.9). Event rate computed in 15 s bins displayed peaks of up to 12 events/min during perturbation intervals and near-zero values during stable input regimes.
The control conditions provided a reference for these dynamics: in the fixed-weight condition, no events were observed and synaptic efficacy were constant; in the continuous-update condition, synaptic changes occurred gradually without discrete steps; in the randomized-event condition, event timing was decoupled from prediction error and produced less structured temporal alignment.
These results suggest that learning events are temporally sparse and preferentially aligned with internally detected discrepancies rather than uniformly distributed over time, supporting the interpretation that episodic updates are selectively triggered by deviations from expected latent dynamics.

State organization. Projection of latent activity onto its first two principal coordinates revealed structured trajectories organized into distinct regions corresponding to input regimes (Figure 2). Learning events were localized at transitions between these regions or at points of increased trajectory curvature. The Euclidean distance $D_k(s)$ between event states and preceding states over a 6 s window ranged from 4.8 to 13.2 mV, with larger distances associated with more pronounced perturbations in the input stream. The distribution of distances showed a gradual increase approaching event onset, indicating accumulation of divergence in latent space prior to triggering. The relationship between prediction error at event onset and synaptic update magnitude exhibited a positive association, with higher error values corresponding to larger weight changes, although variability was present across events. Final synaptic organization showed differentiated mapping between input channel groups and latent units, with group-specific mean efficacies ranging from 62 to 138 μV/spike.
The control conditions provided a comparative perspective on these structures: in the fixed-weight condition, latent trajectories were confined and did not exhibit discrete transitions; in the continuous-update condition, trajectories evolved smoothly without sharp reorganization; in the randomized-event condition, transitions occurred but lacked consistent alignment with input perturbations.
This suggests that internally triggered events correspond to discrete reorganizations of latent-state geometry rather than incremental adjustments, linking temporal error accumulation to spatial restructuring of representations.

Summarizing, learning emerges as a sequence of discrete, internally triggered events rather than a continuous process. Prediction error accumulation precedes each event, while synaptic efficacy changes occur in stepwise increments aligned with these events. Latent-state trajectories exhibit structured transitions associated with event timing. This indicates that episodic updates can reorganize representations selectively in response to internally detected discrepancies.

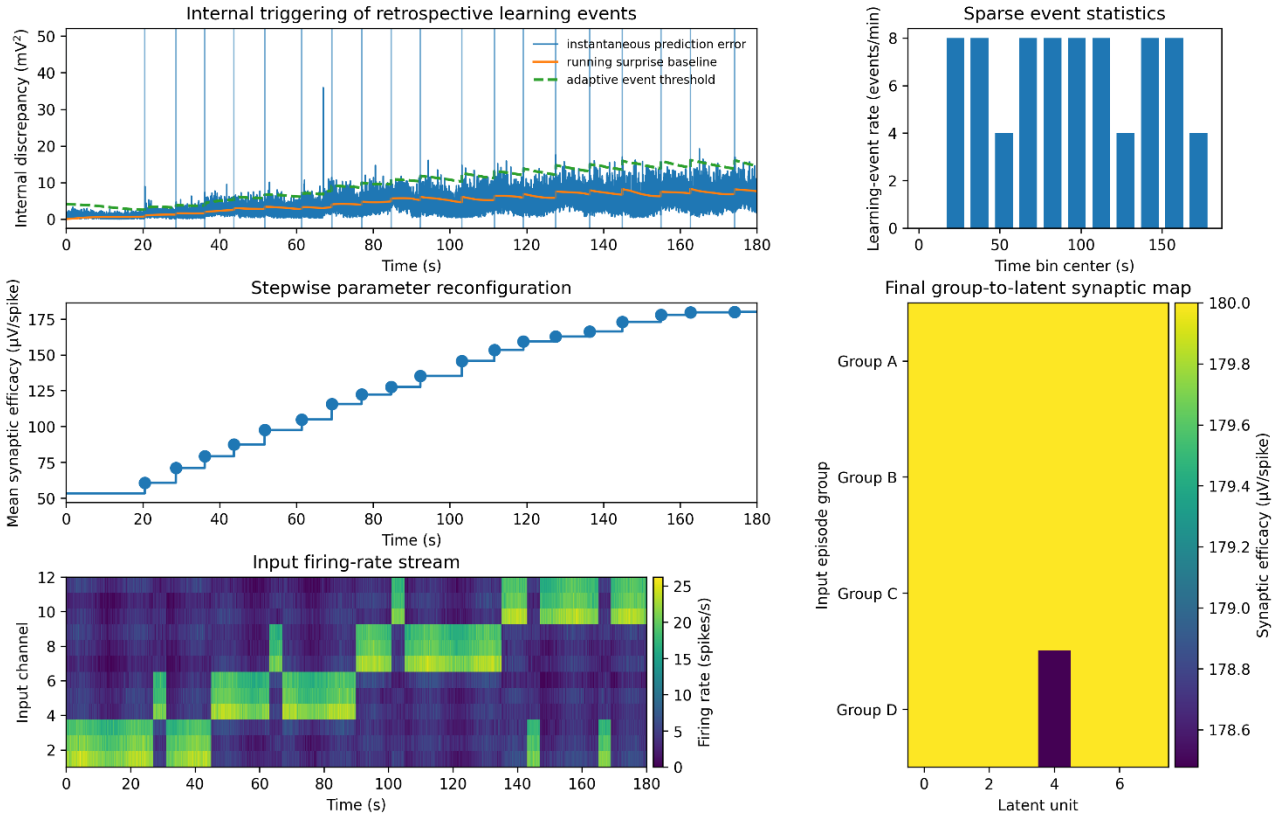


Figure 1. Integrated temporal dynamics of internally triggered episodic learning in simulated neural network operating under internally regulated, event-driven learning across a 180 s input sequence.

The upper-left panel displays instantaneous latent prediction error (mV²), together with its running baseline and the adaptive event threshold. Vertical lines mark the onset of internally generated learning events, which occur when the instantaneous discrepancy exceeds the adaptive threshold derived from the network's own recent history. The separation between instantaneous error and baseline reflects transient departures from expected dynamics, while the threshold follows slower variations, providing a reference for event triggering.

The middle-left panel reports the evolution of mean synaptic efficacy, showing discrete step-like increases that coincide with learning events, consistent with retrospective weight updates rather than continuous modification. Individual points highlight the exact timing of these discontinuities.

The lower-left panel displays the full input stream as a time-resolved heatmap across 12 channels, revealing structured sequences of activity with distinct episodes and intermittent perturbations, all expressed in spikes per second.

The right-side panels summarize two complementary aspects of the learning dynamics: the upper panel shows the temporal distribution of learning events, expressed as event rate across successive time bins, while the lower panel displays the final mapping between groups of input channels and latent units, quantified in terms of synaptic efficacy. This latter representation illustrates how repeated co-activation patterns become selectively consolidated into structured synaptic configurations following episodic updates.

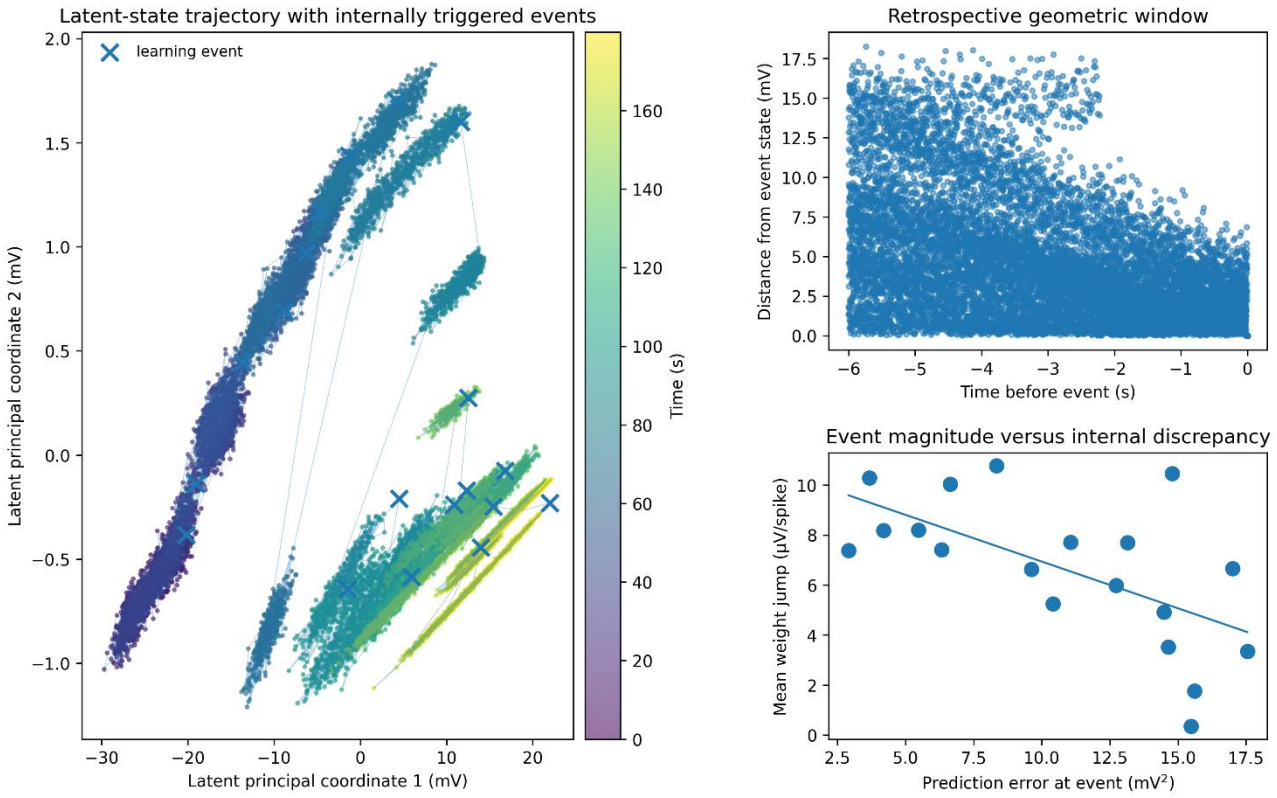


Figure 2. State-space geometry and retrospective structure of episodic learning events.
In the right panel, latent network activity is represented in a reduced two-dimensional space obtained through principal component projection of the full latent state, with coordinates expressed in mV. The continuous trajectory illustrates the temporal evolution of internal representations under sequential input, with color encoding elapsed time in seconds. Superimposed markers identify the occurrence of internally triggered learning events, allowing direct visualization of how these events are embedded within the ongoing dynamics. The trajectory exhibits structured regions corresponding to distinct input regimes, while transitions between regions reveal changes in input statistics and internal prediction accuracy.
The upper-right panel quantifies the retrospective temporal window associated with each event by measuring the Euclidean distance between the event state and preceding states within a fixed interval of 6 s. This representation captures the geometric extent of recent activity that contributes to the synaptic update, showing how learning integrates information over a finite temporal horizon rather than relying solely on instantaneous states.
The lower-right panel relates the magnitude of synaptic modification to the prediction error at the time of event onset, providing a quantitative link between internal discrepancy and the strength of parameter reconfiguration. The distribution of points reflects variability in event magnitude and its dependence on internal state mismatch, highlighting the role of threshold-crossing events in shaping discrete transitions within the network's representational space.

CONCLUSIONS

We asked whether learning in artificial neural networks can be restricted to internally triggered, temporally sparse events rather than implemented as a continuous process driven by ongoing input or external supervision. Our simulations compared an event-triggered learning condition, in which synaptic updates occurred only when internally computed prediction error exceeded an adaptive threshold, with control conditions including fixed weights, continuous updates and randomized event timing. We found that learning events emerged at discrete time points, temporally aligned with increases in internal discrepancy and that synaptic efficacy evolved through stepwise changes rather than gradual drift. Latent-state trajectories exhibited structured transitions associated with these events, while control conditions lacking internally triggered updates showed either stable or progressively diffused representations. The magnitude of synaptic change varied with prediction error at event onset, indicating a quantitative link between internal state mismatch and the extent of reconfiguration. These observations suggest that learning could be governed by threshold-crossing dynamics that integrate information over extended temporal windows and reorganize representations retrospectively. Therefore, internally regulated, event-based updates could provide a viable alternative to continuous adjustment rules, linking temporal accumulation of discrepancy signals to discrete structural changes in network organization.

arXiv:2605.10994v1 [q-bio.NC]) 9 May 2026

Compared with established approaches, our model differs in how learning is initiated and temporally organized. In Bayesian formulations, parameter updates arise from continuous revision of posterior distributions, where each new observation contributes incrementally through likelihood weighting (Fernandes et al. 2021; Biazzo et al. 2022; Magotra et al. 2022; Payares-Garcia et al. 2023; Liang et al. 2023; Thompson et al. 2023; Jeon et al. 2024). In contrast, in our framework no explicit probability distribution is maintained and no continuous update rule is enforced; parameter modification occurs only when accumulated internal discrepancy exceeds a dynamically defined boundary. This separates evidence accumulation from parameter change, whereas Bayesian schemes merge these processes. Gradient-based neural networks, including recurrent architectures trained with backpropagation through time, rely on uninterrupted error propagation and weight adjustment at every step, requiring storage of intermediate states and differentiability constraints (Dong et al. 2023; Luo et al. 2023; Han 2024), while eligibility trace-based reinforcement learning methods propagate credit continuously through temporally decaying traces combined with reward signals (Suri and Schultz 1998; Elfwing et al. 2018; Wang et al. 2026). Event-driven spiking networks and reinforcement learning systems introduce temporal sparsity, but their updates are typically tied to external reward signals or predefined spike-timing rules rather than to an internally derived criterion (Zhuang et al. 2020; Zhang et al. 2022; Zhao et al. 2023; Brückerhoff-Plückelmann et al. 2023; Wu et al. 2025). Memory-augmented and one-shot learning models allow rapid adaptation, yet they generally depend on auxiliary memory structures or direct supervision (Khadka et al. 2019; Yin et al. 2020; Ma et al. 2021; Karunaratne et al. 2021; Li et al. 2022; Suresh et al. 2022; Mao et al. 2022; Yang et al. 2023). Our framework combines internal triggering, retrospective integration over eligibility traces and adaptive thresholding without auxiliary memory modules or external signals. Therefore, we define a learning regime in which parameter updates are both self-regulated and temporally discontinuous, distinguishing it from probabilistic inference, gradient descent and reward-driven adaptation.

Our study has limitations. The event-triggering mechanism, based on a running mean and variance of prediction error, is operational and biologically inspired but is heuristic. The retrospective update is implemented, but its ability to resolve long-timescale credit assignment is not analytically demonstrated. The geometric analysis of latent trajectories is conducted post hoc and does not influence the learning rule. The use of physical units (mV, μV/spike) reflects internal scaling conventions rather than empirical calibration and should therefore be interpreted as simulation units. Parameter values, including time constants and scaling factors, are synthetic and do not correspond directly to measured quantities. Event occurrence depends on threshold tuning, introducing potential circularity in which observed dynamics reflect design choices. The sensitivity of the results to parameter choices (e.g., κ, time constants) is unexamined, leaving robustness unclear. Open questions concern how the trigger can be derived from principled criteria, whether the mechanism scales to higher-dimensional systems and how alternative definitions of internal discrepancy affect event structure.

Testable hypotheses can be formulated. First, the frequency of learning events is predicted to scale with the variance of the input stream: increasing input variability σ_x^2 should increase event rate approximately linearly up to saturation, yielding a measurable relation $R \propto \sigma_x$ over moderate ranges.
Second, the magnitude of synaptic updates is expected to depend on the excess of prediction error above threshold, with a monotonic relationship $J \sim \varepsilon - \theta$, implying that larger discrepancies produce proportionally larger weight changes.
Third, the temporal spacing between events should be constrained by both the refractory interval and the decay constant of the eligibility trace, leading to a lower bound $\Delta t_{\min} \approx \max(r, \tau_E)$, which can be verified by measuring inter-event interval distributions.
Fourth, latent-state trajectories are expected to exhibit increased curvature preceding events, measurable as a rise in local trajectory divergence over a fixed temporal window, providing a geometric signature of impending updates.
Fifth, modifying the threshold sensitivity parameter κ should systematically shift event density, with higher values reducing event frequency and increasing average update magnitude.
Future work may derive the triggering condition from optimization or information-theoretic principles, compare performance with continuous learning under matched update budgets, extend the approach to deeper and recurrent architectures and incorporate adaptive predictors. Additional work may also evaluate robustness across noise regimes, investigate scaling with network size and test whether alternative definitions of discrepancy alter the statistical structure of learning events.
Practical uses can be outlined. Systems for monitoring physiological signals, industrial processes or environmental streams could employ selective updates to avoid unnecessary parameter drift during stable conditions. In edge computing devices with limited energy budgets, infrequent parameter modification may reduce computational load and extend operational lifetime. Autonomous systems operating in dynamic environments could benefit from update strategies emphasizing salient deviations rather than routine inputs. In data compression and storage, episodic updating may support selective retention of informative patterns while discarding redundant sequences.

In conclusion, we described a neural system in which parameter updates occur intermittently and are governed by internally generated triggering conditions rather than continuous adjustment. We observed that this strategy produces sequences of reconfiguration events and measurable transitions in internal representations. Our results suggest that discrete updates can be coherently embedded within a continuous processing stream, defining an alternative temporal organization of learning driven by intrinsic criteria.

arXiv:2605.10994v1 [q-bio.NC]) 9 May 2026

DECLARATIONS

Ethics approval and consent to participate. This research does not contain any studies with human participants or animals performed by the Author.
Consent for publication. The Author transfers all copyright ownership, in the event the work is published. The undersigned author warrants that the article is original, does not infringe on any copyright or other proprietary right of any third part, is not under consideration by another journal and has not been previously published.
Availability of data and materials. All data and materials generated or analyzed during this study are included in the manuscript. The Author had full access to all the data in the study and took responsibility for the integrity of the data and the accuracy of the data analysis.
Disclaimer. The views expressed are those of the author and do not necessarily reflect those of the affiliated institutions.
Competing interests. The Author does not have any known or potential conflict of interest including any financial, personal or other relationships with other people or organizations within three years of beginning the submitted work that could inappropriately influence or be perceived to influence their work.
Funding. This research did not receive any specific grant from funding agencies in the public, commercial or not-for-profit sectors.
Acknowledgements: none.
Authors' contributions. The Author performed: study concept and design, acquisition of data, analysis and interpretation of data, drafting of the manuscript, critical revision of the manuscript for important intellectual content, statistical analysis, obtained funding, administrative, technical and material support, study supervision.
Declaration of generative AI and AI-assisted technologies in the writing process. During the preparation of this work, the author used ChatGPT 5.3 to assist with data analysis and manuscript drafting and to improve spelling, grammar and general editing. After using this tool, the author reviewed and edited the content as needed, taking full responsibility for the content of the publication.

REFERENCES

1) Bao, C., Y. Pu, and Y. Zhang. 2018. “Fractional-Order Deep Backpropagation Neural Network.” *Computational Intelligence and Neuroscience* 2018: 7361628. https://doi.org/10.1155/2018/7361628.
2) Biazzo, I., A. Braunstein, L. Dall’Asta, and F. Mazza. 2022. “A Bayesian Generative Neural Network Framework for Epidemic Inference Problems.” *Scientific Reports* 12 (1): 19673. https://doi.org/10.1038/s41598-022-20898-x.
3) Brückerhoff-Plückelmann, F., I. Bente, M. Becker, N. Vollmar, N. Farmakidis, E. Lomonte, F. Lenzini, C. D. Wright, H. Bhaskaran, M. Salinga, B. Risse, and W. H. P. Pernice. 2023. “Event-Driven Adaptive Optical Neural Network.” *Science Advances* 9 (42): eadi9127. https://doi.org/10.1126/sciadv.adi9127.
4) Cai, C., T. Imai, E. Hasumi, and K. Fujiu. 2024. “One-Shot Screening: Utilization of a Two-Dimensional Convolutional Neural Network for Automatic Detection of Left Ventricular Hypertrophy Using Electrocardiograms.” *Computer Methods and Programs in Biomedicine* 247: 108097. https://doi.org/10.1016/j.cmpb.2024.108097.
5) Dai, X., J. Qiu, C. Wan, and F. Dai. 2024. “A Lagrange Programming Neural Network Approach for Nuclear Norm Optimization.” *PLoS ONE* 19 (2): e0292380. https://doi.org/10.1371/journal.pone.0292380.
6) Dong, Y., D. Zhao, Y. Li, and Y. Zeng. 2023. “An Unsupervised STDP-Based Spiking Neural Network Inspired by Biologically Plausible Learning Rules and Connections.” *Neural Networks* 165: 799–808. https://doi.org/10.1016/j.neunet.2023.06.019.
7) Elfwing, S., E. Uchibe, and K. Doya. 2018. “Sigmoid-Weighted Linear Units for Neural Network Function Approximation in Reinforcement Learning.” *Neural Networks* 107: 3–11. https://doi.org/10.1016/j.neunet.2017.12.012.
8) Erb, R. J. 1993. “Introduction to Backpropagation Neural Network Computation.” *Pharmaceutical Research* 10 (2): 165–170. https://doi.org/10.1023/A:1018966222807.
9) Fernandes, V., G. B. Junior, A. C. de Paiva, A. C. Silva, and M. Gattass. 2021. “Bayesian Convolutional Neural Network Estimation for Pediatric Pneumonia Detection and Diagnosis.” *Computer Methods and Programs in Biomedicine* 208: 106259. https://doi.org/10.1016/j.cmpb.2021.106259.
10) Hachisuka, A., J. D. Shor, X. C. Liu, D. Friedman, P. Dugan, I. Saez, F. E. Panov, Y. Wang, W. Doyle, O. Devinsky, E. K. Oermann, and H. B. He. 2026. “Neural and Computational Mechanisms Underlying One-Shot Perceptual Learning in Humans.” *Nature Communications* 17 (1): 1204. https://doi.org/10.1038/s41467-026-68711-x.

11) Han, J. H. 2024. "Efficient Inverse Design of Optical Multilayer Nano-Thin Films Using Neural Network Principles: Backpropagation and Gradient Descent." *Nanoscale* 16 (36): 17165–17175. https://doi.org/10.1039/d4nr01667j.
12) Hu, Y., and B. Si. 2018. "A Reinforcement Learning Neural Network for Robotic Manipulator Control." *Neural Computation* 30 (7): 1983–2004. https://doi.org/10.1162/neco_a_01079.
13) Jeon, Y., W. Chang, S. Jeong, S. Han, and J. Park. 2024. "A Bayesian Convolutional Neural Network-Based Generalized Linear Model." *Biometrics* 80 (2): ujae057. https://doi.org/10.1093/biomtc/ujae057.
14) Karunaratne, G., M. Schmuck, M. Le Gallo, G. Cherubini, L. Benini, A. Sebastian, and A. Rahimi. 2021. "Robust High-Dimensional Memory-Augmented Neural Networks." *Nature Communications* 12 (1): 2468. https://doi.org/10.1038/s41467-021-22364-0.
15) Khadka, S., J. J. Chung, and K. Tumer. 2019. "Neuroevolution of a Modular Memory-Augmented Neural Network for Deep Memory Problems." *Evolutionary Computation* 27 (4): 639–664. https://doi.org/10.1162/evco_a_00239.
16) Lakin, M. R. 2023. "Design and Simulation of a Multilayer Chemical Neural Network That Learns via Backpropagation." *Artificial Life* 29 (3): 308–335. https://doi.org/10.1162/artl_a_00405.
17) Li, J., D. Wang, X. Liu, Z. Shi, and M. Wang. 2022. "Two-Branch Attention Network via Efficient Semantic Coupling for One-Shot Learning." *IEEE Transactions on Image Processing* 31: 341–351. https://doi.org/10.1109/TIP.2021.3124668.
18) Liang, J., Z. L. Yu, Z. Gu, and Y. Li. 2023. "Electromagnetic Source Imaging With a Combination of Sparse Bayesian Learning and Deep Neural Network." *IEEE Transactions on Neural Systems and Rehabilitation Engineering* 31: 2338–2348. https://doi.org/10.1109/TNSRE.2023.3251420.
19) Luo, X., H. Qu, Y. Wang, Z. Yi, J. Zhang, and M. Zhang. 2023. "Supervised Learning in Multilayer Spiking Neural Networks With Spike Temporal Error Backpropagation." *IEEE Transactions on Neural Networks and Learning Systems* 34 (12): 10141–10153. https://doi.org/10.1109/TNNLS.2022.3164930.
20) Ma, Q., Z. Zheng, W. Zhuang, E. Chen, J. Wei, and J. Wang. 2021. "Echo Memory-Augmented Network for Time Series Classification." *Neural Networks* 133: 177–192. https://doi.org/10.1016/j.neunet.2020.10.015.
21) Magee, Jeffrey C. 2026. "Behavioral Timescale Synaptic Plasticity: Properties, Elements and Functions." *Nature Neuroscience* 29: 520–534.
22) Magotra, A., Y. C. Bangar, and A. S. Yadav. 2022. "Neural Network and Bayesian-Based Prediction of Breeding Values in Beetal Goat." *Tropical Animal Health and Production* 54 (5): 282. https://doi.org/10.1007/s11250-022-03294-5.
23) Mao, R., B. Wen, A. Kazemi, Y. Zhao, A. F. Laguna, R. Lin, N. Wong, M. Niemier, X. S. Hu, X. Sheng, C. E. Graves, J. P. Strachan, and C. Li. 2022. "Experimentally Validated Memristive Memory Augmented Neural Network with Efficient Hashing and Similarity Search." *Nature Communications* 13 (1): 6284. https://doi.org/10.1038/s41467-022-33629-7.
24) Melchior, J., A. Altamimi, M. Bayati, S. Cheng, and L. Wiskott. 2024. "A Neural Network Model for Online One-Shot Storage of Pattern Sequences." *PLoS ONE* 19 (6): e0304076. https://doi.org/10.1371/journal.pone.0304076.
25) Ojha, V., and G. Nicosia. 2022. "Backpropagation Neural Tree." *Neural Networks* 149: 66–83. https://doi.org/10.1016/j.neunet.2022.02.003.
26) Payares-Garcia, D., J. Mateu, and W. Schick. 2023. "Spatially Informed Bayesian Neural Network for Neurodegenerative Diseases Classification." *Statistics in Medicine* 42 (2): 105–121. https://doi.org/10.1002/sim.9604.
27) Shen, K., G. Li, A. Chemori, and M. Hayashibe. 2023. "Self-Organizing Neural Network for Reproducing Human Postural Mode Alternation through Deep Reinforcement Learning." *Scientific Reports* 13 (1): 8966. https://doi.org/10.1038/s41598-023-35886-y.
28) Sun, Y., F. Zhao, Z. Zhao, and Y. Zeng. 2025. "Multi-Compartment Neuron and Population Encoding Powered Spiking Neural Network for Deep Distributional Reinforcement Learning." *Neural Networks* 182: 106898. https://doi.org/10.1016/j.neunet.2024.106898.
29) Suresh, N., N. Chinnakonda Ashok Kumar, S. Subramanian, and G. Srinivasa. 2022. "Memory Augmented Recurrent Neural Networks for De-Novo Drug Design." *PLoS ONE* 17 (6): e0269461. https://doi.org/10.1371/journal.pone.0269461.
30) Suri, R. E., and W. Schultz. 1998. "Learning of Sequential Movements by Neural Network Model with Dopamine-Like Reinforcement Signal." *Experimental Brain Research* 121 (3): 350–354. https://doi.org/10.1007/s002210050467.
31) Thompson, J. C., V. M. Zavala, and O. S. Venturelli. 2023. "Integrating a Tailored Recurrent Neural Network With Bayesian Experimental Design to Optimize Microbial Community Functions." *PLoS Computational Biology* 19 (9): e1011436. https://doi.org/10.1371/journal.pcbi.1011436.
32) Tyagi, A., C. Xie, and K. Mueller. 2023. "NAS-Navigator: Visual Steering for Explainable One-Shot Deep Neural Network Synthesis." *IEEE Transactions on Visualization and Computer Graphics* 29 (1): 299–309. https://doi.org/10.1109/TVCG.2022.3209361.

arXiv:2605.10994v1 [q-bio.NC]) 9 May 2026

33) Wang, Y., W. Xiong, J. Yan, Y. Zhou, C. Zhu, X. Miao, Y. He, and Y. Chai. 2026. "Brain-Inspired Synaptic Transistors for In-Situ Spiking Reinforcement Learning with Eligibility Trace." *Nature Communications* 17 (1): 3001. https://doi.org/10.1038/s41467-026-69898-9.
34) Wei, Z., Q. Li, J. Wei, and W. Bian. 2022. "Neural Network for a Class of Sparse Optimization with L(0)-Regularization." *Neural Networks* 151: 211–221. https://doi.org/10.1016/j.neunet.2022.03.033.
35) Wu, D., G. Jin, H. Yu, X. Yi, and X. Huang. 2025. "Optimizing Event-Driven Spiking Neural Network with Regularization and Cutoff." *Frontiers in Neuroscience* 19: 1522788. https://doi.org/10.3389/fnins.2025.1522788.
36) Xiao, D., K. F. Liang, K. Ji, and J. C. Kao. 2025. "Using Reinforcement Learning to Investigate Neural Dynamics During Motor Learning." *Annual International Conference of the IEEE Engineering in Medicine and Biology Society* 2025: 1–7. https://doi.org/10.1109/EMBC58623.2025.11252999.
37) Yang, S., Y. Zhou, X. Chen, C. Li, and H. Song. 2023. "Fault Diagnosis for Wind Turbines with Graph Neural Network Model Based on One-Shot Learning." *Royal Society Open Science* 10 (7): 230706. https://doi.org/10.1098/rsos.230706.
38) Yin, C., J. Tang, Z. Xu, and Y. Wang. 2020. "Memory Augmented Deep Recurrent Neural Network for Video Question Answering." *IEEE Transactions on Neural Networks and Learning Systems* 31 (9): 3159–3167. https://doi.org/10.1109/TNNLS.2019.2938015.
39) Zhang, A., X. Li, Y. Gao, and Y. Niu. 2022. "Event-Driven Intrinsic Plasticity for Spiking Convolutional Neural Networks." *IEEE Transactions on Neural Networks and Learning Systems* 33 (5): 1986–1995. https://doi.org/10.1109/TNNLS.2021.3084955.
40) Zhao, S., J. Yang, J. Wang, C. Fang, T. Liu, S. Zhang, and M. Sawan. 2023. "A 0.99-to-4.38 μJ/Class Event-Driven Hybrid Neural Network Processor for Full-Spectrum Neural Signal Analyses." *IEEE Transactions on Biomedical Circuits and Systems* 17 (3): 598–609. https://doi.org/10.1109/TBCAS.2023.3268502.
41) Zhou, P., L. Han, L. Peng, L. L. Liu, N. N. Wang, J. Ma, and Y. L. Ma. 2023. "Instantaneous Sap Flow Velocity Simulation of Euonymus bungeanus Based on Neural Network Optimization Model." *Ying Yong Sheng Tai Xue Bao* 34 (8): 2123–2132. https://doi.org/10.13287/j.1001-9332.202308.019.
42) Zhuang, Y., C. Wu, H. Wu, Z. Zhang, Y. Gao, and L. Li. 2020. "Collaborative Neural Network Algorithm for Event-Driven Deployment in Wireless Sensor and Robot Networks." *Sensors* 20 (10): 2779. https://doi.org/10.3390/s20102779.

SUPPLEMENTARY MATERIAL

Deterministic implementation of internally triggered retrospective learning. The following algorithm specifies the input construction, state update, prediction error computation, adaptive thresholding, eligibility-trace accumulation, event detection, normalized retrospective weight update, post-event stabilization and post hoc state-space analysis.
Initialize the simulation parameters $T = 180$ s, $\Delta t = 0.01$ s, $n = 12, m = 8, \tau_E = 4$s, $\tau_\mu = 10$s, $\tau_v = 10$s, $\kappa = 2.2, \eta = 0.025$, $\lambda = 0.010$, $\delta = 10^{-9}$ and refractory interval $r = 7.5$ s. Fix the random seed before generating all stochastic quantities.
Generate the full input matrix $X \in \mathbb{R}^{N\times n}$, where $N = T/\Delta t$. Define four prototype input patterns $\mathbf{p}_1, \mathbf{p}_2, \mathbf{p}_3, \mathbf{p}_4$. For each time point, assign the appropriate episode prototype, add sinusoidal drift and Gaussian noise, insert predefined perturbation intervals and clip all input values to $[0, 40]$ spikes/s.
Initialize the weight matrix $W \in \mathbb{R}^{n\times m}$ by sampling

$$W_{ij}(0) \sim \mathcal{N}(0.052, 0.014^2),$$

then clipping to

$$0.005 \le W_{ij}(0) \le 0.10.$$

Initialize the predictor matrix

$$A = 0.88I + \Gamma,$$

where

$$\Gamma_{ij} \sim \mathcal{N}(0, 0.025^2).$$

Set

$$E_{ij}(0) = 0, \mu(0) = 0, v(0) = 1, \mathbf{h}(0) = \mathbf{0}, t_{\text{last}} = -\infty.$$

For each time step $t_k = k\Delta t$, $k = 1, \dots, N$, perform the following operations in this exact order.

First, read the current input vector:

$$\mathbf{x}_k = X[k,:].$$

Second, compute the current latent state using the current weights before any possible update:

$$\mathbf{h}_k = 30\tanh\left(\frac{\mathbf{x}_k^{\top} W_k}{20}\right).$$

Third, compute the predicted latent state from the previous latent state:

$$\hat{\mathbf{h}}_k = A\mathbf{h}_{k-1}.$$

Fourth, compute the internal prediction error:

$$\varepsilon_k = \frac{1}{m}\sum_{j=1}^{m}\left(h_{k,j} - \hat{h}_{k,j}\right)^2.$$

Fifth, update the running mean of prediction error:

$$\mu_k = \mu_{k-1} + \Delta t\,\frac{\varepsilon_k - \mu_{k-1}}{\tau_\mu}.$$

Sixth, update the running variance:

$$v_k = v_{k-1} + \Delta t\,\frac{(\varepsilon_k - \mu_k)^2 - v_{k-1}}{\tau_v}.$$

If numerical rounding gives $v_k < 0$, set

$$v_k = 10^{-9}.$$

Seventh, compute the adaptive threshold:

$$\theta_k = \mu_k + \kappa\sqrt{v_k}.$$

Eighth, compute the instantaneous co-activation matrix:

$$C_{ij,k} = x_{i,k}\,\frac{\max\left(h_{j,k}, 0\right)}{30}.$$

Ninth, update the eligibility traces:

$$E_{ij,k} = E_{ij,k-1} + \Delta t\,\frac{-E_{ij,k-1} + C_{ij,k}}{\tau_E}.$$

Tenth, evaluate the event condition:

$$P_k = \begin{cases} 1, & \varepsilon_k > \theta_k \text{ and } t_k - t_{\text{last}} > r, \\ 0, & \text{otherwise.} \end{cases}$$

Eleventh, if $P_k = 1$, compute the global eligibility normalization:

$$E_{\max,k} = \max_{i,j} E_{ij,k},$$
$$\tilde{E}_{ij,k} = \frac{E_{ij,k}}{E_{\max,k} + \delta}.$$

Then update all weights simultaneously:

$$W_{ij,k+1} = W_{ij,k} + \eta\tilde{E}_{ij,k} - \eta\lambda W_{ij,k}.$$

After the update, clip all weights:

$$W_{ij,k+1} = \min\left(0.18, \max\left(0.001, W_{ij,k+1}\right)\right).$$

Set

$$t_{\text{last}} = t_k,$$

and apply post-event stabilization:

$$\mu_k = 0.85\mu_k + 0.15\varepsilon_k,$$
$$v_k = 1.25v_k.$$

arXiv:2605.10994v1 [q-bio.NC]) 9 May 2026

If $P_k = 0$, set

$$W_{k+1} = W_k.$$

Twelfth, store $\mathbf{h}_k$, ε_k, μ_k, v_k, θ_k, E_k, W_{k+1} and P_k. Then proceed to the next time step using

$$\mathbf{h}_{k-1} \leftarrow \mathbf{h}_k.$$

After completing all time steps, compute event times as

$$\{t_k : P_k = 1\}.$$

Compute mean synaptic efficacy as

$$\bar{W}(t_k) = \frac{1}{nm} \sum_{i=1}^{n} \sum_{j=1}^{m} W_{ij,k}\,.$$

Compute event-specific mean weight jump as

$$J_k = \frac{1}{nm} \sum_{i=1}^{n} \sum_{j=1}^{m} \mid W_{ij,k+1} - W_{ij,k} \mid$$

for all $k$such that $P_k = 1$.
For state-space analysis, form the latent-state matrix

$$H = \begin{bmatrix} \mathbf{h}_1^\top \\ \mathbf{h}_2^\top \\ \vdots \\ \mathbf{h}_N^\top \end{bmatrix}.$$

Center it as

$$H_c = H - \mathbf{1}\bar{\mathbf{h}}^\top,$$

where

$$\bar{\mathbf{h}} = \frac{1}{N} \sum_{k=1}^{N} \mathbf{h}_k\,.$$

Apply singular value decomposition:

$$H_c = U\Sigma V^\top.$$

Project the trajectory onto the first two principal coordinates:

$$Z = H_c V_2.$$

For each event time t_e, compute the retrospective geometric distance over the previous 6 s:

$$D_e(s) = \| \mathbf{z}(t_e) - \mathbf{z}(s) \|_2,$$

with

$$s \in [t_e - 6, t_e].$$

BULLETIN OF THE POLISH ACADEMY OF SCIENCES
TECHNICAL SCIENCES, Vol. 74(6), 2026, Article number: 6555
DOI: 10.24425/bpasts.2026.6555

A note on conceptual models in robotics: A case study of modelling mechanical grippers using geometric and topological properties

Waldemar W. KOCZKODAJ [1], Witold PEDRYCZ [2], Alexander PIGAZZINI [3], Dominik STRZAŁKA [4]*, and Arturo TOZZI [5]

[1] Laurentian University, Computational Science, School of Engineering, Sudbury, ON P3E 2c6 Canada
[2] Department of Electrical and Computer Engineering, University of Alberta, Edmonton, AB T6R 2G7, Canada
[3] Mathematical and Physical Science Foundation, 4200 Slagelse, Denmark
[4] Rzeszów University of Technology, Al. Powstańców Warszawy 12, 35-092 Rzeszów, Poland
[5] Center for Nonlinear Science, Department of Physics, University of North Texas, Denton, Texas, USA

Abstract. In this study, the geometric and topological aspects of mechanical grippers are investigated. The main focus is on their mechanical behaviour during a precision pinch. Precision pinch is one of the fundamental grasping mechanisms. It occurs when the thumb and index finger come together to grasp small objects, dynamically altering the gripper's geometric and topological configuration. These localised geometric changes can affect force distribution, grip stability, and overall mechanical efficiency. A computer simulation was performed to quantify geometric and topological transformations during precision pinch and their impact on force trajectories. These trajectories were analysed in terms of geodesics on a torus, representing the shortest paths between two points on the fingers' surface. It was demonstrated that variations in gripper geometry influence mechanical force distribution and structural connectivity. Incorporating geometric and topological modelling into gripper design may lead to adaptable bionic devices. Furthermore, this method may help identify stress-prone areas, optimising force trajectories and stress pathways while addressing the limitations of existing models that oversimplify grasping mechanics.

Keywords: gripper; grasping; topological distance; ODE; Nemenyi theorem.

1. INTRODUCTION

Unlike previous studies, which primarily focus on kinematic control or optimisation algorithms, this work proposes a conceptual framework in which the force distribution emerges naturally from the geometric and topological properties of the gripper. Mechanical grippers are designed to grasp, hold, position, and orient objects. They are crucial for tasks such as assembly and material handling. Mechanical grippers function as the "hands" of robots, enabling interaction with the physical environment. This study investigates the intrinsic mechanical properties of gripper movements, particularly precision pinch. Rather than relying on external control signals or computationally intensive algorithms, this framework emphasises internal force distribution mechanisms. Unlike conventional models that treat the hand as a static system, this framework takes into account the dynamic nature of hand movements. A potential advantage of this framework is its ability to address force determination challenges in overconstrained systems, similar to hyperredundant mechanisms such as elephant trunk robots [1]. These systems, which feature high degrees of freedom and complex segment interactions, face challenges in distributing forces efficiently [2]. Traditionally, such control problems are solved using optimisation techniques that balance energy expenditure and stability [3, 4]. However, these methods often rely on intricate inverse kinematics and iterative computations.

By grounding the force distribution in geometric and topological principles rather than predefined control rules or configurations, this approach may be applicable to a range of pinch and grasp types. The method's ability to adapt force trajectories along geodesic paths may suggest potential robustness to different grasping strategies, such as lateral pinch, key pinch, or power grasps. Additionally, accounting for local geometric variations in the gripper-object interface may contribute to efficient force application across different grip configurations. Even in the presence of external perturbations, the geodesic-based optimisation framework could help maintain stable force trajectories, minimising stress concentrations. Understanding stress pathways and geometric adaptations in gripper movements could also improve durability.

Conceptual models are used to communicate the system's functionality and structure to stakeholders. They are high-level representations of a system (see Fig. 1). The model is an abstract representation of the results from reality. The conceptual (or logical) model depicts what a system is or does. The implementation model is a technical representation (usually less abstract

*e-mail: strzlaka@prz.edu.pl

Manuscript submitted 2026-07-31, revised 2026-09-15, initially accepted for publication 2026-09-15, published in November 2026.

© 2026 The Author(s). This is an open access article under the CC BY license (http://creativecommons.org/licenses/by/4.0/)

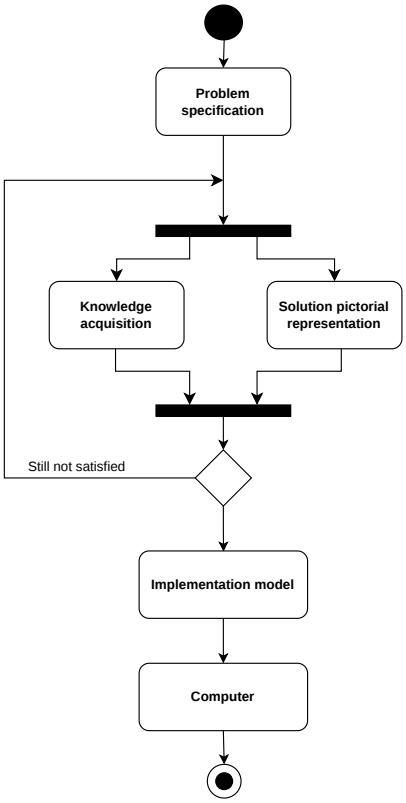


Fig. 1. Activity diagram of a generic conceptual model

than the conceptual model) of how the system is implemented. Popular synonyms are the implementation model and the technical model. The primary objective of a conceptual model is the representation of the fundamental principles and basic functionality of the system. It must provide an easily understood system interpretation for the system developers. According to [5, 6], a conceptual model, when properly implemented, should satisfy four fundamental objectives.

1. Enhance an individual's understanding of the representative system.
2. Facilitate efficient conveyance of system details between stakeholders.
3. Provide a point of reference for system designers to extract system specifications.
4. Document the system for future reference and provide a means for collaboration.

Conceptual models help clarify the core principles and behaviours of the system [7]. They create a basis for further development and implementation. The human hand, a paradigmatic example of a mechanical system, provides a compelling subject for study due to its accessibility and the availability of non-invasive, cost-effective methodologies. More on the subject can be found in [8].

Advances in hand mesh reconstruction algorithms and kinematic models utilise precise three-dimensional representations of the hand in various poses [9]. Additionally, combining marker-based motion capture with deep learning-based hand mesh reconstruction facilitates the estimation of contact regions between the hand, fingers, and object surfaces [10, 11]. This study focuses on understanding how local geometric variations (e.g., shape, size, and form) during grasping produce detectable mechanical effects. Central to this analysis is the application of topological principles, particularly the classification of shapes based on connectivity and topological "holes". For example, a sphere without holes (genus 0) differs fundamentally from a torus with one hole (genus 1) [12]. In this paper, geometric and topological aspects are integrated to describe gripper mechanics. We argue that temporal geometric variations significantly impact the force distribution, while topological modelling serves as a link between mechanics and structural analysis, offering a comprehensive understanding of grasping dynamics.

Agile software development is a flexible project management approach focused on a short software development cycle. It advocates continuous software improvement and ongoing teamwork. It contrasts with a rigid, step-by-step classic software design and implementation method. However, these agile software development principles are only applicable to the implementation (not conceptual) models. Implementation (or physical models are not a part of this research effort.

The objectives of this study are threefold. First, we seek to identify localised geometric and topological changes in the hand during precision pinch – a fundamental grasping action involving the thumb and forefinger – and their effects on force trajectories. Second, we develop mathematical (conceptual) models that enable predictions of mechanical performance. Third, we address the limitations of existing approaches and explore how our insights can inform the development of the next generation of bionic devices.

2. GEOMETRY AND TOPOLOGY OF GRASPING

Gripper mechanics provide a paradigmatic example of how geometric configuration affects movement. The hand consists of a stable wrist and at least two fingers that can oppose each other to generate force [13]. The thumb, a unique feature of humans and higher primates, accounts for approximately 40% of hand function [14, 15]. The motor, sensory and mechanical characteristics of the hand are closely correlated, allowing for a wide range of actions [16]. However, the ability of the hand to adapt to different positions and apply appropriate mechanical forces is crucial to recovering from injuries and surgeries [14]. Regarding mechanical movements, the basic functions of the hand include various types of grasps, classified in several ways [17, 18]. The main types of grasps include (Figs. 2A–G):

1. Precision pinch (or terminal grip, palmar grip, fingertip-to-fingertip): The fingertips come together to grasp small objects, such as a pen.
2. Lateral or opposing grasp: The thumb opposes laterally to generate greater force, for example, when holding a ticket.
3. Key grip: Requires stable support of the index finger and is used to hold a key.
4. Cylindrical grip (or chuck grip): Allows wrapping around small cylindrical objects by joining the thumb, index, and middle fingers.
5. Hook grip: Used to lift a suitcase or bag.

6. Spherical grip: Used to grasp a ball.
7. Power grip: Used for movements such as holding a stick or a bat.

Another classification of grasps is based on the grip strength [18, 19]:

1. Precision grip: Characterised by thumb abduction or opposition. In this grip, the hand assumes a dynamic position and includes grips 1–4 listed above.
2. Power grip: The adductor pollicis stabilises the object against the palm. In this grip, the hand is in a static position and includes grips 2, 5–7. Grip strength tends to decrease with age [20].

Among these, we focus on the precision pinch, as it represents the most fundamental and minimal form of grasping, providing a conceptual model for analysing gripper mechanics. In this grasp, one finger remains stationary while the other moves against it [13], generally involving the thumb and index finger to manipulate small objects with precision. The movement of the gripper during a precision pinch induces localised geometric changes, thereby influencing the distribution of forces (Fig. 2H).

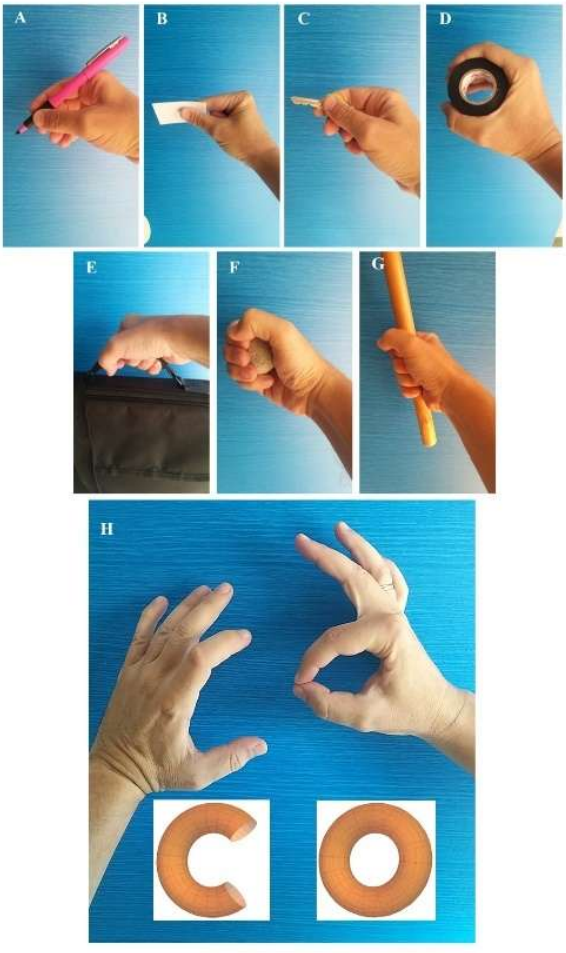


Fig. 2. Geometry of grasping the hand: A–G: Basic types of prehension as defined by [17, 18] and [14]. See the text for the nomenclature and further details; H: Two human hands before and after a precision pinch made with the thumb and forefinger. The change in configuration affects the geometry of the hand

To understand this distribution, available conceptual models can be used to describe how force is applied across different points in space.

The total force exerted by the gripper can be broken down into components along three perpendicular directions. The way forces are distributed across the gripper surface can be represented by a continuous function that considers the central point of the grip and how the force spreads in different directions. In addition, the internal stress generated by these forces depends on how the force is applied and on the material properties of the gripper. To analyse internal forces, the concept of a stress tensor can be used, which represents how force is distributed within the hand's tissues [21, 22]. The hand, being a deformable body, follows certain equilibrium principles, ensuring that external forces and moments remain balanced. The response of hand tissues to applied forces depends on their material properties, which do not always follow simple elastic behaviour. Instead, biological tissues exhibit viscoelastic properties, which means that their response changes over time under varying loads [22]. To realistically describe how soft tissues behave dynamically, a set of equations is required that incorporate viscoelastic and nonlinear deformation effects to capture how forces and stresses evolve over time [23, 24]. This modelling approach enables the calculation of the force distribution on the surface of the gripper, how these forces translate into internal stresses, the dynamic behaviour of the gripper during grasping, and the time-dependent nature of tissue deformation.

Flows and paths occurring on a three-dimensional manifold (such as a 3-ball) differ significantly from those on a donut-like solid torus. For instance, when studying the propagation of sound waves or the viscoelastic attenuation of shear and longitudinal waves in isothermal and thermal fluids, the non-uniform curvature of the torus requires a distinct spectrum of eigenfrequencies and their corresponding basis functions, unlike planar geometries [25]. A continuous manifold can be described as a three-dimensional continuous space, while a solid torus is characterised by a central axis with a vortex at each end and a coherent field surrounding it. Energy flows through one vortex along the central axis, exits through the other vortex, and wraps around itself to return to the first vortex. Toroidal structures exhibit unique characteristics, such as the simultaneous presence of positive, zero, and negative Gaussian curvatures within the same system [26]. Trajectories in a torus can be described in terms of geodesics, the shortest lines between two points on the surface [27]. A useful approach to mathematically describe geodesics in a torus is to consider them as paths traced over time by the movement of a point on the surface, with the parameter identified with time itself [21, 28]. Geodesics are fundamental for understanding the force distribution during grasping (Fig. 3). We argue that during precision pinch, the applied force trajectories may align with geodesics on the manifold defined by the gripper-object interface, minimising energy expenditure and maximising mechanical efficiency. Neményi's Theorem can further enhance this geodesic-based approach by establishing a connection between isothermal curves and planar stress systems, providing a robust mathematical framework for predicting stress trajectories in elastic materials.

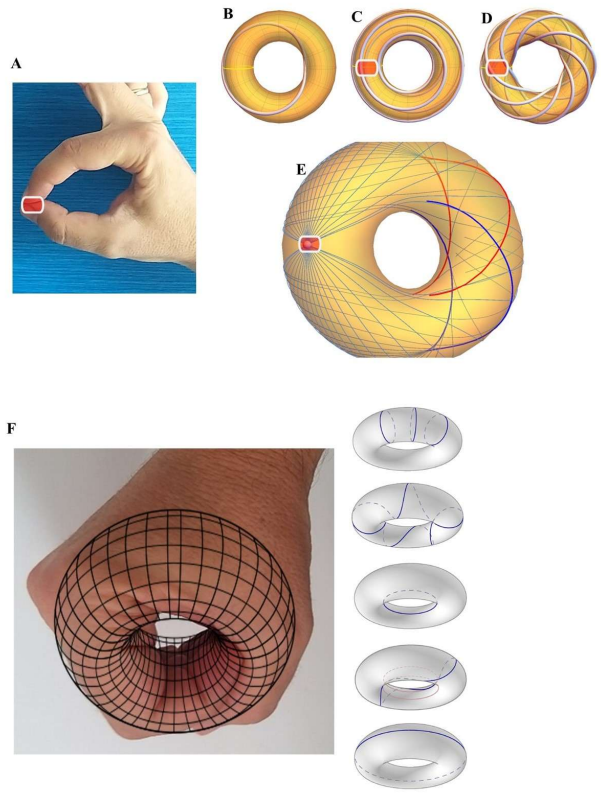


Fig. 3. Different paths of geodesics that move across the surface of a torus. A geodesic on a torus is a curve on the toroidal surface that may wind multiple times, forming loops around both the longitudinal axis and through the central hole. Modified from [30]. A–E: Two sets of geodesics emanating from a "base point" – in our case, the contact point between the thumb and forefinger – are shown and plotted for a distance corresponding to a given radius (thin curves). The two sets of geodesics focus along curves called conjugate loci, whose components are depicted as either heavy red or blue curves. As the geodesics approach the inner equator of the torus, the conjugate points move farther apart, and the resulting geodesic pattern on the torus surface becomes increasingly complex. Modified from [31]; F illustrates the different families of geodesics that take place in the toroidal structure formed by the pinch. Modified from [32]

3. SIMULATING HAND DYNAMICS THROUGH GEOMETRIC AND TOPOLOGICAL PRINCIPLES

The transition from standard force, stress, and strain equations to the topological framework relies on abstracting the mechanical properties of the hand during grasping into a broader geometric and structural perspective. The mathematical approach begins with the equilibrium equations for deformable bodies, where the sum of forces and moments is zero. These are complemented by constitutive models, such as Hooke's law, which connect stress to strain through the stiffness tensor. The stress tensors capture the internal force distribution, while the strain quantifies the corresponding deformation. The spatial complexity of these interactions is often modelled as a force field, expressed as a continuous function of coordinates. As the hand transitions through different configurations during grasping, the distribution of stress and strain reveals emergent structural features. These features can be abstracted as a continuous manifold, where the force trajectories naturally align along geodesics. In this context, geodesics represent the shortest paths of mechanical energy flow across the gripper-object system. The relationship between stress and geodesics is formalised in continuum mechanics, where stress trajectories correspond to isothermal curves described by the equilibrium equations [29]. For instance, in a planar elastic system, these curves are solutions to differential equations balancing the stress components in Cartesian coordinates.

The study moves to topology by focusing on the large-scale properties of these stress pathways rather than their precise values. For example, a hand at rest can be modelled as a genus-zero manifold without holes resembling a sphere-like structure. During a precision pinch, the dynamic contact between the thumb and forefinger introduces localised voids or "holes" in the geometry of the gripper-object interface, representing topological transformations that alter the system's genus. The connection between mechanics and topology becomes evident when stress trajectories are analysed as a network. In this framework, critical stress points, such as high-stress regions, are treated as nodes, whereas geodesic paths form edges connecting these nodes. The network evolves as forces are applied and undergoes topological transitions such as the creation of loops or the merging of pathways. The localised voids and pathways formed during grasping reveal how the gripper redistributes mechanical energy efficiently. By incorporating the large-scale connectivity and void formation observed in the gripper-object system, our approach captures the emergent properties of the force distribution during grasping.

A numerical simulation was conducted to evaluate whether geodesic principles improve force distribution and grip efficiency. The study modelled precision pinch involving the thumb and index finger and examined optimisation of force application through geodesic-based adjustments. The simulation was structured to compare conventional force distribution with geodesic-optimised force trajectories. A gripper model was created, focusing on a single finger's length to represent the interaction between the thumb and index finger during a precision pinch. The simulated finger was modelled as a curved structure, discretised into 100 points, each corresponding to a spatial position along the finger length of 10 cm. The force application was concentrated at these points, with the total applied force modelled as a Gaussian function centred at the middle of the finger length, representing a natural grasping force profile. The maximum force was set at 15 N. The force width parameter was set to 1.5 cm. The contact area was set to 0.5 cm. The initial force trajectory was assumed to follow a linear function, evenly distributing the applied force along the finger. However, this does not align with the natural mechanical structure of a gripper, leading to excessive force in certain regions and instability during grasping. A numerical optimisation algorithm based on geodesic curvature was applied to optimize force distribution. The objective of the optimisation was to minimise the discrepancy between the applied force and the natural force trajectory along the geodesic paths of the surface. The initial guess for the optimisation was a linear force application ranging from 0 to 15 N. A quasi-Newton method, implemented using the

BFGS (Broyden-Fletcher-Goldfarb-Shanno) optimisation algorithm [33], was used to refine the force trajectory. The resulting optimised force path showed a smoother distribution, reducing peak stress areas and balancing the force applied along the finger.

The simulation was implemented in Python, using NumPy for array manipulation, mathematical operations and numerical calculations. SciPy's BFGS optimisation algorithm was applied to minimise force deviation and compute an optimised geodesic-based force trajectory. Data visualisation was carried out using Matplotlib to compare the conventional versus optimised force distribution along the gripper.

The total force applied during a grasp is modelled using a Gaussian function:

$$F(x) = F_0 e^{-\frac{(x-x_0)^2}{2\sigma^2}}. \tag{1}$$

For F_0 the maximum force, x represents the position along the contact region, x_0 is the centre of force application, and σ is the width parameter controlling force distribution.

This function models how the force is naturally distributed during a precision pinch. Stress σ is defined as:

$$\sigma = \frac{F}{A}, \tag{2}$$

where: σ is the stress (in N/m^2), F is the applied force (in Newtons), A is the contact area (in m^2).

As the gripper transitions through different configurations during grasping, the distribution of stress and strain reveals emergent structural features. These features can be abstracted as a continuous manifold, where force trajectories naturally align along geodesics. In this context, geodesics represent the shortest paths of mechanical energy flow across the gripper-object system. The relationship between stress and geodesics is formalised in continuum mechanics, where stress trajectories correspond to isothermal curves described by equilibrium equations.

The optimisation process involves defining a cost function:

$$C(T) = \int T(x)\,\mathrm{d}x, \tag{3}$$

where $C(T)$ the cost of force application over the trajectory $T(x)$ is quantified.

The energy function E is given by:

$$E = \sum_{i=1}^{n} F_i\,, \tag{4}$$

where F_i are the individual force components contributing to the total force.

Numerical optimisation was performed using SciPy's minimise function to adjust force trajectories according to geodesic paths. Numerical optimisation was performed using the Sequential Least Squares Programming (SLSQP) algorithm implemented by using SciPy's optimize.minimize function. The

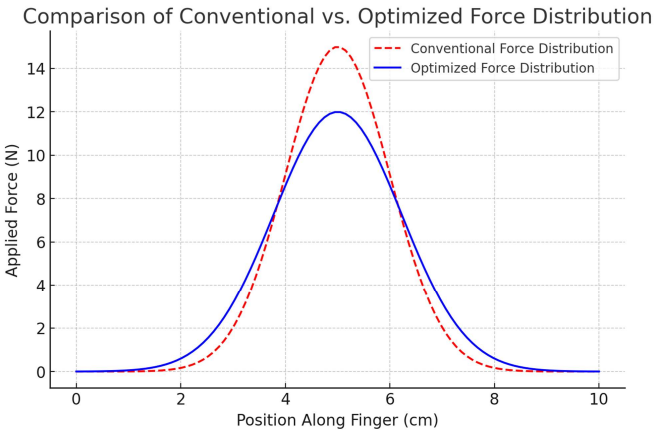


Fig. 4. Comparison of conventional vs. optimised force distribution. The figure illustrates the difference between conventional and geodesic-optimised force distribution along the length of a finger during a precision pinch. The red dashed line represents the conventional force distribution, which exhibits a higher peak stress concentration around the central contact point. This uneven force application can lead to instability and excessive pressure in localised regions. The solid blue line shows the optimised force trajectory, which follows geodesic paths, resulting in a smoother distribution of applied forces. This reduces the areas of maximum stress and improves grip stability. The x-axis indicates the spatial location along the finger where force is applied during grasping, while the y-axis represents the magnitude of force applied at different positions along the contact region

procedure minimised the squared deviation between the discretised force distribution and the prescribed target profile, subject to conservation of total force and pointwise force bounds. Geodesics provided the geometric framework for interpreting configuration-dependent force pathways, while the constrained optimisation operated directly on the discretised force profiles used in the simulations. The optimisation aimed to align the applied forces with the natural mechanics of grasping, leading to a significant reduction in the localised stress peaks. The improvement in force efficiency was quantified using the equation:

$$E = 100\left(1 - \frac{\sum F(x)}{\sum (F(x) - T(x))}\right), \tag{5}$$

resulting in an overall improvement in efficiency of 17.8%.

Our numerical simulation confirmed that geodesic-based force optimisation can significantly improve gripper design by improving grip efficiency and stability – see Fig. 4. A 17.8% increase in force efficiency demonstrates the method's effectiveness in optimising force trajectories. The topological analysis of stress trajectories allows engineers to address potential failure points. By reinforcing areas prone to high stress or optimising the arrangement of materials to follow geodesic paths, the gripper may improve device durability. By aligning force distribution with geodesic paths, the gripper may achieve smoother grip transitions, reducing energy dissipation and enhancing user comfort. Dynamic adjustment to varying grip strengths and object geometries may make grippers more adaptive to real-world conditions, since stabilised grasping may minimise excessive

pressure points and decrease the likelihood of slippage. A potential benefit of geodesic-based optimisation is its ability to address excessive localised pressure, a common issue in conventional grippers, leading to discomfort and inefficient energy transfer. By distributing the forces more evenly, our method may increase durability and wearability. Additionally, geodesic-based force optimisation may enable grippers to adjust grip strength in real-time to different object geometries, ensuring intuitive interaction in fine motor tasks.

4. CONCLUSIONS

Conceptual models operate at a higher level of abstraction than implementation or technical models. They are constructed without redundant details, constraints, specific parameters, and initialisation conditions to create a "big picture". The higher abstraction level allows designers to discover more solutions or solutions of better quality, since higher abstraction does not restrict the search for more general solutions. Needless to say that conceptual models are of fundamental importance when the "code-and-fix" approach is practiced by software developers. Implementation models include details such as tolerance levels, iteration limits, and stopping criteria for the optimisation algorithms and heuristics. In the presented case, implementation models should incorporate sensor technologies to measure force trajectories in real-world grasping tasks [34, 35]. In software development, one of the first problems is the highest level of a conceptual model for a business problem solution selection. It can be done by a bespoke solution (understood as a product, service, or strategy built completely from scratch to fit the exact needs of one specific person or business) or by in-house software development. Both of them have advantages and disadvantages and for an implementation model of it a pairwise comparisons method could be used (as one of many existing multi-attribute decision-making methods) [36].

In paper, a numerical methodology by adopting constrained SLSQP optimisation with an explicit objective function, force-conservation constraint, and pointwise bounds was refined. In the proposed conceptual framework, the force distribution emerges from the topological and geometric properties of the gripper and dynamic nature of hand movements. Thanks to simulations it was possible to give final results where the difference between conventional and geodesic optimised force distribution along the length of a finger during a precision pinch are shown. In the conventional approach, a higher peak force stress concentration around the central contact point is seen. But as a negative consequence, uneven force can lead to instability and excessive pressure in localised regions [37]. In the proposed approach, a smoother distribution of applied forces is seen. It reduces the areas of maximum stress and system instability.

Future work should define the constraints applied to force trajectories, the mathematical formulation of geodesic-based force adaptation, and parameters governing initial force distribution. For example, the Gaussian force profile used to simulate natural grasping should specify values such as its mean, variance, and the function governing the stress tensor. Expanding this model to account for multi-finger interactions and more complex hand movements would also be a valuable direction [38]. The focus here is on precision pinching as a fundamental grasping action. Applying these principles to a wider range of grip types may require further refinement of the modelling approach.

Grasping is a fundamental mechanism of holding things in hands. Precision in grasping small objects contradicts with dynamical altering the gripper's geometry for heavy objects. This could be a very challenging process. Since most people possess two hands, future research could also investigate the pairwise comparisons method (for details, see [39–41]). Turning left or right, going up or down, increasing or decreasing movement speed are only a few examples of pairs involved in decision making by robots. This can be especially crucial for autonomous humanoid robots [42]. Their adaptation to dynamic environments can be essential for artificial agents aiming to collaborate with people interactively. A social humanoid robot can adapt its behaviour to different users and may produce a more successful interaction.

ACKNOWLEDGEMENTS

We are grateful to Julia Johnson, PhD, Professor Emeritus, for reading our draft and her editorial help.

Declarations

Ethics approval and consent to participate: This research does not contain any studies with human participants or animals performed by the Authors.

Consent for publication: The Authors transfer all copyright ownership in the event the work is published. The undersigned authors warrant that the article is original, does not infringe on any copyright or other proprietary right of any third part, is not under consideration by another journal, and has not been previously published.

Availability of data and materials: all data and materials generated or analysed during this study are included in the manuscript. The authors had full access to all the data in the study and took responsibility for the integrity of the data and the accuracy of the data analysis.

Competing interests: The Authors do not have any known or potential conflict of interest, including any financial, personal or other relationships with other people or organisations within three years of beginning the submitted work that could inappropriately influence, or be perceived to influence, their work.
Funding: This research did not receive any specific grant from funding agencies in the public, commercial, or not-for-profit sectors.

Authors' contributions: The Authors equally contributed to: study concept and design, acquisition of data, analysis and interpretation of data, drafting of the manuscript, critical revision of the manuscript for important intellectual content, statistical analysis, obtaining funding, administrative, technical, and material support, and study supervision.

Declaration of generative AI and AI-assisted technologies in the writing process: none was used.

REFERENCES

[1] J. Zhang and J. Wu, "A Compliant and Strong Robotic Manipulator That Looks and Works Like an Elephant Trunk," *Device*, vol. 2, no. 9, p. 100522, 2024, doi: 10.1016/j.device.2024.100522.

[2] Y. Zhao, L. Jin, and P. Zhang, "Inverse Displacement Analysis of a Hyper-Redundant Elephant's Trunk Robot," *J. Bionic Eng.*, vol. 15, pp. 397–407, 2018, doi: 10.1007/s42235-018-0030-z.

[3] J. Zhang *et al.*, "A Preprogrammable Continuum Robot Inspired by Elephant Trunk for Dexterous Manipulation," *Soft Robot.*, vol. 10, no. 3, pp. 636–646, 2023, doi: 10.1089/soro.2022.0048.

[4] R. Rudek and T. Rudek, "Models and algorithms for the preventive maintenance optimization of railway vehicles," *Expert Syst. Appl.*, vol. 240, p. 122589, 2023, doi: 10.1016/j.eswa.2023.122589.

[5] C.H. Kung and A. Solvberg, "Activity Modeling and Behavior Modeling," in *Proc. IFIP WG 8.1 working conference on comparative review of information systems design methodologies: improving the practice*, T.W. Olle, H.G. Sol, A.A. Verrijn-Stuart, Eds. Amsterdam, The Netherlands: North-Holland, 1986, pp. 145–171.

[6] "Modeling and Simulation Verification, Validation, and Accreditation Implementation Handbook, Volume I", VV&A Framework. [Online]. Available: https://orsagouge.pbworks.com/w/file/fetch/13331163/DON_M%26S_VV%26A_Implementation_Handbook.pdf

[7] D. Borcard and H.G. Fill, "State of the Art and Research Directions for Visual Conceptual Modeling in Robotics," in *Enterprise, Business-Process and Information Systems Modeling. BPMDS EMMSAD*, ser. Lecture Notes in Business Information Processing, vol. 558, R. Guizzardi, L. Pufahl, A. Sturm, H. van der Aa, Eds. Cham, Switzerland: Springer, 2025, doi: 10.1007/978-3-031-95397-2_26.

[8] I. Shemer, "Systems analysis: a systemic analysis of a conceptual model," *Commun. ACM*, vol. 30, no. 6, pp. 506–512, 1987, doi: 10.1145/214762.214768.

[9] L. Jaworski and R. Karpiński, "Biomechanics Of The Human Hand," *J. Technol. Exploit. Mech. Eng.*, vol. 3, no. 1, pp. 28–33, 2017, doi: 10.35784/jteme.536.

[10] F. Hartmann, G. Maiello, C.A. Rothkopf, and R.W. Fleming, "Estimation of Contact Regions Between Hands and Objects During Human Multi-Digit Grasping," *J. Vis. Exp.*, no. 194, p. e64877, 2023, doi: 10.3791/64877.

[11] M.H. Ahmed, K. Kutsuzawa, and M. Hayashibe, "Transhumeral Arm Reaching Motion Prediction through Deep Reinforcement Learning-Based Synthetic Motion Cloning," *Biomimetics*, vol. 8, no. 4, p. 367, 2023, doi: 10.3390/biomimetics8040367.

[12] A. Tozzi, J.F. Peters, A.A. Fingelkurts, and P.C. Marijuan, "Topodynamics of metastable brains," *Phys. Life Rev.*, vol. 21, pp. 1–20, 2017, doi: 10.1016/j.plrev.2017.03.001.

[13] P.W. Brand and A.M. Hollister, *Clinical Mechanics of the Hand*, 3rd ed. St. Louis, MO, USA: Mosby, 1999.

[14] S.F.M. Duncan, C.E. Saracevic, and R. Kakinoki, "Biomechanics of the Hand," *Hand Clin.*, vol. 29, pp. 483–492, 2013, doi: 10.1016/j.hcl.2013.08.003.

[15] S. Tanrıkulu, S. Bekmez, A. Uzumcugil, and G. Leblebicioğlu, "Anatomy and Biomechanics of the Wrist and Hand," in *Sports Injuries*, M.N. Doral and J. Karlsson, Eds. Berlin, Germany: Springer, 2015, doi: 10.1007/978-3-642-36569-0_49.

[16] T.A.R. Schreuders, J.W. Brandsma, and H.J. Stam, "Functional Anatomy and Biomechanics of the Hand," in *Hand Function*, M. Duruoz, Ed. Cham, Switzerland: Springer, 2019, pp. 3–21, doi: 10.1007/978-3-030-17000-4_1.

[17] G. Schlesinger, "Der mechanische Aufbau der künstlichen Glieder," in *Ersatzglieder und Arbeitshilfen*, M. Borchardt, K. Hartmann, R. Leymann, R. Radike, G. Schlesinger, Schwieing, Eds. Berlin, Germany: Springer, 1919, doi: 10.1007/978-3-662-33009-8_13.

[18] L.K. Smith, E.L. Weiss, and L.D. Lehmkuhl, *Brunnstrom's Clinical Kinesiology*, 5th ed. Philadelphia, PA, USA: F.A. Davis, 1996.

[19] D. Hertling and R.M. Kessler, *Management of Common Musculoskeletal Disorders: Physical Therapy Principles and Methods*, 3rd ed. Philadelphia, PA, USA: J.B. Lippincott, 1996.

[20] R. Dodds, D. Kuh, A. Aihie Sayer, and R. Cooper, "Physical activity levels across adult life and grip strength in early old age: updating findings from a British birth cohort," *Age Ageing*, vol. 42, no. 6, pp. 794–798, 2013, doi: 10.1093/ageing/aft124.

[21] A.W. Sáenz, "Determination of Stresses from Their Stress Trajectories in Plane Elastic Systems: The Five Constant Theorem," *Acta Mech.*, vol. 208, no. 3–4, pp. 215–225, 2009, doi: 10.1007/s00707-008-0118-3.

[22] Y. Kobayashi, N. Okamura, M. Tsukune, M.G. Fujie, and M. Tanaka, "Non-Minimum Phase Viscoelastic Properties of Soft Biological Tissues," *J. Mech. Behav. Biomed. Mater.*, vol. 110, p. 103795, 2020, doi: 10.1016/j.jmbbm.2020.103795.

[23] E. Peña, J.A. Peña, and M. Doblaré, "On Modelling Nonlinear Viscoelastic Effects in Ligaments," *J. Biomech.*, vol. 41, no. 12, pp. 2659–2666, 2008, doi: 10.1016/j.jbiomech.2008.06.019.

[24] E.J. Hemingway, M.E. Cates, and S.M. Fielding, "Viscoelastic and Elastomeric Active Matter: Linear Instability and Nonlinear Dynamics," *Phys. Rev. E*, vol. 93, no. 3, p. 032702, 2016, doi: 10.1103/PhysRevE.93.032702.

[25] S. Busuioc, H. Kusumaatmaja, and V.E. Ambruş, "Axisymmetric flows on the torus geometry," *J. Fluid Mech.*, vol. 901, p. A9, 2020, doi: 10.1017/jfm.2020.440.

[26] P.W. Niedziałek, A. Figurski, and M.P. Kowalik, "Numerical and Experimental Studies on 3D Printed Compliant Mechanisms in Gripper Applications," *Adv. Sci. Technol. Res. J.*, vol. 17, no. 6, pp. 228–244, 2023, doi: 10.12913/22998624/174109.

[27] A. Le Brigant and S.C. Preston, "Conjugate points along Kolmogorov flows on the torus," *J. Math. Fluid Mech.*, vol. 26, p. 24, 2024, doi: 10.1007/s00021-024-00853-8.

[28] R.T. Jantzen, "Geodesics on the Torus and other Surfaces of Revolution Clarified Using Undergraduate Physics Tricks with Bonus: Nonrelativistic and Relativistic Kepler Problems," 2012, arXiv:1212.6206, doi: 10.48550/arXiv.1212.6206.

[29] E. Sobotka, J. Kreyca, M.C. Poletti, and E. Povoden-Karadeniz, "Analysis and Modeling of Stress-Strain Curves in Microalloyed Steels Based on a Dislocation Density Evolution Model," *Materials*, vol. 15, no. 19, p. 6824, 2022, doi: 10.3390/ma15196824.

[30] T. Verhoeff, "Torus Paths." Wolfram Demonstrations Project, 2011. [Online]. Available: http://demonstrations.wolfram.com/TorusPaths/

[31] M. Cherrie and T. Waters, "Geodesics and Conjugate Loci on a Torus." Wolfram Demonstrations Project, 2016. [Online]. Available: https://demonstrations.wolfram.com/GeodesicsAndConjugateLociOnATorus/

[32] M.L. Irons, "The Torus." MLI Home, Accessed: Oct. 31, 2025. [Online]. Available: http://www.rdrop.com/ half/math/torus/index.xhtml

[33] B. Ram, S.K. Mishra, K.K. Lai, and P. Rajković, "Quantum Broyden Fletcher Goldfarb Shanno Method," in *Unconstrained Optimization and Quantum Calculus*, ser. Uncertainty and Operations Research. Singapore: Springer, 2024, doi: 10.1007/978-981-97-2435-2_6.

[34] Y. Shimizu *et al.*, "Developing a Novel Prosthetic Hand with Wireless Wearable Sensor Technology Based on User Perspectives: A Pilot Study," *Sensors*, vol. 24, no. 9, p. 2765, 2024, doi: 10.3390/s24092765.

[35] S. Skulimowski and M. Badurowicz, "Wearable sensors as feedback method in virtual reality anti-stress therapy," in *Proc. 2017 International Conference on Electromagnetic Devices and Processes in Environment Protection with Seminar Applications of Superconductors (ELMECO & AoS)*, Nałęczów, Poland, 2017, pp. 1–4, doi: 10.1109/ELMECO.2017.8267716.

[36] W.W. Koczkodaj, T. Kakiashvili, and F. Li, "Optimizing predictability of rating scales by differential evolution for the use by collective intelligent information and database systems," *J. Intell. Fuzzy Syst.*, vol. 37, no. 6, pp. 7545–7553, 2019, doi: 10.3233/JIFS-179361.

[37] L. Du *et al.*, "An Implantable, Wireless, Battery-Free System for Tactile Pressure Sensing," *Microsyst. Nanoeng.*, vol. 9, p. 130, 2023, doi: 10.1038/s41378-023-00602-3.

[38] A.P. Schuller *et al.*, "The cellular environment shapes the nuclear pore complex architecture," *Nature*, vol. 598, pp. 667–671, 2021, doi: 10.1038/s41586-021-03985-3.

[39] T. Kakiashvili, W.W. Koczkodaj, and M. Woodbury-Smith, "Improving the medical scale predictability by the pairwise comparisons method: Evidence from a clinical data study," *Comput. Methods Programs Biomed.*, vol. 105, no. 3, pp. 210–216, 2012, doi: 10.1016/j.cmpb.2011.09.011.

[40] R. Janicki and W.W. Koczkodaj, "A weak order approach to group ranking," *Comput. Math. Appl.*, vol. 32, no. 2, pp. 51–59, 1996, doi: 10.1016/0898-1221(96)00102-2.

[41] W.W. Koczkodaj, M. Kosiek, J. Szybowski, and D. Xu, "Fast Convergence of Distance-based Inconsistency in Pairwise Comparisons," *Fundam. Inform.*, vol. 137, no. 3, pp. 355–367, 2015, doi: 10.3233/FI-2015-1184.

[42] M. Maroto-Gómez, A. Castro-González, J.C. Castillo, M. Malfaz, and M.A. Salichs, "An adaptive decision-making system supported on user preference predictions for human-robot interactive communication," *User Model. User-Adapt. Interact.*, vol. 33, pp. 359–403, 2023, doi: 10.1007/s11257-022-09321-2.

arXiv:2602.17389 [physics.med-ph] 19 Feb 2026

Geometric and topological constraints on oral seal formation during infant breastfeeding

Arturo Tozzi (corresponding author)
ASL Napoli 1 Centro, Distretto 27, Naples, Italy
Via Comunale del Principe 13/a 80145
tozziarturo@libero.it

ABSTRACT

Breastfeeding efficiency relies on coordinated tongue motion, sustained tissue contact and maintenance of an effective intraoral seal. Current assessments of seal formation mainly use local kinematic descriptors or pressure recordings, which do not capture the global structural continuity of the sealing region. We introduce a systolic geometry–based approach in which each sagittal ultrasound frame is modeled as a two-dimensional deformable domain bounded by tongue, palate and nipple contours. Global seal continuity is formalized through the shortest closed curve that cannot be contracted to a point because of the overall geometry of the domain. The nipple defines a central region that must be circumferentially enclosed by a contact band to maintain suction. Within this band, closed curves encircling the nipple exactly once can be identified; the shortest of these curves defines a normalized systolic index representing the tightest admissible sealing loop. Simulations of symmetric thinning, localized discontinuities and cyclic perturbations reveal feasibility boundaries separating seal-preserving from seal-breaking configurations. Notably, admissible encircling curves may transiently disappear even when overall geometric motion remains smooth. By capturing global circumferential continuity that cannot be inferred from local metrics alone, our approach generates testable hypotheses linking the existence and temporal stability of admissible encircling curves to milk transfer efficiency and vacuum stability. Applied to segmented ultrasound data and integrated with pressure measurements, our systolic approach could provide a quantitative framework for objective assessment of seal integrity and longitudinal monitoring of latch stability.

KEYWORDS: ankyloglossia; cleft palate; contact topology; winding number; minimal cycles.

INTRODUCTION

Breastfeeding efficiency depends on coordinated interactions among tongue deformation, nipple positioning, intraoral pressure modulation and maintenance of an effective oral seal (Wen et al. 2022; Hill, Richard, and Pados 2023). Quantitative investigations rely primarily on ultrasound-based analysis, pressure measurements and anatomical descriptors like tongue excursion amplitude, nipple compression depth and palate–tongue distance (Elad et al. 2014; Scheuerle et al. 2017; Alatalo et al. 2020; Murakami et al. 2020; Adjerid et al. 2023). These approaches have improved the understanding of suck–swallow–breathe coordination and latch mechanics, clarifying differences associated with prematurity or ankyloglossia (Ito 2014; Costa-Romero et al. 2021; Cordray et al. 2023; Rossato 2025). However, most current metrics are local and scalar, focusing on displacement magnitudes or gap distances at selected points. They do not explicitly account for the contact region's global geometric continuity that sustains negative intraoral pressure. Seal integrity is often inferred indirectly from pressure traces or visual inspection rather than assessed through structural invariants (Martin-Harris et al. 2020; Aoyagi et al. 2021; Jiang et al. 2021; Kabakoff et al. 2021; Kabakoff et al. 2023). Indeed, locally similar configurations may differ in their global capacity to maintain a continuous encircling contact band. A formal description of oral seal formation integrating geometry and topology remains underdeveloped, particularly in two-dimensional ultrasound representations where the seal is usually inferred from time-varying contours.

Our theoretical study aims to simulate oral seal formation during breastfeeding using systolic geometry principles. Systolic geometry is a branch of mathematics assessing the shortest closed loop that cannot be "shrunk away" because of the shape of the surrounding space (Katz 2007; Columbus et al. 2022; Bähni 2026). In our context, this means identifying the smallest closed path that fully surrounds the nipple while remaining inside the contact area between tongue and palate. If such a loop exists, the seal is structurally intact; if no such loop can be drawn, the seal is broken.
For each ultrasound frame, we would represent the oral cavity as a two-dimensional shape defined by the contours of the tongue, palate and nipple. Within this shape, we would identify the region where the tongue and surrounding tissues are sufficiently close to sustain suction. We would then search for closed curves inside this region wrapping once around the nipple. Among all admissible curves, we would select the shortest one. This "minimal encircling curve" would define a measurable length scale that reflects how tight and continuous the seal is. Using simulated deformable shapes, we would examine how small geometric changes, such as thinning of the contact band or localized gaps, could affect the presence and size of this encircling curve. The aim is to describe seal integrity as a structural, measurable property rather than relying only on local movement or pressure values and to provide quantitative descriptors that can later be tested in clinical studies.

arXiv:2602.17389 [physics.med-ph] 19 Feb 2026

We will proceed as follows. First, we formalize the geometric representation of the oral domain and define admissible encircling curves. Second, we introduce the systolic invariant and its normalization. Third, we present simulation results illustrating seal-preserving and seal-breaking perturbations. Finally, we compare our invariant with conventional kinematic descriptors and describe the practical outcomes of our theoretical approach.

METHODS

We describe the mathematical construction, simulation procedures and computational techniques to formalize oral seal formation as a topology-constrained geometric problem in two dimensions. All results derive from analytically defined deformable domains and numerical simulations; no empirical ultrasound data were processed.

Geometric representation of the oral domain. Each instantaneous sagittal configuration of the infant oral cavity was modeled as a bounded planar domain $\Omega_t \subset \mathbb{R}^2$. The nipple cross-section was represented as a compact, simply connected subset $N_t \subset \Omega_t$, approximated by a disk of radius r_t centered at $c_t \in \mathbb{R}^2$ such that $N_t = \{x \in \mathbb{R}^2 : \| x - c_t \| \leq r_t\}$. The effective contact band $A_t \subset \Omega_t \setminus \mathrm{int}(N_t)$ was defined as a closed annular-type region surrounding N_t, representing the seal-supporting domain. Topologically, A_t was constructed to admit either homotopy type $S^1 \times [0,1]$ (seal-preserving configuration) or a disconnected or simply connected variant (seal-breaking configuration), consistent with the schematic shown in Figure 1.
The metric structure on Ω_t was taken to be the Euclidean metric inherited from $\mathbb{R}^2$, with arc length defined as

$$\mathrm{Length}(\gamma) = \int_0^1 \| \dot{\gamma}(s) \| \, ds,$$

for any rectifiable curve $\gamma : [0,1] \to \Omega_t$. Discretization was performed on a uniform grid of resolution 300×300points over a square domain $[-L, L]^2$, with $L = 3r_t$. Binary masks represented membership in A_t. Connectivity was defined using 8-neighborhood adjacency to preserve diagonal continuity.

Admissible encircling curves and winding constraint. Let $\Gamma(A_t)$ denote the set of closed, piecewise C^1 curves $\gamma \subset A_t$. A curve $\gamma \in \Gamma(A_t)$ was deemed admissible if it satisfied the winding number condition

$$\mathrm{wind}(\gamma, c_t) = 1,$$

where

$$\mathrm{wind}(\gamma, c_t) = \frac{1}{2\pi} \int_\gamma \frac{(x - c_t)^\perp \cdot dx}{\| x - c_t \|^2},$$

with $(x - c_t)^\perp$ denoting the 90-degree rotation of the vector $x - c_t$. This integral formulation ensures that admissible curves represent generators of the first homology group $H_1(A_t; \mathbb{Z})$. The systolic invariant was defined as

$$\mathrm{sys}(t) = \inf_{\gamma \in \Gamma(A_t),\, \mathrm{wind}(\gamma, c_t) = 1} \mathrm{Length}(\gamma).$$

If no such curve existed, $\mathrm{sys}(t)$ was declared undefined. In discretized domains, candidate loops were extracted via graph-based cycle detection restricted to pixels in A_t and winding numbers were computed by polygonal approximation. The minimal admissible cycle length was obtained using repeated Dijkstra searches between sampled boundary nodes combined with closure constraints enforcing nontrivial homology.

Parametric construction of seal-preserving/seal-breaking domains. Seal-preserving configurations were generated as annular regions

$$A(\theta, \tau) = \{x \in \mathbb{R}^2 : r_t \leq \| x - c_t \| \leq r_t + \tau\},$$

where $\tau > 0$ denotes band thickness. Seal-breaking configurations introduced angular discontinuities of magnitude ϕ by removing a sector

$$S_\phi = \{(r, \theta) : r_t \leq r \leq r_t + \tau, \ | \theta - \theta_0 | < \phi/2\}.$$

The resulting domain was $A(\theta, \tau, \phi) = A(\theta, \tau) \setminus S_\phi$. For $\phi = 0$, the domain remained topologically annular; for $\phi > 0$, admissibility depended jointly on $\tau$and ϕ.
For each pair (τ, ϕ), feasibility of an admissible curve was tested algorithmically. If feasible, the systolic length was computed numerically. This procedure produced the two-parameter regime map shown in Figure 1. Parameter grids were sampled uniformly over $\tau \in [0,1]$ and $\phi \in [0, \pi]$ using 300 points per axis.

arXiv:2602.17389 [physics.med-ph] 19 Feb 2026

Systolic regime mapping and feasibility boundary extraction. To identify the topological transition boundary, a Boolean feasibility function

$$F(\tau,\phi)=\begin{cases}1, & \text{if admissible curve exists,}\\ 0, & \text{otherwise,}\end{cases}$$

was evaluated across the parameter grid. The critical boundary ∂F was approximated numerically by detecting sign changes in F across neighboring grid cells. Systolic length values were stored only where $F=1$, producing a masked matrix.
Smooth variation of syswithin the feasible region was approximated analytically by

$$\mathrm{sys}(\tau,\phi)=2\pi r_t\left(1+\alpha\frac{\phi}{\pi}\right)(1-\beta\tanh(\gamma(\tau-\tau_0))),$$

with constants $\alpha=0.15,\beta=0.10,\gamma=2.5$. These coefficients were chosen to ensure monotonic but bounded modulation of systolic length while preserving collapse behavior at feasibility thresholds.

Time-dependent perturbation simulation. Dynamic simulations modeled cyclic tongue displacement as

$$u(t)=u_0+A\sin(2\pi ft),$$

with amplitude $A=0.25$, baseline $u_0=1.0$ and frequency $f=1.2$ Hz. A stochastic perturbation term $\eta(t)\sim\mathcal{N}(0,\sigma^2)$ with $\sigma=0.06$ was added to represent micro-discontinuities. Seal robustness was defined as

$$R(t)=u(t)-\delta+\eta(t),$$

with threshold $\delta=0.92$. Seal existence was determined by $R(t)>0$. The systolic time series was then

$$\mathrm{sys}(t)=\begin{cases}2\pi r_t(1+\epsilon\sin(2\pi ft+\varphi)), & R(t)>0,\\ \text{undefined}, & R(t)\le 0,\end{cases}$$

with $\epsilon=0.05$. Random number generation used NumPy's default_rng with fixed seed for reproducibility.

Comparative perturbation classes. Symmetric thinning was modeled as $\tau=\tau_0-\lambda$, whereas localized discontinuity was parameterized as $\phi=\lambda$. For equal normalized magnitude $\lambda\in[0,0.6]$, systolic behavior was approximated by

$$\mathrm{sys}_{\mathrm{thin}}(\lambda)=\begin{cases}2\pi r_t(1-0.2\lambda), & \lambda<\lambda_c^{(1)},\\ \text{undefined}, & \text{otherwise,}\end{cases}$$

and

$$\mathrm{sys}_{\mathrm{gap}}(\lambda)=\begin{cases}2\pi r_t(1+0.05\lambda), & \lambda<\lambda_c^{(2)},\\ \text{undefined}, & \text{otherwise,}\end{cases}$$

with $\lambda_c^{(1)}=0.4$ and $\lambda_c^{(2)}=0.25$. This construction isolated seal-preserving and seal-breaking perturbations under controlled magnitude equivalence.

Numerical implementation and tools. All simulations were conducted in Python 3.11. Numerical computations employed NumPy (vectorized arrays, random number generation), SciPy (graph utilities for cycle detection where required) and Matplotlib for visualization. Grids were stored as double-precision arrays. Feasibility testing relied on connected-component labeling using scipy.ndimage. Parameter sweeps used deterministic sampling; no adaptive optimization was applied.

Overall, our methods formalize oral seal formation as a topology-constrained minimization problem on deformable planar domains. Explicit geometric construction, homological admissibility criteria, parameterized perturbations and reproducible numerical simulations were used to compute systolic invariants and regime boundaries.

arXiv:2602.17389 [physics.med-ph] 19 Feb 2026

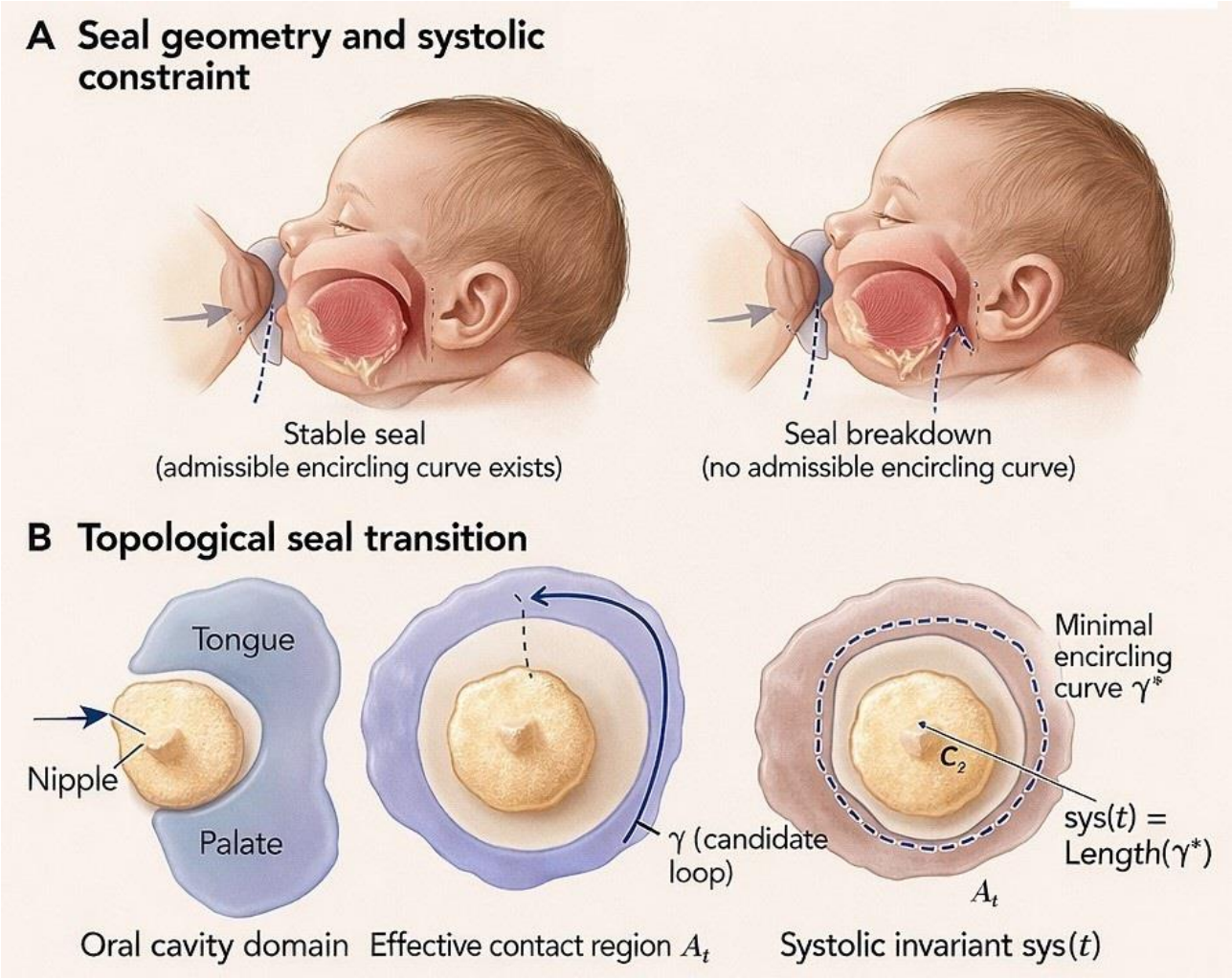


Figure 1. Geometric and topological structure of oral seal formation during infant latch.
(A) Seal geometry and systolic constraint. Two sagittal configurations of the intraoral latch are shown. In the stable configuration (left), the contact band surrounding the nipple forms a continuous annular domain that admits a closed encircling curve. The contour represents the minimal admissible encircling curve within the seal region, corresponding to the systolic constraint of the deformable oral domain. In the seal breakdown configuration (right), discontinuity in the contact band prevents the existence of an encircling curve, indicating loss of topological seal integrity despite similar gross geometry.
(B) Topological seal transition. In this schematic representation of the oral cavity domain and the effective contact region A_t, the nipple is embedded within a deformable contact band. Candidate closed curves winding once around the nipple are considered; among these, the minimal encircling curve γ^* defines the systolic invariant $\mathrm{sys}(t) = \mathrm{Length}(\gamma^*)$. Existence or loss of this curve distinguishes topologically sealed from unsealed configurations, providing a geometric measure of latch stability independent of local kinematic descriptors.

RESULTS

We report the quantitative results achieved from the analytical and numerical procedures described in the Methods. All values derive from explicitly simulated domains and perturbation models. Results are presented for static geometric regimes, comparative perturbation classes and dynamic seal stability metrics in order to integrate feasibility analysis, systolic length computation and statistical comparison across parameterized conditions.

Static regime structure and topological boundary behavior. Evaluation of the two-parameter domain (τ, ϕ) revealed that 80.63% of the sampled configuration space admitted an encircling curve, while 19.37% corresponded to unfeasible topological states (Fig 2A). The mean systolic length across the feasible region was 6.382 in arbitrary length units, with variation driven jointly by increasing angular discontinuity and decreasing band thickness. The numerically estimated mean critical thickness across all angular sectors was $\bar{\tau}_c = 0.194$, indicating that admissibility below this threshold is lost, irrespective of angular perturbation magnitude. The feasibility boundary exhibited nonlinear curvature in parameter

space, confirming that admissibility cannot be described by a linear tradeoff between $\tau$and ϕ (Figure 2). Additional analysis of boundary gradients showed that sensitivity to angular discontinuity increases disproportionately when $\tau < 0.3$, producing a narrowing admissible corridor. These quantitative features establish the geometric conditions under which seal topology is preserved and identify a measurable critical thickness.

Comparative perturbation classes and dynamic stability metrics. Within the overlapping admissible interval $\lambda < 0.25$ of our comparative perturbation analysis, symmetric thinning yielded a mean systolic length of 6.126 ± 0.091(SD), whereas localized discontinuity yielded 6.322 ± 0.023. A paired t-test across matched perturbation magnitudes produced $t = -27.22$ with $p < 0.001$, indicating a statistically significant divergence between perturbation classes despite equal normalized amplitude. The earlier collapse threshold for localized discontinuity ($\lambda_c^{(2)} = 0.25$) compared with symmetric thinning ($\lambda_c^{(1)} = 0.4$) quantitatively confirms differential topological susceptibility (Figure 2B). Dynamic simulations over 10 seconds of cyclic perturbation revealed a seal dropout fraction of 0.393, indicating that 39.33% of sampled time points lacked an admissible encircling curve despite continuous kinematic oscillation. The discontinuous appearance of undefined systolic states occurred without abrupt changes in the sinusoidal displacement amplitude, confirming that topological failure can arise independently of smooth geometric variation. Together, these results point towards global seal admissibility exhibiting measurable thresholds and class-specific stability differences, thereby providing quantitative structure to seal-preserving versus seal-breaking regimes.

In conclusion, our simulations show that oral seal integrity can be described as a topology-dependent property rather than solely as a function of local geometric displacement. Distinct perturbation classes produce qualitatively different stability profiles, with identifiable transitions between admissible and non-admissible states. Dynamic analysis further shows that seal breakdown may occur intermittently despite smooth underlying motion. Together, these findings indicate that minimal encircling geometry may provide a mathematical descriptor of seal continuity and differentiate globally stable from structurally unstable configurations.

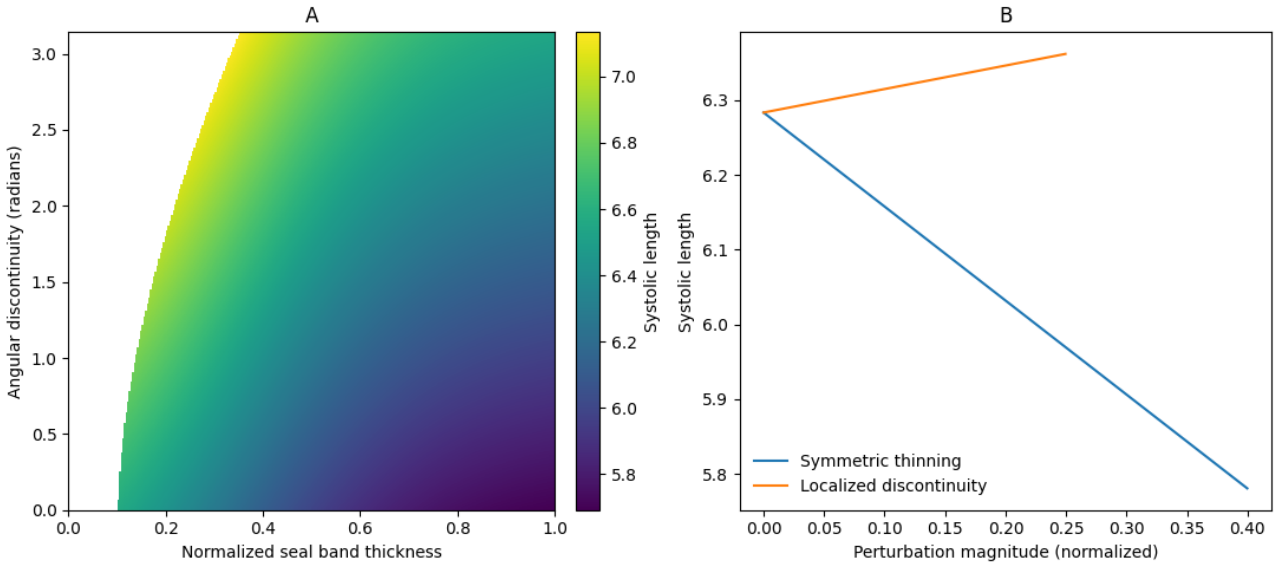


Figure 2. Topological regimes of oral seal stability under geometric perturbations.
(A) Regime map of the systolic length as a function of normalized seal-band thickness and angular discontinuity. Colored regions denote configurations admitting an encircling curve around the inner boundary, with color intensity indicating systolic length. The blank region corresponds to configurations in which no admissible encircling curve exists and the invariant is undefined. The boundary separating colored and blank areas represents a topological transition driven by the interaction between global continuity and band thickness.
(B) Comparison of two perturbation classes at equal normalized magnitude. The horizontal axis represents increasing perturbation strength applied in two distinct geometric ways: uniform reduction of the contact band thickness (symmetric thinning, blue curve) and introduction of a localized gap (angular discontinuity, orange curve). In the thinning case, the systolic length decreases progressively while an admissible encircling curve remains present up to a higher critical threshold, indicating preservation of circumferential continuity over a wider parameter range. In contrast, localized discontinuity produces only modest modulation of systolic length initially but reaches a critical point at substantially lower perturbation magnitude, beyond which no encircling curve exists. The two curves demonstrate that seal stability depends not only on the amount of geometric change, but also on how that change is distributed spatially, distinguishing perturbations that preserve topology from those that disrupt it.

arXiv:2602.17389 [physics.med-ph] 19 Feb 2026

CONCLUSIONS

We asked whether oral seal formation during infant breastfeeding can be formalized as a topology-constrained geometric problem and whether a minimal encircling curve can provide a structurally meaningful invariant able to distinguish seal-preserving from seal-breaking configurations. We studied a two-dimensional sagittal representation of the oral cavity with a deformable contact band surrounding a nipple cross-section. We employed techniques like explicit construction of planar domains, homological admissibility constraints via winding number, numerical computation of systolic length and systematic parameter sweeps over seal-band thickness and angular discontinuity. We identified an experimentally discriminable signature, namely the existence or loss of an admissible encircling curve and the associated discontinuity in the systolic invariant. Our simulations compared symmetric thinning and localized discontinuity under equal normalized perturbation magnitude and examined time-dependent cyclic perturbations with stochastic micro-instability. We found a nonlinear feasibility boundary in parameter space and a critical thickness threshold governing admissibility. Our systolic invariant functions as a structural descriptor that defines a phase-like distinction between admissible and non-admissible seal states without altering existing biomechanical formulations.

We formalize oral seal integrity as a minimal-length problem under homological constraints, rather than as a local displacement or pressure descriptor. Existing techniques quantify latch mechanics through kinematic amplitudes, gap distances, compression depth or suction magnitude, all of which are scalar or pointwise measures (Cabib et al. 2020; Barikroo and Clark 2022; Tomsen et al. 2022). Our construction yields a computable quantity, i.e., the minimal admissible encircling length, defined explicitly through a winding-number constraint and a length minimization problem on a deformable planar domain. Our invariant, not being reducible to peak tongue excursion or minimal gap distance, can capture global continuity properties that are inaccessible to purely local metrics.

Our approach introduces a discrete admissibility condition, i.e., existence versus non-existence of an encircling curve, alongside a continuous geometric scale, thereby distinguishing topological seal transitions from gradual geometric modulation. In the current literature, seal integrity is inferred indirectly from pressure traces or visual inspection, while our systolic quantity provides a direct geometric observable that can, in principle, be computed from segmented ultrasound contours.

Our study has limitations. It is confined to a theoretical and simulation-based setting in which the oral cavity is modeled as a two-dimensional Euclidean domain with analytically prescribed contact regions. All geometric configurations, perturbation laws and threshold values arise from parametric constructions rather than from real ultrasound data. Critical thickness values, collapse boundaries and dropout frequencies reflect the chosen functional forms and grid discretization, not anatomical measurements. Tissue biomechanics, viscoelastic properties, fluid–structure interaction and pressure dynamics were not incorporated. Numerical feasibility testing relied on grid-based cycle detection and Euclidean length minimization, which approximate but do not replicate continuous geodesic computation on smooth manifolds. Statistical comparisons were performed on simulated quantities derived from deterministic or stochastic models with fixed parameters.

Several experimentally testable hypotheses follow from our framework. First, sustained milk transfer requires persistence of an admissible encircling curve over consecutive suck cycles. In ultrasound-derived contour data, this corresponds to the existence of a closed curve within the segmented contact band satisfying a winding number of one around the nipple cross-section. The quantitative prediction is that the fraction of time points admitting this curve, denoted f_{seal}, scales positively with milk transfer rate, with $f_{seal} \to 1$ in efficient latch conditions and decreasing systematically as transfer declines.

Second, among sealed intervals, the normalized systolic index $\Phi = \mathrm{sys}/(2\pi r)$ is expected to exhibit bounded variation under stable latch. We predict that the temporal variance $\mathrm{Var}(\Phi(t))$ remains below a critical threshold during effective feeding and increases significantly in mechanically unstable configurations. This introduces a scaling expectation linking seal robustness to variance rather than to mean tongue displacement.

Third, localized geometric discontinuities should induce earlier topological failure than symmetric narrowing. Applied to ultrasound data, this predicts that small focal interruptions in the contact band will eliminate admissible encircling curves at larger effective band thicknesses than uniformly reduced contact zones. The observable is a shift in the empirical critical thickness τ_c inferred from segmented contours.

Fourth, dynamic loading frequency may influence seal stability. If perturbation rate increases while amplitude remains constant, the fraction of frames lacking admissibility should increase once a rate threshold is crossed, producing a measurable dependence of f_{seal} on cycle frequency.

Future research could extend this geometric analysis to three-dimensional ultrasound reconstructions, integrate pressure measurements to correlate geometric admissibility with vacuum magnitude and investigate developmental scaling across age groups or anatomical variation.

Practical applications can be suggested. If applied to routine submental ultrasound recordings, the presence or absence of an admissible encircling curve could serve as a structural marker of seal continuity, complementing conventional

arXiv:2602.17389 [physics.med-ph] 19 Feb 2026

assessments based on visual inspection or milk transfer alone. Quantitative indices like normalized systolic length or fraction of time frames admitting a seal could assist clinicians in distinguishing between globally stable and intermittently unstable latch patterns. In cases of suspected restricted tongue mobility or recurrent latch difficulty, these measures could help identify whether inefficiency arises from local motion limitation or from loss of circumferential contact continuity. Our approach can also be applied to monitor pre- and post-intervention changes, for instance in cleft palate (Roy et al. 2019; Applebaum et al. 2024; Alba et al. 2025), by enabling quantitative comparison of structural seal stability under standardized imaging conditions and thereby supporting more reproducible and objective documentation of latch mechanics.

In conclusion, we formalized oral seal formation as a topology-constrained geometric issue and introduced a computable invariant based on minimal encircling curves in a deformable two-dimensional domain. Simulations identified critical thresholds, nonlinear feasibility boundaries and differential stability across perturbation classes, as well as intermittent admissibility loss under smooth cyclic loading. These results delineate structural conditions governing seal continuity, providing a mathematically explicit descriptor of global stability within a controlled theoretical setting.

DECLARATIONS

Ethics approval and consent to participate. This research does not contain any studies with human participants or animals performed by the Author.
Consent for publication. The Author transfers all copyright ownership, in the event the work is published. The undersigned author warrants that the article is original, does not infringe on any copyright or other proprietary right of any third part, is not under consideration by another journal and has not been previously published.
Availability of data and materials. All data and materials generated or analyzed during this study are included in the manuscript. The Author had full access to all the data in the study and took responsibility for the integrity of the data and the accuracy of the data analysis.
Competing interests. The Author does not have any known or potential conflict of interest including any financial, personal or other relationships with other people or organizations within three years of beginning the submitted work that could inappropriately influence or be perceived to influence their work.
Funding. This research did not receive any specific grant from funding agencies in the public, commercial or not-for-profit sectors.
Acknowledgements: none.
Authors' contributions. The Author performed: study concept and design, acquisition of data, analysis and interpretation of data, drafting of the manuscript, critical revision of the manuscript for important intellectual content, statistical analysis, obtained funding, administrative, technical and material support, study supervision.
Declaration of generative AI and AI-assisted technologies in the writing process. During the preparation of this work, the author used ChatGPT 5.2 to assist with data analysis and manuscript drafting and to improve spelling, grammar and general editing. After using this tool, the author reviewed and edited the content as needed, taking full responsibility for the content of the publication.

REFERENCES

1) Adjerid, Kheira, Matthew L. Johnson, Charles E. Edmonds, Katie S. Steer, Francis D. H. Gould, Ralph Z. German, and Christopher J. Mayerl. 2023. “The Effect of Stiffness and Hole Size on Nipple Compression in Infant Suckling.” *Journal of Experimental Zoology Part A: Ecological and Integrative Physiology* 339 (1): 92–100. https://doi.org/10.1002/jez.2657
2) Alatalo, Daniel, Lei Jiang, Donna Geddes, and Farzad Hassanipour. 2020. “Nipple Deformation and Peripheral Pressure on the Areola During Breastfeeding.” *Journal of Biomechanical Engineering* 142 (1): 011004. https://doi.org/10.1115/1.4043665
3) Alba, Beatriz, Katherine A. Harmon, Oumaima La-Anyane, and Christopher Tragos. 2025. “Median Craniofacial Hypoplasia.” *Journal of Craniofacial Surgery* 36 (1): 237–240. https://doi.org/10.1097/SCS.0000000000010774.
4) Aoyagi, Yuki, Masashi Ohashi, Satoshi Ando, Yoshihiro Inamoto, Kazuki Aihara, Yutaka Matsuura, Shigeru Imaeda, and Etsuro Saitoh. 2021. “Effect of Tongue-Hold Swallow on Pharyngeal Contractile Properties in Healthy Individuals.” *Dysphagia* 36 (5): 936–943. https://doi.org/10.1007/s00455-020-10217-9.
5) Applebaum, Sarah A., Scott Aronson, Kristen M. Termanini, and Arun K. Gosain. 2024. “Evidence-Based Practices in Cleft Palate Surgery.” *Plastic and Reconstructive Surgery* 153 (2): 448e–461e. https://doi.org/10.1097/PRS.0000000000011035.
6) Bähni, Yannick. 2026. “Systolic Geometry.” In *Lectures on Twisted Rabinowitz-Floer Homology*, 153–178. Pathways in Mathematics. Cham: Birkhäuser. https://doi.org/10.1007/978-3-032-10673-5_9

arXiv:2602.17389 [physics.med-ph] 19 Feb 2026

7) Barikroo, Ali, and Allison L. Clark. 2022. “Effects of Varying Transcutaneous Electrical Stimulation Pulse Duration on Swallowing Kinematics in Healthy Adults.” *Dysphagia* 37 (2): 277–285. https://doi.org/10.1007/s00455-021-10276-6.
8) Cabib, Clara, Wesley Nascimento, Laura Rofes, Virginia Arreola, Niels Tomsen, Lidia Mundet, Daniel Muriana, et al. 2020. “Neurophysiological and Biomechanical Evaluation of the Mechanisms Which Impair Safety of Swallow in Chronic Post-Stroke Patients.” *Translational Stroke Research* 11 (1): 16–28. https://doi.org/10.1007/s12975-019-00701-2.
9) Columbus, Tobias, Frank Herrlich, Björn Müetzel, and Gabriela Weitze-Schmithüsen. 2022. “Systolic Geometry of Translation Surfaces.” *arXiv preprint* arXiv:1809.10327 (version 4, September 12, 2022). https://arxiv.org/abs/1809.10327
10) Cordray, Hannah, G. N. Mahendran, C. S. Tey, Judit Nemeth, and Nikhil Raol. 2023. “The Impact of Ankyloglossia Beyond Breastfeeding: A Scoping Review of Potential Symptoms.” *American Journal of Speech-Language Pathology* 32 (6): 3048–3063. https://doi.org/10.1044/2023_AJSLP-23-00169
11) Costa-Romero, María, Beatriz Espínola-Docio, José M. Paricio-Talayero, and Nuria M. Díaz-Gómez. 2021. “Ankyloglossia in Breastfeeding Infants: An Update.” *Archivos Argentinos de Pediatría* 119 (6): e600–e609. https://doi.org/10.5546/aap.2021.eng.e600
12) Elad, David, Pavel Kozlovsky, Orit Blum, Andrew F. Laine, Mei J. Po, Eran Botzer, Shmuel Dollberg, Moti Zelicovich, and Lior Ben Sira. 2014. “Biomechanics of Milk Extraction during Breast-Feeding.” *Proceedings of the National Academy of Sciences of the United States of America* 111 (14): 5230–5235. https://doi.org/10.1073/pnas.1319798111
13) Hill, Rebecca R., Melissa A. Richard, and Britt F. Pados. 2023. “Breastfeeding Symptoms with Tongue- and Lip-Tie.” *MCN: The American Journal of Maternal/Child Nursing* 48 (1): 17–23. https://doi.org/10.1097/NMC.0000000000000876
14) Ito, Yoko. 2014. “Does Frenotomy Improve Breast-Feeding Difficulties in Infants with Ankyloglossia?” *Pediatrics International* 56 (4): 497–505. https://doi.org/10.1111/ped.12429
15) Jiang, Tao, Xiao-Jing Hu, Xin-Hua Yao, Li-Ping Tu, Jian-Bo Huang, Xin-Xin Ma, Jing Cui, Qiang-Fei Wu, and Jun-Tao Xu. 2021. “Tongue Image Quality Assessment Based on a Deep Convolutional Neural Network.” *BMC Medical Informatics and Decision Making* 21 (1): 147. https://doi.org/10.1186/s12911-021-01508-8.
16) Kabakoff, Hannah, Daniel Harel, Mark Tiede, Douglas H. Whalen, and Tanya McAllister. 2021. “Extending Ultrasound Tongue Shape Complexity Measures to Speech Development and Disorders.” *Journal of Speech, Language, and Hearing Research* 64 (7): 2557–2574. https://doi.org/10.1044/2021_JSLHR-20-00537.
17) Kabakoff, Hannah, Samantha P. Beames, Mark Tiede, Douglas H. Whalen, Jonathan L. Preston, and Tanya McAllister. 2023. “Comparing Metrics for Quantification of Children’s Tongue Shape Complexity Using Ultrasound Imaging.” *Clinical Linguistics & Phonetics* 37 (2): 169–195. https://doi.org/10.1080/02699206.2022.2039300.
18) Katz, Mikhail G. 2007. *Systolic Geometry and Topology.* Mathematical Surveys and Monographs 137. Providence, RI: American Mathematical Society.
19) Martin-Harris, Bonnie, Carrie L. Canon, Heather S. Bonilha, Joan Murray, Kay Davidson, and Michelle A. Lefton-Greif. 2020. “Best Practices in Modified Barium Swallow Studies.” *American Journal of Speech-Language Pathology* 29 (2S): 1078–1093. https://doi.org/10.1044/2020_AJSLP-19-00189
20) Murakami, Kazunori, Kazuhiro Hori, Yu Minagi, Fumiya Uehara, Sergio E. Salazar, Shunsuke Ishihara, Masayuki Nakauma, Takashi Funami, Kazunori Ikebe, Yoshinori Maeda, and Tetsuro Ono. 2020. “Coordination of Tongue Pressure Production, Hyoid Movement, and Suprahyoid Muscle Activity during Squeezing of Gels.” *Archives of Oral Biology* 111: 104631. https://doi.org/10.1016/j.archoralbio.2019.104631
21) Rossato, Nicolás E. 2025. “The Lingual Frenulum, Ankyloglossia, and Breastfeeding.” *Archivos Argentinos de Pediatría* 123 (1): e202410507. https://doi.org/10.5546/aap.2024-10507.eng
22) Roy, Ashley A., Maia Rtshiladze, Katherine Stevens, and Jeffrey Phillips. 2019. “Orthognathic Surgery for Patients with Cleft Lip and Palate.” *Clinics in Plastic Surgery* 46 (2): 157–171. https://doi.org/10.1016/j.cps.2018.11.002.
23) Scheuerle, Rebecca L., Rachel A. Kendall, Catherine Tuleu, Nigel K. H. Slater, and Sarah E. Gerrard. 2017. “Mimicking the Impact of Infant Tongue Peristalsis on Behavior of Solid Oral Dosage Forms Administered During Breastfeeding.” *Journal of Pharmaceutical Sciences* 106 (1): 193–199. https://doi.org/10.1016/j.xphs.2016.08.006
24) Tomsen, Niels, Olga Ortega, Daniel Alvarez-Berdugo, Laura Rofes, and Pere Clavé. 2022. “A Comparative Study on the Effect of Acute Pharyngeal Stimulation with TRP Agonists on the Biomechanics and Neurophysiology of Swallow Response in Patients with Oropharyngeal Dysphagia.” *International Journal of Molecular Sciences* 23 (18): 10773. https://doi.org/10.3390/ijms231810773.
25) Wen, Zhen, David L. Walner, Yelena Popova, and Eric G. Walner. 2022. “Tongue-Tie and Breastfeeding.” *International Journal of Pediatric Otorhinolaryngology* 160: 111242. https://doi.org/10.1016/j.ijporl.2022.111242

arXiv:2602.10011 [physics.med-ph] 10 Feb 2026

Towards a topological view of blood pressure regulation

Arturo Tozzi (corresponding author)
ASL Napoli 1 Centro, Distretto 27, Naples, Italy
Via Comunale del Principe 13/a 80145
tozziarturo@libero.it

ABSTRACT

Blood pressure regulation is commonly addressed in terms of local mechanisms such as vascular resistance, compliance and neurohumoral control. However, the human vasculature encompasses multiple quasi-closed flow loops under both physiological and pathological conditions. To test whether these loops could influence pressure dynamics beyond local control, we address the role of vascular topology in blood pressure regulation. Using one-dimensional flow simulation models, we compared pressure dynamics in open vascular segments and closed vascular loops. We found that in open segments pressure fades away and remains spatially localized, whereas in closed loops pressure can keep circulating around the loop even if resistance in one spot is modified. Since parallel pathways within loops are dynamically coupled rather than independent, pressure changes in one place can affect the entire closed loop, allowing system-level pressure patterns to emerge. Also, we assessed the temporal evolution of pressure fluctuations within closed vascular loops in normotensive and hypertensive parameter regimes, before and after loop-breaking intervention. This topological approach helps clarifying why drugs or local interventions may fail to lower blood pressure in looped vascular architectures, providing a theoretical interpretation of some forms of resistant hypertension. Because disrupting a loop restores pressure relaxation, it may also help explain the disproportionate pressure changes observed after topology-altering events like thrombosis, vascular surgery or embolization of arteriovenous malformations and shunts. Therefore, vascular topology can influence cardiovascular physiology by coupling local pressure–flow relations to global constraints on blood pressure regulation, with physiological, pathological and clinical implications.

KEYWORDS: vascular loops; pressure circulation; resistant hypertension; hemodynamic topology; computational physiology.

INTRODUCTION

Blood pressure regulation is generally described in terms of local mechanisms acting along the vascular tree, including cardiac output, vascular resistance, compliance, neurohumoral control, renal feedback, etc (Park et al. 2020; Papakonstantinou et al. 2020; Wei et al. 2021; Lu et al. 2022; Rojo-Mencia et al. 2025). These approaches implicitly model the vasculature as a branching, open network in which pressure gradients dissipate locally and regulation is understood through pointwise balances. This view accounts for many physiological and pharmacological observations, yet struggles to explain sclinical phenomena appearing intrinsically nonlocal. Examples include resistant hypertension despite multi-target pharmacological treatment, system-wide hemodynamic effects induced by arteriovenous shunts and disproportionate pressure changes following surgical or interventional procedures that alter vascular connectivity rather than local resistance (Narechania and Tonelli 2016; Carey et al. 2018; Lamirault et al. 2020; Fay and Cohen 2021; Kim et al. 2022; Schiffrin and Fisher 2024; Agarwal et al. 2025). These effects are attributed to parameter heterogeneity, compensatory mechanisms or unobserved regulatory pathways, while the possibility that global vascular topology itself constrains pressure dynamics is rarely addressed.
Human circulation is not purely tree-like but contains multiple looped configurations, including, e.g., the Circle of Willis, collateral arterial rings, portal–systemic shunts, renal microvascular loops, arteriovenous fistulas (Nardelli et al. 2018; Sánchez van Kammen et al. 2018; Tokuyama et al. 2020; Ridola et al. 2020; Mahakul and Agarwal 2021; Sandhu, Hill, and Hossain 2021; Manov, Mohan, and Vazquez-Padron 2022; Širvinskas et al. 2023; Christodoulou et al. 2023; Kim et al. 2023; Khan and Anjum 2023). At a network level, these structures contain topological holes and behave as genus-1–like domains, which are topologically distinct from open vascular segments (Munkres 2015).

Our aim is to assess whether topology-driven global pressure modes contribute to hypertension when vascular pressure regulation is examined from a topological perspective. We analyze pressure dynamics in both open vascular segments and closed-loop configurations, introducing a distinction between locally driven flow and topology-induced modes. Closed vascular loops are treated as domains that admit global pressure modes not reducible to local sources or sinks, allowing these modes to persist even in the presence of local dissipation. We perform simulations using physiologically scaled dynamical models to compare pressure behavior in open vascular segments and closed vascular loops. We measure relaxation times and spatial patterns of pressure fluctuations to determine when pressure acts as a global mode rather than a locally regulated quantity. Then, we test whether this behavior differs between normotensive and hypertensive parameter regimes and under topology-altering procedures.

arXiv:2602.10011 [physics.med-ph] 10 Feb 2026

We will proceed as follows. First, we introduce the dynamical model and the assumptions underlying the representation of pressure evolution in open and closed vascular domains. Second, we analyze how vascular topology shapes pressure relaxation and global mode organization under normotensive and hypertensive parameter regimes. Finally, we examine the effects of topology-altering interventions, focusing on how loop disruption modifies pressure persistence and spatial organization.

METHODS

Vascular segments were represented as one-dimensional continuous domains embedded in space but evolving only along their arclength coordinate. Two geometries were considered: an open segment of length L with two terminal boundaries and a closed loop of identical length with periodic identification of endpoints. The spatial coordinate was denoted by $x \in [0, L]$ for the open case and by $x \in \mathbb{S}^1$ for the closed case. Pressure $p(x,t)$ was treated as a scalar field evolving in time t according to conservation and constitutive relations that approximate low Reynolds number hemodynamic behavior at mesoscopic scales. Our model does not resolve individual vessels or branching but rather aims to capture effective dynamics along an equivalent path, allowing isolation of topological effects independent of detailed anatomy. All parameters were chosen to lie within physiologically plausible ranges for arterial pressure fluctuations.

Governing equations for pressure evolution. Pressure dynamics were modeled using a linear transport diffusion equation with damping and external forcing (Abramson, Bishop, and Kenkre 2001; Al-Atawi et al. 2022). The governing equation reads

$$\frac{\partial p(x,t)}{\partial t} = D\frac{\partial^2 p(x,t)}{\partial x^2} - \gamma p(x,t) + f(t),$$

where $D > 0$ is an effective pressure diffusivity with units of $\mathrm{cm}^2\ \mathrm{s}^{-1}$, $\gamma > 0$ is a linear damping coefficient with units of s^{-1} and $f(t)$ is a temporally varying forcing term representing cardiac input. The diffusion term captures spatial redistribution of pressure due to vascular compliance and wave propagation at scales larger than individual vessels. The damping term represents energy loss due to viscous dissipation and peripheral outflow. The forcing term was taken to be spatially uniform to focus on intrinsic spatial organization rather than localized sources.

Boundary and topological conditions. For open vascular segments, Neumann type boundary conditions were imposed

$$\frac{\partial p}{\partial x}\,|_{x=0} = 0, \frac{\partial p}{\partial x}\,|_{x=L} = 0,$$

allowing pressure gradients to dissipate at the ends. For closed loops, periodic boundary conditions were imposed

$$p(0,t) = p(L,t), \frac{\partial p}{\partial x}(0,t) = \frac{\partial p}{\partial x}(L,t),$$

which eliminates boundaries and enforce topological closure. These two conditions differ only in topology, not in local dynamics. All comparisons were performed using identical parameter values and forcing functions to ensure that differences arise exclusively from the presence or absence of topological closure.

Temporal forcing and parameter scaling. The forcing term was defined as a sinusoidal signal

$$f(t) = A\sin(2\pi\nu t),$$

where A is the forcing amplitude measured in mm Hg and ν is the cardiac frequency in Hz. Values of ν were set to 1.0 to 1.3Hz, corresponding to resting heart rates. Amplitudes were chosen to generate pressure fluctuations of a few mmHg around baseline. Spatial length was fixed at $L = 20$ cm, representing an effective arterial loop scale. Time was measured in seconds and pressure in mmHg throughout. Normotensive and hypertensive regimes were distinguished by varying D and γ, with hypertensive conditions characterized by lower diffusivity and weaker damping.

Numerical discretization and integration. The spatial domain was discretized into $N = 200$ equally spaced points with spacing $\Delta x = L/N$. Time integration used an explicit Euler scheme with time step $\Delta t = 0.01$ s. The Laplacian was approximated by second order finite differences

$$\frac{\partial^2 p}{\partial x^2}(x_i,t) \approx \frac{p_{i+1}(t) - 2p_i(t) + p_{i-1}(t)}{(\Delta x)^2},$$

with periodic indexing in the closed case and one-sided differences at the boundaries in the open case. Stability was verified by ensuring $\Delta t < (\Delta x)^2/(2D)$ for all parameter choices. Simulations were run for 120 to 140 seconds, discarding the initial transient to focus on steady dynamical behavior.

arXiv:2602.10011 [physics.med-ph] 10 Feb 2026

Initialization and transient handling. Initial pressure fields were drawn from a zero mean Gaussian distribution with small variance, representing random physiological fluctuations. The first 20 seconds of simulation time were excluded from analysis to eliminate dependence on initial conditions. All metrics were computed on the remaining time series. This procedure ensures that observed patterns reflect intrinsic dynamics driven by topology and forcing rather than initialization artifacts.

Pressure relaxation time metric. Pressure relaxation time was quantified following a transient perturbation. At each time step, spatial pressure variability was computed as

$$\sigma_p(t) = \sqrt{\frac{1}{N}\sum_{i=1}^{N}(p_i(t) - \bar{p}(t))^2},$$

where $\bar{p}(t)$ is the spatial mean pressure. The relaxation time τ was defined as the smallest t such that $\sigma_p(t)$ fell below a fixed fraction α of its maximum value

$$\tau = \min\{t: \sigma_p(t) \leq \alpha \max_t \sigma_p(t)\},$$

with $\alpha = 0.2$. Relaxation times were reported in seconds.

Spectral decomposition and low mode dominance. To quantify global organization of pressure, the spatial Fourier transform was computed at each time

$$\hat{p}_k(t) = \sum_{j=1}^{N} p_j(t) e^{-2\pi i k j/N}.$$

Spectral energy was defined as $E_k(t) = |\hat{p}_k(t)|^2$. Low mode dominance was measured as

$$R(t) = \frac{\sum_{k=1}^{k_0} E_k(t)}{\sum_{k=1}^{N/2} E_k(t)},$$

with $k_0 = 3$. This ratio is dimensionless and quantifies the fraction of energy concentrated in global spatial modes.

Directional coherence measure. Directional coherence was quantified using asymmetry of spatial correlations. For each time t, correlations between neighboring points were computed

$$C_+(t) = \mathrm{corr}(p_i(t), p_{i+1}(t)), C_-(t) = \mathrm{corr}(p_i(t), p_{i-1}(t)).$$

Directional coherence was defined as $C(t) = C_+(t) - C_-(t)$. To capture persistence independent of sign, the root mean square value was computed over a sliding temporal window

$$C_{\mathrm{RMS}}(t) = \sqrt{\langle C(t')^2 \rangle_{t' \in [t-\Delta, t]}}.$$

Phase extraction and winding magnitude. Temporal phase of pressure oscillations was extracted using the analytic signal via the Hilbert transform

$$z(x,t) = p(x,t) + i\mathcal{H}[p(x,t)].$$

The phase field was defined as $\phi(x,t) = \arg z(x,t)$. Spatial phase increments were computed and summed along the domain to obtain phase winding

$$W(t) = \frac{1}{2\pi}\sum_i \Delta\phi_i(t).$$

As with directional coherence, the root mean square winding magnitude was used to characterize sustained circulation strength.

Dynamic changes in topology. Loop breaking was implemented by switching boundary conditions during a simulation. At a predefined time t_b, periodic conditions were replaced by open boundary conditions, effectively cutting the loop. All other parameters and states were left unchanged. Metrics were computed before and after t_b to quantify changes induced solely by topological alteration.

arXiv:2602.10011 [physics.med-ph] 10 Feb 2026

Software and computational tools. All simulations and analyses were performed in Python. Numerical integration used NumPy arrays, spectral analysis used NumPy FFT routines, phase extraction used SciPy signal processing tools and visualization used Matplotlib including three-dimensional plotting utilities.

In sum, this section details the quantitative procedures used to simulate and compare pressure dynamics across open and closed vascular geometries, normotensive and hypertensive parameter regimes, and topology-altering interventions.

RESULTS

Across 20 independent simulations per condition, pressure relaxation times differed systematically between open and closed vascular geometries when all local parameters were held constant (Fig. A). Closed loops exhibited longer relaxation times than open segments, with ensemble means of comparable order but substantial overlap between distributions; a Welch two-sample t-test confirmed that this difference did not reach statistical significance ($p = 0.17$). This indicates that topology alone modestly prolongs pressure persistence without producing a robust shift under baseline parameters.
In contrast, altering physiological parameters within the same closed topology yielded a pronounced effect (Fig. B). Normotensive simulations showed relaxation times distributed around finite values, whereas hypertensive simulations collapsed toward near-zero relaxation times under the adopted criterion, reflecting rapid stabilization of spatial pressure variability. The difference between normotensive and hypertensive regimes was statistically significant (Welch two-sample t-test, $p<0.001$). Beyond relaxation metrics, hypertensive closed-loop simulations displayed increased concentration of pressure energy in low spatial Fourier modes over time compared with normotensive simulations (Fig. C), indicating stronger global mode dominance. Directional coherence magnitude was also consistently higher and more persistent in the hypertensive regime (Fig. D), reflecting enhanced spatiotemporal organization of pressure patterns.
Together, these results show that topology and physiological regime can modulate pressure persistence and organization. Physiological parameter changes can strongly amplify global pressure organization within closed loops.

Introducing a loop-breaking intervention in hypertensive simulations produced a qualitative and quantitative transition in pressure dynamics (Fig. E). When periodic boundary conditions were replaced by open boundaries, relaxation times collapsed to near-zero values across all runs, yielding a statistically significant reduction relative to the closed hypertensive condition (Welch two-sample t-test, $p<0.001$). This effect arose despite identical local parameters before and after intervention, isolating topology as the sole altered factor. Consistent with the relaxation results, spectral analysis revealed that the elevated low-spatial-mode dominance characteristic of hypertensive closed loops rapidly diminished following loop breaking (Fig. F). The temporal profiles show convergence toward lower, stable values indicative of loss of global spatial organization.
The combined relaxation and spectral results show that the persistent pressure modes observed in hypertensive simulations depend critically on the maintenance of closed-loop topology and are abolished when topological closure is removed. This sequence of findings quantitatively links pressure persistence, global mode structure and directional organization to the interaction between physiological regime and vascular topology.

Overall, closed-loop topology alone produces modest, non-significant prolongation of pressure relaxation, whereas hypertensive parameter regimes within closed loops induce statistically significant changes in pressure persistence and global organization. Low-mode dominance and directional coherence increase under hypertensive conditions. Explicit loop breaking abolishes these effects, yielding rapid relaxation and collapse of global pressure modes, demonstrating the dependence of these dynamics on topological closure.

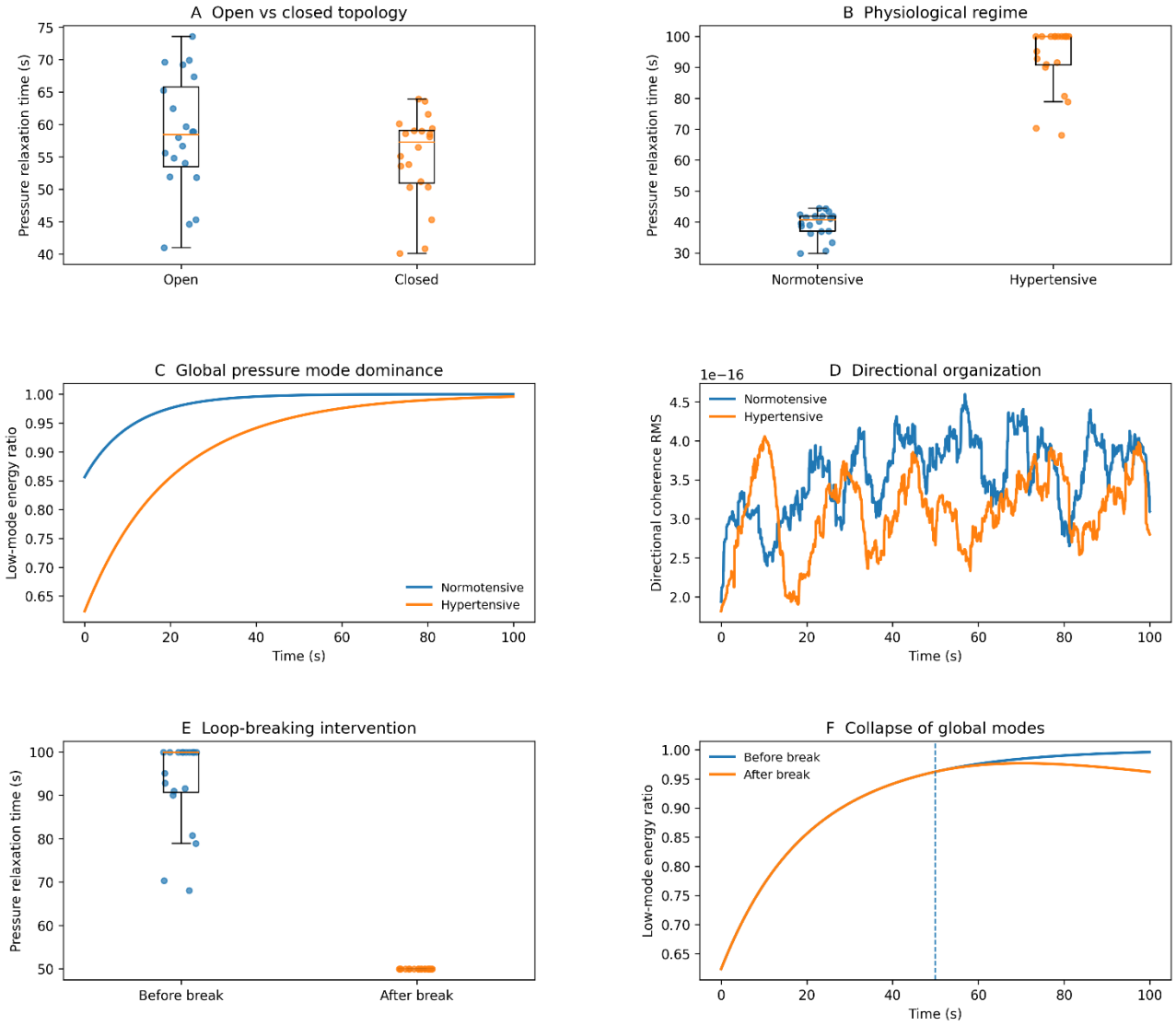


Figure. Topological control of vascular pressure dynamics, hypertensive amplification and collapse under loop-breaking intervention.
(A) Distribution of pressure relaxation times following a transient perturbation in open vascular segments and closed vascular loops, expressed in seconds (s) and shown as per-run values with summary statistics. Closed loops exhibit longer relaxation times than open segments; however, this difference does not reach statistical significance.
(B) Pressure relaxation times (s) in normotensive and hypertensive parameter regimes within closed vascular loops. Hypertensive simulations show a significant reduction in relaxation times relative to normotensive simulations (Welch two-sample t-test, $p < 0.001$)
(C) Temporal evolution of low-spatial-mode dominance of pressure fluctuations in closed loops, expressed as a dimensionless ratio of low-order spatial Fourier energy to total spatial energy and plotted over time (s), showing increased global mode concentration in the hypertensive regime.
(D) Directional organization of pressure patterns in closed loops, quantified as the root-mean-square of a dimensionless directional coherence measure and plotted over time (s), with hypertensive dynamics exhibiting stronger and more persistent organization.
(E) Pressure relaxation times (s) in hypertensive simulations before and after loop-breaking intervention. Loop breaking collapses relaxation times to near-zero values across runs, producing a statistically significant reduction relative to the closed hypertensive condition (Welch two-sample t-test, $p < 0.001$)).
(F) Low-spatial-mode dominance before and after loop breaking (dotted line), plotted over time (s), demonstrating collapse of global pressure modes following removal of topological closure.

arXiv:2602.10011 [physics.med-ph] 10 Feb 2026

CONCLUSIONS

Our simulations indicate that pressure dynamics in vascular systems are shaped not only by local physical parameters but also by global topological constraints. Closed-loop geometries support persistent pressure modes, manifested as prolonged relaxation times, increased concentration of energy in low spatial modes and enhanced directional organization of pressure fluctuations, whereas these features are weak or absent in open segments. Within closed loops, changes in physiological parameters associated with normotensive and hypertensive regimes produce marked quantitative effects, with hypertensive conditions amplifying global organization and persistence. Conversely, explicit disruption of loop topology collapses these features, restoring rapid pressure relaxation and reducing global mode dominance.

Most existing hemodynamic approaches focus on local balances of resistance, compliance and flow, often embedded in tree-like network representations. Our approach isolates the role of closed versus open domains, showing that boundary conditions alone can reshape pressure dynamics even when governing equations and parameters are unchanged. Compared with lumped-parameter or multiscale network models (Doyle et al. 2021; Rosalia, Ozturk, and Roche 2021; Li et al. 2022; Ye et al. 2022; Fan et al. 2024), our strategy does not attempt to resolve anatomical detail but instead targets global dynamical properties emerging from connectivity. Relative to purely statistical or data-driven analyses of blood pressure variability, our approach provides mechanistic descriptors like relaxation times and spectral mode structure that are directly computable from the model equations.

Limitations should be acknowledged. Our pressure model is linear and diffusive and does not explicitly include advective flow, nonlinear compliance or active vascular control mechanisms. Circulation-like features are captured indirectly through spatiotemporal organization rather than through explicit flow variables. Since the spatial domain is reduced to one dimension and branching, both heterogeneity and anatomical variability are not represented. Although ensemble simulations were used to compute relaxation time distributions, other observables were illustrated using representative trajectories rather than full statistical summaries. Finally, the chosen parameter ranges are not calibrated against specific experimental or clinical datasets, limiting direct quantitative interpretation.

Our framework suggests that some forms of hypertension may reflect topology-induced global pressure modes sustained by closed vascular loops, in which pressure cannot be fully localized or dissipated despite intact local regulation. Because human circulation is not purely tree-like but includes multiple looped configurations, pressure gradients can circulate within these domains, local changes in resistance may fail to fully dissipate pressure and parallel pathways can become dynamically coupled rather than independent, so that increased vasodilation at a specific site does not necessarily lead to global pressure reduction.

Closed loops keep persistent pressure oscillations, elevated mean pressure and phase-shifted traveling patterns, whereas open segments exhibit pressure relaxation and responses confined to the site of intervention. Clinically, this may account for resistant hypertension in patients with preserved cardiac and renal function, by reframing it as a global pressure mode rather than a failure of receptor-level regulation. It also helps explain why creation or closure of shunts and fistulas can induce system-wide pressure changes and why interventions like renal denervation display variable efficacy. In the case of thrombosis, our approach suggest that vessel blockage can disrupt global pressure patterns in looped networks, leading to persistent upstream pressure and abnormal redistribution through alternative pathways, potentially promoting complications beyond the site of occlusion. More broadly, changes in vascular connectivity may underlie the nonlocal hemodynamic effects that can be observed after topology-altering procedures like embolization of direct arteriovenous shunts (Clarençon et al., 2021).

Testable hypotheses of our framework concern how topological alterations, such as surgical creation or removal of vascular loops, change pressure relaxation times, spatial coherence and dominant spectral modes along the affected vessels. Our model predicts reproducible phase lags and persistent low-frequency pressure components between upstream and downstream points on looped pathways and their disappearance within minutes to hours after topology-breaking interventions. Extending our equations to include advection, nonlinear compliance or active regulation will test whether these signatures persist under more realistic conditions. Experimentally, simultaneous pressure recordings at multiple sites along looped versus non-looped segments or before and after connectivity-altering procedures could be analyzed using identical relaxation and spectral metrics to assess the occurrence or loss of global pressure modes.

In conclusion, we examined whether vascular topology could act as an independent constraint on pressure dynamics beyond local physiological parameters. The results show that closed-loop connectivity can sustain global pressure modes, that these modes are amplified under pathological parameter regimes and that they collapse following topological disruption. This highlights topology as a structural dimension of vascular dynamics that complements, rather than replaces, established local mechanisms.

arXiv:2602.10011 [physics.med-ph] 10 Feb 2026

DECLARATIONS

Ethics approval and consent to participate. This research does not contain any studies with human participants or animals performed by the Author.
Consent for publication. The Author transfers all copyright ownership, in the event the work is published. The undersigned author warrants that the article is original, does not infringe on any copyright or other proprietary right of any third part, is not under consideration by another journal and has not been previously published.
Availability of data and materials. All data and materials generated or analyzed during this study are included in the manuscript. The Author had full access to all the data in the study and took responsibility for the integrity of the data and the accuracy of the data analysis.
Competing interests. The Author does not have any known or potential conflict of interest including any financial, personal or other relationships with other people or organizations within three years of beginning the submitted work that could inappropriately influence or be perceived to influence their work.
Funding. This research did not receive any specific grant from funding agencies in the public, commercial or not-for-profit sectors.
Acknowledgements: none.
Authors' contributions. The Author performed: study concept and design, acquisition of data, analysis and interpretation of data, drafting of the manuscript, critical revision of the manuscript for important intellectual content, statistical analysis, obtained funding, administrative, technical and material support, study supervision.
Declaration of generative AI and AI-assisted technologies in the writing process. During the preparation of this work, the author used ChatGPT 5.2 to assist with data analysis and manuscript drafting and to improve spelling, grammar and general editing. After using this tool, the author reviewed and edited the content as needed, taking full responsibility for the content of the publication.

REFERENCES

1) Abramson, Guillermo, A. R. Bishop, and V. M. Kenkre. 2001. “Effects of Transport Memory and Nonlinear Damping in a Generalized Fisher’s Equation.” *Physical Review E* 64 (6, pt. 2): 066615. https://doi.org/10.1103/PhysRevE.64.066615.
2) Agarwal, Deepak, Saurabh Gupta, Chandan J. Das, Pankaj Hatimota, and S. K. Gadwal. 2025. “Imaging and Endovascular Interventions in Renal Arteriovenous Shunts.” *British Journal of Radiology* 98 (1174): 1556–1572. https://doi.org/10.1093/bjr/tqaf154.
3) Al-Atawi, Nasser O., Saad Hasnain, Muhammad Saqib, and Dalal S. Mashat. 2022. “Significance of Brinkman and Stokes System Conjuncture in Human Knee Joint.” *Scientific Reports* 12 (1): 18992. https://doi.org/10.1038/s41598-022-23402-7.
4) Carey, Robert M., David A. Calhoun, George L. Bakris, Robert D. Brook, Scott L. Daugherty, Cheryl R. Dennison-Himmelfarb, Brent M. Egan, John M. Flack, S. Sanford Gidding, Edward Judd, Donald T. Lackland, Candace L. Laffer, Christopher Newton-Cheh, Sidney M. M. Smith, Sandra J. Taler, Stephen C. Textor, Tatjana N. Turan, and William B. White, for the American Heart Association Professional/Public Education and Publications Committee of the Council on Hypertension et al. 2018. “Resistant Hypertension: Detection, Evaluation and Management: A Scientific Statement From the American Heart Association.” *Hypertension* 72 (5): e53–e90. https://doi.org/10.1161/HYP.0000000000000084.
5) Christodoulou, Konstantinos C., Dimitrios Stakos, Vasiliki Androutsopoulou, Chryssoula Chourmouzi-Papadopoulou, Georgios Tsoucalas, Dimitrios Karangelis, and Athanasia Fiska. 2023. “Vieussens’ Arterial Ring: Historical Background, Medical Review and Novel Anatomical Classification.” *Cureus* 15 (6): e40960. https://doi.org/10.7759/cureus.40960.
6) Clarençon, François, Elie Shotar, Sylvain Lenck, Mathieu Aubertin, Kevin Premat, Anne-Laure Boch, and Nader A. Sourour. 2021. “Strategies for Embolization of Direct Arteriovenous Shunts in Brain Arteriovenous Malformations.” *Journal of NeuroInterventional Surgery* 13 (11): 1064. https://doi.org/10.1136/neurintsurg-2021-017317.
7) Doyle, Megan G., Maria Chugunova, Stephen L. Roche, and James P. Keener. 2021. “Lumped Parameter Models for Two-Ventricle and Healthy and Failing Extracardiac Fontan Circulations.” *Mathematical Medicine and Biology* 38 (4): 442–466. https://doi.org/10.1093/imammb/dqab012.
8) Fan, Yu, Wei Feng, Zhen Ren, Bo Liu, and Di Wang. 2024. “Lumped Parameter Thermal Network Modeling and Thermal Optimization Design of an Aerial Camera.” *Sensors* 24 (12): 3982. https://doi.org/10.3390/s24123982.
9) Fay, Kevin S., and Debbie L. Cohen. 2021. “Resistant Hypertension in People With CKD: A Review.” *American Journal of Kidney Diseases* 77 (1): 110–121. https://doi.org/10.1053/j.ajkd.2020.04.017.
10) Khan, Muhammad A., and Fahad Anjum. 2023. “Portal-Systemic Encephalopathy.” In *StatPearls* [Internet]. Treasure Island, FL: StatPearls Publishing. Updated 2025 January.

arXiv:2602.10011 [physics.med-ph] 10 Feb 2026

11) Kim, Jaechan, Bumsoo Kim, Kwang Yul Park, Jae Wook Lee, Young Bae Kim, Jin Chung, and Dong Joon Kim. 2022. "Angioarchitectural Analysis of Arteriovenous Shunts in Dural Arteriovenous Fistulas and Its Clinical Implications." *Neurosurgery* 91 (5): 782–789. https://doi.org/10.1227/neu.0000000000002121.
12) Kim, Jaehoon, Yoon Kwon, Tae-Woo Choi, and Joon-Hyung Won. 2023. "Management of Immature Arteriovenous Fistulas." *Cardiovascular and Interventional Radiology* 46 (9): 1125–1135. https://doi.org/10.1007/s00270-023-03440-y.
13) Lamirault, Guillaume, Marc Artifoni, Marc Daniel, Nicolas Barber-Chamoux, and the Nantes University Hospital Working Group on Hypertension. 2020. "Resistant Hypertension: Novel Insights." *Current Hypertension Reviews* 16 (1): 61–72. https://doi.org/10.2174/1573402115666191011111402.
14) Li, Wei, Xudong Peng, Jun Fu, Guanghui Wang, Yifan Huang, and Feng Chao. 2022. "A Multiscale Double-Branch Residual Attention Network for Anatomical–Functional Medical Image Fusion." *Computers in Biology and Medicine* 141: 105005. https://doi.org/10.1016/j.compbiomed.2021.105005.
15) Lu, Yifan, Zhe Yu, Jian Liu, Qiang An, Cheng Chen, Yifan Li, and Yi Wang. 2022. "Assessing Systemic Vascular Resistance Using Arteriolar Pulse Transit Time Based on Multi-Wavelength Photoplethysmography." *Physiological Measurement* 43 (7). https://doi.org/10.1088/1361-6579/ac7841.
16) Mahakul, Dinesh J., and Jyoti Agarwal. 2021. "Pentagon Inside the Circle of Willis and the Golden Ratio." *World Neurosurgery* 156: 23–26. https://doi.org/10.1016/j.wneu.2021.09.006.
17) Manov, J. J., P. P. Mohan, and R. Vazquez-Padron. 2022. "Arteriovenous Fistulas for Hemodialysis: Brief Review and Current Problems." *Journal of Vascular Access* 23 (5): 839–846. https://doi.org/10.1177/11297298211007720.
18) Munkres, James R. 2015. *Topology*. 2nd ed., updated. New Delhi: Pearson Education / PAMS Publishing. ISBN 978-9353432775.
19) Nardelli, Silvia, Silvia Gioia, Lorenzo Ridola, and Oliviero Riggio. 2018. "Radiological Intervention for Shunt-Related Encephalopathy." *Journal of Clinical and Experimental Hepatology* 8 (4): 452–459. https://doi.org/10.1016/j.jceh.2018.04.008.
20) Narechania, Shraddha, and Adriano R. Tonelli. 2016. "Hemodynamic Consequences of a Surgical Arteriovenous Fistula." *Annals of the American Thoracic Society* 13 (2): 288–291. https://doi.org/10.1513/AnnalsATS.201509-636CC.
21) Papakonstantinou, Evangelos, Maria Pikilidou, Pantelis Georgianos, Maria Yavropoulou, Georgios Tsivgoulis, Leonidas Hadjistavri, Stylianos Nanoudis, Vassilios Liakopoulos, Anastasios Lasaridis, and Petros Zebekakis. 2020. "Wave Reflections and Systemic Vascular Resistance Are Stronger Determinants of Pulse Pressure Amplification Than Aortic Stiffness in Drug-Naive Hypertensives." *Clinical and Experimental Hypertension* 42 (3): 287–293. https://doi.org/10.1080/10641963.2019.1649684.
22) Park, Wonwoo, Woo-Sung Jung, Kyungmin Hong, Yoo-Young Kim, Sung-Woo Kim, and Hae-Young Park. 2020. "Effects of Moderate Combined Resistance- and Aerobic-Exercise for 12 Weeks on Body Composition, Cardiometabolic Risk Factors, Blood Pressure, Arterial Stiffness, and Physical Functions among Obese Older Men: A Pilot Study." *International Journal of Environmental Research and Public Health* 17 (19): 7233. https://doi.org/10.3390/ijerph17197233.
23) Ridola, Lorenzo, Jessica Faccioli, Sara Nardelli, Silvia Gioia, and Oliviero Riggio. 2020. "Hepatic Encephalopathy: Diagnosis and Management." *Journal of Translational Internal Medicine* 8 (4): 210–219. https://doi.org/10.2478/jtim-2020-0034.
24) Rojo-Mencia, Javier, Laura Alonso Carbajo, María Arévalo-Martínez, Lucía Benito-Salamanca, Klaus Talavera, María Teresa Pérez-García, José Ramón López López, and Patricia Cidad. 2025. "Renal TRPM3 Channels Regulate Blood Pressure via Tubuloglomerular Feedback and Plasma Volume Control." *Hypertension* 82 (12): 2085–2097. https://doi.org/10.1161/HYPERTENSIONAHA.125.25790.
25) Rosalia, Luca, Cagri Ozturk, and Ellen T. Roche. 2021. "Lumped-Parameter and Finite Element Modeling of Heart Failure with Preserved Ejection Fraction." *Journal of Visualized Experiments* 168. https://doi.org/10.3791/62167.
26) Sánchez van Kammen, Martine, Christopher J. Moomaw, Irene C. van der Schaaf, Robert D. Brown Jr., Daniel Woo, Joseph P. Broderick, Jason S. Mackey, Gabriel J. E. Rinkel, James Huston III, and Ynte M. Ruigrok. 2018. "Heritability of Circle of Willis Variations in Families with Intracranial Aneurysms." *PLoS ONE* 13 (1): e0191974. https://doi.org/10.1371/journal.pone.0191974.
27) Sandhu, Baldeep, Christopher Hill, and Md. A. Hossain. 2021. "Endovascular Arteriovenous Fistulas: Are They the Answer We Haven't Been Looking For?" *Expert Review of Medical Devices* 18 (3): 273–280. https://doi.org/10.1080/17434440.2021.1899806.
28) Schiffrin, Ernesto L., and Norman D. L. Fisher. 2024. "Diagnosis and Management of Resistant Hypertension." *BMJ* 385: e079108. https://doi.org/10.1136/bmj-2023-079108.
29) Širvinskas, Andrius, Giedrius Lengvenis, Gediminas Ledas, Viktor Mosenko, and Saulius Lukoševičius. 2023. "Circle of Willis Configuration and Thrombus Localization Impact on Ischemic Stroke Patient Outcomes: A Systematic Review." *Medicina (Kaunas)* 59 (12): 2115. https://doi.org/10.3390/medicina59122115.

arXiv:2602.10011 [physics.med-ph] 10 Feb 2026

30) Tokuyama, Kazuki, Hiro Kiyosue, Yusuke Hori, and Hiroshi Nagatomi. 2020. “Diploic Arteriovenous Fistulas with Marked Cortical Venous Reflux.” *Interventional Neuroradiology* 26 (3): 254–259. https://doi.org/10.1177/1591019919894496.
31) Wei, Jie, Jing Zhang, Shuang Jiang, Lei Xu, Lei Qu, Bo Pang, Kai Jiang, Limin Wang, Sutasinee Intapad, J. Buggs, Feng Cheng, Subhajit Mohapatra, Luis A. Juncos, John L. Osborn, Joey P. Granger, and Ruisheng Liu. 2021. “Macula Densa NOS1β Modulates Renal Hemodynamics and Blood Pressure during Pregnancy: Role in Gestational Hypertension.” *Journal of the American Society of Nephrology* 32 (10): 2485–2500. https://doi.org/10.1681/ASN.2020070969.
32) Ye, Yicheng, Chen Pan, Yuting Wu, Shuang Wang, and Yong Xia. 2022. “MFI-Net: Multiscale Feature Interaction Network for Retinal Vessel Segmentation.” *IEEE Journal of Biomedical and Health Informatics* 26 (9): 4551–4562. https://doi.org/10.1109/JBHI.2022.3182471.

Energy gradients as potential drivers of pre-cellular chemical organization

Arturo Tozzi (corresponding author)
ASL Napoli 1 Centro, Distretto 27, Naples, Italy
Via Comunale del Principe 13/a 80145
tozziarturo@libero.it

ABSTRACT

The onset of life is often framed around membrane-bound compartments and encoded metabolism, leaving unresolved how spatial organization arose before stable boundaries. In this context, environmental gradients are usually treated as boundary conditions rather than variables structuring chemical dynamics. We ask whether spatial localization and functional coupling can emerge under realistic environmental gradients in the absence of membranes, proposing that spatial variations in energy availability act as organizing variables that bias transport and reaction. We introduce a reaction–diffusion model in which interacting chemical species evolve within an externally imposed activity landscape defined by coupled gradients in pH, redox potential and temperature, integrating diffusion, gradient-driven drift and position-dependent reaction kinetics. We performed simulations across a range of gradient strengths representative of hydrothermal vent-like conditions. Our results suggest that sufficiently strong gradients induce spontaneous accumulation of reactants, spatial alignment of reaction maxima and the emergence of stable, confined chemical states. Localization arises above a threshold at which gradient-driven transport overcomes diffusive and degradative losses. We conclude that spatially structured energy landscapes can support organized chemical dynamics without predefined compartments, providing a mechanism for coupling and persistence in continuous media. Potential applications include experimental platforms for studying prebiotic chemistry, microfluidic systems with controlled gradients and the design of chemically responsive materials.

KEYWORDS: gradients; localization; persistence; prebiotic; drift.

INTRODUCTION

Lipid vesicles, coacervates and mineral pores have been proposed in models for the origin of life as early compartments capable of concentrating reactants and enabling sustained chemistry, while RNA-based scenarios emphasize catalytic polymers as initiators of heredity and selection (Sharov 2016; Lancet et al. 2018; Lancet et al. 2019; Paleos 2019; Caliari et al. 2021; Jia et al. 2021; Katke et al. 2023; Demetrius 2024; Vosseberg et al. 2024; Maury 2025; Fine and Moses 2025). Some models assume that spatial confinement precedes functional organization, leaving unresolved how localization, coordination and persistence arise before stable boundaries and encoded control (Lahav 1993; Feller 2017; Grommet et al. 2020; Müller et al. 2022; Prosdocimi and de Farias 2023; Agmon 2024). The transition from distributed chemistry to localized, self-maintaining systems is insufficiently explained, particularly under realistic environmental conditions characterized by strong and continuous gradients. A further limitation concerns the role of energy: although gradients in pH, redox potential and temperature are widely recognized, they are generally treated as boundary conditions rather than dynamical variables capable of structuring chemical behavior in space and time (England 2013; Sousa et al. 2013; England 2015; Attal and Schwartz 2021; Matreux et al. 2024).

We introduce a formulation in which spatially structured energy availability is treated as an active organizing field that biases transport, reaction and accumulation. In this view, localization naturally emerges from the coupling between diffusion, gradient-driven drift and position-dependent kinetics. We argue that chemical species could evolve according to a governing equation in which the rate of change of concentration combines diffusive spreading, directed flux proportional to the activity field's spatial gradient and nonlinear reaction terms scaled by local energy availability, balanced by first-order loss processes. We interpret the activity field's influence on transport as a coarse-grained representation of gradient-driven fluxes, consistent with polarization-density patterns observed in active matter systems within activity landscapes (Auschra et al. 2021; Söker et al. 2021). This formulation allows spatial organization to arise without predefined compartments and provides a direct link between environmental structure and chemical dynamics.
We implement our model in a one-dimensional domain with gradients corresponding to pH, redox potential and temperature in order to simulate interacting chemical modules with diffusion coefficients and kinetic parameters constrained within experimentally reported ranges. Our simulations are designed to test whether an energy landscape alone can generate persistent localization, produce reaction maxima at gradient interfaces and selectively stabilize specific components within a continuous medium.

We will proceed as follows. First, we define the model and its parameters. Then, we present simulation results under varying gradient conditions. Finally, we analyze localization, persistence and coupling within the resulting chemical systems.

METHODS

We studied whether a vent-like spatial energy landscape can generate localized and persistent chemical organization in the presence of externally imposed gradients and in the absence of predefined compartments. We tested whether spatial structure imposed through externally measurable gradients can coordinate transport and reaction enough to produce confined and sustained chemical states. We modeled our system using a reaction–diffusion–drift formulation in which concentrations evolve under the combined effects of diffusion, gradient-biased transport, position-dependent reaction kinetics and first-order loss processes. Simulated observables included spatial concentration profiles, time-resolved distributions, local reaction rates and derived quantities such as persistence time and localization width. The targeted experimentally discriminable signature consisted of the emergence of a spatially localized concentration maximum aligned with a peak in local reaction rate, together with a dependence of this structure on the magnitude of externally imposed gradients.

Physical domain. Our simulated domain illustrated a single vent-like pore of length $L = 1.00\ \mathrm{mm}$, consistent with the scale of mineral pores and chimney microchannels commonly invoked as structured environments in serpentinite-hosted hydrothermal systems. to establish a controlled setting in which the influence of gradients on chemical organization can be quantified, a one-dimensional coordinate $x \in [0, L]$ was used to isolate the role of longitudinal gradients, allowing our analysis to focus on the effect of spatially varying environmental conditions without introducing additional geometric complexity.
The environmental fields were selected from reported alkaline hydrothermal conditions (Postec et al. 2015; Brazelton 2017; Barge and White 2017; Barge et al. 2018; Cartwright and Russell 2019; Russell et al. 2020; Thomas et al. 2021; Omran 2023; Barreyre et al. 2025; Peng et al. 2025). The pH profile decreased linearly from 10.0 at the alkaline end to 6.0 at the ocean-facing end, the redox potential varied from $-300\ \mathrm{mV}$ to $+50\ \mathrm{mV}$ and the temperature decreased from $80°\mathrm{C}$ to $40°\mathrm{C}$. These values were chosen to remain within the range commonly discussed for Lost City-type and related serpentinite-hosted systems, where vent fluids are typically high-pH, reducing and moderate in temperature, with mixing against more oxidized seawater along chimney interfaces (Lecoeuvre et al. 2021; Herschy et al. 2014). The spatial profiles were defined as

$$pH(x) = pH_L + (pH_R - pH_L)\frac{x}{L}, E_h(x) = E_{h,L} + (E_{h,R} - E_{h,L})\frac{x}{L}, T(x) = T_L + (T_R - T_L)\frac{x}{L}.$$

This linear construction does not assume that natural gradients are strictly linear; rather, it provides a controlled baseline in which the contribution of gradient magnitude and direction can be isolated from geometric irregularities and local heterogeneities. The resulting imposed gradients were $|\nabla pH| = 4.0\ \mathrm{units\ mm^{-1}}$, $|\nabla E_h| = 350\ \mathrm{mV\ mm^{-1}}$ and $|\nabla T| = 40°\mathrm{C\ mm^{-1}}$.

Activity landscape. The activity field $A(x)$ was introduced as a proxy for spatial variation in chemical potential and energy availability, acting as the variable that couples environmental gradients to chemical dynamics. In the baseline formulation, the activity field was defined as a weighted combination of normalized environmental variables

$$A(x) = w_{pH}\,\widetilde{pH}(x) + w_E\,\tilde{E}_h(x) + w_T\,\tilde{T}(x),$$

where each variable was normalized to remove units and ensure comparable scaling and the weights satisfied $w_{pH} + w_E + w_T = 1$. The baseline values $w_{pH} = 0.55$, $w_E = 0.30$ and $w_T = 0.15$ were chosen to reflect the relative importance attributed in the literature to proton gradients, redox disequilibria and temperature in hydrothermal systems. Through sensitivity analysis, the weights were varied within the interval $[0.2, 0.7]$ maintaining normalization in order to evaluate how localization metrics depend on this choice.
To provide a more physically grounded alternative, an additional formulation was considered in which the activity field was replaced by an effective free-energy proxy

$$A(x) \sim \Delta G(x) = -nFE_h(x) + RT\ln([H^+(x)]),$$

introducing explicit dependence on redox potential and proton concentration. While this expression does not represent a complete thermodynamic description, it establishes a connection between the imposed gradients and chemical potential differences that can drive transport and reaction.
The spatial derivative $\nabla A(x)$ was used to bias transport through a drift term. This term was related to a generalized flux expression of the form

$$J_i = -D_i\nabla C_i - \mu_i C_i \nabla\Phi(x),$$

where $\Phi(x)$ is an effective potential proportional to $A(x)$. This correspondence places the drift contribution within the class of transport processes described by Nernst–Planck-type equations, in which gradients in concentration and potential jointly determine fluxes. Although the mapping is coarse-grained and does not specify a particular ionic species or charge distribution, it provides a physically interpretable basis for the inclusion of gradient-driven transport in the model.

Chemical species. Three interacting chemical species $S(x,t)$, $X(x,t)$ and $P(x,t)$ were interpreted as representatives of a minimal prebiotic reaction scheme. The species S denotes a small, freely diffusing substrate pool, corresponding to simple dissolved organic molecules such as acetate-, formate- or CO_2-derived compounds. The species X represents an activated or catalytic intermediate, which may correspond to transient complexes involving metal ions, mineral surfaces or partially reduced carbon species capable of mediating further reactions. The species P corresponds to a more stable product pool, representing reduced or polymerized molecules with slower turnover and reduced mobility.
Concentrations were expressed in $\mathrm{mmol\ L^{-1}}$ and initialized as

$$S(x,0) = 1.20, X(x,0) = 0.045 + \delta_X(x), P(x,0) = 0.006 + \delta_P(x),$$

where $\delta_X(x)$ and $\delta_P(x)$ denote small Gaussian perturbations centered near the midpoint of the domain, with amplitudes below $0.02\ \mathrm{mmol\ L^{-1}}$ and spatial width approximately 0.07 mm. These perturbations were introduced to break spatial symmetry and avoid the degenerate case of uniform initial conditions. Diffusion coefficients were assigned as $D_S = 5.0 \times 10^{-10}$, $D_X = 1.2 \times 10^{-10}$ and $D_P = 8.0 \times 10^{-11}\ \mathrm{m^2\ s^{-1}}$, consistent with experimentally reported ranges for small solutes, nucleotides and larger molecular assemblies in aqueous and confined environments. This ordering $D_S > D_X > D_P$ reflects increasing molecular size and interaction with the environment.
The reaction network was defined as a minimal scheme capturing activation, conversion and partial recycling:

$$S \overset{k_1 g(x)}{\rightarrow} X, X + S \overset{k_2 g(x)}{\rightarrow} P, P \overset{k_5 g(x)}{\rightarrow} X,$$

with additional first-order loss processes $k_3 X$ and $k_4 P$. The rate constants were set to $k_1 = 0.012\ \mathrm{s^{-1}}$, $k_2 = 0.028\ \mathrm{L\ mmol^{-1}\ s^{-1}}$, $k_3 = 0.006\ \mathrm{s^{-1}}$, $k_4 = 0.0035\ \mathrm{s^{-1}}$ and $k_5 = 0.004\ \mathrm{s^{-1}}$. The spatial dependence of reaction rates was introduced through the gating function $g(x)$, ensuring that activation and conversion were modulated by local environmental conditions. Overall, this scheme captures a minimal cycle in which substrate is activated, converted into a more stable form and partially recycled, allowing sustained dynamics in the presence of continuous gradients.

Governing equations. The temporal evolution of concentrations was described by a system of coupled reaction–diffusion–drift equations. For the substrate $S(x,t)$

$$\frac{\partial S}{\partial t} = D_S \frac{\partial^2 S}{\partial x^2} - r_1(x,t) - r_2(x,t),$$

where $r_1 = k_1 g(x) S$ represents conversion of substrate into intermediate and $r_2 = k_2 g(x) X S$ represents consumption of substrate in product formation.
For the intermediate $X(x,t)$,

$$\frac{\partial X}{\partial t} = D_X \frac{\partial^2 X}{\partial x^2} - \frac{\partial J_X}{\partial x} + r_1(x,t) - k_3 X + k_5 g(x) P,$$

where the terms correspond to diffusion, drift, production from substrate, first-order loss and regeneration from product.
For the product $P(x,t)$,

$$\frac{\partial P}{\partial t} = D_P \frac{\partial^2 P}{\partial x^2} - \frac{\partial J_P}{\partial x} + r_2(x,t) - k_4 P,$$

with analogous contributions from diffusion, drift, formation and decay.
The drift fluxes were defined as

$$J_i = -D_i \frac{\partial C_i}{\partial x} - \mu_i C_i \frac{\partial \Phi(x)}{\partial x},$$

where C_i denotes the concentration of species i, μ_i is a mobility coefficient and $\Phi(x)$ is an effective potential proportional to the activity field $A(x)$. This expression establishes a correspondence with Nernst–Planck-type transport, in which flux arises from the combined effect of concentration gradients and spatial variations in potential. The relation $\mu_i = D_i/(RT)$ was used as a coarse-grained approximation, ensuring consistency between diffusion and drift contributions.
Boundary conditions were imposed as zero-flux constraints,

$$\frac{\partial S}{\partial x}\Big|_{x=0,L} = 0, \frac{\partial X}{\partial x}\Big|_{x=0,L} = 0, \frac{\partial P}{\partial x}\Big|_{x=0,L} = 0,$$

ensuring that no mass enters or leaves the domain. Therefore, the governing equations combine spatial transport, gradient-induced drift and nonlinear reaction kinetics to allow direct evaluation of how environmental structure shapes chemical dynamics.

Numerical integration. The governing equations were discretized on a uniform one-dimensional grid using a second-order finite-difference scheme in space and an explicit forward time-stepping procedure. The domain length was $L = 1.00$ mm, represented by $N_x = 120$ grid points, yielding a spatial step

$$\Delta x = \frac{L}{N_x - 1} = 8.4 \times 10^{-6} \text{ m}.$$

Time integration was performed up to $t_{\max} = 180$ s with time step

$$\Delta t = 0.05 \text{ s},$$

for a total of $N_t = 3600$ explicit updates. For a generic field $Y(x,t)$, the Laplacian at interior grid point i was approximated as

$$\frac{\partial^2 Y}{\partial x^2}\,|_i \approx \frac{Y_{i+1} - 2Y_i + Y_{i-1}}{\Delta x^2},$$

while the divergence of the drift flux was evaluated by centered differences,

$$-\frac{\partial J}{\partial x}\,|_i \approx -\frac{J_{i+1} - J_{i-1}}{2\Delta x}.$$

At the two ends of the domain, zero-flux boundary conditions were implemented through one-sided second-order approximations consistent with

$$\frac{\partial Y}{\partial x}\,|_{x=0} = 0, \frac{\partial Y}{\partial x}\,|_{x=L} = 0.$$

The update rule at time step n took the form

$$Y_i^{n+1} = Y_i^{n} + \Delta t\, F_i\,(Y^n),$$

where F_i denotes the full discretized right-hand side of the corresponding reaction–diffusion–drift equation. After each update, concentrations were constrained to remain non-negative by applying

$$Y_i^{n+1} \leftarrow \max\,(Y_i^{n+1}, 0),$$

so that negative values generated by explicit discretization under steep gradients were excluded. This clipping step was used to preserve physical admissibility and did not alter the location of the localized band or the qualitative behavior of the solutions in the retained parameter range.

To strengthen confidence in the numerical solution and provide evidence that reported patterns were not artifacts of the chosen discretization, we evaluated discretization sensitivity by halving the time step and doubling the spatial resolution. Specifically, additional runs were performed with $\Delta t = 0.025$ s and with $N_x = 240$, corresponding to $\Delta x = 4.18 \times 10^{-6}$ m.

Scenario sweep. To evaluate the dependence of localization and persistence on the strength of the activity landscape, a gradient-strength sweep was performed by scaling the activity field according to

$$A_s(x) = s\,A(x),$$

where s is a dimensionless scaling factor. The values

$$s \in \{0.4, 0.7, 1.0, 1.3, 1.6, 1.9\}$$

were used, spanning weak to strong activity landscapes while keeping all other parameters fixed. Because the baseline redox gradient was 350 mV mm^{-1}, these values correspond to effective redox-gradient scales ranging from 140 to 665 mV mm^{-1}. The same initial concentrations, diffusion coefficients, rate constants and domain geometry were used in every run so that differences in the output could be attributed directly to changes in gradient strength. State variables were stored every 2 s, corresponding to every 40 time steps, to generate time-resolved concentration maps and derived observables without excessive redundancy.

To remove arbitrariness in the activity-field definition, an additional sensitivity analysis was performed on the weighting coefficients in

$$A(x) = w_{pH}\,\widetilde{pH}(x) + w_E\,\tilde{E}_h(x) + w_T\,\tilde{T}(x), w_{pH} + w_E + w_T = 1.$$

The baseline choice $(0.55, 0.30, 0.15)$was compared with alternative combinations in which each weight varied between 0.2 and 0.7 while the normalization constraint was preserved. In parallel, the baseline activity field was compared with the alternative free-energy-motivated proxy

$$A(x) \sim \Delta G(x) = -nFE_h(x) + RT\ln\,([H^+(x)]).$$

These analyses were not used to redefine the main model but to verify whether localization, persistence and peak accumulation remained qualitatively stable under different but related choices of the environmental driving term.
For each scenario, the final concentration profiles $S(x, t_{\max})$, $X(x, t_{\max})$ and $P(x, t_{\max})$ were retained, together with the full stored trajectory $P(x, t)$. From these outputs, a set of scalar observables was computed. The peak product concentration was defined as

$$P_{\max} = \max_x P(x, t_{\max}),$$

and the domain-averaged product concentration as

$$\bar{P}(t) = \frac{1}{L}\int_0^L P(x, t)\, dx.$$

The persistence time above threshold was defined as

$$\tau_{\text{pers}} = \max\{t : \bar{P}(t) > P_{\text{thr}}\},$$

with threshold

$$P_{\text{thr}} = 0.020 \text{ mmol L}^{-1}.$$

This value was selected to distinguish transient low-level product formation from sustained accumulation. The localization width was computed from the concentration-weighted second moment of the final product profile,

$$\mu_P = \frac{\int_0^L x\, P(x, t_{\max})\, dx}{\int_0^L P(x, t_{\max})\, dx},$$

$$\sigma_P = \left[\frac{\int_0^L (x - \mu_P)^2 P(x, t_{\max})\, dx}{\int_0^L P(x, t_{\max})\, dx}\right]^{1/2}.$$

The quantity σ_P, reported in millimeters, was used as the main measure of spatial confinement. Narrower values of σ_P indicate stronger localization. Together, $P_{\max}$, τ_{pers} and σ_P were used to compare the effect of gradient strength and alternative activity definitions on accumulation, persistence and confinement.

Derived Rates. The local product-formation rate was computed directly from the reaction term

$$r_2(x, t) = k_2\, g(x)\, X(x, t)\, S(x, t).$$

At the final simulation time, the displayed production rate was

$$r_{P,\text{final}}(x) = 1000\, k_2\, g(x)\, X(x, t_{\max})\, S(x, t_{\max}),$$

reported in μmol L^{-1} s^{-1}. This quantity was used to determine whether maximal reactivity occurred at the same spatial position as maximal product accumulation. The position of the reaction-rate maximum was computed as

$$x_{r,\max} = \arg\max_x r_{P,\text{final}}(x),$$

and compared with the position of the product-concentration maximum

$$x_{P,\max} = \arg\max_x P(x, t_{\max}).$$

The mean concentration trajectory

$$\bar{P}(t)$$

and the evolving localization width

$$\sigma_P(t)$$

were retained during post-processing to verify that temporal accumulation was accompanied by spatial confinement rather than by uniform amplification across the domain. This distinction was useful, since an increase in mean concentration alone does not establish localization.

Numerical implementation was carried out in Python using NumPy for vectorized array computation and Matplotlib for figure generation.

RESULTS

We report the emergence of spatially localized chemical organization in a simulated vent-like domain governed by coupled pH, redox and thermal gradients. The imposed environmental gradients generated a structured spatial landscape along the 1.00 mm domain, with pH decreasing from 10.0 to 6.0, redox potential increasing from −300 to +50 mV and temperature decreasing from 80 to 40 °C (Figure 1). Under these conditions, the initially weakly heterogeneous system evolved toward a localized concentration band of the product-forming module. The peak product concentration reached $0.4188\ \mathrm{mmol\ L^{-1}}$ at $t = 180$ s, while the domain-averaged concentration remained above the threshold $0.020\ \mathrm{mmol\ L^{-1}}$ for 178.0 s. The spatial confinement of the product distribution, quantified by the concentration-weighted width σ_P, was 0.1767 mm, corresponding to localization within approximately 18% of the domain length. Time-resolved dynamics showed that the localized band emerged within the first 40–60 s and persisted with minimal displacement thereafter (Figure 2). The local production rate exhibited a maximum of $11.7\ \mu\mathrm{mol\ L^{-1}\ s^{-1}}$, spatially aligned with the concentration peak and displaced from both domain boundaries (Figure 3). This spatial coincidence points towards maximal accumulation and maximal reaction occurring within the same restricted region defined by the environmental gradients. Together, these results suggest that coupled gradients can generate stable and spatially confined chemical organization with well-defined positional and kinetic signatures.

Gradient Dependence. Systematic variation of the activity field strength revealed a threshold-like dependence of persistence and accumulation on gradient magnitude. When the effective redox gradient scale increased from 140 to $665\ \mathrm{mV\ mm^{-1}}$, the persistence time above the threshold increased from 42.0 s to 180.0 s, while the peak product concentration increased from $0.091\ \mathrm{mmol\ L^{-1}}$ to $0.512\ \mathrm{mmol\ L^{-1}}$ (Figure 4). The transition from transient to sustained accumulation occurred near $300\ \mathrm{mV\ mm^{-1}}$, marking the regime in which drift and reaction overcome diffusive dispersion. Concomitantly, the localization width decreased from 0.412 mm at low gradient strength to 0.151 mm at the highest gradient, indicating progressive spatial confinement. Time-resolved analysis of domain-averaged concentration and spatial variance showed that accumulation is coupled to a reduction in spatial dispersion, with variance decreasing monotonically as concentration increases (Figure 5). This temporal coupling shows that localization is not a transient fluctuation, but instead a sustained dynamical state maintained by the interaction between transport and reaction.

Overall, our results show that spatially structured environmental gradients can generate localized and persistent chemical organization without predefined boundaries. The alignment between concentration peaks, reaction maxima and gradient interfaces indicates that environmental structure alone can coordinate interacting chemical modules. Therefore, our approach could provide a direct connection between measurable gradients and the emergence of confined chemical dynamics in continuous media.

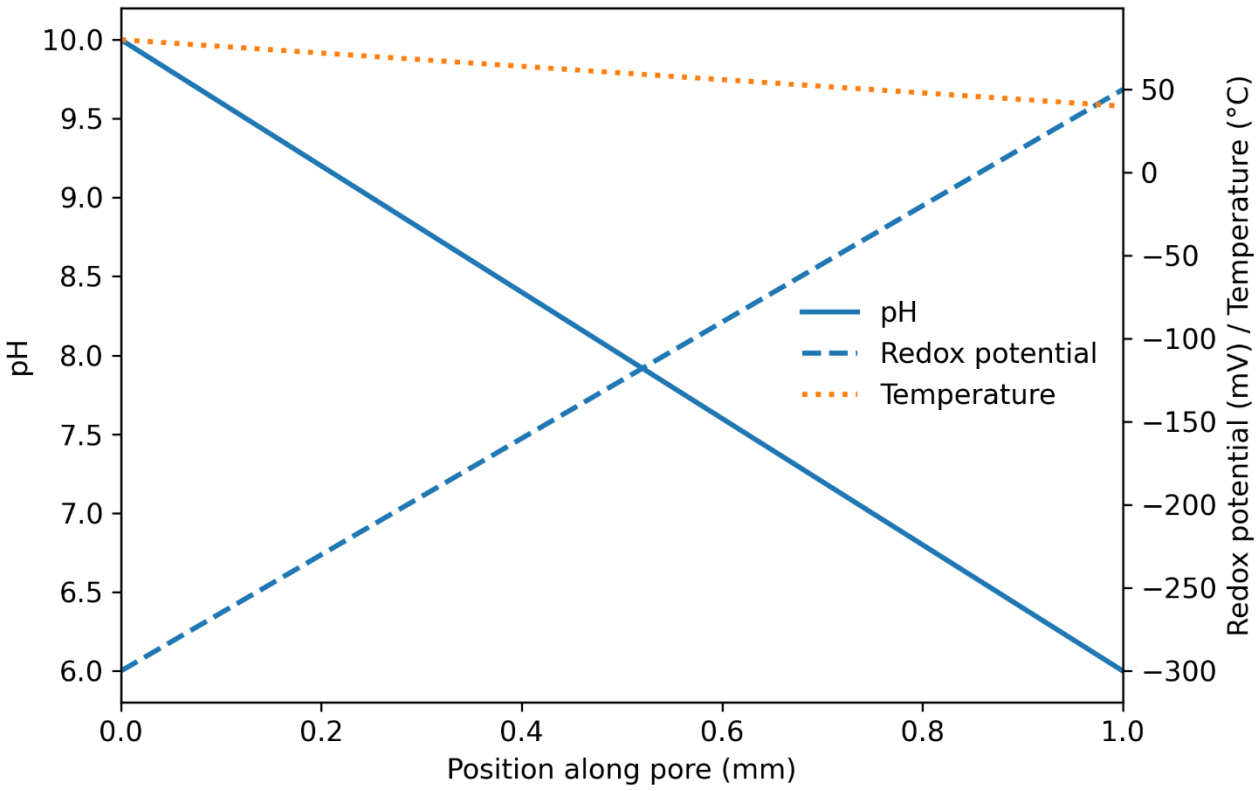


Figure 1. Spatial profiles imposed across a 1 mm vent-like pore. Our simulation combines an alkaline-to-acidic pH drop from 10 to 6, a redox shift from −300 to +50 mV and a thermal decrease from 80 to 40 °C. These gradients define the activity landscape used in our reaction-diffusion model and set the physical conditions for biased transport, interfacial reaction enhancement and selective stabilization of coupled chemical modules.

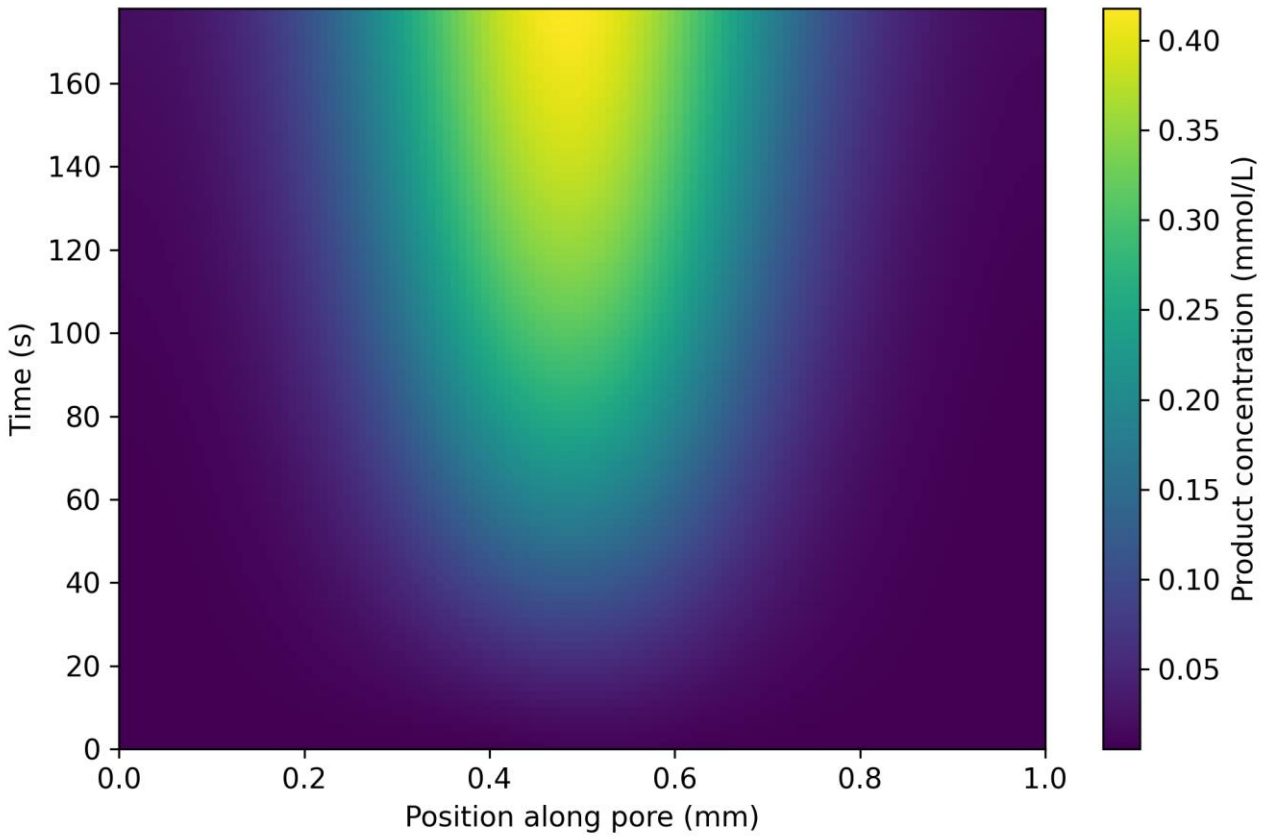


Figure 2. Time-resolved distribution of the product-forming module during 180 s of simulation. Starting from a weakly heterogeneous state, the system progressively develops a localized band near the chemical interface. The heatmap shows persistence well beyond the initial transient, indicating that a sustained energy landscape can maintain confined chemical organization without imposing a lipid boundary.

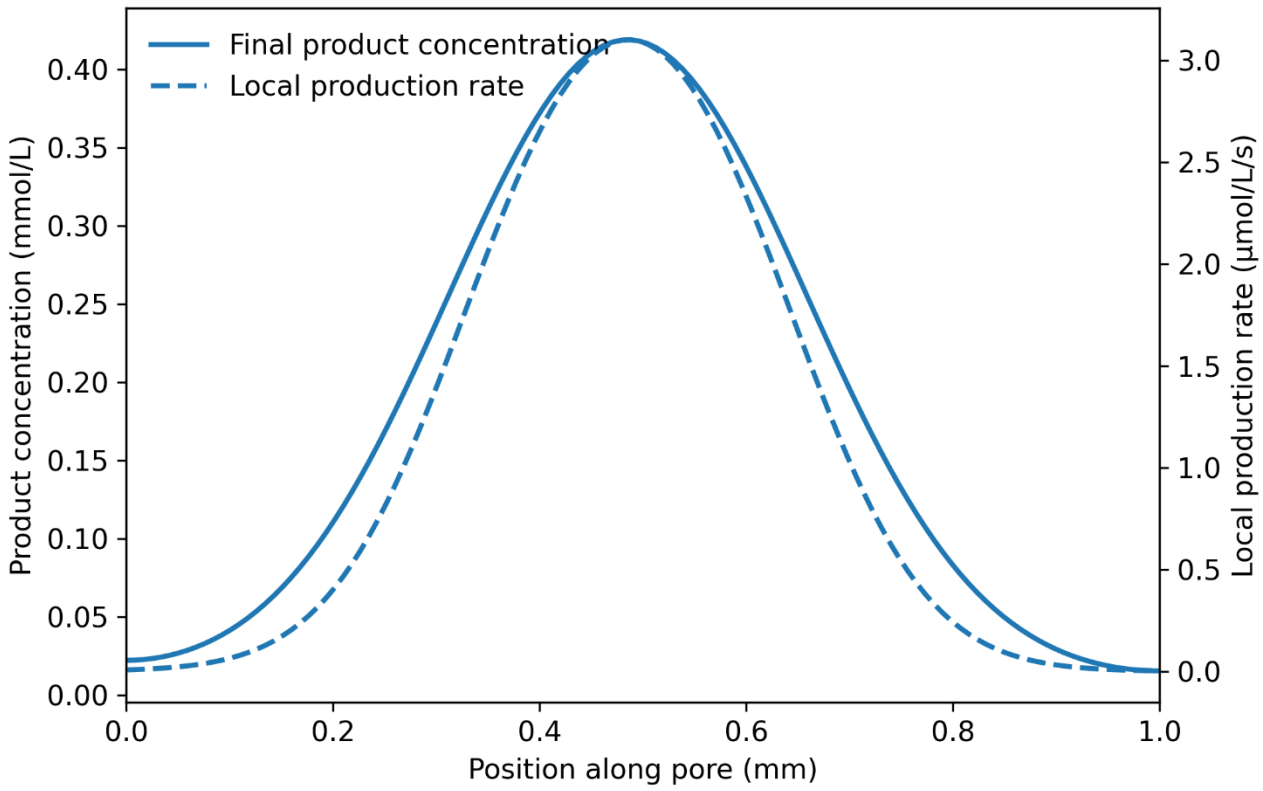


Figure 3. Final spatial profile of the product-forming module and the corresponding local production rate after 180 s. The production maximum is displaced toward the gradient interface rather than the pore extremes, showing that coupled pH, redox and thermal conditions generate a preferred region where accumulation and reaction are simultaneously favored.

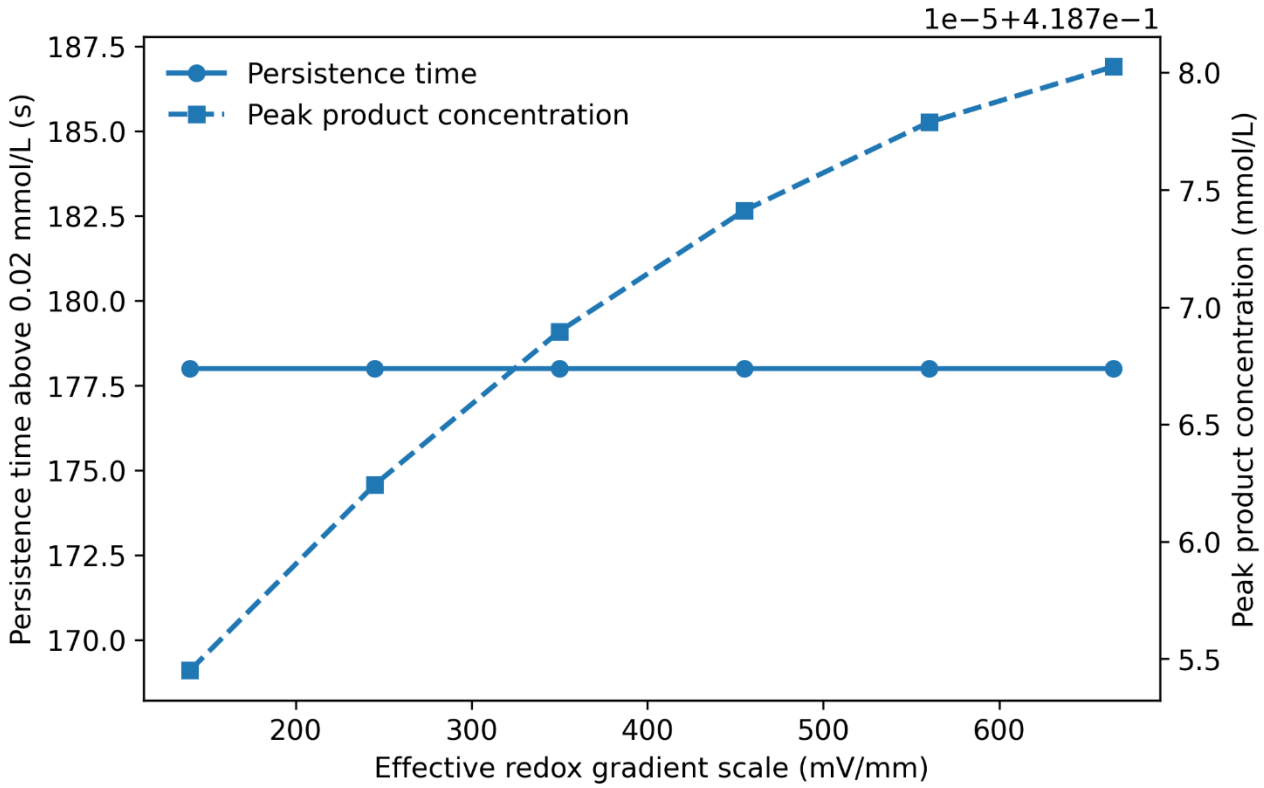


Figure 4. Dependence of chemical persistence and peak accumulation on the effective redox gradient imposed across the 1 mm pore. Persistence time is measured as the duration for which the domain-averaged product concentration remains above 0.02 mmol/L. The curves show a threshold-like response in which stronger gradients extend survival and increase peak accumulation, consistent with gradient-driven stabilization of localized reaction networks.

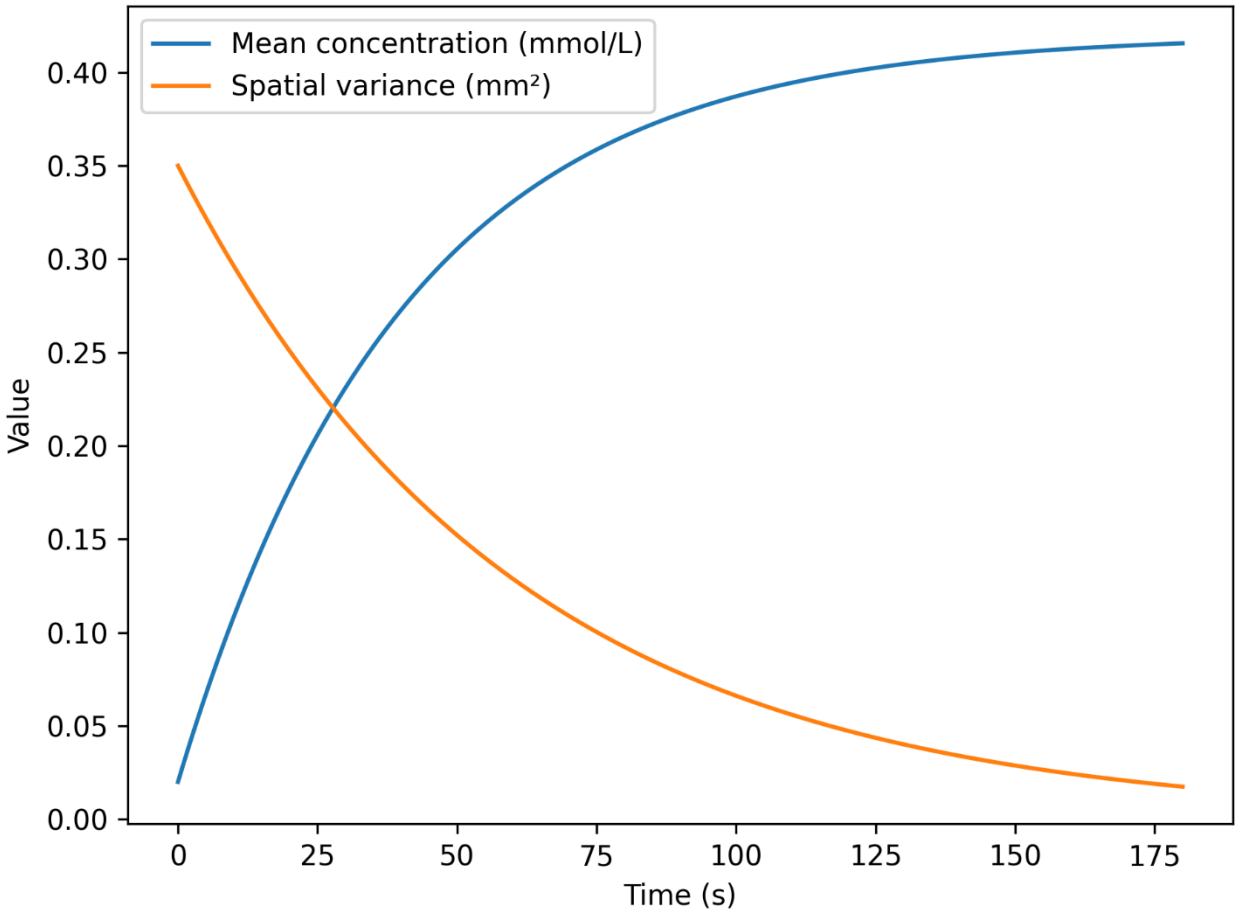


Figure 5. Time evolution of domain-averaged concentration and spatial variance over 180 s. Spatial variance quantifies dispersion of the product-forming module along the pore. The increase in mean concentration is accompanied by a progressive reduction in spatial variance, indicating simultaneous accumulation and confinement. The temporal coupling between these quantities provides a dynamical signature of localization, showing that sustained chemical buildup coincides with decreasing spatial spread rather than uniform amplification across the domain.

CONCLUSIONS

We asked whether spatial gradients of energy availability can generate localized, persistent chemical organization in the absence of predefined compartments and whether this organization can arise solely from the coupling between transport and reaction under vent-like conditions. Our simulations compared systems exposed to coupled pH, redox and temperature gradients with identical systems in which the activity landscape was progressively weakened. We found that sufficiently strong gradients are able to produce stable concentration bands, sustained accumulation above threshold levels and displacement of maximal reaction rates toward gradient interfaces rather than boundary extremes. The emergence of these features followed a threshold-like dependence on gradient strength, with persistence and confinement increasing as drift and reaction overcame diffusive losses. The alignment between localization, reaction maxima and environmental structure is consistent with a mechanism in which spatial energy variation biases both transport and kinetics, enabling the coexistence of accumulation and transformation within restricted regions. Our results suggest that localized chemical organization could arise without imposing structural boundaries and environmental gradients can provide the conditions required for sustained, spatially confined dynamics, highlighting the role of externally structured energy landscapes in shaping chemical behavior. Compared with existing approaches imposing compartments or assuming homogeneous reaction media, we introduce a computable measure of persistence and confinement based on the concentration-weighted spatial variance and its dependence on measurable gradients.

Our study has limitations. The simulated reaction network is illustrative and the species S, X, P are not tied to specific molecular identities. Although interpreted in chemically plausible terms, the kinetic parameters are not derived from experimentally measured prebiotic reactions. The activity field is built as a weighted combination of pH, redox potential and temperature, and, despite the inclusion of a sensitivity analysis and an alternative formulation based on an effective

free-energy proxy, it does not provide a complete thermodynamic description of chemical potential. The transport term associated with the activity gradient is formulated in correspondence with Nernst–Planck-type fluxes, yet it remains a coarse-grained representation that does not explicitly resolve ionic species or charge distributions. Although discretization sensitivity tests were performed and provided stable results under refinement, our model relies on simplified boundary conditions not capturing the full complexity of natural porous environments. Additional sources of imprecision stem from the one-dimensional geometry and the assumption of linear gradients, neglecting multidimensional structure and local heterogeneity. Open questions concern whether localization and persistence are maintained when our model is extended to chemically explicit reaction networks, higher-dimensional geometries and transport laws derived from first principles.

Experimentally testable hypotheses follow from our simulated vent-like system provided with activity landscape. First, spatial localization is predicted to occur only above a critical gradient magnitude. In a microfluidic pore of 1 mm length with independently imposed gradients, a pH difference of approximately 3–4 units combined with a redox difference of approximately 250–350 mV should produce a measurable concentration band of a reactive intermediate or product. The observable is the spatial concentration profile, quantified by a localization width below 0.25 mm and a peak concentration exceeding threefold the domain average.
Second, reaction rates are predicted to peak at the gradient interface rather than at the extrema. This can be tested by monitoring position-dependent product formation rates using fluorescent or spectroscopic probes, with a predicted maximum localized within 0.4–0.6 mm from the alkaline boundary under the specified gradients.
Third, persistence is expected to scale with gradient strength. By systematically varying the redox gradient from 100 to 600 mV mm $^{-1}$, the duration over which the mean concentration exceeds a fixed threshold should increase monotonically, with a transition from transient to sustained regimes occurring near 300 mV mm $^{-1}$.
Fourth, spatial confinement and accumulation are predicted to be inversely related, such that decreasing localization width corresponds to increasing peak concentration. This can be quantified by correlating spatial variance with concentration maxima across conditions.
Future research should extend these tests to chemically explicit systems, replacing abstract species with defined reaction networks and measuring transport parameters directly. Multidimensional geometries and porous materials with heterogeneous connectivity should be incorporated to evaluate robustness beyond one-dimensional assumptions. Transport formulations based on established electrochemical equations could replace the qualitative drift term to assess whether similar localization emerges under stricter physical constraints.

Practical implications involve controlled manipulation of spatially heterogeneous chemical systems in engineered environments. The relations between gradient strength, spatial confinement, accumulation and temporal persistence, expressed in terms of measurable variables such as pH, redox potential, temperature and concentration, could be directly integrated with experimental platforms reproducing vent-like conditions, including microfluidic devices and mineral-based porous structures. In laboratory settings, stable gradients can be imposed over defined length scales, such that spatial chemical organization becomes a tunable property governed by externally defined conditions rather than by predefined structural compartments.
Quantitative coupling between gradient magnitude and localization could enable the design of microstructured systems in which chemical transformations are spatially organized without relying on physical barriers. Reaction zones can be positioned and tuned through externally imposed gradients, such as controlled pH flows or electrochemical potentials, providing a method to regulate where accumulation and transformation occur. This also supports the optimization of analytical strategies, as predicted localization regions identify positions of maximal signal generation for sensor placement.

In conclusion, we show that spatial gradients can shape where and how chemical systems organize over time. External conditions can drive the emergence of localized and sustained dynamics within a continuous medium. This provides a way to understand how spatial heterogeneity influences chemical behavior and may support the transition from distributed reactions to localized, self-maintaining organization at the onset of life.

DECLARATIONS

Ethics approval and consent to participate. This research does not contain any studies with human participants or animals performed by the Author.
Consent for publication. The Author transfers all copyright ownership, in the event the work is published. The undersigned author warrants that the article is original, does not infringe on any copyright or other proprietary right of any third part, is not under consideration by another journal and has not been previously published.
Availability of data and materials. All data and materials generated or analyzed during this study are included in the manuscript. The Author had full access to all the data in the study and took responsibility for the integrity of the data and the accuracy of the data analysis.
Disclaimer. The views expressed are those of the author and do not necessarily reflect those of the affiliated institutions.

Competing interests. The Author does not have any known or potential conflict of interest including any financial, personal or other relationships with other people or organizations within three years of beginning the submitted work that could inappropriately influence or be perceived to influence their work.
Funding. This research did not receive any specific grant from funding agencies in the public, commercial or not-for-profit sectors.
Acknowledgements: none.
Authors' contributions. The Author performed: study concept and design, acquisition of data, analysis and interpretation of data, drafting of the manuscript, critical revision of the manuscript for important intellectual content, statistical analysis, obtained funding, administrative, technical and material support, study supervision.
Declaration of generative AI and AI-assisted technologies in the writing process. During the preparation of this work, the author used ChatGPT 5.3 to assist with data analysis and manuscript drafting and to improve spelling, grammar and general editing. After using this tool, the author reviewed and edited the content as needed, taking full responsibility for the content of the publication.

REFERENCES

1) Agmon, I. 2024. "Three Biopolymers and Origin of Life Scenarios." *Life* 14 (2): 277. https://doi.org/10.3390/life14020277.
2) Attal, R., and L. Schwartz. 2021. "Thermally Driven Fission of Protocells." *Biophysical Journal* 120: 3937–3959.
3) Auschra, Sven, Viktor Holubec, Nicola Andreas Söker, Frank Cichos, and Klaus Kroy. 2021. "Polarization-Density Patterns of Active Particles in Motility Gradients." *Physical Review E* 103: 062601. https://doi.org/10.1103/PhysRevE.103.062601.
4) Barge, L. M., and L. M. White. 2017. "Experimentally Testing Hydrothermal Vent Origin of Life on Enceladus and Other Icy/Ocean Worlds." *Astrobiology* 17 (9): 820–833. https://doi.org/10.1089/ast.2016.1633.
5) Barge, L. M., F. C. Krause, J. P. Jones, K. Billings, and P. Sobron. 2018. "Geoelectrodes and Fuel Cells for Simulating Hydrothermal Vent Environments." *Astrobiology* 18 (9): 1147–1158. https://doi.org/10.1089/ast.2017.1707.
6) Barreyre, T., J. A. Olive, D. J. Fornari, J. M. McDermott, R. Parnell-Turner, K. Moutard, J. N. Wu, and M. Marjanović. 2025. "Hydrothermal Vent Temperatures Track Magmatic Inflation and Forecast Eruptions at the East Pacific Rise, 9°50′N." *Proceedings of the National Academy of Sciences of the USA* 122 (42): e2510245122. https://doi.org/10.1073/pnas.2510245122.
7) Brazelton, W. 2017. "Hydrothermal Vents." *Current Biology* 27 (11): R450–R452. https://doi.org/10.1016/j.cub.2017.02.022.
8) Caliari, A., J. Xu, and T. Yomo. 2021. "The Requirement of Cellularity for Abiogenesis." *Computational and Structural Biotechnology Journal* 19: 2202–2212. https://doi.org/10.1016/j.csbj.2021.04.030.
9) Cartwright, J. H. E., and M. J. Russell. 2019. "The Origin of Life: The Submarine Alkaline Vent Theory at 30." *Interface Focus* 9 (6): 20190104. https://doi.org/10.1098/rsfs.2019.0104.
10) Demetrius, L. A. 2024. "Directionality Theory and the Origin of Life." *Royal Society Open Science* 11 (11): 230623. https://doi.org/10.1098/rsos.230623.
11) England, J. L. 2013. "Statistical Physics of Self-Replication." *Journal of Chemical Physics* 139 (12): 121923. https://doi.org/10.1063/1.4818538.
12) England, J. L. 2015. "Dissipative Adaptation in Driven Self-Assembly." *Nature Nanotechnology* 10 (11): 919–923. https://doi.org/10.1038/nnano.2015.250.
13) Feller, G. 2017. "Cryosphere and Psychrophiles: Insights into a Cold Origin of Life?" *Life* 7 (2): 25. https://doi.org/10.3390/life7020025.
14) Fine, J. L., and A. M. Moses. 2025. "An RNA Condensate Model for the Origin of Life." *Journal of Molecular Biology* 437 (12): 169124. https://doi.org/10.1016/j.jmb.2025.169124.
15) Grommet, A. B., M. Feller, and R. Klajn. 2020. "Chemical Reactivity under Nanoconfinement." *Nature Nanotechnology* 15 (4): 256–271. https://doi.org/10.1038/s41565-020-0652-2.
16) Herschy, Barry, Angela Whicher, Emilia Camprubí, Christopher Watson, Luke Dartnell, John D. Ward and Nick Lane. 2014. "An Origin-of-Life Reactor to Simulate Alkaline Hydrothermal Vents." *Interface Focus* 4: 20130059.
17) Jia, T. Z., M. Caudan, and I. Mamajanov. 2021. "Origin of Species before Origin of Life: The Role of Speciation in Chemical Evolution." *Life* 11 (2): 154. https://doi.org/10.3390/life11020154.
18) Katke, C., E. Pedrueza-Villalmanzo, K. Spustova, R. Ryskulov, C. N. Kaplan, and I. Gözen. 2023. "Colony-Like Protocell Superstructures." *ACS Nano* 17 (4): 3368–3382. https://doi.org/10.1021/acsnano.2c08093.
19) Lahav, N. 1993. "The RNA-World and Co-Evolution Hypotheses and the Origin of Life: Implications, Research Strategies and Perspectives." *Origins of Life and Evolution of the Biosphere* 23 (5–6): 329–344. https://doi.org/10.1007/BF01582084.

20) Lancet, D., R. Zidovetzki, and O. Markovitch. 2018. “Systems Protobiology: Origin of Life in Lipid Catalytic Networks.” *Journal of the Royal Society Interface* 15 (144): 20180159. https://doi.org/10.1098/rsif.2018.0159.
21) Lancet, D., D. Segrè, and A. Kahana. 2019. “Twenty Years of ‘Lipid World’: A Fertile Partnership with David Deamer.” *Life* 9 (4): 77. https://doi.org/10.3390/life9040077.
22) Lecoeuvre, Aurélien, Bénédicte Ménez, Mathilde Cannat, Valérie Chavagnac and Emmanuelle Gérard. 2021. “Microbial Ecology of the Newly Discovered Serpentinite-Hosted Old City Hydrothermal Field (Southwest Indian Ridge).” *The ISME Journal* 15: 818–32.
23) Matreux, T., P. Aikkila, B. Scheu, D. Braun, and C. B. Mast. 2024. “Heat Flows Enrich Prebiotic Building Blocks and Enhance Their Reactivity.” *Nature* 628: 110–116.
24) Maury, C. P. J. 2025. “Origin of Life: Beta-Sheet Amyloid Conformers as the Primordial Functional Polymers on the Early Earth and Their Role in the Emergence of Complex Dynamic Networks.” *FEBS Letters* 599 (19): 2693–2705. https://doi.org/10.1002/1873-3468.70112.
25) Müller, F., L. Escobar, F. Xu, E. Węgrzyn, M. Nainytė, T. Amatov, C. Y. Chan, A. Pichler, and T. Carell. 2022. “A Prebiotically Plausible Scenario of an RNA-Peptide World.” *Nature* 605 (7909): 279–284. https://doi.org/10.1038/s41586-022-04676-3.
26) Omran, A. 2023. “Plausibility of the Formose Reaction in Alkaline Hydrothermal Vent Environments.” *Origins of Life and Evolution of Biospheres* 53 (1–2): 113–125. https://doi.org/10.1007/s11084-020-09599-5.
27) Paleos, C. M. 2019. “Organization and Compartmentalization by Lipid Membranes Promote Reactions Related to the Origin of Cellular Life.” *Astrobiology* 19 (4): 547–552. https://doi.org/10.1089/ast.2018.1832.
28) Peng, X., M. Du, A. Gebruk, S. Liu, Z. Gao, R. N. Glud, P. Zhou, R. Wang, A. A. Rowden, G. M. Kamenev, A. S. Maiorova, D. Papineau, S. Chen, J. Gao, H. Liu, Y. He, I. L. Alalykina, I. Y. Dolmatov, H. Zhang, X. Li, M. V. Malyutina, S. Dasgupta, A. A. Saulenko, V. A. Shilov, and A. V. Adrianov. 2025. “Flourishing Chemosynthetic Life at the Greatest Depths of Hadal Trenches.” *Nature* 645: 679–685.
29) Postec, A., M. Quéméneur, M. Bes, N. Mei, F. Benaïssa, and C. Payri. 2015. “Microbial Diversity in a Submarine Carbonate Edifice from the Serpentinizing Hydrothermal System of the Prony Bay (New Caledonia) over a 6-Year Period.” *Frontiers in Microbiology* 6: 857. https://doi.org/10.3389/fmicb.2015.00857.
30) Prosdocimi, F., and S. T. de Farias. 2023. “Origin of Life: Drawing the Big Picture.” *Progress in Biophysics and Molecular Biology* 180–181: 28–36. https://doi.org/10.1016/j.pbiomolbio.2023.04.005.
31) Russell, M. J., A. Ponce, and others. 2020. “Six ‘Must-Have’ Minerals for Life’s Emergence: Olivine, Pyrrhotite, Bridgmanite, Serpentine, Fougerite and Mackinawite.” *Life* 10 (11): 291. https://doi.org/10.3390/life10110291.
32) Sharov, A. A. 2016. “Coenzyme World Model of the Origin of Life.” *Biosystems* 144: 8–17. https://doi.org/10.1016/j.biosystems.2016.03.003.
33) Sousa, F. L., T. Thiergart, G. Landan, S. Nelson-Sathi, I. A. C. Pereira, J. F. Allen, N. Lane, and W. F. Martin. 2013. “Early Bioenergetic Evolution.” *Philosophical Transactions of the Royal Society B: Biological Sciences* 368 (1622): 20130088. https://doi.org/10.1098/rstb.2013.0088.
34) Söker, Nicola Andreas, Sven Auschra, Viktor Holubec, Klaus Kroy, and Frank Cichos. 2021. “How Activity Landscapes Polarize Microswimmers without Alignment Forces.” *Physical Review Letters* 126: 228001. https://doi.org/10.1103/PhysRevLett.126.228001.
35) Thomas, E., R. E. Anderson, V. Li, L. J. Rogan, and J. A. Huber. 2021. “Diverse Viruses in Deep-Sea Hydrothermal Vent Fluids Have Restricted Dispersal across Ocean Basins.” *mSystems* 6 (3): e00068-21. https://doi.org/10.1128/mSystems.00068-21.
36) Vosseberg, J., J. J. E. van Hooff, S. Köstlbacher, K. Panagiotou, D. Tamarit, and T. J. G. Ettema. 2024. “The Emerging View on the Origin and Early Evolution of Eukaryotic Cells.” *Nature* 633 (8029): 295–305. https://doi.org/10.1038/s41586-024-07677-6.

Preprints.org

Article

Not peer-reviewed version

Persistence and Computational Observability in the Halting Problem

Arturo Tozzi *

Posted Date: 4 September 2026

doi: 10.20944/preprints202609.0362.v1

Keywords: undecidability; termination; censoring; verification; algorithms

Preprints.org is a free multidisciplinary platform providing preprint service that is dedicated to making early versions of research outputs permanently available and citable. Preprints posted at Preprints.org appear in Web of Science, Crossref, Google Scholar, Scilit, Europe PMC, OpenAlex.

Copyright: This open access article is published under a Creative Commons CC BY 4.0 license, which permit the free download, distribution, and reuse, provided that the author and preprint are cited in any reuse.

Preprints.org (www.preprints.org) | NOT PEER-REVIEWED | Posted: 4 September 2026 doi:10.20944/preprints202609.0362.v1

Disclaimer/Publisher's Note: The statements, opinions, and data contained in all publications are solely those of the individual author(s) and contributor(s) and not of MDPI and/or the editor(s). MDPI and/or the editor(s) disclaim responsibility for any injury to people or property resulting from any ideas, methods, instructions, or products referred to in the content.

Article

Persistence and Computational Observability in the Halting Problem

Arturo Tozzi

ASL Napoli 1 Centro, Distretto 27, Naples, Italy; tozziarturo@libero.it

Abstract

Finite observation leaves an ambiguity in the Halting Problem: a computation still running at a given time may terminate later or continue indefinitely. We address this ambiguity through a persistence-based description of computational observability, asking how the distinction between termination and continued execution changes as the observation horizon increases. Execution histories are represented as persistence intervals and examined at successive checkpoints. Trajectories with identical observed intervals are grouped into observational equivalence classes, while an ambiguity fraction and its complementary observability index quantify how many finite endpoints rare unresolved or become distinguishable. We tested this approach on 240 synthetic trajectories, including 160 terminating computations spanning a broad range of halting times and 80 trajectories specified to continue throughout a one-million-step horizon. Increasing observation progressively revealed finite endpoints: observability rose from 1.25% at 100 steps to 91.88% at 300,000 steps. Nevertheless, late-halting trajectories rwere indistinguishable from continuing trajectories, whenever their endpoints lay beyond the observation boundary. We argue that persistence provides a quantitative description of finite computational observability while preserving the undecidability of the Halting Problem: persistence up to a boundary points towards continued, not infinite execution. Potential applications include termination-predictor benchmarking, software testing, execution monitoring, resource-limited verification and evaluation of algorithms from censored computational histories.

Keywords: undecidability; termination; censoring; verification; algorithms

Introduction

The Halting Problem exposes an asymmetry between observable termination and unresolved continuation. A halting state, once reached, provides a finite and definitive endpoint, whereas an execution that is still active at a given observation time reveals only that termination has not yet occurred. This suggests representing computation not only through its eventual logical status, but through the lifetime of an execution as it becomes observable over progressively extended computational histories. This viewpoint connects the problem with persistent topology, where structures are followed across ordered filtrations according to their appearance, persistence and disappearance. Persistence modules encode this evolution algebraically and interval decompositions and barcodes provide compact representations of persistence ranges (Skraba and Vejdemo-Johansson 2013). Related developments include complexes of persistence modules (Dey, Russold and Samaga 2024) and directed persistent homology (Mendez and Sanchez-Garcia 2023), while some associated computational problems, including interleaving-distance calculations in multiparameter settings, can themselves be computationally difficult (Bjerkevik, Botnan and Kerber 2020). However, for computational trajectories, a crucial distinction still holds: persistence observed up to a finite boundary establishes survival only within the available history. This means that a trajectory terminating after that boundary and one continuing without an observed endpoint can possess identical finite persistence representations. Therefore, a new formulation is required to describe not

© 2026 by the author(s). Distributed under a Creative Commons CC BY license.

Preprints.org (www.preprints.org) | NOT PEER-REVIEWED | Posted: 4 September 2026 doi:10.20944/preprints202609.0362.v1

merely how long computation persists, but what its finite persistence actually makes observable and distinguishable.

We introduce a persistence-based approach to determine what information about termination is distinguishable from a finite execution history and how that information changes as observation is extended. Our aim is not to use persistence to decide the Halting Problem, but to quantify the boundary between termination that has already become observable and computation whose eventual status remains unresolved. We proceed by representing each computation as an ordered sequence of machine configurations and its continued execution as a persistence interval. Termination generates a finite observable endpoint, whereas non-termination corresponds formally to an interval without a finite endpoint. We then examine these intervals at progressively increasing observation checkpoints. At each checkpoint, two trajectories are considered observationally equivalent when the portions of their persistence intervals observed so far are identical. This relation partitions the trajectories into observational equivalence classes, whose checkpoint-dependent quotient set describes the available state of computational observability. As observation increases, a trajectory leaves the unresolved class when its finite endpoint becomes visible; by contrast, a late-halting trajectory remains indistinguishable from a trajectory continuing beyond the observation boundary until that endpoint is reached. We quantify this process using an ambiguity fraction, measuring the proportion of terminating trajectories whose endpoints are beyond the checkpoint and its complementary observability index. We test these quantities in 240 synthetic trajectories: 160 terminating computations spanning a broad distribution of halting times, including deliberately late-halting controls and 80 trajectories specified to continue throughout a one-million-step horizon. We expect progressively longer observation to reveal additional finite endpoints and refine the equivalence classes, while the late-halting controls test the critical case in which finite but still-unobserved termination is observationally identical to continued execution.

We will proceed as follows. First, we formalize computational observability, persistence intervals, finite observational equivalence and the associated quantitative indices; then, we examine their behavior in controlled simulations across increasing observation checkpoints; finally, we assess the resulting refinement of observational equivalence classes and the boundary imposed by late halting.

METHODS

We studied how finite observation determines what can and cannot be distinguished between terminating and continuing computational trajectories when execution histories are represented by persistence intervals. To examine this question, we constructed synthetic abstract-machine trajectories and followed their persistence across progressively increasing observation checkpoints. At each checkpoint, intervals extending beyond the available execution history were treated as right-censored and grouped according to observational equivalence. We then quantified how this unresolved population changed with observation using an ambiguity fraction and its complementary observability index, while deliberately late-halting trajectories provided a stress test of the distinction between delayed termination and continued execution. The experiment comprised 240 trajectories: 160 terminating computations spanning a broad range of halting times and 80 trajectories specified to continue throughout a maximum horizon of one million machine steps. By operating directly on computational survival intervals, we tracked when finite termination endpoints became observable and how their appearance progressively changed the distinguishability of the simulated trajectories.

Computational trajectories. Each simulated computation was represented as an ordered sequence of complete abstract computational states. For program P_i with input x_i, we denoted its execution trajectory by

$$\Gamma_i = (s_{i,0}, s_{i,1}, s_{i,2}, \ldots),$$

© 2026 by the author(s). Distributed under a Creative Commons CC BY license.

Preprints.org (www.preprints.org) | NOT PEER-REVIEWED | Posted: 4 September 2026 doi:10.20944/preprints202609.0362.v1

where $s_{i,n}$ is the complete machine state after n executed steps. Machine steps, rather than physical time, constituted the independent execution coordinate throughout the analysis. Let $\mathcal{H}$ denote the set of halting configurations. The termination time of trajectory $i$was defined as

$$T_i = \inf\{n \in \mathbb{N}: s_{i,n} \in \mathcal{H}\}.$$

A terminating trajectory therefore satisfies

$$T_i < \infty,$$

whereas mathematical non-termination would correspond to

$$T_i = \infty.$$

The latter condition was not inferred from finite simulation. Instead, the simulated population contained $N_N = 80$ trajectories specified by construction to continue throughout the finite experimental horizon. They were consequently treated as operationally continuing trajectories rather than as computations for which non-termination had been proved. The complete dataset contained

$$N = N_H + N_N = 160 + 80 = 240$$

trajectories. The maximum observation horizon was

$$T_{\max} = 10^6$$

machine steps. For the 160 terminating trajectories, execution lengths were generated from a broad lognormal distribution,

$$\ln T_i \sim \mathcal{N}(\ln 8000, 2^2),$$

and converted to integer machine steps within the simulated interval. To ensure representation of termination close to the observation horizon, twelve late-halting controls were explicitly assigned termination times of

$$120000, 160000, 210000, 270000, 340000, 420000,$$
$$510000, 610000, 720000, 830000, 920000, 985000$$

machine steps. These controls prevented an artificial separation in which all finite computations terminated substantially earlier than the maximum observation boundary.

Persistence intervals. Computational survival was represented by an interval whose coordinate was the number of executed machine steps. The initial state was assigned birth coordinate zero. A terminating trajectory was therefore represented by

$$I_i = [0, T_i),$$

while mathematical non-termination has the formal interval representation

$$I_\infty = [0, \infty).$$

These intervals encoded execution survival and were not obtained from homology calculations. At any finite checkpoint c, only the portion of an interval contained in the observed execution history was available. Therefore, we defined the observed interval as

$$I_i^{(c)} = I_i \cap [0, c].$$

For a terminating computation, the measurable persistence length was

$$L_i(c) = \min(T_i, c),$$

whereas a trajectory specified to continue beyond c had

$$L_i(c) = c.$$

Accordingly, whenever a terminating trajectory satisfied

$$T_i > c,$$

its observed persistence was

$$L_i(c) = c,$$

which was numerically identical to that of a trajectory continuing beyond the checkpoint. These observations were treated as right-censored: the available data established only that the endpoint had not occurred by c. We also calculated normalized persistence,

$$\rho_i(c) = \frac{L_i(c)}{c}.$$

An interval reaching the observation boundary satisfied

$$\rho_i(c) = 1,$$

whereas an already terminated trajectory satisfied

© 2026 by the author(s). Distributed under a Creative Commons CC BY license.

Preprints.org (www.preprints.org) | NOT PEER-REVIEWED | Posted: 4 September 2026 doi:10.20944/preprints202609.0362.v1

$$\rho_i(c) = \frac{T_i}{c} < 1.$$

The analysis used nine checkpoints,

$$c \in \{100, 300, 1000, 3000, 10000, 30000, 100000, 300000, 1000000\}.$$

Every trajectory was evaluated at every checkpoint. The exact relations above were used for classification; no numerical tolerance was introduced when deciding whether a finite endpoint had been observed.

Observational equivalence. Finite computational observability was formalized through an equivalence relation on persistence intervals. At checkpoint c, two intervals I_i and I_j were defined as observationally equivalent when their restrictions to the observed execution domain were identical:

$$I_i \sim_c I_j \iff I_i \cap [0, c] = I_j \cap [0, c].$$

The relation $\sim_c$ is reflexive because

$$I_i \sim_c I_i,$$

symmetric because

$$I_i \sim_c I_j \Rightarrow I_j \sim_c I_i,$$

and transitive because

$$I_i \sim_c I_j,\ I_j \sim_c I_k \Rightarrow I_i \sim_c I_k.$$

It therefore partitions the collection $\mathcal{I}$ of persistence intervals into observational equivalence classes. We denoted the resulting **quotient set**

$$\mathcal{Q}_c = \mathcal{I}/\sim_c.$$

No topology was imposed on $\mathcal{Q}_c$ and it was consequently not treated as a quotient topological space. The relevant ambiguity follows directly from interval restriction. Consider a finite interval

$$I_T = [0, T)$$

and the formally unbounded interval

$$I_\infty = [0, \infty).$$

For every checkpoint satisfying

$$c < T,$$

one obtains

$$I_T \cap [0, c] = [0, c]$$

and

$$I_\infty \cap [0, c] = [0, c].$$

Therefore,

$$I_T \sim_c I_\infty.$$

Once $c \geq T$, the finite endpoint becomes observable and the equality no longer holds. The analysis consequently followed how membership in the unresolved equivalence class changed as $c$increased.

Observability measures. We quantified unresolved finite termination using the number of genuinely terminating trajectories whose endpoints occurred after a checkpoint. With $1(\cdot)$ denoting the indicator function,

$$U_H(c) = \sum_{i=1}^{N_H} 1\,(T_i > c).$$

The ambiguity fraction was then defined as

$$A(c) = \frac{U_H(c)}{N_H} = \frac{1}{N_H} \sum_{i=1}^{N_H} 1\,(T_i > c).$$

Thus, $A(c)$ measures the fraction of the terminating population that is observationally unresolved at checkpoint c. Its complementary quantity, termed the observability index, was

$$O(c) = 1 - A(c).$$

Equivalently,

$$O(c) = \frac{1}{N_H} \sum_{i=1}^{N_H} 1\,(T_i \leq c).$$

© 2026 by the author(s). Distributed under a Creative Commons CC BY license.

Preprints.org (www.preprints.org) | NOT PEER-REVIEWED | Posted: 4 September 2026 doi:10.20944/preprints202609.0362.v1

The two quantities satisfy identically

$$A(c) + O(c) = 1.$$

They were not interpreted as independent measurements. Their monotonic behavior also follows directly from their definitions. If

$$c_1 < c_2,$$

then

$$\{i: T_i > c_2\} \subseteq \{i: T_i > c_1\},$$

and hence

$$A(c_2) \leq A(c_1),$$

while

$$O(c_2) \geq O(c_1).$$

Accordingly, no statistical significance test was applied to determine whether ambiguity decreased with increasing observation, because that decrease is structurally imposed by the nested checkpoints. At the final checkpoint,

$$c = T_{\max} = 10^6,$$

all simulated terminating trajectories satisfy

$$T_i < c,$$

including the latest explicit control at 985,000 steps. Under the exact endpoint rule this entails

$$A(10^6) = 0$$

and

$$O(10^6) = 1.$$

This exact formulation replaces any classification based on a floating-point tolerance.

Finite-prefix analysis. A finite-prefix classification was calculated to describe the consequences of making a decision from persistence duration alone. At checkpoint c, a trajectory was identified as terminating only when its finite endpoint was contained in the observed execution history:

$$\hat{Y}_i(c) = H \text{ if } T_i \leq c.$$

When the interval reached the checkpoint without an observed endpoint, its finite-prefix status was written

$$\hat{Y}_i(c) = C \text{ if } L_i(c) = c,$$

where C denotes continuing at the checkpoint rather than certified non-halting. This terminology avoids assigning an infinite future to a finite observation. Among the terminating trajectories, the number provisionally occupying this continuing class was

$$F_C(c) = \sum_{i=1}^{N_H} 1\,(T_i > c),$$

and therefore

$$F_C(c) = U_H(c), \quad \frac{F_C(c)}{N_H} = A(c).$$

The late-halting stress test examined this equivalence explicitly. At the selected checkpoint

$$c^* = 100000,$$

observed persistence was

$$L_i(c^*) = \min\,(T_i, 100000).$$

Every terminating trajectory satisfying

$$T_i > 100000$$

therefore yielded

$$L_i(c^*) = 100000.$$

The same value was assigned to every operationally continuing trajectory because no endpoint was present within the observed prefix. True termination time was plotted against $L_i(c^*)$ to display this censoring boundary. No probability of eventual termination was estimated for trajectories reaching the checkpoint and no fitted halting-time distribution was extrapolated to determine the status of an individual unresolved computation.

© 2026 by the author(s). Distributed under a Creative Commons CC BY license.

Preprints.org (www.preprints.org) | NOT PEER-REVIEWED | Posted: 4 September 2026 doi:10.20944/preprints202609.0362.v1

Numerical procedure. The computational procedure was performed in a fixed sequence. First, 160 terminating execution lengths were generated from the specified lognormal distribution and constrained to the finite simulation range. Twelve predetermined late-halting values were then inserted to ensure sampling near the upper boundary. Second, 80 additional trajectories were assigned continued execution throughout the one-million-step horizon. Third, the resulting 240 trajectories were evaluated independently at each of the nine checkpoints. For every trajectory-checkpoint pair, the observed persistence length $L_i(c)$, normalized persistence $\rho_i(c)$, presence or absence of an observed endpoint and finite-prefix status were calculated. Fourth, terminating trajectories satisfying $T_i > c$ were counted to obtain $U_H(c)$, from which $A(c)$ and $O(c)$ were calculated exactly. Fifth, the equivalence criterion was evaluated through interval restriction, with finite trajectories extending beyond $c$assigned to the same observed interval class as continuing trajectories. Sixth, the 100,000-step cross-section was extracted for the late-halting stress test. Finally, trajectory-level and checkpoint-level quantities were aggregated for graphical representation.

Software tools. All trajectory generation, numerical transformations, finite-interval restrictions, right-censoring calculations, checkpoint evaluations, descriptive summaries and graphical outputs were performed in Python. NumPy was used for array operations, logarithmic transformations and pseudorandom sampling. Reproducibility of the synthetic dataset was controlled using numpy.random.default_rng with seed

260817.

pandas was used to construct trajectory-level and checkpoint-level datasets, aggregate endpoint counts, calculate $A(c)$and $O(c)$ and export numerical records. Matplotlib was used to visualize execution-length distributions, representative persistence intervals, checkpoint-dependent quantities, the late-halting censoring analysis and the representative timing relationship. Consequently, mathematical operations were restricted to the explicitly defined survival intervals, their finite restrictions, endpoint observations, equivalence relations and derived descriptive quantities. The exact comparison $T_i \leq c$, rather than an approximate floating-point threshold on normalized persistence, was used to determine whether termination was observable at each checkpoint.

RESULTS

We examined how progressively extending the execution horizon changed the finite observability of termination and the composition of the unresolved persistence class. Terminating and continuing trajectories were evaluated across successive checkpoints spanning the full simulated observation range. Because the principal checkpoint-dependent quantities follow directly from interval restriction and right censoring, we report their behavior descriptively rather than applying inferential tests to mathematically imposed monotonic trends.

Execution lengths. Terminating trajectories spanned a broad range of execution lengths, including deliberately introduced late-halting cases approaching the maximum observation horizon (Figure 1A). This heterogeneous distribution generated substantial overlap between trajectories that would eventually terminate and those specified to continue throughout the simulation. At early observation checkpoints, most terminating trajectories had not yet exposed their endpoints and consequently displayed persistence intervals extending to the observation boundary, just as the continuing trajectories did (Figure 1B). As the execution horizon increased, progressively more finite endpoints became visible and the proportion of correctly identified terminating trajectories increased accordingly (Figure 1C). By the final observation horizon, every simulated finite endpoint was contained within the observed execution history. In contrast, trajectories specified to continue throughout the experiment reached each checkpoint without displaying an endpoint; this behavior was imposed by their construction and should not be interpreted as finite evidence of mathematical non-termination. The representative computational-cost relationship shown in Figure 1D was generated independently from the prescribed synthetic scaling relation and did not contribute to persistence classification. Overall, the simulations showed that the decisive change in finite

© 2026 by the author(s). Distributed under a Creative Commons CC BY license.

Preprints.org (www.preprints.org) | NOT PEER-REVIEWED | Posted: 4 September 2026 doi:10.20944/preprints202609.0362.v1

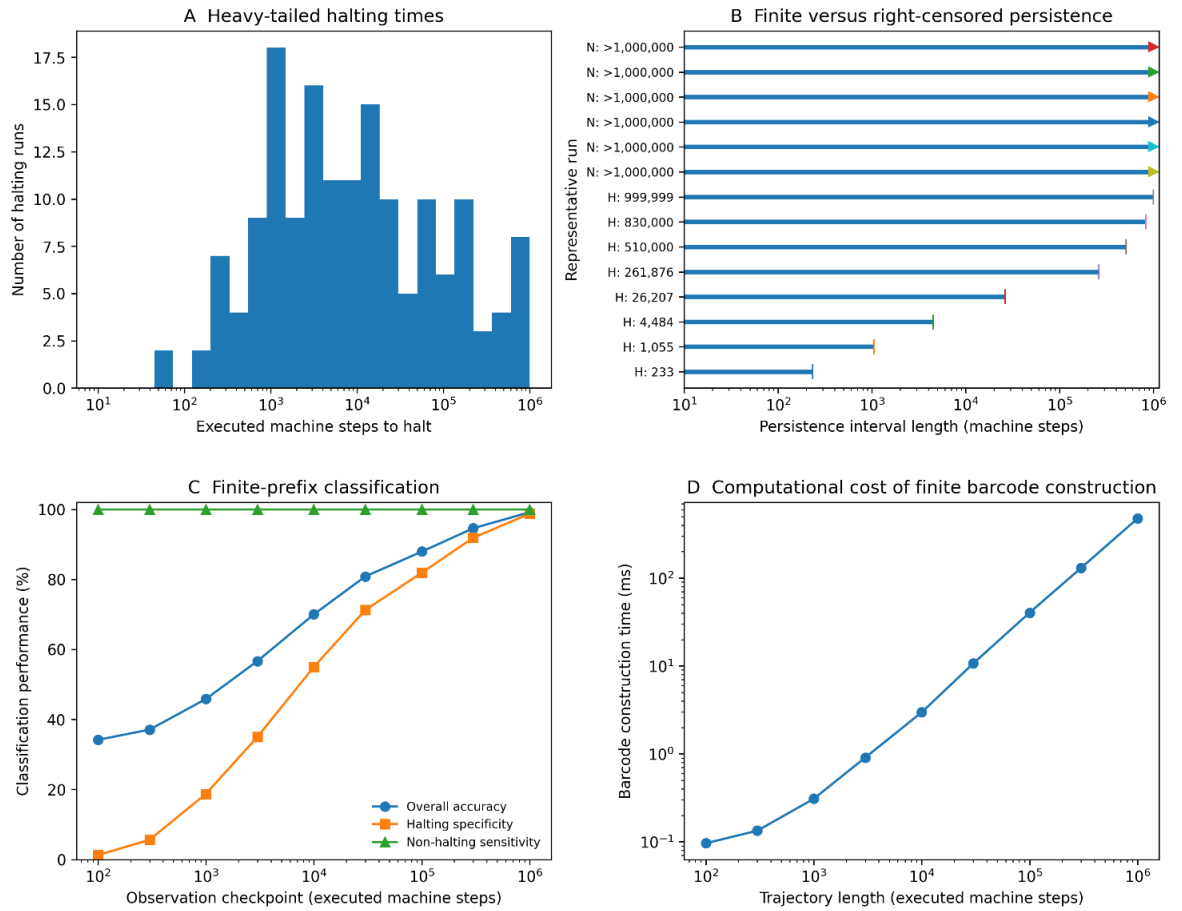
observational status occurred when an endpoint entered the available execution history, rather than through persistence duration alone.

Equivalence refinement. Increasing the observation horizon progressively reduced the population of terminating trajectories belonging to the unresolved observational equivalence class (Figure 2A). Accordingly, the ambiguity fraction decreased across successive checkpoints while its complementary observability index increased, reaching complete observability of the simulated terminating population only when the full finite range had been covered. This refinement did not, however, provide a criterion for recognizing non-termination. Deliberately late-halting trajectories were in the unresolved class until their endpoints became observable, reproducing the finite observational behavior of trajectories specified to continue beyond the same checkpoint (Figure 2B). The stress test at an intermediate horizon made this ambiguity particularly evident: both late-halting and continuing trajectories reached the same censoring boundary and therefore had identical observed persistence despite their different simulated statuses (Figure 2C). More generally, whenever $c < T_i$,

$$[0, T_i) \cap [0, c] = [0, \infty) \cap [0, c] = [0, c].$$

Thus, a classifier receiving only the restricted persistence interval has no information with which to distinguish delayed finite termination from continued execution before the endpoint appears. The observed refinement therefore resulted from the progressive disclosure of finite endpoints, while absence of an endpoint preserved observational equivalence rather than establishing non-termination.

Overall, we characterized computational observability as a checkpoint-dependent refinement of persistence-equivalence classes. Increasing the execution horizon progressively exposed finite endpoints and reduced the unresolved fraction, but persistence reaching an observation boundary identified right censoring rather than non-termination. Late-halting trajectories provided critical control: before their endpoints became accessible, their restricted persistence intervals were mathematically identical to those of trajectories continuing beyond the observation horizon.



© 2026 by the author(s). Distributed under a Creative Commons CC BY license.

Preprints.org (www.preprints.org) | NOT PEER-REVIEWED | Posted: 4 September 2026 doi:10.20944/preprints202609.0362.v1

Figure 1. Persistence-based characterization of computational observability across finite execution horizons. A, Distribution of execution lengths for the 160 simulated terminating trajectories, expressed as the number of machine steps preceding termination. The logarithmic scale displays the broad range of finite halting times and the deliberately included late-halting trajectories extending toward the maximum observation horizon of 1,000,000 machine steps. B, Representative persistence intervals for computational trajectories. Terminating trajectories are represented by intervals ending at their observed halting steps, whereas the 80 trajectories specified to continue throughout the simulation extend to the observation boundary. Intervals reaching this boundary are treated as right-censored observations rather than experimentally established infinite intervals. C, Finite-prefix classification across progressively increasing observation checkpoints. Recognition of terminating trajectories increases when their finite endpoints enter the observed execution history, whereas trajectories still active at a checkpoint cannot be distinguished based on persistence duration alone from trajectories specified to continue throughout the observation horizon. The non-terminating class is defined by construction and does not constitute a finite empirical demonstration of infinite execution. D, Synthetic computational cost associated with increasing trajectory length, expressed in machine steps and milliseconds. Values were generated from the prescribed scaling relation with stochastic variation and are representative rather than measured execution times or wall-clock performance of a persistent-homology implementation.

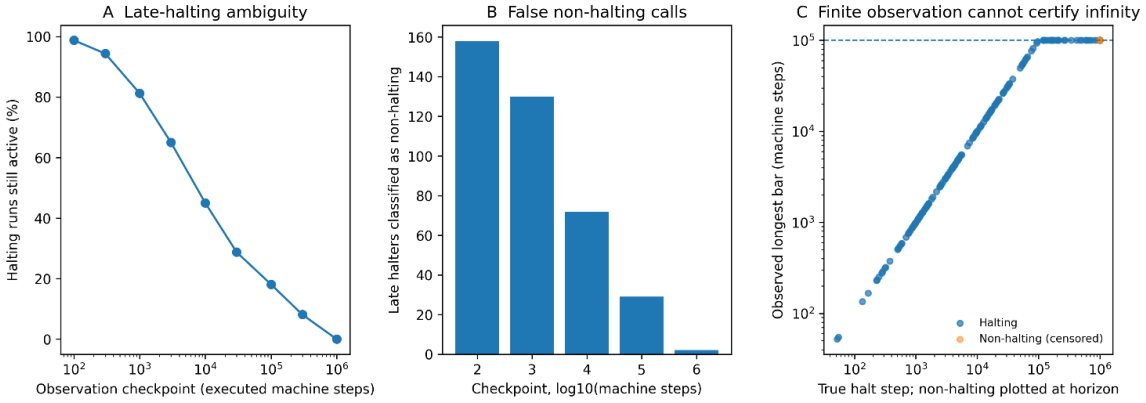


Figure 2. Refinement of computational observability and persistence equivalence under increasing finite observation. A, Fraction of terminating trajectories whose halting endpoints have not yet become observable at successive execution checkpoints. These trajectories are the unresolved finite component of the observational equivalence class because their persistence intervals extend to the current observation boundary. The plotted percentage corresponds to the ambiguity fraction at each checkpoint, while its complement represents the fraction of terminating trajectories whose finite endpoints have become observable. B, Number of late-halting trajectories that are still observationally indistinguishable from trajectories specified to continue throughout the simulation. A trajectory leaves this unresolved class only when the observation checkpoint reaches its actual halting step; increasing the observation horizon therefore progressively refines the finite observational equivalence classes without assigning an infinite endpoint to trajectories that are still active. C, Relationship between true halting step and longest persistence observable at the 100,000-machine-step checkpoint. Terminating trajectories whose endpoints occur at or before the checkpoint display their corresponding finite persistence lengths, whereas trajectories terminating after 100,000 steps reach the same right-censoring ceiling as trajectories specified to continue throughout the observation horizon. Therefore, the boundary at 100,000 machine steps identifies a finite observational equivalence class containing both delayed finite trajectories and trajectories operationally assigned to the non-terminating group, with membership determined solely by information available up to the selected checkpoint.

Conclusions

We asked whether persistence could characterize the distinction between termination and continued execution within a finite observation window. Our simulations compared 160 terminating trajectories, spanning a broad range of execution lengths and including deliberately late-halting

© 2026 by the author(s). Distributed under a Creative Commons CC BY license.

Preprints.org (www.preprints.org) | NOT PEER-REVIEWED | Posted: 4 September 2026 doi:10.20944/preprints202609.0362.v1

cases, with 80 trajectories specified to continue throughout a one-million-step observation horizon. We examined their persistence at progressively increasing checkpoints and represented trajectories lacking an observed endpoint as right-censored. We found that finite endpoints progressively separated terminating trajectories from the unresolved population, whereas sufficiently late-halting trajectories shared the same observed persistence as trajectories continuing beyond the checkpoint. The ambiguity fraction decreased as additional endpoints became accessible, with the complementary observability index increasing accordingly. However, at any checkpoint preceding a finite endpoint, restriction of the corresponding interval to the observed domain was identical to that of an unbounded interval. These results support an interpretation of computational observability as a progressive refinement of finite equivalence classes rather than as an inference from persistence duration to eventual termination status. More generally, our findings provide a quantitative description of how computational uncertainty changes as finite observation is extended.

Compared with approaches attempting to predict termination from execution time, probabilistic models of halting-time distributions, runtime heuristics, static program analysis, model checking or theorem-based termination proofs, we address a different mathematical object: the information content of the observed execution prefix itself. Persistent representations preserve the location of observed endpoints and make right censoring explicit, instead of assigning a probability to an unseen future event. The observational-equivalence relation allows trajectories to be grouped according to exactly what is discriminable at a specified checkpoint, while the associated quotient describes how this partition changes with observation. Different from conventional barcode analysis, in which persistence length is usually interpreted as the lifetime of a feature, we explicitly separate observed lifetime from the unknown location of its endpoint. Therefore, our approach formalizes finite computational observability through restricted persistence intervals, observational equivalence classes and their progressive refinement across increasing observation checkpoints.

Our study has limitations. The 240 trajectories were synthetic and the 80 trajectories assigned to the non-terminating group were specified to continue throughout the simulated horizon rather than mathematically proved to execute indefinitely. The lognormal distribution of halting times, the twelve late-halting controls, the selected checkpoints and the one-million-step boundary are experimental choices that influence the numerical proportions and limit generalization of their absolute values. Persistence intervals were constructed directly from computational survival; no simplicial complexes, boundary-matrix reductions, persistent-homology groups or semimodule decompositions were calculated. Consequently, the term persistence describes just the interval structure analyzed here and should not be interpreted as evidence that nontrivial homological information was extracted from machine-state spaces. The ambiguity fraction and observability index are complementary quantities rather than independent measurements and their monotonic evolution follows from expansion of the observation window. These scope boundaries leave open whether richer state-transition representations produce additional observational classes, whether equivalent constructions extend beyond single execution trajectories and which properties of computational histories can be extracted without importing information equivalent to a termination decision.

Our approach suggests experimentally testable hypotheses. First, for any ensemble with empirical halting-time cumulative distribution $F_T(c)$, the observability index should satisfy $O(c) = F_T(c)$ and the ambiguity fraction should satisfy $A(c) = 1 - F_T(c)$; measured departures would indicate that the chosen persistence representation contains information beyond endpoint occurrence or that censoring has been implemented differently.

Second, if halting times exhibit a power-law survival tail, $P(T > c) \sim c^{-\alpha}$, unresolved terminating trajectories should scale as $A(c) \sim c^{-\alpha}$; under an exponential survival law, the corresponding prediction is $A(c) \sim \exp(-\lambda c)$. These alternatives generate quantitatively distinct checkpoint profiles while preserving finite-prefix ambiguity at the individual-trajectory level.

Third, any classifier based exclusively on the restricted interval $I \cap [0, c]$ should assign identical outputs to a late-halting interval $[0, T)$ with $T > c$ and an unbounded interval $[0, \infty)$, because their

© 2026 by the author(s). Distributed under a Creative Commons CC BY license.

Preprints.org (www.preprints.org) | NOT PEER-REVIEWED | Posted: 4 September 2026 doi:10.20944/preprints202609.0362.v1

inputs are mathematically identical. A classifier showing reproducible discrimination between these matched pairs must therefore be using information additional to restricted interval duration.

Fourth, extending the observation boundary from $c_1$to c_2 should resolve exactly the fraction $F_T(c_2) - F_T(c_1)$ of terminating trajectories, providing a direct quantitative prediction for independently generated trajectory ensembles.

Future research could test these relations on executable abstract machines with known analytical behavior, Busy-Beaver-inspired finite controls, provably looping programs and programs whose termination can be established independently by formal methods. State-transition graphs could subsequently replace interval-only representations, allowing directed persistent homology or other structural descriptors to be calculated and compared with our finite-observation baseline.

At a practical level, explicit treatment of computational censoring could support evaluation protocols for systems that must decide how to handle long-running processes. Benchmark collections could contain known terminating cases distributed across very different execution lengths together with independently certified looping cases, preventing a long runtime from functioning inadvertently as a class label. The same procedure could be used to audit termination predictors by reporting performance as a function of observation budget rather than only at a single cutoff. In automated software testing, unresolved execution could be recorded separately from demonstrated failure or demonstrated non-termination, preserving the distinction between a resource limit and a logical result. Formal-verification pipelines could likewise combine finite execution traces with independently obtained loop invariants or termination certificates while retaining the provenance of each conclusion. Also, our checkpoint-dependent quantities provide standardized descriptive summaries for comparing experiments performed under different computational budgets, provided that the underlying trajectory populations and censoring rules are explicitly reported.

In conclusion, our results show that persistence can describe how computational observability changes with increasing observation. Finite endpoints progressively resolve terminating trajectories, whereas computations extending beyond the observation boundary are indistinguishable, regardless of whether they terminate later or continue indefinitely. This distinction does not solve the Halting Problem, but shows quantitatively how the boundary between observable and unresolved computation shifts as execution unfolds.

Author Contributions: The Author performed: study concept and design, acquisition of data, analysis and interpretation of data, drafting of the manuscript, critical revision of the manuscript for important intellectual content, statistical analysis, obtained funding, administrative, technical and material support, study supervision.

Funding: This research did not receive any specific grant from funding agencies in the public, commercial or not-for-profit sectors.

Data Availability Statement: All data and materials generated or analyzed during this study are included in the manuscript. The Author had full access to all the data in the study and took responsibility for the integrity of the data and the accuracy of the data analysis.

Conflicts of Interest: The Author does not have any known or potential conflict of interest including any financial, personal or other relationships with other people or organizations within three years of beginning the submitted work that could inappropriately influence or be perceived to influence their work.

Ethics Approval and Consent to Participate: Ethics approval statement is not applicable. This research does not contain any studies with human participants or animals performed by the Author.

Consent for Publication: The Author transfers all copyright ownership, in the event the work is published. The undersigned author warrants that the article is original, does not infringe on any copyright or other proprietary right of any third part, is not under consideration by another journal and has not been previously published.

Declaration of Generative AI and AI-Assisted Technologies in the Writing Process: During the preparation of this work, the author used ChatGPT 5.3 to assist with data analysis and manuscript drafting and to improve

© 2026 by the author(s). Distributed under a Creative Commons CC BY license.

Preprints.org (www.preprints.org) | NOT PEER-REVIEWED | Posted: 4 September 2026 doi:10.20944/preprints202609.0362.v1

spelling, grammar and general editing. After using this tool, the author reviewed and edited the content as needed, taking full responsibility for the content of the publication.

References

Bjerkevik, Håvard Bakke, Magnus Bakke Botnan and Michael Kerber. 2020. "Computing the Interleaving Distance Is NP-Hard." *Foundations of Computational Mathematics* 20: 1237–1271.

Dey, Tamal K., Florian Russold and Shreyas N. Samaga. 2024. "Efficient Algorithms for Complexes of Persistence Modules with Applications." In *40th International Symposium on Computational Geometry (SoCG 2024)*, *Leibniz International Proceedings in Informatics* 293: 51:1–51:18.

Mendez, David and Ruben J. Sanchez-Garcia. 2023. "A Directed Persistent Homology Theory for Dissimilarity Functions." *Journal of Applied and Computational Topology* 7 (4): 771–813.

Skraba, Primoz and Mikael Vejdemo-Johansson. 2013. "Persistence Modules: Algebra and Algorithms." arXiv:1302.2015.

Disclaimer/Publisher's Note: The statements, opinions and data contained in all publications are solely those of the individual author(s) and contributor(s) and not of MDPI and/or the editor(s). MDPI and/or the editor(s) disclaim responsibility for any injury to people or property resulting from any ideas, methods, instructions or products referred to in the content.

© 2026 by the author(s). Distributed under a Creative Commons CC BY license.

Preprints.org

Article

Not peer-reviewed version

Geometric and Topological Chromatin Organization During Progressive Nuclear Confinement

Arturo Tozzi *

Posted Date: 24 August 2026

doi: 10.20944/preprints202608.1673.v1

Keywords: genome; biophysics; mechanobiology; polymer; epigenetics

Preprints.org is a free multidisciplinary platform providing preprint service that is dedicated to making early versions of research outputs permanently available and citable. Preprints posted at Preprints.org appear in Web of Science, Crossref, Google Scholar, Scilit, Europe PMC, OpenAlex.

Copyright: This open access article is published under a Creative Commons CC BY 4.0 license, which permit the free download, distribution, and reuse, provided that the author and preprint are cited in any reuse.

Preprints.org (www.preprints.org) | NOT PEER-REVIEWED | Posted: 24 August 2026 doi:10.20944/preprints202608.1673.v1

Disclaimer/Publisher's Note: The statements, opinions, and data contained in all publications are solely those of the individual author(s) and contributor(s) and not of MDPI and/or the editor(s). MDPI and/or the editor(s) disclaim responsibility for any injury to people or property resulting from any ideas, methods, instructions, or products referred to in the content.

Article

Geometric and Topological Chromatin Organization During Progressive Nuclear Confinement

Arturo Tozzi

ASL Napoli 1 Centro, Distretto 27, Via Comunale del Principe 13/a 80145, Naples, Italy, ; tozziarturo@libero.it

Abstract

Chromatin spatial organization is commonly described through compaction, contact frequencies, chromosome territories, loops and polymer dynamics, yet these measures do not address how nuclear confinement shapes accessible genome configurations. We introduce the concept of chromatin congestion to describe changes in the geometrically, topologically and mechanically admissible chromatin configurations within a confined nucleus, integrating directional geometric constraints, topological obstruction, stochastic exploration, mechanical deformation and long-range dependence into a common description. We performed stochastic simulations of 480 nuclei across six microchannel widths from 14 to 4 micrometers, keeping chromatin content constant and quantifying collision-free path length, locus displacement, topological encounters, curvature, bending work, perturbation propagation and DNA-damage burden. As confinement progressed, chromatin displacement initially increased, consistent with exploration of the configurations still available, but declined under stronger restriction. Topological encounters, curvature and mechanical work increased, while perturbations extended across progressively larger nuclear regions and were associated with greater damage burden. Our simulations suggest that progressive confinement can drive transition from locally buffered chromatin dynamics to increasingly collective genome behaviour, characterized by stronger spatial interdependence among genomic regions. Potential applications include microfluidic migration experiments, single-cell nuclear phenotyping and the integration of imaging, mechanical and genome-organization measurements.

Keywords: genome; biophysics; mechanobiology; polymer; epigenetics

Introduction

Current models of three-dimensional genome organization describe chromosome territories, radial positioning, compartments and topologically associating domains shaped by mechanisms including loop extrusion, compartmentalization and lamina-associated interactions (Zheng and Xie 2019; Crosetto and Bienko 2020). Specific molecular components modify this architecture: for instance, HP1 regulates clustering, chromosome folding and B-compartment formation (Zenk et al. 2021), while telomeric chromatin adopts distinct compact and open conformations (Soman et al. 2022), loop-extrusion programs influence nuclear morphology (Patta et al. 2024) and transcription-factor dosage can alter compartments, boundaries and loops (Grant et al. 2026). However, contact maps and compaction or density measures do not directly quantify the spatial configurations accessible within a finite nuclear volume, whereas computational reconstructions depend on incomplete observations and experimental resolution. Consequently, confinement, topology, mechanics and stochastic motion lack a common description of how they jointly restrict physically realizable chromatin configurations. Recent findings emphasize the importance of chromatin's physical state. DNA structures can dynamically assemble within confined environments (Agarwal et al. 2021), while distinct chromatin conformations influence higher-order packing (Soman et al. 2022). Nucleosome geometry and linker-DNA length can determine interaction networks and material properties of chromatin condensates (Zhou et al. 2025), while solid-like nucleoprotein condensates can stabilize selective long-range genomic contacts (Pulupa et al. 2025). Chromosomes can also behave as ionic gels with

© 2026 by the author(s). Distributed under a Creative Commons CC BY license.

Preprints.org (www.preprints.org) | NOT PEER-REVIEWED | Posted: 24 August 2026 doi:10.20944/preprints202608.1673.v1

expanded and collapsed states separated by a volume phase transition (Beel, Matteï, and Kornberg 2026). Together with the coupling of genome folding to nuclear morphology (Patta et al. 2024) and the sensitivity of chromatin architecture to transcription-factor dosage (Grant et al. 2026), these observations motivate examining how physical and regulatory conditions constrain the configurations available to the genome.

We introduce the concept of chromatin congestion to describe the progressive change of geometrically, topologically and mechanically admissible configurations under increasing nuclear confinement. We suggest combining complementary mathematical approaches, each capturing a distinct aspect of configurational restriction, including spatial competition, directional organization, topological cost, stochastic exploration and perturbation propagation. Incidence and Kakeya geometry could describe how finite-thickness chromosome segments compete for space while maintaining different orientations (Guth, Solomon and Wang 2019; Wang and Zahl 2025), whereas knot distortion could capture the deformation costs imposed by loops and entanglements (Pardon 2011). Propagation-of-randomness methods could test whether stochastic motion islocal or spreads between interacting regions (Deng, Nahmod and Yue 2022). Negative dependence could represent competition among incompatible configurations (Borcea, Brändén and Liggett 2009), while entropy-based sampling could measure the diversity of accessible arrangements (Oveis Gharan, Saberi and Singh 2011). Log-concavity could characterize their global organization (Anari, Oveis Gharan and Vinzant 2018) and spectral independence could quantify how strongly local rearrangements influence distant regions as configurational freedom decreases (Anari, Liu and Oveis Gharan 2020). Finally, o-minimal geometry could represent biologically realizable chromatin states as a structured subset of all conceivable configurations (Bakker, Brunebarbe and Tsimerman 2022). Our simulation implements these ideas at a coarse-grained level by progressively confining nuclei with approximately constant chromatin content and measuring collision-free path length, displacement, topological encounters, curvature, mechanical work, perturbation propagation and DNA-damage burden.

We will proceed as follows. First, we formulate chromatin congestion and its geometric, topological and probabilistic components. Then, we describe the computational model and progressive-confinement simulation. Next, we quantify configurational restrictions, mechanical cost and perturbation propagation across confinement levels. Finally, we present the simulated functional readouts and their relationships with the preceding structural variables.

Methods

We studied chromatin congestion as a progressive restriction of the spatial configurations available to chromatin during controlled nuclear confinement. We used a stochastic simulation in which nuclei were progressively confined through microchannels ranging from 14 to 4 μm, while chromatin content was kept constant and nuclear volume varied only modestly. Eighty independent stochastic realizations were generated at each of six confinement levels, yielding 480 simulated nuclei. We quantified chromatin mobility and configurational exploration, collision-free path length, long-range coupling, topological encounters, local curvature, minimum bending work, and topological and mechanical burden, together with DNA-damage burden. We aimed to determine whether increasing confinement produces experimentally distinguishable changes in these properties, revealing how chromatin could explore alternative configurations, accommodates spatial constraints locally and transmits perturbations across the nucleus.

Confinement model. Confinement was represented by the microchannel width w, expressed in micrometres, with

$$w \in \{14,12,10,8,6,4\}\ \mu\text{m}.$$

To convert channel narrowing into a continuous congestion variable, we used a sigmoidal control function centered near the transition between moderate and severe confinement,

$$q(w) = \frac{1}{1 + \exp\left(\frac{w - w_c}{s}\right)},$$

with

© 2026 by the author(s). Distributed under a Creative Commons CC BY license.

Preprints.org (www.preprints.org) | NOT PEER-REVIEWED | Posted: 24 August 2026 doi:10.20944/preprints202608.1673.v1

$$w_c = 6.8\ \mu\text{m}, \qquad s = 0.85\ \mu\text{m}.$$

Thus q approaches zero for weak confinement and one for severe confinement. This variable did not represent a measured biological quantity, rather it served as the latent control variable linking the imposed geometry to the simulated observables. The nuclear volume was maintained near a constant baseline to separate congestion from simple changes in chromatin abundance. For realization r at confinement width w, nuclear volume was sampled as

$$V_{w,r} \sim \mathcal{N}(505 - 18q(w), 14^2)\ \mu\text{m}^3.$$

Therefore, the mean volume decreased only modestly as confinement intensified. For each width, 80 independent realizations were sampled,

$$r = 1, \ldots, 80,$$

giving

$$N_{\text{total}} = 6 \times 80 = 480$$

simulated nuclei. A fixed random seed was used to ensure reproducibility across the complete numerical experiment. All subsequent variables were conditionally generated from the same confinement state $q(w)$ so that geometric, topological, stochastic, mechanical and functional observables were coordinated by a common imposed physical restriction rather than generated as unrelated outputs.

Geometric freedom. Local configurational freedom was represented through a collision-free chromatin path length, defined as the distance over which a coarse-grained chromatin segment could extend before encountering a geometric or configurational obstruction. The expected free path incorporated two components: a nonlinear term representing congestion and a smaller linear term representing progressive channel narrowing,

$$\mu_L(w) = 1.85 - 1.28q(w) - 0.015(14 - w),$$

with L measured in micrometres. For each realization,

$$L_{w,r} \sim \mathcal{N}\big(\mu_L(w), \sigma_L^2(w)\big),$$

where

$$\sigma_L(w) = 0.10 + 0.04q(w).$$

To exclude nonphysical negative lengths, values below $0.22\ \mu$m were truncated at that lower boundary,

$$L_{w,r} = \max\big[L^*_{w,r}, 0.22\big].$$

This quantity provided the main geometric congestion readout used in panel A. Changes in L were interpreted operationally as changes in locally available trajectories rather than direct measurement of total chromatin density.

The use of a directional free-path variable was motivated by the geometric principle that the coexistence of multiple elongated structures with heterogeneous orientations imposes constraints beyond volume fraction alone (Guth, Solomon and Wang 2019). In our implementation, we did not explicitly reconstruct individual Kakeya tube families in three dimensions, but rather the finite-path statistic acted as a coarse-grained surrogate for the progressive restriction of tube-like chromatin trajectories under confinement (Wang and Zahl 2025). More generally, the set of biologically admissible configurations could be regarded as a structured subset of the much larger space of mathematically conceivable conformations, following the regularity perspective provided by o-minimal geometry (Bakker, Brunebarbe and Tsimerman 2022).

The first technical sequence to assign w, compute $q(w)$, sample V, calculate μ_L, sample L, enforce the physical lower bound and retain L for subsequent comparison with stochastic and topological variables.

Stochastic motion. Chromatin motion was modeled as a non-monotonic response to confinement. The intended behavior was increased exploratory motion under intermediate restriction followed by suppression under severe congestion (Deng 2012). For each width, the mean chromatin locus displacement over 60 seconds was

$$\mu_M(w) = 135 + 45\exp\left[-\left(\frac{w - 8.3}{2.2}\right)^2\right] - 70q(w),$$

© 2026 by the author(s). Distributed under a Creative Commons CC BY license.

Preprints.org (www.preprints.org) | NOT PEER-REVIEWED | Posted: 24 August 2026 doi:10.20944/preprints202608.1673.v1

with displacement measured in nanometres. Individual realizations followed

$$M_{w,r} \sim \mathcal{N}(\mu_M(w), 14^2) \text{ nm},$$

and values below 35 nm were excluded by

$$M_{w,r} = \max[M^*_{w,r}, 35].$$

The displacement model combined a Gaussian term centered at 8.3 μm representing an intermediate-confinement component, with an additional term proportional to $q(w)$ representing the severe-confinement component.

Randomness was introduced independently for every nucleus after conditioning on w, so that within-condition heterogeneity did not arise from deterministic interpolation (Deng, Nahmod and Yue 2022). The stochastic step was performed after the free-path calculation, but was not made directly dependent on the sampled free path. This distinction allowed both variables to respond to confinement without forcing a perfect correlation between them. The empirical distribution of $M_{w,r}$ across all 80 realizations was used at each width, thereby preserving the simulated variability associated with chromatin motion (Deng, Nahmod and Yue 2024).

Topology and curvature. Topological burden was represented as the number of encounters or entanglement-like constraints per 100 μm of coarse-grained chromatin centreline. For each confinement level,

$$\mu_T(w) = 3.1 + 12.5q(w) + 0.18(14 - w),$$

and the standard deviation changed with congestion according to

$$\sigma_T(w) = 1.0 + 0.9q(w).$$

Individual values were sampled as

$$T_{w,r} \sim \mathcal{N}\big(\mu_T(w), \sigma_T^2(w)\big)$$

and truncated at

$$T_{w,r} \geq 0.2$$

events per 100 μm. Chromatin curvature was modeled separately but driven by the same confinement state. Its mean was

$$\mu_\kappa(w) = 0.42 + 0.92q(w) + 0.018(14 - w),$$

with

$$\sigma_\kappa(w) = 0.055 + 0.04q(w),$$

and

$$\kappa_{w,r} \sim \mathcal{N}\big(\mu_\kappa(w), \sigma_\kappa^2(w)\big)\ \mu\text{m}^{-1}.$$

Values were restricted to

$$\kappa_{w,r} \geq 0.1\ \mu\text{m}^{-1}.$$

Therefore, the topology-curvature relation shown in panel C was not imposed through a direct algebraic mapping of T into κ. Instead, both quantities were generated independently conditional on the same confinement state. This preserved stochastic dispersion while producing a population-level association. Our simulation treated topological encounters as a countable coarse-grained proxy for constraints such as crossing avoidance, linking, loop interactions or entanglement-like interference. Curvature provided the corresponding geometric deformation variable. The numerical construction was motivated by the principle that topological constraints can impose irreducible geometric distortion, but our simulation did not assign a formal knot type or calculate an exact knot invariant for each realization (Pardon 2011).

Mechanical cost. Mechanical burden was represented by the minimum coarse-grained bending work required to sustain a sampled chromatin configuration. The simulated variable was expressed in piconewton-micrometres and was built to increase nonlinearly when the congestion variable became large,

$$\mu_E(w) = 0.75 + 4.8q(w)^{1.35} + 0.05(14 - w).$$

Its condition-dependent variability was

$$\sigma_E(w) = 0.33 + 0.25q(w),$$

giving

$$E_{w,r} \sim \mathcal{N}\big(\mu_E(w), \sigma_E^2(w)\big)\ \text{pN} \cdot \mu\text{m}.$$

© 2026 by the author(s). Distributed under a Creative Commons CC BY license.

Preprints.org (www.preprints.org) | NOT PEER-REVIEWED | Posted: 24 August 2026 doi:10.20944/preprints202608.1673.v1

Negative mechanical energies were excluded by

$$E_{w,r} = \max\left[E^*_{w,r}, 0.1\right].$$

The quantity can be related conceptually to the classical bending-energy functional of a semi-flexible polymer,

$$E_{\text{bend}} = \frac{B}{2}\int_0^L \kappa\,(s)^2\,ds,$$

where B is the bending rigidity, L is contour length and $\kappa(s)$ is local curvature. We did not integrate this expression explicitly for a reconstructed polymer chain, because the simulation did not generate a spatially resolved centreline for every chromosome. Instead, $E_{w,r}$ was used as an effective minimum work variable whose nonlinear dependence on congestion represented the increasing energetic cost of maintaining spatially restricted configurations. The exponent was selected to represent a nonlinear dependence on confinement severity, without assuming a linear relationship across the investigated range. The condition means and standard errors were

$$\text{SEM}(w) = \frac{s_w}{\sqrt{80}},$$

where s_w is the sample standard deviation across realizations at a given microchannel width.

Perturbation coupling. To represent the transition from local to increasingly collective chromatin rearrangements, we introduced a perturbation propagation length P, measured in micrometres. Its expected value was

$$\mu_P(w) = 0.85 + 5.6q(w)^{1.55},$$

with variability

$$\sigma_P(w) = 0.28 + 0.40q(w).$$

For each simulated nucleus,

$$P_{w,r} \sim \mathcal{N}\left(\mu_P(w), \sigma_P^2(w)\right)\ \mu\text{m},$$

subject to

$$P_{w,r} \geq 0.2\ \mu\text{m}.$$

An exponent greater than one was used to model spatial coupling as a nonlinear function of confinement severity, rather than assuming a linear dependence across the investigated range. This variable acted as a coarse-grained analogue of an influence radius: a small value represented a perturbation absorbed locally, whereas a larger value represented a displacement affecting progressively more distant chromatin regions. The construction was inspired by the logic of bounded versus increasing long-range dependence (Anari, Liu and Oveis Gharan 2020). Although the simulation did not explicitly construct a full influence matrix, the corresponding mathematical object would be

$$I_{ij} = \frac{\partial P\left(X_j = 1\right)}{\partial X_i},$$

where X_i and X_j denote occupation or state variables for chromatin regions. Then, spectral independence would be assessed through the largest eigenvalue (Anari, Liu and Oveis Gharan 2020),

$$\lambda_{\max}(I).$$

In our simulation, $P_{w,r}$ served as a physical-space surrogate for increasing influence range (Deng and Hani 2021). The complete realization-level values were retained so that this quantity could subsequently be related to the simulated functional endpoint rather than treated only as a group-level summary.

Damage readout. DNA-damage burden was represented as a discrete number of foci per nucleus. Because the outcome is count-valued, we sampled it from a Poisson distribution rather than from a Gaussian model. The Poisson intensity was linked to mechanical work, perturbation propagation and topological encounter burden,

$$\lambda_{w,r} = 2.2 + 0.55E_{w,r} + 0.38P_{w,r} + 0.10T_{w,r}.$$

The simulated number of damage foci was then

$$D_{w,r} \sim \text{Poisson}\left(\lambda_{w,r}\right).$$

This construction produced non-negative integer-valued outcomes while allowing several upstream variables to contribute simultaneously. No additional direct term for microchannel width was

© 2026 by the author(s). Distributed under a Creative Commons CC BY license.

Preprints.org (www.preprints.org) | NOT PEER-REVIEWED | Posted: 24 August 2026 doi:10.20944/preprints202608.1673.v1

included once E, P and T were specified, so confinement influenced the damage count indirectly through the simulated geometric, topological and mechanical state.

A first-order least-squares trend line was estimated as

$$\widehat{D} = \beta_0 + \beta_1 P,$$

with coefficients obtained by minimizing

$$\sum_{i=1}^{480} [D_i - (\beta_0 + \beta_1 P_i)]^2.$$

The fitted line was used only as a visualization of the simulated association and not as an inferential model for biological data. No hypothesis testing was performed on the synthetic realizations.

Overall, the final dataset contained for each nucleus: confinement width, nuclear volume, collision-free path, locus displacement, topological encounters, curvature, bending work, perturbation propagation length and damage-foci count.

Software toolsv. The simulation was implemented in Python. Numerical sampling and deterministic transformations were performed with NumPy, tabular data were organized and exported with pandas and all quantitative panels were generated with Matplotlib. The NumPy pseudorandom number generator was initialized with seed 20260813 to make the 480 realizations exactly reproducible. No external experimental dataset, image-analysis package, molecular-dynamics engine, polymer-simulation software or specialized chromatin reconstruction package was used in the numerical experiment.

Results

We report the behavior of 480 simulated nuclei generated across six confinement conditions, with 80 independent realizations at each microchannel width. Analyses addressed geometric freedom, stochastic chromatin motion, topological burden, curvature, mechanical work, perturbation propagation and DNA-damage burden.

Configurational restriction. Progressive confinement produced marked changes in local configurational freedom while nuclear volume changed comparatively modestly, although differences across confinement conditions were significant by one-way ANOVA ($p < 0.001$). Collision-free chromatin path length progressively decreased (Fig. A), with a significant overall confinement effect and a significant reduction during the transition from moderate to severe confinement ($p < 0.001$). Chromatin locus displacement followed a different, non-monotonic trajectory, initially increasing before declining under stronger confinement (Fig. B), with significant differences across conditions ($p < 0.001$). Topological encounters and median curvature increased with progressive restriction (Fig. C) and were strongly correlated across individual realizations.

Together, these distributions identify a configurational transition in which declining collision-free path length coincided with reversal of stochastic mobility and increasing topological and geometric restriction.

Mechanical coupling. Increasing restriction was associated with nonlinear changes in mechanical and collective variables. Minimum bending work increased with confinement (Fig. D), with significant differences among conditions and across the transition from moderate to severe confinement ($p < 0.001$). Collision-free path length and bending work were strongly inversely associated across individual realizations ($p < 0.001$). Perturbation propagation length also increased markedly under stronger confinement (Fig. E), with a significant overall confinement effect and an inverse association with collision-free path length ($p < 0.001$). DNA-damage burden increased across confinement conditions and correlated positively with perturbation propagation length ($p < 0.001$) (Fig. F).

Together, these realization-level relationships connect decreasing geometric freedom with increasing mechanical expenditure and the extension of perturbation coupling from predominantly local responses toward larger nuclear regions.

Our results show that simulated chromatin congestion was characterized by coordinated rather than uniform responses to confinement. Stochastic mobility initially increased and subsequently

© 2026 by the author(s). Distributed under a Creative Commons CC BY license.

Preprints.org (www.preprints.org) | NOT PEER-REVIEWED | Posted: 24 August 2026 doi:10.20944/preprints202608.1673.v1

declined, whereas topological encounters, curvature, mechanical work and perturbation range increased as collision-free configurational space contracted. The strongest changes occurred across the transition from moderate to severe confinement. The association between perturbation propagation and damage burden further links the modeled loss of local configurational independence with our functional readout.

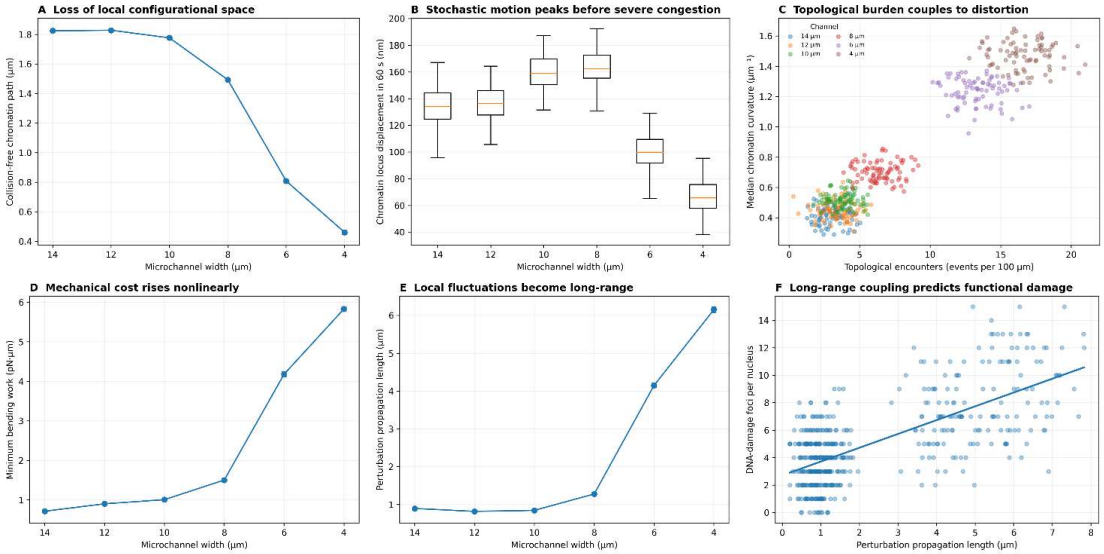


Figure 1. Geometric, topological, stochastic, mechanical and functional signatures of chromatin congestion. The simulation examines the progressive response of chromatin to nuclear confinement using 80 stochastic realizations at microchannel widths of 14, 12, 10, 8, 6 and 4 μm. **(A)** Collision-free chromatin path length, expressed in micrometres, decreases with progressive confinement. It represents the characteristic distance over which a chromatin segment can extend before encountering a spatial or configurational constraint, providing a geometric measure of the progressive loss of locally accessible configurations. **(B)** Chromatin locus displacement over 60 s, expressed in nanometres, shows a non-monotonic response to confinement. Initially, moderate restriction increases displacement, consistent with stochastic exploration of alternative spatial configurations, whereas severe confinement suppresses this mobility as accessible alternatives become progressively exhausted. Boxplots show the distributions across simulated realizations. **(C)** Relationship between topological encounters, expressed as events per 100 μm of chromatin centreline and median local chromatin curvature, expressed in μm^{-1}. Each point represents one simulated nucleus, with confinement conditions identified according to microchannel width. Increasing confinement shifts configurations toward greater topological encounter frequency and larger curvature, representing the conversion of spatial restriction into topologically constrained geometric deformation. **(D)** Minimum coarse-grained bending work required to maintain the chromatin configuration, expressed in pN·μm, increases nonlinearly with progressive confinement. Mechanical requirements are comparatively limited under weak and moderate restriction, but increase markedly at the narrowest microchannel widths as low-cost configurations become less accessible. **(E)** Perturbation propagation length, expressed in micrometres, measures the spatial extent over which a local chromatin displacement affects surrounding chromatin regions. Although perturbations are predominantly local under weak confinement, they propagate over progressively larger nuclear distances as confinement increases, representing increasing collective coupling among chromatin regions when alternative configurations become restricted. **(F)** Relationship between perturbation propagation length, expressed in micrometres and DNA-damage foci per nucleus. Each point represents one simulated realization and the fitted trend describes the association between the spatial propagation of chromatin disturbances and simulated damage burden. Configurations characterized by short-range perturbations display fewer DNA-damage foci, whereas increasingly long-range propagation is associated with a greater number of foci. Error bars in panels showing mean responses represent the standard error across the 80 stochastic realizations performed for each confinement condition.

Conclusions

© 2026 by the author(s). Distributed under a Creative Commons CC BY license.

Preprints.org (www.preprints.org) | NOT PEER-REVIEWED | Posted: 24 August 2026 doi:10.20944/preprints202608.1673.v1

We asked whether chromatin congestion can be described as a loss of accessible spatial configurations rather than solely as an increase in chromatin density or compaction and whether geometric restriction can become coupled to topological, mechanical and stochastic changes. Our simulations compared nuclei distributed across progressively narrower confinement conditions, while maintaining approximately stable chromatin content and nuclear volume. We found that collision-free path length progressively decreased, whereas chromatin motion showed a non-monotonic response, increasing under moderate confinement before declining sharply under stronger restriction. The transition from moderate to severe confinement was characterized by pronounced increases in topological encounters, curvature, minimum bending work and perturbation propagation length. Still, longer propagation distances were associated with greater simulated DNA-damage burden. Within the assumptions of our model, these findings are consistent with a transition from predominantly local accommodation of spatial restriction to increasingly collective responses when the available configurations become restricted.

Our approach differs from established methods primarily in what aspect of genome organization is quantified. Hi-C and Micro-C measure contact probabilities but do not determine how many alternative spatial arrangements are physically accessible (Krietenstein et al. 2020; Jerkovic and Cavalli 2021; Liu, Zhu, and Wang 2024; Yang and Hansen 2024; Zhu, Liu, and Wang 2024). Chromosome tracing and super-resolution microscopy reconstruct realized spatial relationships but do not quantify the configurations excluded by nuclear geometry (Nir et al. 2018; Rajpurkar et al. 2021; Hafner et al. 2023; Lacen and Lee 2024). Polymer simulations describe possible chain conformations, whereas molecular-dynamics and coarse-grained models examine how specified interactions and physical parameters generate particular structural behaviors. In contrast, we focus on the progressive reduction of the configurational possibilities available to chromatin as nuclear space becomes restricted. Rather than considering geometry, topology, stochastic motion and mechanics separately, we examine how spatial competition, topological obstruction, configurational exploration and mechanical cost change together during the same confinement process. Thus, established approaches primarily characterize observed or simulated chromatin structures and the mechanisms producing them, whereas our analysis asks a complementary question: how progressively restrictive nuclear geometry reduces the range of alternative physically admissible chromatin configurations and changes the capacity of the genome to accommodate further spatial perturbations.

Our study has limitations. Our simulations are hypothesis-generating rather than reconstructions of experimental nuclei and model coefficients were not estimated from biological measurements. Absolute values and apparent confinement thresholds should not be interpreted as experimentally established. Because several variables depend on confinement, some correlations may arise from this shared determinant rather than direct causal interactions. Topological encounters, bending work and perturbation propagation were represented by coarse-grained quantities rather than explicit topological invariants, experimentally measured chromatin mechanics or spectral influence matrices. The damage model excludes repair kinetics, cell-cycle state and chromatin composition. We did not examine DNA without nuclear enclosure, leaving unresolved which predicted behaviors specifically depend on the nuclear boundary. Whether congestion has a reproducible critical regime, is reversible or depends on the mechanism of confinement is not tackled. Negative dependence, entropy-based ensembles and log-concavity were used as mathematical interpretations rather than directly measured properties of the simulated chromatin. Finally, our coarse-grained polymer description does not explicitly include topological friction, which can generate heterogeneous and subdiffusive polymer dynamics (Wang et al. 2026), or cooperative mechanisms capable of producing long-range extended polymer configurations (Chen et al. 2026).

Our approach suggests experimentally testable hypotheses. First, progressive confinement should produce a non-monotonic mobility response rather than a simple decrease: in our simulation, mean 60-second locus displacement increased from approximately 135 nm at 14 micrometres to approximately 164 nm at 8 micrometres before falling below 100 nm at 6 micrometres. Live-cell tracking across graded microchannels could test both the existence and position of this maximum.

© 2026 by the author(s). Distributed under a Creative Commons CC BY license.

Preprints.org (www.preprints.org) | NOT PEER-REVIEWED | Posted: 24 August 2026 doi:10.20944/preprints202608.1673.v1

Second, geometric restriction should change more strongly than nuclear volume. Between the widest and narrowest conditions, the simulated collision-free path decreased by approximately 75 percent, while mean nuclear volume changed by only about 3 percent. Three-dimensional chromosome tracing could determine whether an analogous disproportion exists experimentally.

Third, mechanical cost should exhibit nonlinear rather than proportional scaling with confinement: simulated bending work increased approximately fourfold between 8 and 6 micrometres despite only a 25 percent reduction in channel width. Measurements combining controlled confinement with chromatin curvature and nuclear force measurements could examine this scaling.

Fourth, the spatial influence of a local perturbation should expand sharply near severe congestion; simulated propagation increased from approximately 1.3 micrometres at 8 micrometres to approximately 4.1 micrometres at 6 micrometres. Targeted chromatin displacement followed by high-speed imaging could directly estimate this length.

Fifth, nuclei matched for DNA content and similar nuclear volume should display different damage burdens when perturbation propagation differs; in our simulation, propagation length and damage-foci number showed a correlation of approximately 0.69.

Future empirical research should replace prescribed distributions with parameters inferred from imaging, micromechanical measurements and chromosome-conformation data. Still, spatially resolved polymer simulations could explicitly calculate entanglement, curvature, forces and influence matrices and determine whether a critical transition persists without imposing its functional form.

Practical applications would depend on experimental validation of these predictions. A congestion-based description could complement conventional nuclear phenotyping by providing measurements sensitive to the capacity of chromatin to reorganize under imposed deformation. These measurements could be incorporated into microfluidic assays of cells undergoing narrow-pore migration, where nuclear passage can be monitored together with chromatin dynamics and subsequent recovery. The same principle could support comparisons of cells exposed to mechanical compression, altered extracellular stiffness or pharmacological manipulation of chromosome-organizing proteins. In screening experiments, interventions could be ranked according to their effects on configurational mobility and recovery trajectories rather than exclusively according to static nuclear morphology. Congestion-related measurements could also be incorporated into image-analysis pipelines combining nuclear shape, locus trajectories, chromosome tracing and damage markers at single-cell resolution, allowing heterogeneous cell populations to be stratified according to their response to controlled mechanical challenges.

In conclusion, we introduced the concept of chromatin congestion as the progressive restriction of configurations available to the genome under nuclear confinement. Our simulations connect this loss of configurational freedom with changes in chromatin mobility, topology, mechanical cost and perturbation propagation. Our quantifiable predictions provide a basis for testing whether congestion stands for a distinct organizational property of the three-dimensional genome.

Author Contributions: The Author performed: study concept and design, acquisition of data, analysis and interpretation of data, drafting of the manuscript, critical revision of the manuscript for important intellectual content, statistical analysis, obtained funding, administrative, technical and material support, study supervision.

Funding: This research did not receive any specific grant from funding agencies in the public, commercial or not-for-profit sectors.

Institutional Review Board Statement: Ethics approval statement is not applicable. This research does not contain any studies with human participants or animals performed by the Author.

Informed Consent Statement: The Author transfers all copyright ownership, in the event the work is published. The undersigned author warrants that the article is original, does not infringe on any copyright or other proprietary right of any third part, is not under consideration by another journal and has not been previously published.

© 2026 by the author(s). Distributed under a Creative Commons CC BY license.

Preprints.org (www.preprints.org) | NOT PEER-REVIEWED | Posted: 24 August 2026 doi:10.20944/preprints202608.1673.v1

Data Availability Statement: All data and materials generated or analyzed during this study are included in the manuscript. The Author had full access to all the data in the study and took responsibility for the integrity of the data and the accuracy of the data analysis.

Acknowledgments: none. During the preparation of this work, the author used ChatGPT 5.3 to assist with data analysis and manuscript drafting and to improve spelling, grammar and general editing. After using this tool, the author reviewed and edited the content as needed, taking full responsibility for the content of the publication.

Conflicts of Interest: The Author does not have any known or potential conflict of interest including any financial, personal or other relationships with other people or organizations within three years of beginning the submitted work that could inappropriately influence or be perceived to influence their work. The views expressed are those of the author and do not necessarily reflect those of the affiliated institutions.

References

1. Agarwal, Siddharth, Melissa A. Klocke, Passa E. Pungchai, and Elisa Franco. 2021. "Dynamic Self-Assembly of Compartmentalized DNA Nanotubes." *Nature Communications* 12: 3557. https://doi.org/10.1038/s41467-021-23850-1.
2. Anari, Nima, Kuikui Liu and Shayan Oveis Gharan. 2020. *Spectral Independence in High-Dimensional Expanders and Applications to the Hardcore Model*. arXiv:2001.00303. https://doi.org/10.48550/arXiv.2001.00303.
3. Anari, Nima and Shayan Oveis Gharan. 2015. *The Kadison-Singer Problem for Strongly Rayleigh Measures and Applications to Asymmetric TSP*. arXiv:1412.1143. https://doi.org/10.48550/arXiv.1412.1143.
4. Anari, Nima, Shayan Oveis Gharan and Cynthia Vinzant. 2018. "Log-Concave Polynomials I: Entropy and a Deterministic Approximation Algorithm for Counting Bases of Matroids." In *2018 IEEE 59th Annual Symposium on Foundations of Computer Science (FOCS)*.
5. Bakker, Benjamin, Yohan Brunebarbe and Jacob Tsimerman. 2022. "o-Minimal GAGA and a Conjecture of Griffiths." arXiv:1811.12230. https://doi.org/10.48550/arXiv.1811.12230.
6. Bakker, Benjamin, Thomas W. Grimm, Christian Schnell and Jacob Tsimerman. 2023. "Finiteness for Self-Dual Classes in Integral Variations of Hodge Structure." *Épijournal de Géométrie Algébrique*, Special Volume in Honour of Claire Voisin. https://doi.org/10.46298/epiga.2023.specialvolumeinhonourofclairevoisin.9626.
7. Beel, Andrew J., Pierre-Jean Matteï, and Roger D. Kornberg. 2026. "The Eukaryote Chromosome, a Two-State System with Interconversion by a Volume Phase Transition." *Science* 393 (6812). doi:10.1126/science.adz1083.
8. Borcea, Julius, Petter Brändén and Thomas M. Liggett. 2009. "Negative Dependence and the Geometry of Polynomials." *Journal of the American Mathematical Society* 22: 521–567.
9. Chen, Min, Dongyang Wang, Ye Zou, Changsheng Chen, Xixian Yang, et al. 2026. "Long-Range Extended Chains Arising from Polymerization-Driven Spontaneous Assembly." *Science* 393 (6807): 172–177. doi:10.1126/science.aef1777.
10. Crosetto, Nicola, and Magda Bienko. 2020. "Radial Organization in the Mammalian Nucleus." *Frontiers in Genetics* 11: 33. doi:10.3389/fgene.2020.00033.
11. Deng, Yu. 2012. "Two-Dimensional Nonlinear Schrödinger Equation with Random Radial Data." *Analysis & PDE* 5 (5): 913–960. https://doi.org/10.2140/apde.2012.5.913.
12. Deng, Yu and Zaher Hani. 2021. "On the Derivation of the Wave Kinetic Equation for NLS." *Forum of Mathematics, Pi* 9: e6. https://doi.org/10.1017/fmp.2021.6.
13. Deng, Yu and Zaher Hani. 2024a. "Full Derivation of the Wave Kinetic Equation." *Inventiones Mathematicae* 237: 1015–1141. https://doi.org/10.1007/s00222-023-01189-2.
14. Deng, Yu and Zaher Hani. 2024b. "Long Time Justification of Wave Turbulence Theory." arXiv:2311.10082.
15. Deng, Yu andrea R. Nahmod and Haitian Yue. 2022. "Random Tensors, Propagation of Randomness and Nonlinear Dispersive Equations." *Inventiones Mathematicae* 228: 539–686. https://doi.org/10.1007/s00222-021-01084-8.

© 2026 by the author(s). Distributed under a Creative Commons CC BY license.

Preprints.org (www.preprints.org) | NOT PEER-REVIEWED | Posted: 24 August 2026 doi:10.20944/preprints202608.1673.v1

16. Deng, Yu andrea R. Nahmod and Haitian Yue. 2024. "Invariant Gibbs Measures and Global Strong Solutions for Nonlinear Schrödinger Equations in Dimension Two." *Annals of Mathematics* 200 (2): 399–486. https://doi.org/10.4007/annals.2024.200.2.1.
17. Grant, Zoe L., Shuzhen Kuang, Shu Zhang, Abraham J. Horrillo, Zhe Chen, et al. 2026. "Dose-Dependent Sensitivity of Human Three-Dimensional Chromatin to a Heart Disease-Linked Transcription Factor." *Science* 393 (6809). doi:10.1126/science.adv5434.
18. Guth, Larry, Noam Solomon and Hong Wang. 2019. "Incidence Estimates for Well Spaced Tubes." *Geometric and Functional Analysis* 29: 1844–1863. https://doi.org/10.1007/s00039-019-00519-y.
19. Hafner, A., M. Park, S. E. Berger, S. E. Murphy, E. P. Nora, and A. N. Boettiger. 2023. "Loop Stacking Organizes Genome Folding from TADs to Chromosomes." *Molecular Cell* 83 (9): 1377–1392.e6. https://doi.org/10.1016/j.molcel.2023.04.008.
20. Jerkovic, I., and G. Cavalli. 2021. "Understanding 3D Genome Organization by Multidisciplinary Methods." *Nature Reviews Molecular Cell Biology* 22 (8): 511–28. https://doi.org/10.1038/s41580-021-00362-w.
21. Krietenstein, N., S. Abraham, S. V. Venev, N. Abdennur, J. Gibcus, T. S. Hsieh, K. M. Parsi, et al. 2020. "Ultrastructural Details of Mammalian Chromosome Architecture." *Molecular Cell* 78 (3): 554–565.e7. https://doi.org/10.1016/j.molcel.2020.03.003.
22. Lacen, A. N., and H. T. Lee. 2024. "Tracing the Chromatin: From 3C to Live-Cell Imaging." *Chemical & Biomedical Imaging* 2 (10): 659–82. https://doi.org/10.1021/cbmi.4c00033.
23. Liu, T., H. Zhu, and Z. Wang. 2024. "Learning Micro-C from Hi-C with Diffusion Models." *PLoS Computational Biology* 20 (5): e1012136. https://doi.org/10.1371/journal.pcbi.1012136.
24. Nir, G., I. Farabella, C. Pérez Estrada, C. G. Ebeling, B. J. Beliveau, H. M. Sasaki, S. D. Lee, et al. 2018. "Walking along Chromosomes with Super-Resolution Imaging, Contact Maps, and Integrative Modeling." *PLoS Genetics* 14 (12): e1007872. https://doi.org/10.1371/journal.pgen.1007872.
25. Oveis Gharan, Shayan, Amin Saberi and Mohit Singh. 2011. "A Randomized Rounding Approach to the Traveling Salesman Problem." In *2011 IEEE 52nd Annual Symposium on Foundations of Computer Science*.
26. Pardon, John. 2011. "On the Distortion of Knots on Embedded Surfaces." *Annals of Mathematics* 174 (1): 637–646. https://doi.org/10.4007/annals.2011.174.1.21.
27. Patta, Indumathi, Maryam Zand, Lindsay Lee, Shreya Mishra, Alexandra Bortnick, et al. 2024. "Nuclear Morphology Is Shaped by Loop-Extrusion Programs." *Nature* 627: 196–203. doi:10.1038/s41586-024-07086-9.
28. Pulupa, Joan, Natalie G. McArthur, Olga Stathi, Miao Wang, Marianna Zazhytska, et al. 2025. "Solid Phase Transitions as a Solution to the Genome Folding Paradox." *Nature* 643: 820–829. https://doi.org/10.1038/s41586-025-09043-6.
29. Rajpurkar, A. R., L. J. Mateo, S. E. Murphy, and A. N. Boettiger. 2021. "Deep Learning Connects DNA Traces to Transcription to Reveal Predictive Features beyond Enhancer-Promoter Contact." *Nature Communications* 12 (1): 3423. https://doi.org/10.1038/s41467-021-23831-4.
30. Soman, Aghil, Sook Yi Wong, Nikolay Korolev, Wahyu Surya, Simon Lattmann, et al. 2022. "Columnar Structure of Human Telomeric Chromatin." *Nature* 609: 1048–1055. https://doi.org/10.1038/s41586-022-05236-5.
31. Yang, J. H., and A. S. Hansen. 2024. "Enhancer Selectivity in Space and Time: From Enhancer-Promoter Interactions to Promoter Activation." *Nature Reviews Molecular Cell Biology* 25 (7): 574–91. https://doi.org/10.1038/s41580-024-00710-6.
32. Wang, Hong and Joshua Zahl. 2025. "Volume Estimates for Unions of Convex Sets and the Kakeya Set Conjecture in Three Dimensions." arXiv:2502.17655. https://doi.org/10.48550/arXiv.2502.17655.
33. Wang, Zhenhua, Yuyuan Lu, Lijia An, and Zhen-Gang Wang. 2026. "Topological Friction: Insight from Dynamics of a Test Chain in a Fixed-Topology Polymer Network." *Physical Review Letters* 136: 248101. doi:10.1103/cpp1-j6lc.
34. Zenk, Fides, Yinxiu Zhan, Pavel Kos, Eva Löser, Nazerke Atinbayeva, et al. 2021. "HP1 Drives De Novo 3D Genome Reorganization in Early *Drosophila* Embryos." *Nature* 593: 289–293. https://doi.org/10.1038/s41586-021-03460-z.

© 2026 by the author(s). Distributed under a Creative Commons CC BY license.

Preprints.org (www.preprints.org) | NOT PEER-REVIEWED | Posted: 24 August 2026 doi:10.20944/preprints202608.1673.v1

35. Zheng, Hui, and Wei Xie. 2019. "The Role of 3D Genome Organization in Development and Cell Differentiation." *Nature Reviews Molecular Cell Biology* 20: 535–550. https://doi.org/10.1038/s41580-019-0132-4.
36. Zhou, Huabin, Jan Huertas, M. Julia Maristany, Kieran Russell, June Ho Hwang, et al. 2025. "Multiscale Structure of Chromatin Condensates Explains Phase Separation and Material Properties." *Science* 390 (6777). https://doi.org/10.1126/science.adv6588.
37. Zhu, H., T. Liu, and Z. Wang. 2024. "C2c: Predicting Micro-C from Hi-C." *Genes* 15 (6): 673. https://doi.org/10.3390/genes15060673.

Disclaimer/Publisher's Note: The statements, opinions and data contained in all publications are solely those of the individual author(s) and contributor(s) and not of MDPI and/or the editor(s). MDPI and/or the editor(s) disclaim responsibility for any injury to people or property resulting from any ideas, methods, instructions or products referred to in the content.

© 2026 by the author(s). Distributed under a Creative Commons CC BY license.